Characterisation of Layered Scattering Media Using Polarized Light

by Ian M. Stockford, MEng

Thesis submitted to
The University of Nottingham for the degree of
Doctor of Philosophy, September 2004

The University of
Nottingham

Abstract

This thesis investigates the properties of backscattered polarized light from layered scattering media with a view to application in the imaging of *in-vivo* skin for medical application. The research includes investigation of numerically simulated samples, tissue phantoms and *in-vivo* tissue.

The aim of the early research is to identify the differences in behaviour between initially linearly and circularly polarized illumination concerning the rates of depolarization with scattering. Initial examination is made through Monte Carlo simulations. The analysis yields results which indicate, for forward scattering media, circular polarizations maintain their initial state to greater depths within a scattering medium than linearly polarized light. This result is exploited to show sensitivity of the different polarizations to different layers within a medium and indicates the potential to achieve coarse optical sectioning.

These fundamental properties are extended to a full field imaging arrangement, using both simulated and experimental results to illustrate polarization gating to perform sub-surface object imaging in a medium composed of uniform scatterers. The concepts are extended to imaging an *in-vivo* sample. The removal of multiple scatter and surface reflections is performed using a combination of linearly and circularly polarized illumination coupled with image subtraction, to provide a sub-surface, localised tissue image. This provides an improvement on currently applied techniques, which use linearly polarized light and the application of a flat glass plate and matching fluid.

To exploit the spectral properties of tissue, the development and construction of a fully automated, multiple wavelength, polarization imaging system, suitable for testing in a clinical setting is presented.

Theoretical investigation into the potential to perform the determination of the optical properties of a two layered sample, using simulated results in-keeping with the system's detection regime, is performed. It is illustrated that the variation of top layer thickness, bottom layer scattering, top and bottom layer absorption coefficient provides well-conditioned data when combining polarization and spectral information.

Acknowledgements

I would like to thank my supervisor Dr Steve Morgan for his guidance, enthusiasm and support throughout the project.

I would also like to thank Dr John Walker and Dr John Crowe for useful meetings early in the project, along with Dr Peter Chang for supplying the polarized light Monte Carlo engine, applied in this study. Thanks must also go to Dr Nick Sawyer and Dr Mark Pitter for their general day to day advice and, of course, Graham Stabler for his assistance with design and construction of the automated system components along with useful discussions and endless philosophical insight.

I would like to acknowledge the Engineering and Physical Science Research Council for supplying a studentship and thank Dr Andrew Affleck of Queens Medical Centre Dermatology Clinic for enduring the ethical approval process and for useful discussions on dermatological issues.

I would like to say thank you to my family for their encouragement, support and endless loans.

Finally, I'd like to thank Jessica for her love, support and making sure I never forget how to smile.

Contents

Chapter 1

Introduction

1.1 Background

Problems involving the propagation of light through media containing many small inhomogeneities occur frequently in applications utilising optical solutions. These applications can be wide ranging and may involve attempts to determine the properties of an object through turbid sea water[1], or perform the retrieval of information at a cellular level from a biomedical sample[2].

Whatever the scale of the final application, the fundamental issues are the same where the propagation of light in media such as these are concerned. Problems arise due to the scattering effect caused by the small inhomogeneities resulting in an uncertainty determining the path of propagation taken by incident light[3]. This leads to a lack of knowledge concerning the exact regions from which light has emanated or the exact volumes through which the light has passed. These uncertainties manifest themselves as a loss of resolution in both lateral directions and in terms of depth confinement in a reflection arrangement. In an imaging regime this would lead to a lack of definition of the imaged object or, in a problem concerned with the characterisation of the medium's properties, uncertainty would arise when determining the regions probed by the propagating light.

An illustration of the loss in lateral resolution due to scattering, which would form a

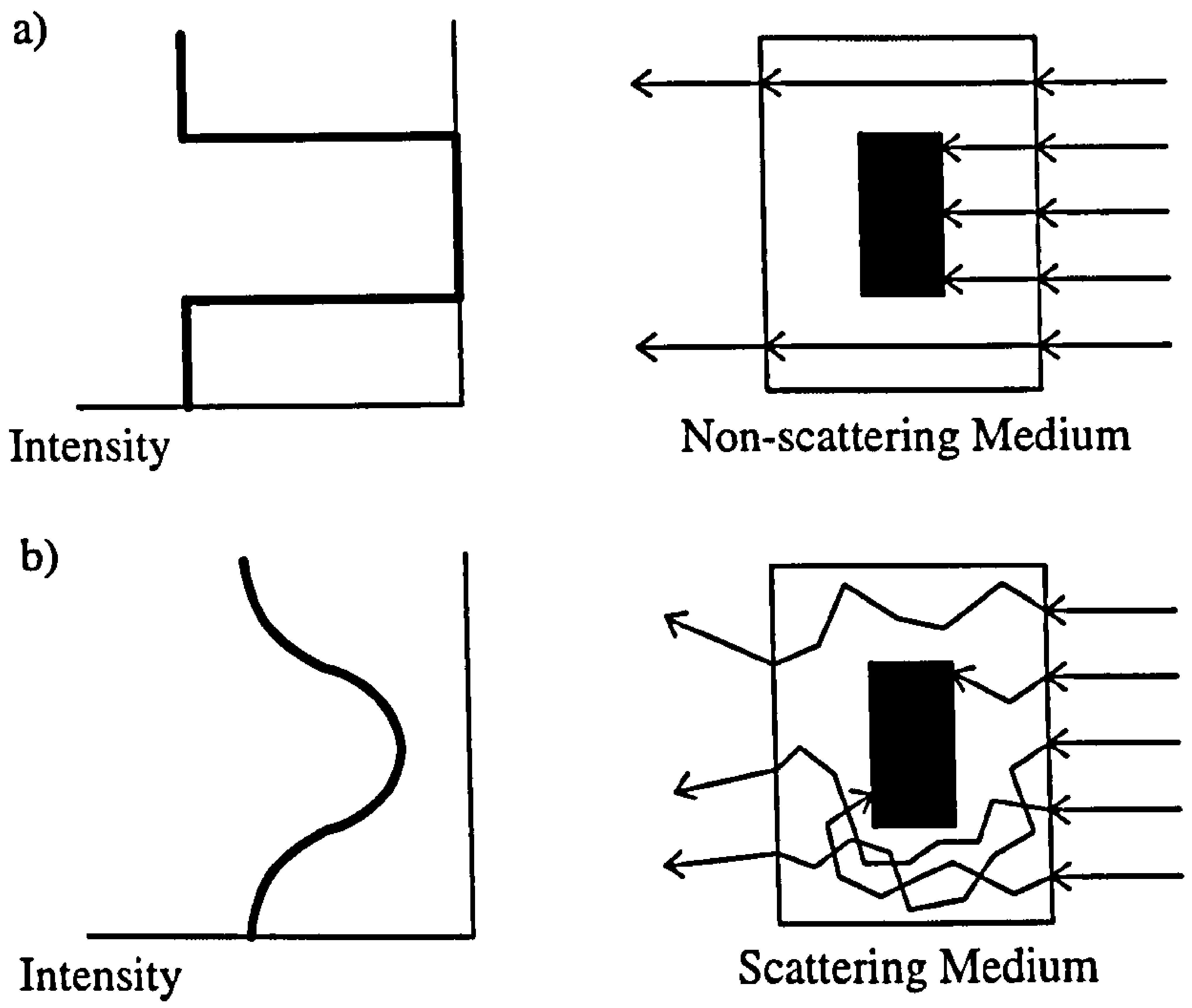

Figure 1.1: *In a non-scattering system a) an undeviated path through the medium is possible, producing a high resolution shadowgraph of any encountered feature. This is in contrast to b) a scattering medium, where the path of propagation is ill-defined and therefore feature edges become increasingly unclear.*

problem when trying to image through a turbid medium, can be seen in figure 1.1.

One area where scattering theory is relevant is in biomedical optics due to the naturally occurring cellular, and hence inhomogeneous, nature of biological tissue[4, 5]. This study is more specifically concerned with the effect of human skin tissue on the propagation of light. There are many reasons why knowledge of this behaviour is important, not least of which is to aid the development of optical instruments for use in the diagnosis of medical conditions. Such applications are discussed in section 1.3.

Due to the issues considered here being concerned with the examination of skin *in-vivo*, it is necessary to analyse light that is backscattered from the area of interest as opposed to light that is transmitted through the sample (as was the case in figure 1.1). Therefore, resolution in terms of depth becomes a significant consideration in addition to that in the lateral directions, especially when analysing layered media such as the skin. For this reason it would be highly desirable to be able to localise light in terms of the depth to which it has visited within a sample. Such issues form a large part of the early research.

Even though the investigation of the skin is subject to the problems outlined above, optical techniques have one overriding advantage making their application highly desirable in a medical setting; the fact that they are non-invasive. This means that any experimental procedure can be performed *in-vivo* with no discomfort being experienced by the patient due to the examination procedure. This therefore allows any such technique to be readily applied in a medical diagnostic tool, with the examination of a healthy subject causing no detriment to the patient.

The research performed in this thesis aims to move toward the non-invasive characterisation of *in-vivo* human skin tissue to aid the diagnostic practices of a clinical dermatologist. The ultimate aim is to provide a system which can extract accurate information concerning the structure of the examined tissue from a well-defined region.

1.2 Optical Properties of Scattering Media

Problems concerning scattering media are not solely prevalent when attempting to image an object through a scattering medium. It may be the case, as it is in many tissue analysis applications, that it is the properties of the medium itself that is of interest. It is intuitive to expect a physical difference in structure between two samples to result in a difference in the way that light interacts with those samples. Therefore, if the optical properties of a sample can be determined, this is the first step toward gaining knowledge concerning the sample's morphology, or at least some sensitivity to its change. The presence of scattering is therefore used as a tool for characterisation in this case as the levels of scattering may indicate the physical properties. It should be noted however that localisation is still important to allow determination of the regions of sample which possess the determined properties and to minimise the contributions from regions in which we have no interest.

As discussed above, the aim of the research is to enable the determination of the properties of tissue. Therefore, it is necessary to define parameters by which the scattering media considered here can be quantified. Such properties are discussed in the following section.

1.2.1 Scattering Properties

The scattering coefficient, μ_s, provides an indication of the mean number of scattering events that are encountered per unit distance of propagation. Therefore, the inverse of this value represents the mean distance between scattering events, or as it is more commonly known, the mean free path (MFP). Counter-intuitively, these values are not solely dependent on the physical geometry of a sample's internal structure, i.e. scatterers per unit volume, but are also dependent on the wavelength of light used for examination. This is due to the subtleties of particle light scattering and, considering a single particle of diameter appropriate here, more specifically on Mie theory[3] which is discussed in section 3.2.1. However, taking a qualitative approach, understanding of this dependence comes from the knowledge that the *geometric* cross-section of a particle does not fully define its region of influence on propagating radiation. Mie theory dictates that the volume over which the particle has influence is defined by the particle's *scattering* cross-section, which is greatly wavelength dependent. It is the variation of this value with wavelength that will alter the observed MFP.

Another parameter which has a large influence on the scattering properties of a medium is the anisotropy factor, g. This value is the mean cosine of the scattering angle subtended by the incoming and outgoing paths due to a photon-particle collision, as shown in figure 1.2. Therefore, by definition, g falls within the range -1 (indicating direct backscatter) to 1 (direct forward scatter). This value is derived from the phase function (figure 1.2) of a particle which is also defined by Mie theory. The phase function defines the angular distribution of luminous intensity as a function of azimuthal angle, θ. When used in a

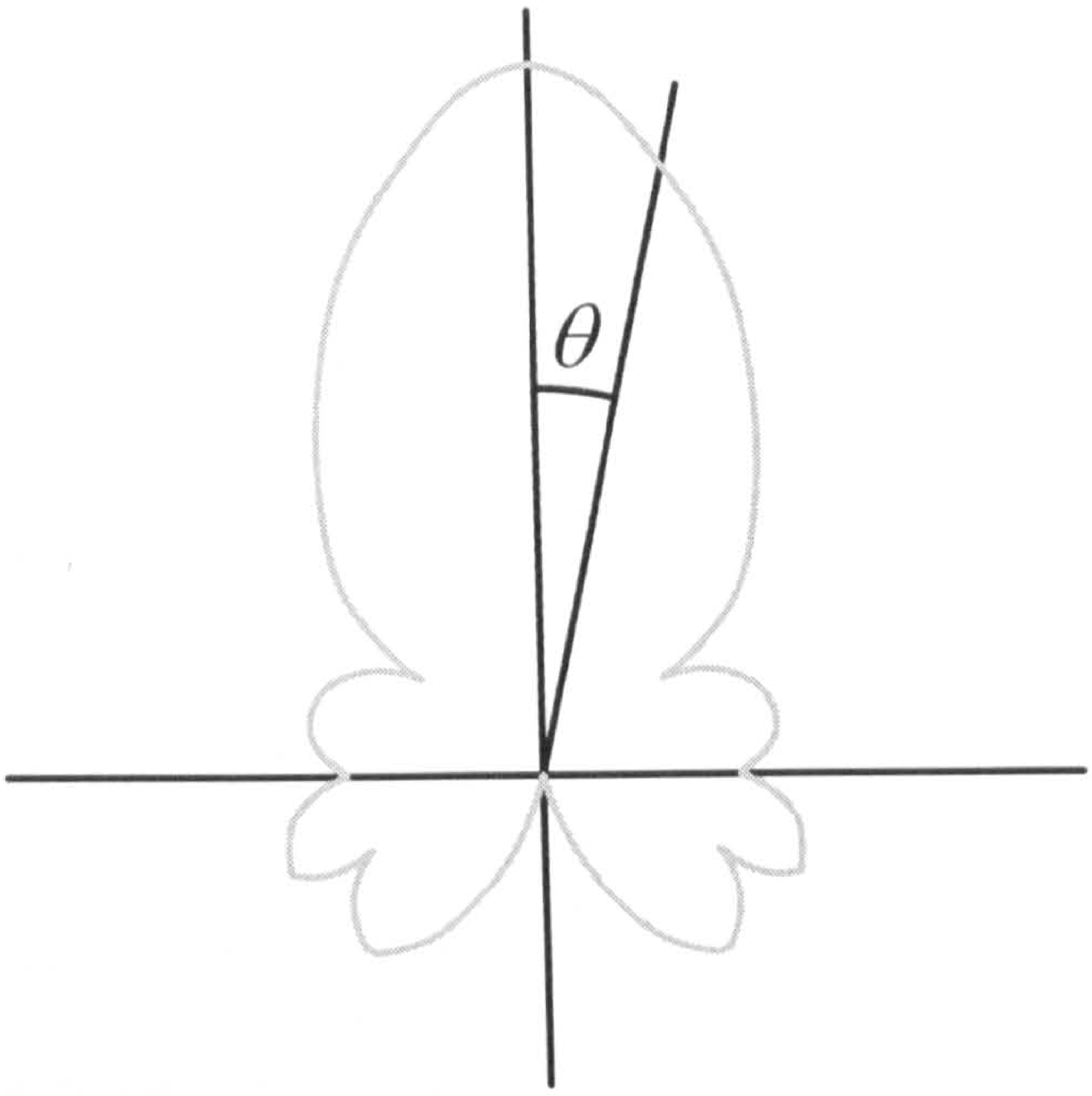

Figure 1.2: *An example phase function indicating the mean scattering angle.*

modelled situation it can represent the probability density function that a photon moving in direction s is scattered into another direction s'. The anisotropy factor has dependencies on the refractive index mismatch between the particle and its surrounding medium, along with the size parameter, x, associated with the illuminated scatterer. This value, x, is defined in equation 1.1.

$$x = \frac{2\pi d}{\lambda} \tag{1.1}$$

where d is the geometric particle diameter and λ is the wavelength of the incident light.

The two values μ_s and g are frequently combined in the form of the reduced scattering coefficient, μ_s'. This value is defined as:

$$\mu_s' = \mu_s(1 - g) \tag{1.2}$$

and represents the mean distance for which light will propagate before having its direction randomised[6].

1.2.2 Absorption Properties

When light interacts with atoms within the medium through which it is propagating, the electronic state of the atom can be changed due to the incident photon energy matching that of an electron transition to an excited state. This leads to a transfer of energy between the electromagnetic radiation and the atoms in the medium, observable as thermal energy. This energy transfer is observed as a reduction in the intensity of the light and represents optical absorption.

The absorption coefficient, μ_a, represents the bulk effect that the medium has on the intensity of the propagating light. A high value of μ_a indicates a resulting lower intensity after traveling through a unit distance in comparison with a medium of lower absorption. The intensity of light transmitted through a medium is calculated from the Lambert-Beer law shown in equation 1.3.

$$I = I_0 \exp(-\mu_a t) \tag{1.3}$$

where I is the resulting intensity of light after propagation, I_0 is the initial illumination intensity and t is the optical pathlength. This parameter is also wavelength sensitive due to the variation of energy with optical frequency. The variation of μ_a with wavelength traces out the medium specific absorption spectrum. The problem posed in a scattering regime is that t is generally unknown and therefore determination of the absorption coefficient is not trivial.

1.3 Medical Application

As mentioned previously in the introduction to this chapter, systems used to extract the optical, and hence physical, properties of a scattering sample can be readily applied in medical instrumentation. Two such applications for investigation of the skin are considered in this section. However, for completeness and to aid the understanding of both the clinical

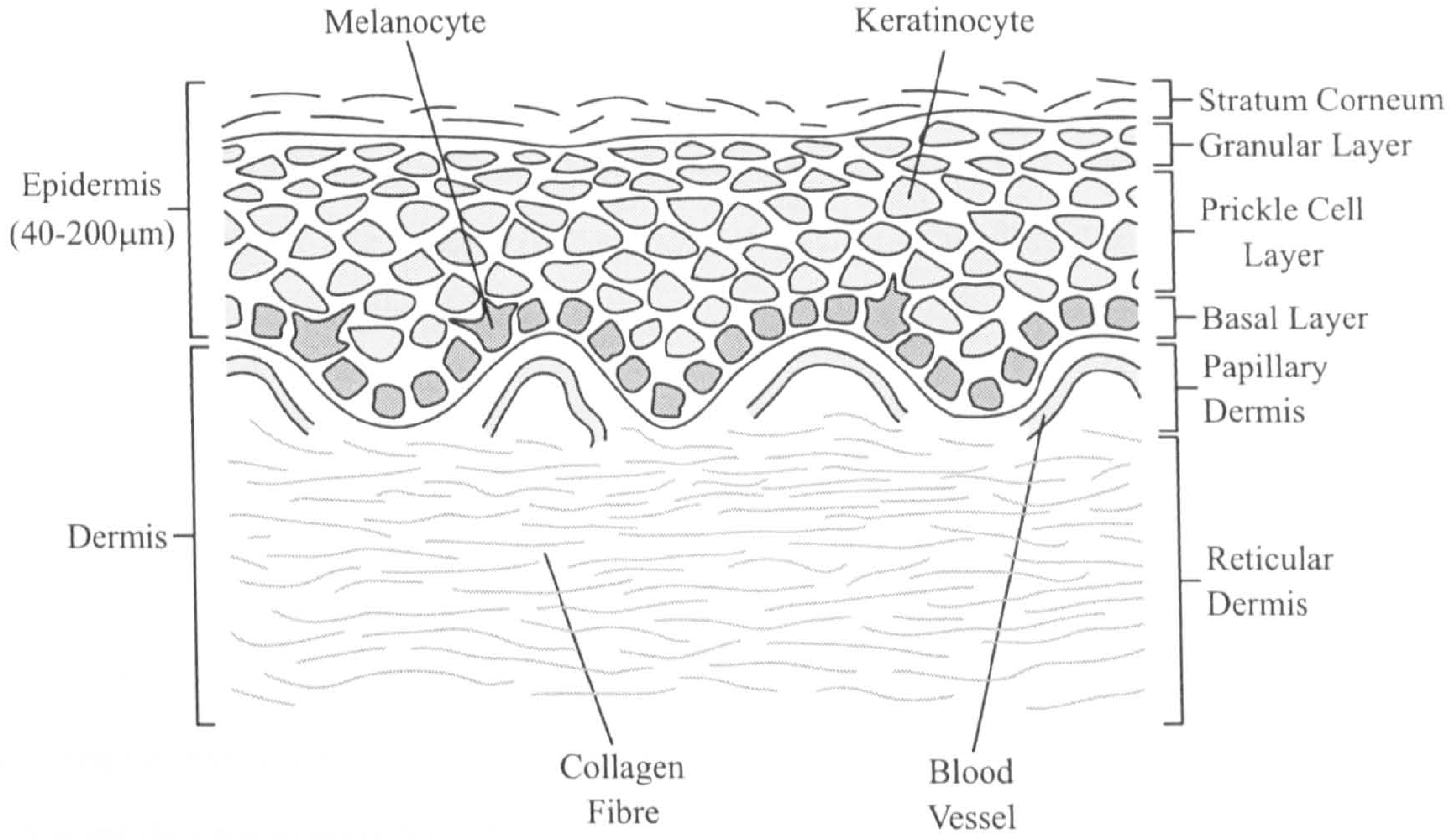

Figure 1.3: *A simplified model of the structure of superficial skin tissue.*

scenarios and the models of skin tissue developed later in the study, a brief introduction into the histology of healthy skin tissue is necessary.

1.3.1 Structure of the Skin

The superficial regions of skin tissue can be broadly divided into two layers; the outermost being the epidermis and, beneath this, the dermis. A simplified representation of the skin's structure in cross-section is shown in figure 1.3.

The epidermis forms the protective barrier of the skin, with the outermost layer being the stratum corneum, composed of keratin, which gives the skin its slightly scaly appearance. The main body of the epidermis beneath this layer is highly cellular and is mainly composed of keratinocytes (responsible for the production of protective keratin). These regions are termed the granular and prickle layers. The basal layer forms the lower regions of the epidermis and it is in this region where melanocytes are located. Melanocytes are responsible for the production of melanin, which is the main pigment found in human skin tissue[4]. The levels of pigment are controlled by the number of melanosomes active within the melanocytes.

The structure of the underlying dermis is not cellular like the epidermis, but has a largely fibrous structure formed by collagen. In the upper regions of the dermis, termed the papillary dermis, the presence of functional structures such as blood vessels and nerves indent into the epidermis forming the oscillating epidermal/dermal boundary shown in figure 1.3. At deeper levels within the dermis (reticular dermis) are the collagen fibres which form the main structure of the skin. This is along with blood vessels and many other appendages which have been omitted from the above diagram (and future consideration in this study) for simplicity. A more complete discussion of the histology of human skin can be found in [7].

1.3.2 Clinical Relevance

If the optical properties of the skin can be established, the development of dermatological diagnostic tools becomes feasible. The main field of application addressed by the techniques presented in this study are pigmented skin lesions, and more specifically skin cancer. Skin cancer is rapidly on the increase due to many environmental, lifestyle and social developments. In a study performed by Cancer Research UK[1] is was reported that in the UK in the year 2000, there were nearly 7,000 diagnosed cases of malignant melanoma, of which 1,640 proved fatal. More than 62,000 incidences of non-melanoma skin cancers were also reported. Similar trends are mirrored across numerous other studies[8, 9, 10]. Due to the increase in the public awareness of the condition, along with the increase in its occurrence, it is desirable to have a diagnostic tool available that can be used, in the ideal case, to provide an automatic and correct assessment of the malignancy of a suspicious lesion, or at least provide more detailed and reliable information concerning the

---

[1] www.cancerresearchuk.org

histopathology of the skin for a clinician.

Current techniques for the analysis of suspicious skin lesions generally rely on assessment by a clinician based on experience[11]. Used as a guide for dermatologists, specifically for the diagnosis of malignant melanoma, is the seven point check-list[12] which forms the outline for what signifiers indicate a malignant lesion. Another simplified version of this is the ABCD rule[13] which looks at asymmetry, border irregularity, colour and diameter.

The human assessment process opens up the possibility for error in the diagnosis. Furthermore, a system able to supply information concerning possible malignancy may enable a non-specialist individual to make a more informed decision concerning the appropriate referral of a patient.

The final possibility considered here for such a system in the analysis of pigmented lesions is for use during Mohs' surgery[14]. Mohs' surgery is a widely used technique for the excision of skin lesions where a tapered volume of tissue is removed under microscopic examination in an attempt to remove only cancerous tissue. Any enhancement that could be provided concerning the location of margins in a malignant lesion would be highly advantageous as it may reduce the amount of tissue that could be excised from around the affected region. This would increase the quality of life of a patient in terms of recovery time and disfigurement.

As indicated above, a widespread form of skin cancer is malignant melanoma. This cancer affects the melanocytes which, in healthy skin, are present in the basal layer of the epidermis (figure 1.3). Simple excision can be performed if the condition is discovered in the early stages. However, once metastasis has occurred, malignant melanoma is very difficult to treat and can prove fatal[15]. Therefore, accurate diagnosis and identification of the affected area is key to treatment. In malignant melanoma the affected melanocytes grow and spread into other regions of tissue. When the spreading occurs in the lateral directions only the lesion is termed an *in-situ* melanoma. Invasive melanoma occurs in more advanced cases where melanocytes tunnel through the epidermal/dermal boundary and affect the underlying structure[7]. The depth of penetration of a melanoma is defined by Clark levels or more exactly by the Breslow thickness[16]. The Clark levels define a five point scale of classification dependent on the layers of skin in which cancerous cells can be observed and the Breslow thickness is a direct measure of tumour thickness after biopsy. Non-invasive determination of these values would prove of great diagnostic use.

The most common manifestation of skin cancer is the basal cell carcinoma (BCC)[15]. These can be caused by long periods of low level exposure to UV rays in contrast to malignant melanoma which show correlation with isolated events of high level sunburn possibly resulting in blistering. BCCs are relatively easy to diagnose and rarely metastasize, however, characterisation of their extent is highly desirable. Around 75% of BCCs occur on the face[15] and therefore, as stated above, if the area of excised tissue can be reduced and disfigurement minimised, it would be greatly beneficial to the patient. The pathology of BCCs is highly varied and dependent on the subclass into which they fall. For this reason it is not discussed fully here. However, variations in pigmentation, epidermal thickness and epidermal/dermal boundary definition are all useful indicators in classification[15].

A full discussion of skin cancer histopathology is not necessary in this study, but extensive consideration of both malignant and benign conditions can be found elsewhere[7, 15, 16, 17].

The application of the techniques developed here are not restricted solely to cancers. Another application of such a technology is in the assessment of burn injuries. Current techniques for this classification are once again based on human assessment to differentiate between second and third degree burns. This is a key distinction as the latter requires skin grafting whereas the former can be left to heal naturally. Should an effective assessment tool of burn thickness be available, this evaluation could become quicker and more reliable, therefore providing the patient with an increased level of care.

The determination of the optical properties of human skin tissue are not limited to use in diagnosis. In phototherapy the optical properties of the treated skin will clearly influence the tissue's response to the illumination[18]. Therefore, if these tissue properties are more accurately assessed, dosimetry can become more accurate leading to both safer and more effective treatment.

1.4 Analysis Techniques

Many different approaches have been taken for the assessment and imaging of scattering media for a range of final applications where an improvement in resolution and localisation are sought. These all aim to use a property which is well conditioned for light which has probed a certain region. This property may be defined by the system, i.e time or location variation, or be an inherent property of the light, such as phase or polarization state. A full review of attempts to perform such analysis is presented in chapter 2, however, a brief summary of some techniques is provided here, along with a discussion of the basis of the proposed technique for investigation.

1.4.1 Temporal Domain Techniques

As previously mentioned, localisation techniques generally use a property of light (polarization, coherence or time) which is well conditioned for certain regions of sample. The first analysis technique discussed uses temporal information for the classification of propagating light[19, 20]. In general this is achieved through the illumination of the sample with a very short pulse of light of the order of picoseconds. The pulse spreads spatially and temporally due to scattering and then the 'time of flight' properties of the emerging light are used for optical property characterisation and/or localisation. This can be performed through either rejection of light outside the desired time gate or through analysis of the temporal point spread function. This general concept is illustrated for a backscatter arrangement in figure 1.4.

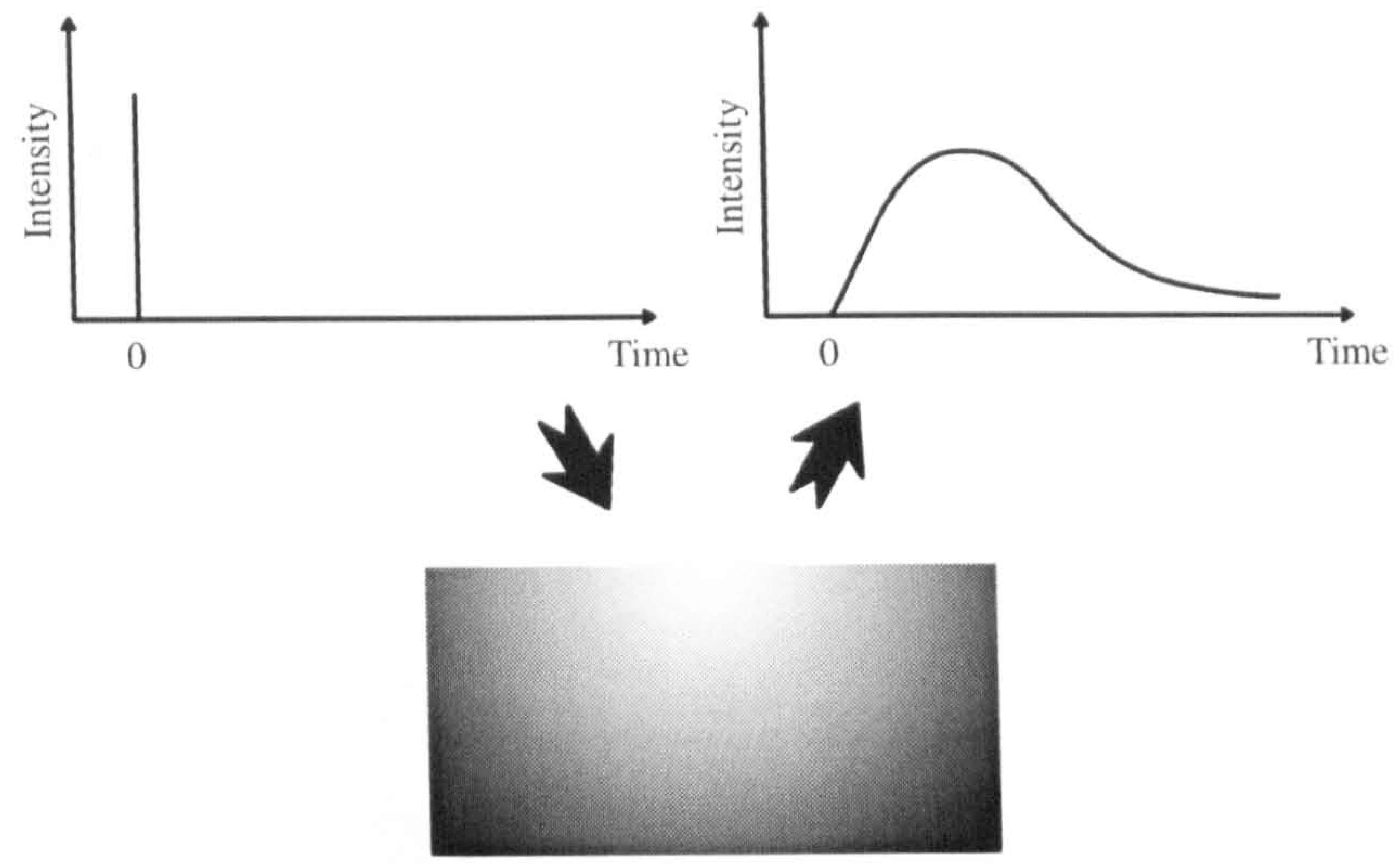

Figure 1.4: *An example of the time-of-flight information returned from a scattering medium due to a pulse input.*

1.4.2 Frequency Domain Techniques

Frequency domain techniques[21, 22] require modulation of the source illumination to give the light properties which can be used to determine the regions of tissue that have been probed. Modulation of the intensity of the illumination means that the levels of emergent ac amplitude, dc amplitude, modulation depth and phase difference can be recorded. This is illustrated in figure 1.5. To extract sample information these are frequently mapped back to parameter variations using different photon propagation or radiative transfer models.

1.4.3 Optical Coherence Tomography

A relatively recent technology that has been developed to analyse the structural properties of human tissue is optical coherence tomography (OCT)[2, 23, 24]. This technique is concerned with the microscopic examination of tissue samples rather than the bulk properties to with other techniques are sensitive. OCT uses a broadband source and exploits the short coherence length of the illumination to provide localisation. This is achieved

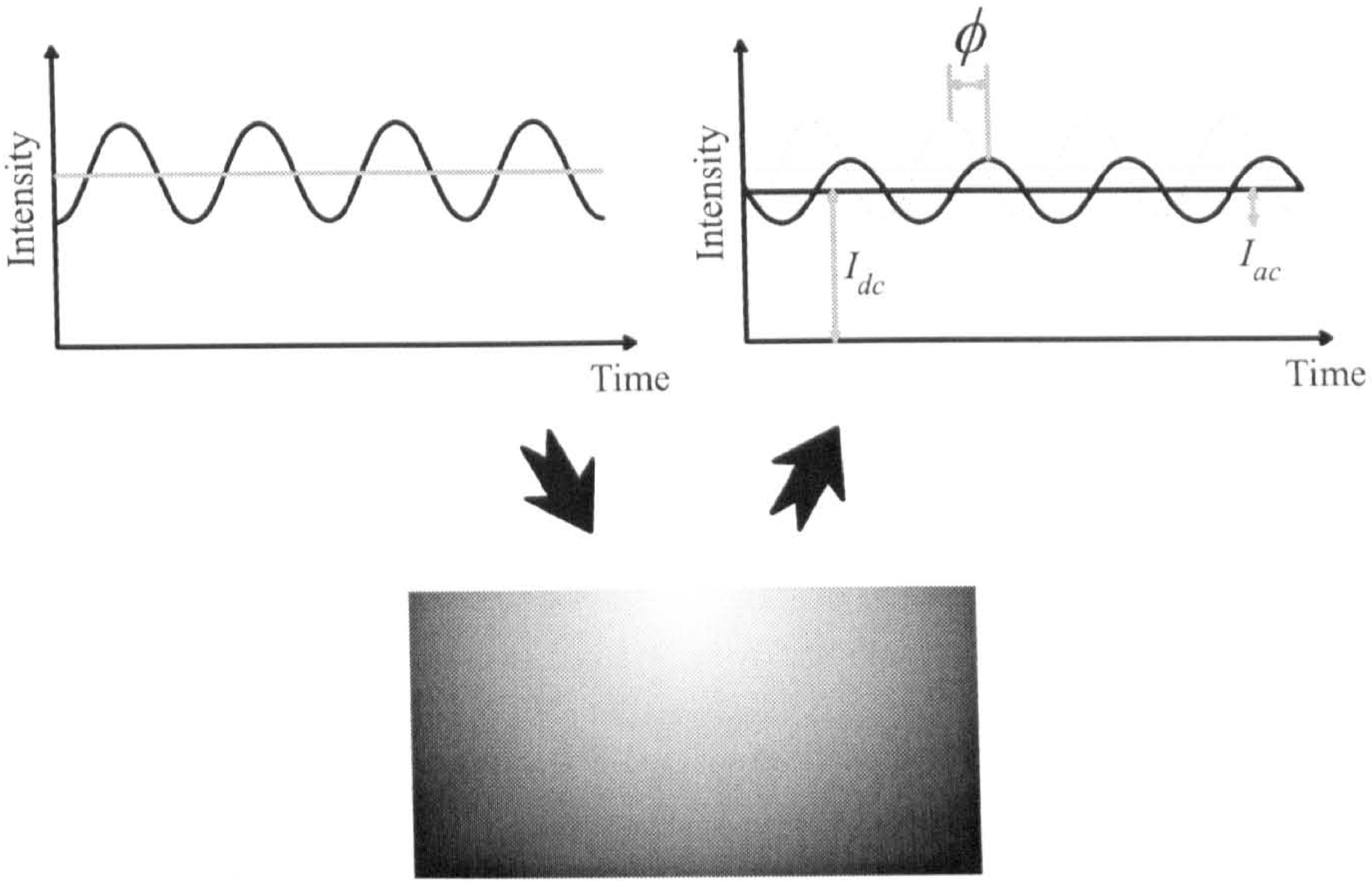

Figure 1.5: *Shown is an example response from an intensity modulated source after being backscattered from a sample. ϕ is the phase difference, I_{dc} is the dc amplitude and I_{ac} is the ac amplitude.*

through interferometry where the tissue is illuminated with the low coherence light and then mixed with a reference. The interference fringes are only observable while the paths are matched and therefore, due to the short coherence length, localisation is achieved. The composition of a basic scanning OCT system is shown in figure 1.6. This is based on the representation given in [23] using a free-space interferometer for clarity.

1.4.4 Polarization Analysis

The property of light which is used here as a tool to achieve sensitivity to a known region of scattering medium is polarization. As light propagates through scattering media the initial state of polarization is modified[25]. Such a technique holds the possibility to probe different regions within scattering media with different initial states of polarization. This study is based around the investigation of how different polarization states interact

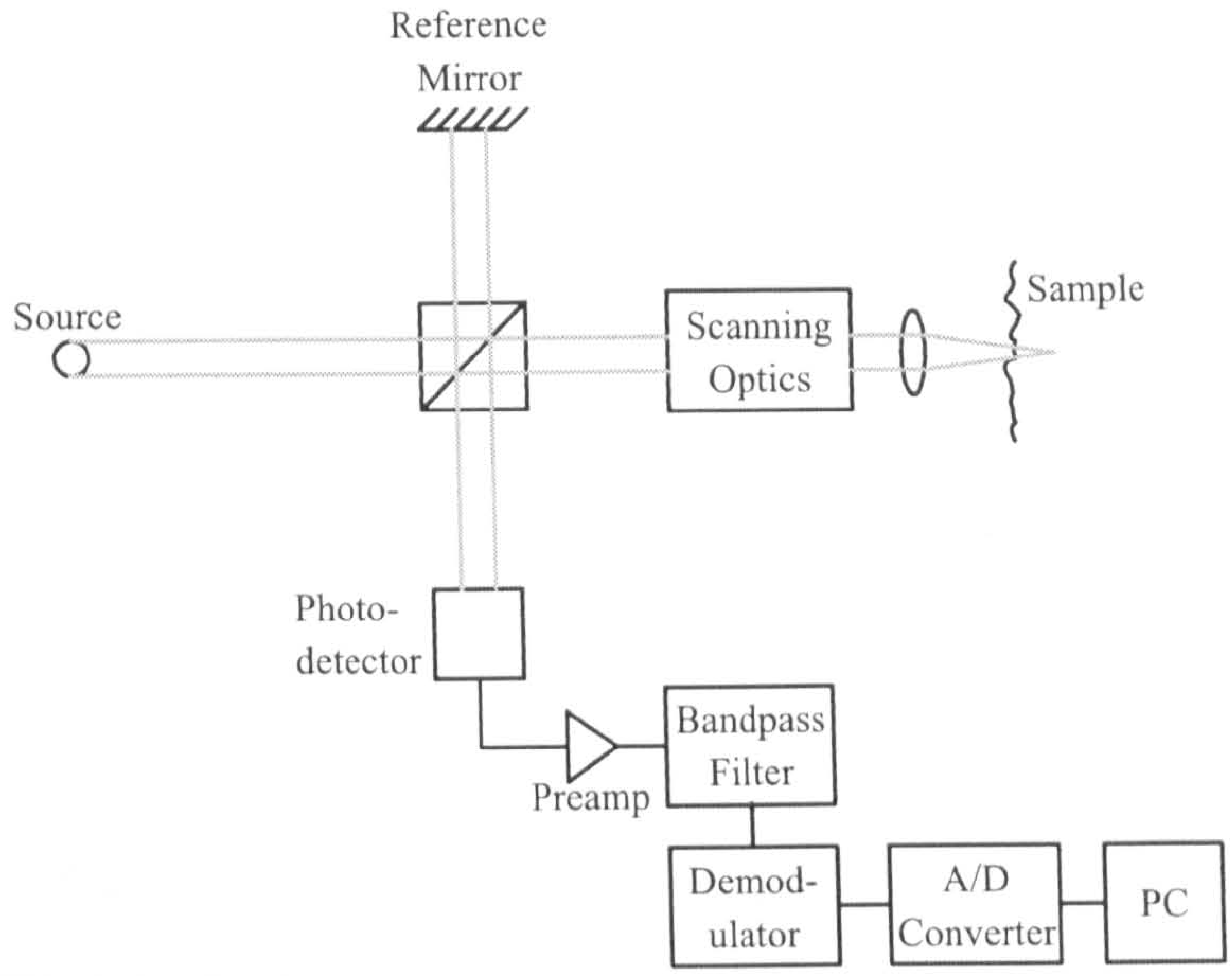

Figure 1.6: *Basic components of a scanning OCT system.*

with general layered scattering media and biological samples encountered in the medical applications discussed in 1.3. A full discussion of the theory and techniques are delayed until later in this thesis.

1.5 Thesis Objectives

As has been discussed so far, it is apparent that the determination of the optical and physical properties of layered scattering media is highly desirable. Specifically considered is the analysis of human skin tissue with the development of medical diagnostic tools in mind. The proposed technique for analysis of such samples is the use of polarized light to achieve localisation in terms of the volumes of tissue probed, along with extraction of the properties of the different layers within the medium.

A review of the wide range of techniques which have been applied to solve the problem of scattering media characterisation and systems developed with skin cancer diagnosis in mind is presented in chapter 2. This discussion is expressed alongside a consideration of the previously applied techniques to perform theoretical modelling of light propagating in such media.

The first main objective of the thesis is addressed in chapter 3. This aim is to assess the behaviour of linearly and circularly polarized states of illumination under scattering conditions through the use of a polarized Monte Carlo model. More specifically, considered here is the examination of the polarization memory property, initially presented by MacKintosh[25], in a layered medium to indicate how the different polarization states provide sensitivity to different regions.

The fundamental ideas of localisation using polarization investigated in chapter 3 are taken a step further in chapter 4 where full-field illumination is used in an experimental set-up to monitor the sensitivity of the different polarization states to sub-surface features within microsphere suspensions. These results are presented alongside modelled results assessing the contrast and lateral resolution theoretically available to verify the observed occurrences in the experimental results. This laboratory based system is then used to perform some early imaging of human skin tissue to verify the appropriateness of such a technique in a dermatological setting.

The design of the system used to perform this early imaging of skin is re-assessed in chapter 5 to provide a appropriate implementation. Here the specification, design and development of a multiple wavelength polarization imaging prototype system to assess the performance of the proposed technique is presented. This results in the production of a system suitable for the analysis of human skin tissue in a clinical environment and early indications of the usefulness of the technique are shown in chapter 6.

In chapter 7 the determination of sample parameters from detected measurables is considered. This involves a theoretical assessment of the feasibility of performing this inversion using the information which can be detected using the developed system.

A summary of the research performed and a discussion of the findings is presented in the concluding chapter. This is along with suggestions for future work and final conclusions.

Chapter 2

Literature Review

2.1 Introduction

The aim of this chapter is to provide a review of previous and current areas of research relevant to the issues introduced in chapter 1. However, the most important objective is to explain the reasons behind the development of the techniques in this study and to put them in context relative to current solutions.

The chapter begins with a brief discussion of photon migration models which are applied widely in studies concerning the optics of scattering media. These are applied as predictive models or to assist in the inversion from detected system measurables to sample properties. This is followed by a discussion of a range of optical techniques which can be applied to achieve enhanced examination of scattering media by allowing interrogation of localised sample depths or use of detected or derived system measurables to characterise the examined medium. The techniques considered can be applied to many different types of sample. Here, the discussion will be mainly based around application in the examination of human tissue or phantoms designed to represent such structures. Following this, discussions consider currently available commercial systems that aim to perform diagnosis of pigmented lesions which focus on mainly numerical processing techniques. A review of the techniques and the performance of the systems are considered. A summary of the discussions concludes the chapter, putting the research performed in this study into context.

2.2 Photon Migration Models

To examine the theoretical behaviour of light propagating through scattering media, various modelling techniques have been developed. These models enable evaluation of the performance of different optical techniques analysing a variety of media with different properties. However, application of such modelling does not stop at technique assessment. Many systems seek to determine the optical and physical properties of scattering media through experimental analysis, and therefore, numerical modelling of the system can be used to solve the inverse problem. This is concerned with mapping from system measurables to optical sample properties. For this reason development of accurate modelling techniques is of increased importance.

A review of these modelling techniques has been performed extensively elsewhere [26, 27, 28] and therefore only a brief review of the theory is presented here to allow discussion of more application based issues. A full comparison of the performance and trade-offs involved with applying the models discussed here is provided by Flock et al[29].

2.2.1 Radiative Transport

To achieve a complete electromagnetic definition of the interaction of light with scattering media, Maxwell's equations can be used to provide an analytical representation. However, due to the many inhomogeneities involved in the analysis of a scattering medium, it is desirable to consider interactions based on transport theory. This interprets light as a particle rather than an electromagnetic disturbance. Early research into such behaviour led to the Boltzmann equation[30] as given in equation 2.1.

$$\frac{1}{c_n}\frac{\partial I(r,\hat{s},t)}{\partial t}+\hat{s}.\nabla I(r,\hat{s},t)=-(\mu_s+\mu_a)I(r,\hat{s},t)+\frac{\mu_s}{4\pi}\iint_{4\pi}I(r,\hat{s},t)p(\hat{s},\hat{s}')d\omega'+\varepsilon(r,\hat{s},t) \tag{2.1}$$

This equation describes the radiance $I(r,\hat{s},t)$ in $\mathrm{Wm}^{-2}sr^{-1}$, which is defined as the energy along the unit vector $\hat{s}$, per unit time, per unit solid angle, per unit area perpendicular to the $\hat{s}$ vector. The scattering phase function (as briefly discussed in section 1.2) is denoted by $p(\hat{s},\hat{s}')$. The scattering and absorption coefficients, μ_s and μ_a, are as defined in section 1.2. The final term, $\varepsilon(r,\hat{s},t)$, is the source term.

The left hand side of equation 2.1 can be seen to represent the diffuse intensity as a function of time. The right hand side includes the effect of optical absorption and scattering of light propagating along $\hat{s}$, along with the contribution to the radiance provided by light scattered into the $\hat{s}$ direction. The final term defines the characteristics of the source in terms of its temporal and spatial emittance. Boltzmann's equation describes the propagation of light under elastic scattering conditions and does not take into account electromagnetic wave properties such as polarization. The inclusion of this property in the modelling process is discussed in section 2.2.3.

It is apparent that the complexity of expression required to fully define the interaction of light with heterogeneous media renders its solution non-trivial for even simple scattering sample geometries. To allow easier solution of equation 2.1, approximations concerning the conditions of the scattered light have been made to simplify the solution.

2.2.2 Diffusion Approximation

A widely applied approximation to radiative transport theory is the assumption that the scattering of the propagating light is diffuse. This is valid for highly scattering media where $\mu_s' \gg \mu_a$[31]. According to van Gemert et al[32] this is appropriate for non-pigmented skin.

The diffusion equation is not applied for the theoretical analysis of samples in this study due to its inability to model polarization and our interest in superficial regions where this approximation is invalid. It is discussed here for completeness due to the application in various studies considered in this chapter.

The expression quoted in equation 2.1 can be simplified by assuming the radiance is weakly anisotropic, the scattering is isotropic and the source is an isotropic point emitter. The mathematical consequences of these assumptions have been widely illustrated[30, 31] and therefore only the resulting diffusion equation is quoted in equation 2.2.

$$\frac{1}{c_n}\frac{\partial\phi(r,t)}{\partial t} + D\nabla^2\phi(r,t) = -\mu_a\phi(r,t) + S(r,t) \tag{2.2}$$

where $\phi(r,t)$ is the isotropic photon density, $S(r,t)$ is the modified source term and the diffusion coefficient, D, is defined as:

$$D = \frac{1}{3(\mu_a + \mu_s')} = \frac{1}{3(\mu_a + (1-g)\mu_s)} \tag{2.3}$$

D indicates the spatial rate of diffusion. Equation 2.2 now provides a more manageable expression to be solved either iteratively or analytically[30, 31, 33].

2.2.3 Monte Carlo Method

If the approximations specified in the derivation of the diffusion equation are not valid, application of Monte Carlo techniques provide an alternative solution. These methods are based around the numerical solution of equation 2.1 and are especially relevant when considering sensitivity to superficially penetrating light which will be non-diffuse. Evaluation is performed by simulating the propagation of light in a random medium on a photon-by-photon basis[1]. The scattering angle after a photon-particle collision and distance to the next collision are drawn from medium specific distributions, the point on which is determined by a random number generator. The direction of propagation is drawn from the

---

[1] The 'light packets' considered in Monte Carlo simulations are not strictly photons due to the application of partial absorption or scattering in some implementations. However, the term photon is used here, and almost universally, for simplicity.

scattering phase function (as discussed in section 1.2.1) generally derived through either Henyey-Greenstien[34], Rayleigh-Gans[3] or Mie theory[3, 35].

The main advantage of applying models such as these are their flexibility, as the modelled geometry can be easily modified. However, the consequence of using Monte Carlo techniques to achieve a realistic representation of the scattering problem is the extensive amount of time required to model the propagation of sufficient photons to form an accurate physical representation. Attempts have been made to combat this limitation by providing simplifications to the model, known as variance reduction techniques[36, 37]. Problems with Monte Carlo computation time has reduced in recent years due to the availability of low cost, high speed computers, however, the techniques considered here are still valid as they may prove useful when a large number of simulations with varying properties are required.

A simple method of reducing the time required for numerical simulation is provided by Kienle and Patterson[36]. This involves reducing the number of necessary simulations rather than reducing the time required to perform the modelling. Rather than the simulation of a single layer semi-infinite structure with a range of scattering properties being performed, a single Monte Carlo data set is produced and the relevant distributions are scaled appropriately to represent variation of the scattering coefficient. This is clearly only valid for simulation of a non-absorbing medium.

More advanced Monte Carlo model acceleration methods are presented by Chatigny et al[37]. The two considered methods are Russian Roulette and splitting techniques. The Russian Roulette technique involves application of probability thresholding at each scattering event. A random number is generated between zero and one and compared to a reference 'survival probability', which is dependent on the photon location to determine if the probability of a photon reaching the detector is sufficiently high to warrant continuing its propagation. This technique means that the processing time is spent more efficiently by evaluating 'useful' photons only. Splitting is another closely related technique, which aims to concentrate on the most important photons for a given arrangement. At each scattering event a photon is split into many parts of equal weighting, the number of parts into which it is split is dependent on an indicator of the photons 'usefulness'. This allows more accurate assessment of the sample areas of interest. However, caution should be taken when applying splitting, as if the scope of 'interesting regions' is too large the simulation time can exceed that of standard Monte Carlo techniques.

The simulations applied here are based on single layer fully polarized Monte Carlo code developed by Chang et al[38]. It was stated earlier that wave behaviour such as polarization could not be modelled using radiative transfer techniques. However, such a property is included here through assessment of how the polarization state is adjusted in the Mie scattering regime at each photon-particle collision. The polarization properties of each photon are tracked through adjustment of the associated Stokes' parameters[39] dependent on the photon's scattering angle. A variance reduction technique applied in this model is the exclusion of absorption effects during simulation. This allows processing of a single simulation for a range of optical absorptions through post-simulation application of Lambert-Beer's law (equation 1.3).

2.3 Optical Examination of Scattering Samples

The examination of scattering media using optical techniques can involve direct tomographical imaging, sample optical property determination or a combination of both. Techniques such as optical coherence tomography[2] and confocal microscopy[40, 41] have been widely applied to perform high resolution microscopic imaging of biological structures. Techniques such as temporal domain, frequency domain and polarization analysis have also been applied to achieve coarse optical sectioning in addition to determination of the optical properties of the medium through which the light has propagated. All of these systems aim to take advantage of inherent and given properties of light propagating in tissue to provide sensitivity to known regions. These techniques are considered in the following sections.

2.3.1 Spectral Analysis

When analysing the skin a great deal of knowledge can be obtained about its morphology by analysing its spectral properties[42]. This is useful for the analysis of pigmented lesions as it is clearly the spectral properties of the affected region of tissue that signifies its presence. It is also reasonable to suggest that a variation in this pigment, possibly indicating malignancy, will be directly represented by an alteration in the observed spectrum. Furthermore, when considering the determination of a sample's optical properties, more information can be gleaned from the use of multiple wavelength illumination. This is due to the optical properties all exhibiting wavelength dependence.

Application of skin spectroscopy, not concerned with pigmentation, was performed by Anselmo and Zawacki[43], showing that the spectral properties of burn injuries are highly correlated with the time taken for the wound to heal. This has lead to research performed by Afromowitz et al[44] toward development of a clinical instrument for burn assessment and involved using the ratio of reflectances obtained from clinical images at three wavelengths (565nm, 635nm and 880nm) to construct a map of burn severity. The technique seeks to monitor the volume fraction of blood just below the denatured region through comparison with data resultant from a Kubelka-Munk model[45]. The technique provided promising but not reliably quantifiable performance.

Spectroscopy is frequently applied to determine the concentration of absorbing matter in biological samples. Matcher and Cooper[46] present a review of spectroscopic techniques including research focused on assessment of deoxyhæmoglobin levels using NIR illumination. Also contained here is a consideration of spectroscopy performed on *in-vivo* samples and how compensation for the presence of scattering can be performed.

A study incorporating examination over a wide continuous band of wavelengths in the visible range was performed by Perelman et al[47]. This study aimed to determine the size and size variation of nuclei in a layer of epithelial cells, with a view to detecting early signs of cancer through observation of dysplasia. The mathematical definition of scattering cross-section shows a periodic variation of this value with wavelength[3]. The characteristics of this periodic variation contains information concerning the size parameter, x (equation 1.1), and its distribution, Δx[47]. Therefore, comparison of experimentally obtained spectra with modelled scattering can yield determination of x and Δx. It should be noted that this variation is obtainable only from examination of a single layer of cells and in normal tissue examination these trends are undetectable under the large multiple scattered background. An enhancement to the technique is presented by Backman et al[48] and Bartlett and Jiang[49] which aimed to use polarized light to extract only the single scatter contribution from epithelial cells without prior knowledge of the underlying structure. Quantitative discussion of the system's performance is not presented. Polarization techniques to extract short path length photons are discussed fully in section 2.3.6.

All currently available commercial systems concerned with the automated examination and diagnosis of pigmented lesions (see section 2.4) apply techniques which require quantification of the 'colour' of the tissue or its variation across a lesion. This is due to the 'spectral signature' of a lesion having been shown to contain vital information for diagnosis[42]. The specifics of how the spectral properties are used are discussed on consideration of each system (sections 2.4.1 to 2.4.4).

The final technique considered here, applied by Demos et al[50, 51], uses the spectral properties of tissue for location rather that characterisation. The variations in the depths of tissue reached by backscattered light of different wavelengths are used to provide coarse localisation at large depths into tissue. Images are recorded at multiple wavelengths and then subtracted to leave the contribution from the region of tissue where the depth profiles differ. In [51] images are recorded using, cross-polar detection, at 600nm, 690nm, 770nm and 970nm, from *in vitro* chicken tissue containing an absorbing target at a depth of 1.0cm or 1.5cm. Various combinations of the wavelength difference images provided differing degrees of sensitivity to the absorber with differing signal-to-noise characteristics. Improvements in contrast of around 600% can be observed from the presented findings. Improvements in the resolution are minimal due to the large submergence of the absorbing target. Localisation in this manner clearly removes the ability to perform localised spectroscopy, possible with other localisation mechanisms.

2.3.2 Optical Coherence Tomography

OCT is a relatively new technique which uses the coherence properties of light to achieve sub-surface sample localisation. The fundamental concept of OCT was introduced in section 1.4.3 and will therefore not be repeated here. A discussion and early demonstration of the principles of the technique are provided by Huang et al[2], along with the first results obtained from an *in-vitro* human retina and coronary artery using 9μm thick optical sections. Standard scanning OCT experiments map a cross-sectional plane formed by a lateral scan axis and the optical axis. These can provide sensitivity in human tissue up to depths of 1 to 2mm using NIR illumination[23], with improvement in contrast and sensitivity to the deeper regions becoming available through the application of topical agents[24]. Such thicknesses are ample for the assessment of the superficial regions in which we are interested, however, to improve contrast at the limits of these depths topical agents can be applied to the skin allowing enhanced construction of the deeper regions.

The poor axial resolution presented by Huang et al[2] is due to the bandwidth of the super-luminescence diode used as a source being insufficient (32nm). Wide-band sources will exhibit low coherence levels leading to increased axial resolution[52]. Another physical limit on the achievable resolution is presented by multiple scatter, as light which has penetrated shallower depths than the target plane, but has been delayed due to multiple scattering, may fall within the detected coherence signal. This effect, which will reduce image contrast, has been examined by Wang[53] using Monte Carlo simulations.

Drexler et al[54] improve the axial resolution through the use of a femtosecond laser combined with chirp mirrors. This provides a 350nm bandwidth source centred on 800nm. This results in the presented images achieving 1μm axial resolution combined with a lateral resolution of 3μm.

Recent advances in the technique attempt to produce two-dimensional *en face* images using full-field OCT, such as the research presented by Dubois et al[55]. The presented results showed *en face* optical sections 500μm × 500μm with axial resolutions of 0.7μm and 0.9μm in lateral directions. This was achieved by modulating the detected coherence signal through oscillation of the reference path mirror at 7.5Hz (amplitude 0.22μm).

As well as the direct imaging of the microscopic structure of a biological sample, advances are being made towards determination of optical properties of a sample using OCT. One such study has been performed by Thrane et al[56] which aims to extract μ_s and g of the two layers forming a semi-infinite medium. This research involves the use of a Monte Carlo model to produce the 'experimental' results for comparison with an OCT model based on the extended Huygens-Fresnel principle developed by the same research group[57]. Errors of 0.4% and 1.6% were obtained for top layer scattering coefficient and anisotropy factor, and $< 10\%$ and $< 6.1\%$ inaccuracies were obtained over the range of bottom layer properties.

Other attempts to improve the level of information retrieved from OCT experiments have involved the inclusion of spectroscopic analysis. This has been performed by Morgner et al[58] presenting image enhancement of various chromophores within a sample. Standard OCT extracts its information from the envelope of the interferogram produced by scanning through the axial direction. Here the interferogram is processed directly to extract information concerning the spectral properties.

These techniques hold great potential for the examination of the microscopic structures within biological samples. From a practical perspective, application on *in-vivo* samples proves problematic due to sample movement during examination. In addition, systems applied in a clinical setting must be rugged, as they require adjustment of position for examination of different sites and must not require precise adjustment or frequent maintenance. Although the microscopic information extracted through the use of systems such as OCT will provide a detailed histology of the sample and should therefore provide excellent diagnostic information, its clinical application and appropriateness to lesion characterisation is debatable. Clinical signifiers to diagnosis are available from the macroscopic properties of a lesion (size, shape and irregularity) which are well understood by clinicians. Development of a system to perform diagnosis or diagnostic assistance to a dermatologist based around these parameters may therefore prove a more useful tool. Realisation of such a system may also be achievable at lower cost, which is important if a commercial solution is sought. OCT instrumentation becomes increasingly complicated, and therefore expensive, in comparison with figure 1.6 due to the large spectral width of the illumination. Chromatic aberration and fibre dispersion become factors and compensation for these effects complicate the system, thus increasing cost.

The objectives of this study outline the requirement for a fast, rugged, easy to use solution which is not provided by OCT.

2.3.3 Temporal Domain Techniques

Temporal domain techniques were briefly introduced in section 1.4.1. The theory on which these techniques are based is discussed by Delpy et al[19] and states that the time-of-flight information of light propagating through a scattering medium is related to its path length. This may therefore provide an indicator the path of propagation and therefore provide enhanced sensitivity to these regions.

Systems analysing the temporal response of a sample can be broadly divided into two categories. The first aim to use temporal gating to extract light which has probed a restricted region of sample. The second category of system derives measurables from the temporal point spread function (TPSF) and uses these to solve the inverse problem and extract the optical properties of the analysed medium. Use of temporal domain techniques is extensive and therefore only a brief consideration is possible here.

Early research performed by Hebden and co-workers[59, 60] illustrates examples of ballistic photon extraction to improve the imaging resolution in transmission arrangements which seek to image objects through, or embedded in, a medium. The system demonstrated in [60] used a source capable of 10ps pulse widths and 76MHz repetition rate. Detection was performed using a streak camera capable of 10ps temporal resolution with a view to evaluating the resolution improvements available from different temporal detection gates. Imaging of a submerged absorbing edge through a heavily forward scattering ($g = 0.93$), 50mm thick medium with $\mu_s' = 0.2\text{mm}^{-1}$ was shown to improve the resolution from 32mm for the 900ps temporal gate to 5mm for the shortest path 10ps gate. Detection in such an early gate was possible due to the low optical thickness of the sample providing a manageable signal-to-noise (SNR). Phantoms more representative of human tissue (thickness = 54mm, $\mu_s' = 1.0\text{mm}^{-1}$) were analysed in a later study[61] and encountered problems with the SNR for time gates less than 700ps. To combat this problem, the TPSF was extrapolated back to zero time using an analytical radiative transport model. The study concluded that 5mm resolution is achievable through such tissue thicknesses using the processing techniques.

A study presented by Mitic et al[62] performed the examination of *in vivo* samples to reiterate the findings of the above phantom studies. Also attempted was the determination of the absorption coefficient, μ_a, and reduced scattering coefficient, μ_s', through comparison with temporal responses generated by diffusion theory. Good agreement between the experimental data and the modelled response was shown, provided the sample's scattering properties ensured multiple scattered emerging light in fitting with the approximation defined by diffusion theory.

Considering *in-vivo* tissue examination, more appropriate to this study, time-resolved measurements in reflection were performed by Jacques[63] aiming to determine the sample's absorption coefficient. This is achieved through characterisation of the log slope of the TPSF 'tail' which was shown to be largely independent of the scattering coefficient. Solution was achieved through an analytical expression derived from diffusion theory. Problems in the application of such a technique are inevitable due to the reduced SNR available at large delays past the peak in the TPSF. An improvement on this study is provided by Madsen et al[64] where both μ_s and μ_a are extracted from the backscattered TPSF using a closed form solution of the time-resolved diffusion equation. Both μ_a and μ_s were determined with less than 10% error.

In an attempt to remove the inaccuracies introduced into parameter extraction due to approximation associated with diffusion theory and increase the range of possible samples Pifferi et al[65] attempted to fit experimental TPSFs to libraries of Monte Carlo simulated data to determine μ_s' and μ_a. Over the range of μ_s' and μ_a values selected for testing, the fitting errors for the Monte Carlo simulations are generally around 10% in contrast to around 30% error introduced using the diffusion equation solution provided the value of g is known.

In more recent studies, multiple wavelengths in the visible and NIR bands have been used to enhance temporal techniques in both transmission[66] and reflection[67].

Torricelli et al[67] have implemented a time resolved spectroscopy system using illumination in the band 620nm to 1010nm allowing determination of water and lipid concentrations from *in-vivo* samples. The results show good agreement with the physiological predictions.

Temporal domain techniques have been demonstrated by as the 'gold standard' for optical coefficient determination[28, 68]. However, such systems are not suitable to meet the objectives of this study. The aim is to develop a low cost, rugged solution. Solutions applying temporal domain techniques are therefore inappropriate due to the high cost of the system components and the inability to provide full field detection over a sufficiently narrow time gate to allow examination of the most superficial regions of a sample.

2.3.4 Frequency Domain Analysis

As mentioned in the section 1.4.2, frequency domain techniques can be applied to extract the optical properties of media. These involve the modulation of the illuminating source and detection of various properties of emerging light including: phase shift relative to the illumination, ϕ, resultant modulation depth, M, the dc amplitude, I_{dc} and the ac amplitude I_{ac}. These values were indicated in figure 1.5. Discussion of frequency domain techniques presented here is brief as they do not permit full field detection and hence imaging of a sample. Therefore, these techniques do not meet the objectives of this study which will be clarified in section 2.5.

Madsen et al[69] have presented application of frequency domain techniques to extract the absorption and reduced scattering coefficients from biological tissue. Determined values of phase difference with respect to the input and modulation depth are used to perform the inversion using a closed form of the diffusion equation. The values determined from comparison with the model were used to compare the properties of the uterus in pre- and post-menopausal patients.

Kienle and Patterson[70] reported the improvement provided by using Monte Carlo simulations over the diffusion approximation for small source-detector separations. Without considering experimental errors, the calculation of μ_s' and μ_a was calculated as being less than 5%. However, experimental errors included in the phase detection due to the small source-detector separation when analysing more superficial regions were reported to be greater than 10%.

These techniques have also been extended to analyse two-layer media for potential skin analysis[21, 22]. Such a study is presented by Alexandrakis et al[22] which tries to extract the reduced scattering coefficients and absorption coefficients of the two layers along with the top layer thickness. Analysis of the sample illustrated that the problem was ill-conditioned for the five variable case requiring knowledge of three of the parameters to provide accuracy better than 10%.

The final application of the frequency domain techniques is usually based around examination of deep regions of tissue (of the order of millimeters) due to physical limitations of the system. Therefore, the samples designed in the studies of two-layer media[22, 71] have been designed to mimic a dermal layer and subcutaneous fat or muscle, as opposed to the superficial regions of concern here.

2.3.5 Spatial Analysis

The spatial point of emergence of light from a scattering medium can provide information concerning the predictability of the path of propagation. Detection of light removed a large distance from the optical axis of the illumination will clearly provide bias towards heavily scattered light when compared with on-axis detection. This is true for both transmission and reflection arrangements. The analysis of the spatial variation of emergent light is not generally applied in its own right for implementation in a characterisation tool due to the large dynamic range required for detection of extended regions of the intensity distribution. Radial sensitivity considerations are generally combined within other techniques such as those described in the preceding sections to achieve some selectivity over the regions through which the detected light has passed.

Bays et al[72] apply evaluation of the log derivative of the radial intensity distribution at two distinct points. Analysed samples are polyoxymethylene scattering phantoms and the human esophageal wall with the view to extract the reduced scattering coefficient, μ_s', optical absorption, μ_a, and the refractive index of the examined tissue, n_{tissue}. The determined values were then compared with values derived from a combination of diffusion theory and Monte Carlo simulations. To counter the low SNR available at large displacements from the point of illumination, the source was modulated to allow lock-in detection. To tackle problems with dynamic range mentioned above prior knowledge of the approximate optical properties is required to ensure the radial distribution is sampled at the correct point to match the detector sensitivity.

A study performed by Kienle et al[73] aims to determine μ_s and μ_a using a neural network trained on Monte Carlo simulation data. The proposed system uses the absolute intensity distribution of the light backscattered into orthogonal linear polarization channels. Errors on the determined values are quoted as 2.6% and 14% for μ_s and μ_a respectively.

Although analysis of the radial intensity distribution for characterisation encounters many problems, examination of the spatial distribution of backscattered light has been used to gain a better understanding of the behaviour of scattered light with different properties[74, 75, 76]. Analysis of the radial distribution of backscattered photons is applied in this study to evaluate the sensitivity of polarized light to different depths of a layered sample and to provide an indication of lateral resolution enhancement provided by the extraction of polarization maintaining light.

2.3.6 Polarization Techniques

It is widely known that as light propagates through scattering media, both its direction and polarization properties are altered[6, 25, 77, 78, 79].

MacKintosh et al[25] presented a theoretical discussion of the levels of 'polarization memory' exhibited by different polarization states. This effect described how an initial polarization is maintained over varying numbers of scattering events dependent on the polarization state of illumination. This is discussed further in section 3.2. Experimental verification of this theory was performed illustrating the dependence of this effect on scatterer size. The results indicated that large scatterer diameters, d, ($d \geq \lambda$) maintained circular polarization to a greater extent than linearly polarized states. The opposite was shown for small particles ($d \ll \lambda$) due to the increase in scattering in the backward direction, leading to many photons experiencing a flip in helicity (and hence depolarization from the initial state) for circular polarizations.

Research following this has been concerned with exploitation of the polarization memory property to achieve localisation or analysis of specific regions of a sample. A study by Schmitt et al[80] utilised the improvements provided by preferential detection of forward scattered circularly polarized light in a transmission imaging system. This seeks to reduce the contribution of photons which have propagated away from a ballistic trajectory to improve the definition of sub-surface absorbing structure imaged by scanning a single illuminating spot. An improvement due to the preferential detection of circularly polarized light for a range of scatterer sizes and hence anisotropy factors is presented along with a comparison of linear and circular polarization was also performed with $g = 0.919$. This showed that, due to the longer maintenance of the circularly polarized states, the degree of polarization (or equivalent factor defined in the paper) is lower for linear polarizations[2], however linear polarizations provide improved imaging resolution due to its more direct path. This results in a very poor SNR due to the low degree of polarization (DOP). In an attempt to try and take advantage of this improved localisation of linearly polarized light, but reduce the problems due to low SNR, Emile et al[81] proposed modulation of the illuminating polarization. This was achieved through mechanical rotation of the input polarizer leading to a sinusoidal modulation of the polarization maintaining component on top of a constant amplitude multiple scatter background allowing lock-in detection. Contrast can be seen to improve by five times for the case of modulated illumination.

Investigation of the polarization maintenance in a reflection arrangement is performed by Morgan and Ridgway[82] through assessment of the DOP of the emerging light. Results showed that the maximum DOP for linear polarizations occurs at the minimum optical thickness. This implies that increased scattering will reduce the DOP. For circular polarization states however, the DOP peak occurs away from the minimum optical thickness implying detection of circular polarization maintaining light will provide sensitivity to sub-surface regions preferentially over the surface contributions.

---

[2] Quantification of the difference between the polarizations is not possible due to inconsistencies in the optical thickness used for linearly and circularly polarized states.

To examine more closely the behaviour of different polarization states and confirm the reasoning behind the polarization memory effect presented by MacKintosh et al[25], Hielscher et al[74] and Raković et al[75] have analysed the two dimensional spatial distribution of backscattered polarized light. Hielscher et al[74] verify the azimuthal variation of linearly polarized backscatter from both microsphere solutions and biological tissue showing the effects of scatterer size and have determined this value from comparison with known distributions. Whereas, Raković et al[75] reconstruct the full Mueller matrix through experiments and Monte Carlo simulations displaying the inherent circular asymmetry and symmetry of linear and circular polarizations respectively, as will be considered in section 3.2.

The research presented in this section thus far has been limited to single-point illumination. However, derived from these studies is the ability to perform full field, depth localised, imaging of scattering samples.

This was demonstrated by Demos and Alfano[50] using linearly polarized light. Images were recorded from the back of a human hand using off-axis detection (to reduce surface glare) in polarization planes parallel and perpendicular to the plane of illumination. Simple subtraction of the co-polar and cross-polar channels (which will be discussed in section 3.6) was shown to extract the surface and shallow penetrating polarization maintaining component. Contrast enhancements of the surface features were quoted as improving by a factor of 4.5.

The surface contribution detected in [50] is undesirable when attempting to determine the sub-surface structure of samples. Therefore, a widely applied technique of removing this component is to simply detect emerging light in the plane orthogonal to the plane of illumination. This was initially suggested for application in tissue imaging by Anderson[83]. If applied to skin images this would result in sensitivity to depths greater than 300μm below the surface as stated by Jacques et al[84].

Studies by Jacques et al[84, 85] seek to remove both the multiple scatter component as in [50] and also reflections from the sample's surface. This is to provide sensitivity to near sub-surface regions. The extraction of polarization maintaining light is performed through subtraction of the co-polar and cross-polar images[50]. Surface contributions are removed by applying a flat glass plate and matching fluid to the sample's surface and performing detection off-axis to avoid the specular reflection. The research aimed to remove effects of non-uniform illumination and effects due to pigmentation. This was attempted by normalising the extracted polarization maintaining light by the total unpolarized intensity on a pixel-by-pixel basis. This provides a representation of the variation of scattering, but will remove any effects due to pigmentation. For this reason application of this processing in the diagnosis of pigmented lesions in debatable since, as discussed in 2.3.1 pigmentation has an important role to play in lesion diagnosis.

Referring back to the discussion presented in section 2.3.1, polarization gating has also been used to perform localised spectroscopy demonstrated by Backman et al[48] and Bartlett and Jiang[49] for extraction of surface features. If a technique allowed localisation below the surface of a sample, sub-surface spectroscopy may prove viable. The techniques presented in this thesis indicate the potential to achieve this.

A property of tissue which can provide structural information is birefringence. The effect is due to the fibrous nature of dermal collagen and is of interest to polarized light studies as the alignment of the sample's fast axis[86] in relation to incident linearly polarized light will determine the behaviour of the polarization properties. The propagation of circularly polarized light under birefringent conditions is also of interest as its inherent circular symmetry will be affected. Such issues are discussed by Wang and Wang[76] through time-resolved Monte Carlo simulations. Tissue birefringence is examined experimentally on *in-vitro* samples using circularly polarized OCT by de Boer et al[87] and more thoroughly by Yang et al[88] showing regions of varying birefringence in a cross-sectional scan.

2.4 Computational Image Analysis Techniques

The techniques considered up to this point have all been concerned with either the localisation of volumes of tissue, the extraction of the optical properties of the sample or both of these issues. This has been achieved by comparing properties of light before and after interaction with the medium. However, commercially available skin lesion diagnosis systems do not generally take advantage of these optical techniques which have been extensively studied in an academic setting. Possible reasons for this will be discussed in section 2.5.

As far back as 1987 Cascinelli et al[89] proposed the possible implementation of computer assisted analysis of melanoma diagnosis. Early studies performed determination of basic lesion properties such as size, shape and colour from the raw clinical photograph of a lesion with some level of success[90, 91, 92, 93], however, none provided performance above that already achievable by a trained clinician.

The introduction of epillumenescence light microscopy (ELM)[94] into standard clinical practice is reported to have increased the diagnostic accuracy of clinicians from 64% to 80%[95]. The technique simply involves the application of a refractive index matching oil being applied to a flat glass plate and placed on the skin. The matching of refractive indices seeks to render the epidermis translucent (assuming no epidermal scattering). Therefore, application of such a technique coupled with digital imaging and analysis should provide enhanced information concerning the properties of a lesion.

Considered in this section are four commercially available systems designed to aid the diagnosis of pigmented lesions. Unfortunately, when reviewing the operation of commercially based systems, the content of the literature can prove somewhat vague in comparison to academic studies due to protection of the developed technique.

2.4.1 PolarProbe/SolarScan®

Presented by Bischof et al[10] is a proposed technique toward the development of an automated melanoma diagnosis system. The techniques presented describe the concepts behind the PolarProbe, developed by Polartechnics Ltd[3] in Sydney, Australia, which has been renamed the SolarScan®. This device aims to diagnose malignant melanoma through the processing of clinical ELM images and should not be confused with the device developed by the same company called PolarProbe to detect the occurrence of cervical cancer using electronic stimulation[96] now called the TruScreen®.

The processing involved in this system aims to find a balance between the extracted lesion properties generally considered of clinical significance (conforming to the recognised ABCD classification[13] as discussed in section 1.3.2) and determination of abstract parameters concerning the subtleties of the lesion geometry. As well as lesion geometry, the spectral properties were also crudely analysed by defining six colours through their RGB values and identifying the number of these colours occurring across a single lesion.

To perform classification of the determined parameters a decision tree[97] was implemented, repeatedly filtering data through comparison of the recorded data with those from a known training set. The performance of the system reported as a sensitivity between 88.9% and 100% and specificity between 80.0% and 84.1%. This technique showed a marked improvement on a previous iteration of the system quoting a sensitivity of 92% and specificity of 71%[98].

Practical issues encountered during the use of this system have involved image distortion due to the presence of bubbles in the recorded images. Therefore, as an enhancement to the system, processing developed by Gutenev et al[99] flags the presence of these artifacts and prompts re-imaging of the lesion.

A further study presented by Menzies et al[100] uses the developed system for monitoring of a sample of lesions over extended periods. This indicates that key diagnostic

---

[3] www.polartechnics.com.au

information is contained within the evolution of a lesions properties in addition to the properties recorded at any instant in time.

2.4.2 MicroDERM®

The implementation of the device described above in section 2.4.1 involved the assessment of various signifiers and design of a decision tree. Hoffmann et al[101] present the trial results of the MicroDERM®, developed by Visiomed AG[4] in Bochum, Germany. This system attempts to avoid the need for manual mathematical analysis of the training data, by applying a neural network in an attempt to build an expert system to perform diagnosis. The aim of this study was to record white light ELM images of pigmented skin lesions at thirteen dermatology clinics across nine European countries. These images were then used, coupled with the clinical diagnosis by specialists, to train the expert system.

To make the images compatible for input into a neural network, the images are preprocessed performing lesion segmentation and hair removal (example routines are provided in [10, 102, 103, 104]). As inputs to the neural network, the asymmetry percentage[105], border irregularity[106], colour variation[104] and texture[105] were quantified.

The full data set contains 2218 images obtained from 1173 different patients, classified as twenty-three different conditions. To evaluate the conditioning of the data, two expert systems were constructed: one using data recorded at a single clinic and one with data from all clinics. As the system performance is considered for a range of neural network threshold levels a receiver operating characteristic (ROC)[107] curve can be defined mapping the trade-off between sensitivity and specificity. As an assessment of performance, the area under the ROC curve, A_{ROC}, is evaluated[5].

---

[4] www.visiomed.de

[5] Use of A_{ROC} for performance evaluation can be slightly misleading. A system which randomly selects a diagnosis would result in a linear ROC characteristic producing an area of 0.5 resulting in the limits of the area being $0.5 \leq A_{ROC} \leq 1.0$. Therefore, use of this value is convenient for comparison, but should be used with caution when quoted as an absolute measure of performance.

The best performance achieved by the system ($A_{ROC} = 0.845$) was obtained by the single site expert system being tested on images from the same site, whereas testing of this system on multi-site images reduced the performance to provide a characteristic with $A_{ROC} = 0.807$. Testing of the full multi-site trained expert system provides intermediate performance ($A_{ROC} = 0.826$), but is clearly the most significant as final clinical implementation would mimic this test. The performance of this system produced results comparable to human clinical diagnosis which, as suggested by Bischof et al[10], is the maximum performance available to a system based on imitation of human decision making such as the ABCD assessment scheme[13].

For difficult to diagnose cases however, the lesions correctly diagnosed by expert system differ to those from human examination. This indicated that there may be some improvement in diagnosis if the clinician and microDERM® are used in tandem.

2.4.3 DBDermo-MIPS

An alternative system called DBDermo-MIPS designed for the diagnosis of malignant melanoma has been developed by Scientific Informations in Italy[6]. Assessment of the instrument and training of the diagnostic neural network is reported by Rubegni et al[108]. For characterisation, 147 pigmented skin lesions previously digitally imaged using ELM were analysed extracting an initial forty-eight different parameters from each recorded colour image. The parameters were based upon the lesion's geometry, colour, texture and colour clusters. Analysis of the data was implemented using a neural network initially formed using all forty-eight parameters. However, when implementing neural network solutions, non-optimal performance can occur due to over definition of the training set. Therefore, the most influential ten parameters, determined by the neural network's derived weighting of the parameter, were selected to train and test the final neural network.

Using different neural network thresholds diagnostic performance was quoted as having

---

[6] www.skinlesions.net

a sensitivity of 99.0% with 80.60% specificity or 93% sensitivity with 92.75% specificity. These results are an improvement on the the initial implementation reported by Bauer et al[109]. This iteration used computer generated representations of the ABCD scheme characteristics in a similar manner to the MicroDERM® system discussed in the previous section. This also provided results considered no better than human assessment.

A study discussing the specifics of the applied neural network is presented by Rubegui et al[110] applying thirteen of the derived parameters. Also contained here is the ROC plot describing the system's performance.

2.4.4 SIAscope^{TM}

The techniques presented in sections 2.4.1 to 2.4.3 used colour information contained within the imaged lesion to aid diagnosis through examination of the RGB channel levels resultant from white light illumination. Seeking to improve on these techniques the SIAscope^{TM}, developed by Astron Clinica Ltd[7] in Cambridge, UK, considers more closely the behaviour of different wavelengths of light propagating in the skin and applies sample illumination with discrete narrow band sources. The main principles of the system and results of its clinical testing are reported by Moncrieff et al[111]. The processing techniques use a numerical model of tissue to simulate the behaviour of illumination at different wavelengths. This is followed by reference to a look-up table to extract morphological information from the sample images.

Illumination by the system is provided at four wavelengths using LEDs with a view to achieving varying sensitivity to different sample depths and the contained chromophores. The system aims to determine morphological properties of the examined sample rather than anonymous data processing to supply an answer to the question of diagnosis and is intended to act as a diagnostic aid to a clinician rather than an automated diagnosis machine.

---

[7] www.astronclinica.com

The developed system records data using Spectrophotometric Intracutaneous Analysis (SIA^{TM}), resulting in distributions termed SIAgraphs. As stated above these graphs seek to represent directly the histological properties of a pigmented lesion rather than merely assigning numbers to signifiers of visual properties. To aid the design of the system and ensure that the output of the system reports significant properties, nine lesion features (defined in standard terms by Bahmer et al[112]) were evaluated to determine their significance. The study found that the most useful information retrieved from a lesion is the presence or distribution of dermal melanin, blood displacement, dermal melanin globules, blood displacement with blush, collagen holes and erythemateous blush. The sensitivity and specificity of these individual features range from 63.5% to 96.2% and 56.8% to 74.0% respectively in the diagnosis of malignant melanoma. The system therefore aims to combine the reporting of these features through the SIAgraphs to provide increased information to a clinician for diagnosis. The properties which the system seeks to map in the SIAgraphs to contain the above features are total melanin (biaxial symmetry and asymmetry), dermal melanin, localised blood saturation (blood displacement and erthematous blood) and collagen density (collagen holes).

2.5 Summary

Presented in this chapter has been a review of the techniques applied for the determination of the optical properties of a scattering medium, focusing on application in the field of tissue examination, along with a discussion of the technology currently available to perform computerised analysis or diagnosis of pigmented skin lesions. A wider but more general review of commercially available techniques for melanoma diagnosis is provided by Marghoob et al[113].

Considering the optical techniques discussed in sections 2.3.1 to 2.3.6, it can be seen that the current solutions do not meet the requirement of this study. Temporal domain techniques do not provide the low cost solution required, whereas the lack of ruggedness and practical implementation of an OCT system means that its application is not suitable. Other localisation technique such as spatial analysis and frequency domain techniques do not meet the requirements due to their inability to provide full field analysis.

It is clear from the discussion of commercially available systems provided in sections 2.4.1 to 2.4.4 that the diagnostic performance achieved can be impressive. However, problems have frequently been touched upon in the literature concerning image quality and the use of matching fluid. It is apparent that many images recorded for the clinical studies were omitted from either the training sets or testing due to the presence of image artifacts. The study reported by Hoffmann et al[101] stated that only 70% of the recorded images were considered of high enough quality for processing. Of these, 10% of the lesions could not be sucessfully segmented. These figures are acceptable for application in a trial where data can be easily omitted, however, this becomes more of a concern in clinical application. The SolarScan® discussed by Bischof et al[10] also ran into problems due to the use of matching fluid and required additional processing to indicate the presence of an unusable image. In addition to this, the physical practice of applying a glass plate to the surface of the skin could result in distortion of the properties which are trying to be measured. More specifically, evacuation of blood from dermal capiliaries and in extreme cases disturbance of collagen architecture may occur. This having been said, these contact issues can be largely removed through sensible probe design.

After review of the proposed techniques for diagnosis of skin lesions a clear split can be observed between the approaches: those techniques applied to achieve the localisation and characterisation of samples through extracting the optical coefficients and raw processing of digital lesion images. The overall objective of this study is to combine these ideologies into a system capable of determining the optical properties of tissue over the dimensions of a typical lesion and use these distributions to perform the inversion to either tissue morphology or a clinical diagnosis.

As discussed in the introduction to this thesis the proposed method is to apply polarization gating techniques to achieve localisation of the superficial regions of a sample. This is with a view to producing a simple, low cost and robust solution producing a localisation system more appropriate than the techniques described in section 2.3. Application of these techniques may also provide an improvement to current commercial systems described in section 2.4 as they may allow imaging without the need for glass plates and matching fluid to remove surface contributions. Improvement to these systems could also be provided by the incorporation of localisation techniques. If the depth of interest can be isolated, the sensitivity to the region's properties will be improved. Imaging without a localisation mechanism will be fundamentally limited in terms of the achievable resolution due to scattering. The developed technique may also provide improvement to current optical coefficient determination systems due to the application of advanced processing techniques applied in the commercial systems once the distribution of optical property variation is extracted.

In summary, addressing the issues discussed in this review, this thesis aims to indicate the ability to perform depth discrimination using polarization gating in uniform scattering samples in chapters 3 and 4. This is extended to localised sub-surface *in-vivo* tissue imaging, without the need for matching fluid and glass plates in chapter 6, using the imaging system developed in chapter 5. Assessment of the condition of the data, to indicate the potential for optical property determination using the developed system is given in chapter 7.

Chapter 3

Polarized Light Scattering: Theory and Simulation

3.1 Introduction

The fundamental mechanism for discriminating between paths of propagation in this study is the use of polarization state and the degree to which that polarization is maintained as the light scatters and propagates. This is with a view to application in a medical diagnostic setting. However, before addressing the biomedical application directly, and more specifically the propagation of polarized light in human skin tissue, it is necessary to address the polarized light scattering problem at a more fundamental level. This investigation involves the examination of the rate of depolarization of polarized light incident on a sample and assessment of the volumes which have been probed by the different emerging polarization states. To perform this analysis it is necessary to be able to rigorously analyse the behaviour and changing properties of light as it propagates and is ultimately backscattered. One widely used technique which is appropriate for application in a situation such as this is a Monte Carlo simulation, where photons are propagated and tracked through a layered scattering medium on a photon-by-photon basis. A general discussion of such techniques was presented in section 2.2.3.

This chapter will discuss the fundamental behaviour of polarized light interacting with scattering media to assess the sensitivity of light backscattered in different polarization states to the illuminated sample. The fundamentals of the polarized light Monte Carlo simulation and the samples which can be theoretically examined in these simulations will also be discussed. In addition to this, the results of these simulations on layered media, their analysis and how the results indicate the potential for using polarization discrimination to achieve the goals of the study is discussed. The majority of these results have been presented previously in [114].

3.2 The Scattering of Polarized Light

The direction of light propagating in scattering media is adjusted due to interactions with small inhomogeneities, mathematically represented as a modification of the light's propagation vector, $\vec{k}$. For a ray propagating in a volume, this direction of propagation can be represented on the surface of a unit sphere as shown in figure 3.1. The random propagation of a ray scattering through a turbid medium can be represented as a continuous random walk taken around the surface of this sphere[25]. The change in direction also affects the polarization state of the ray, resulting in depolarizing of the light as it propagates[77, 78]. If a mechanism could be applied to enable analysis of light which had not had its polarization state randomised by many scattering events, it would suggest that sensitivity to superficial regions through which this polarization maintaining light had propagated is available.

The case of polarized light scattering can be extended from this simplistic view of either fully polarized or unpolarized by investigating the effects of scattering on the rates of depolarization of different initial polarization states. Discussion performed here is in-line with the concepts presented in [25]. To aid the mathematical representation of polarization, the Poincaré sphere forms a useful tool[115]. The Poincaré sphere is defined along

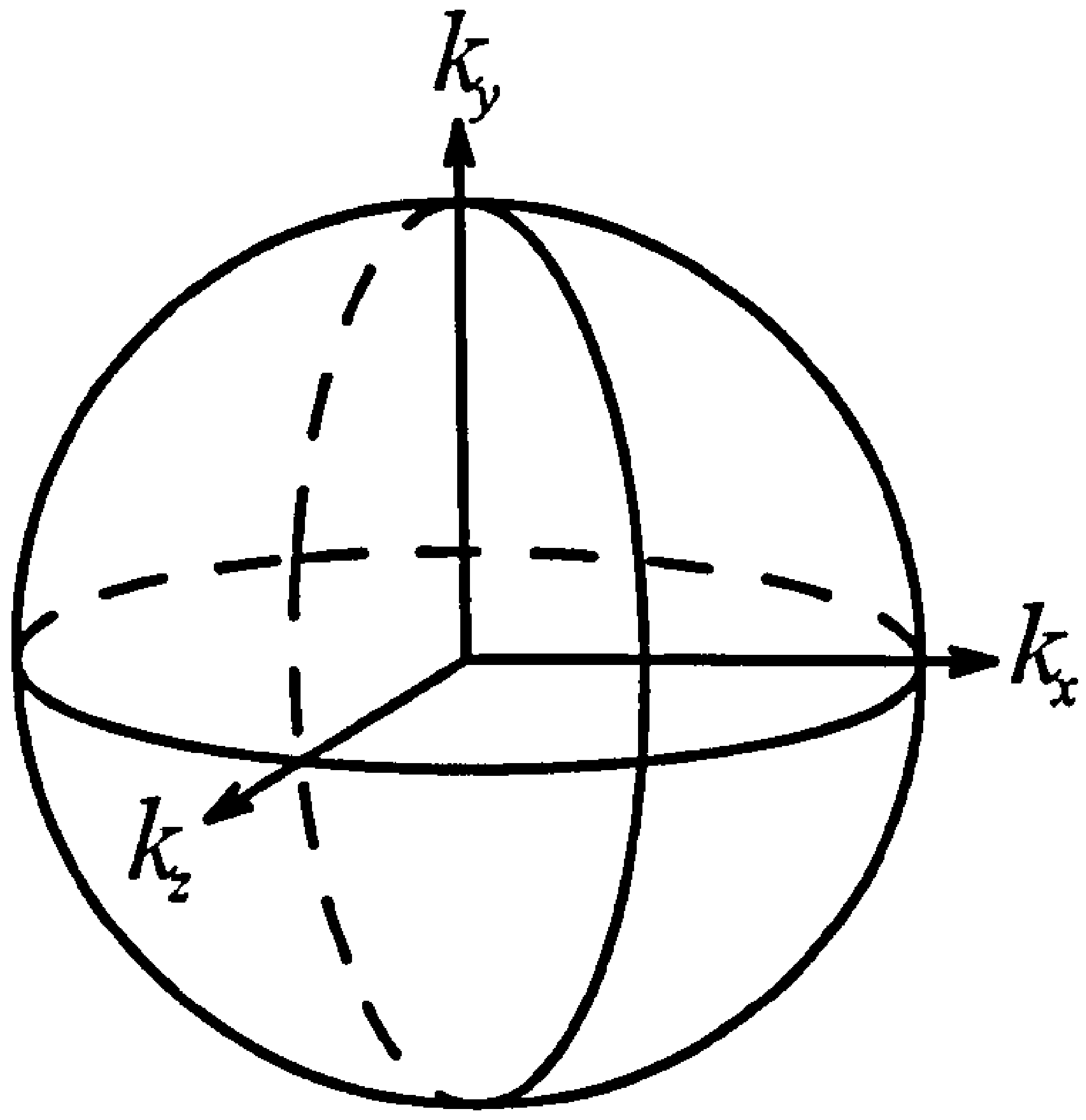

Figure 3.1: *The unit sphere representing the direction of propagation as components of* $\vec{k}$.

three axes by the three Stokes' parameters which define polarization[39]. Considering fully polarized light, it can be seen from figure 3.2 that the cases of linearly polarized ($\sqrt{Q^2+U^2} = I$, $V = 0$)[1] and circularly polarized light ($Q = 0$, $U = 0$, $V = \pm I$) provide the extremes in the range of behaviour of fully polarized light with linear polarizations falling on the equatorial plane and pure circular polarizations occurring at the sphere's poles. It can be seen that intermediate states (elliptical polarizations) fall between these states ($Q^2 + U^2 \neq 0$, $V \neq 0$) and it is therefore postulated[25] that they have scattering properties between these two extremes and are therefore not considered fully here.

The behaviour of different polarizations under scattering conditions is dependent on the anisotropy of the scattering by a single particle [25, 77, 78]. It has been discussed previously [116, 117, 118] that the scattering properties of superficial tissue regions, such as the epidermal and dermal layers, are in the forward direction[119]. For this reason the discussion performed here focuses on this case, but the general nature of the analysis indicates that the trends are scalable to the limits of anisotropy as g tends to ± 1.

As discussed previously in section 1.2 the range of pathlengths resultant in backscatter from a scattering media have a tendency to the transport mean free path[6]. Therefore,

---

[1] Using the standard notation for the Stokes' parameters.

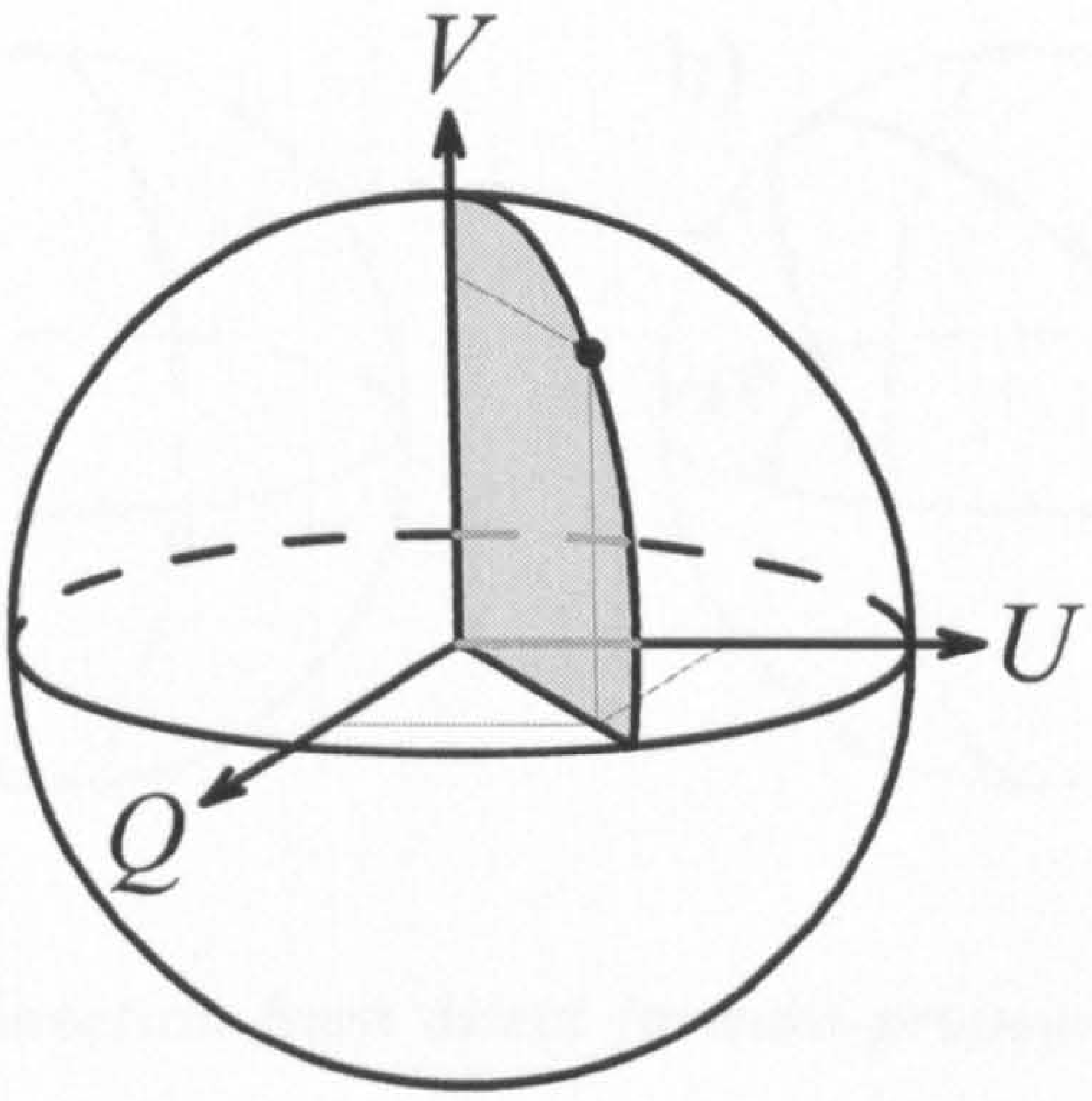

Figure 3.2: *The Poincarè sphere using standard notation for Stokes' parameters.*

investigating the behaviour of a photon propagating exactly this distance before being backscattered will form a good basis on which to hypothesise concerning overall behaviour. Using the representation of propagation using the unit sphere (figure 3.1), the simplest mechanism resulting in backscatter is to travel around the unit sphere from the point representing the illumination angle directly to its antipole, as shown in the examples illustrated in figure 3.3.

When evaluating the differing behaviour of the polarization states under scattering a key point is to analyse the effect of an azimuthal rotation of the polarization components. Considering first linearly polarized light it is clear that any path around the unit sphere either parallel or perpendicular to the plane of illumination will result in the maintenance of its initial state (figure 3.3a). However, should the path of propagation be taken at a 45 degree azimuthal angle (figure 3.3b) the emergent state is perpendicular the initial polarization plane. Azimuthal variation of backscattered linear polarizations is considered extensively in [74] and [75] illustrating this effect. This azimuthal dependence indicates that, for path lengths greater than or equal to the expected transport mean free path, there is an equal contribution to the co-polar and cross-polar components in the case of linearly polarized illumination[25].

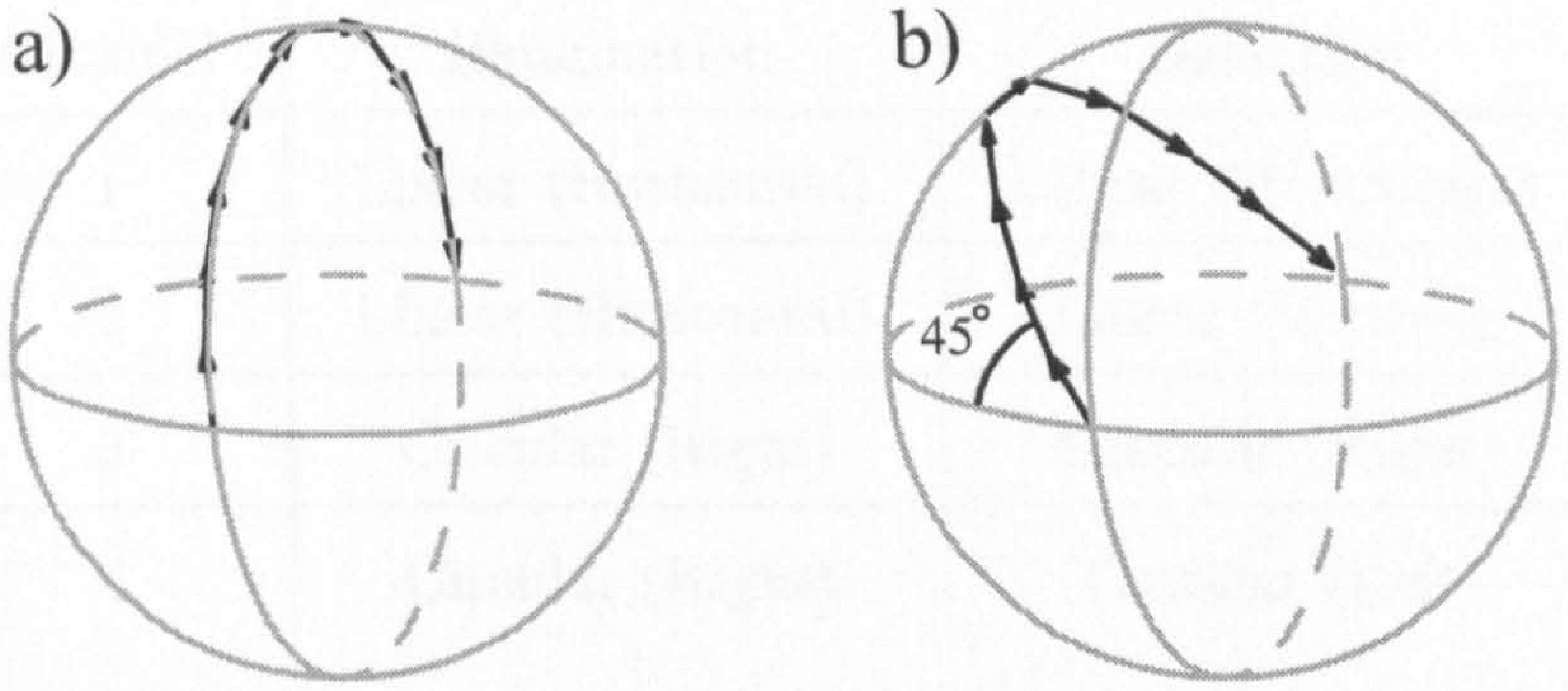

Figure 3.3: *Alteration in direction from direct forward propagation ($k_x = k_y = 0,\ k_z = 1$) to direct back propagation ($k_x = k_y = 0,\ k_z = -1$) a) along the plane of linear polarization resulting in polarization maintenance and b) at 45 degrees to the polarization plane resulting in a cross-polar state.*

Circularly polarized light however is insensitive to an azimuthal rotation of polarization components. Intuitively, this is explained due to circular polarization states being, by definition, circularly symmetrical and therefore their rotation in this azimuthal plane does not result in any depolarization away from its initial state.

3.2.1 Mie Scattering

During this study an effort is made to approximate the properties of producible scattering phantoms to the properties of skin tissue samples. Clearly, however, the model must simplify the structures significantly due to the complex structure of tissue. One model, widely used as a first approximation, is spherical scattering centres suspended in a homogeneous supporting medium. The numerical modelling of such an arrangement can be implemented using a range of models concerning the scattering behaviour of the individual particles. These include the Henyey-Greenstein approximation[34], Rayleigh scattering[3] and Mie theory[3, 35].

The model selected here is defined by Mie theory. This allows the simulation of scatterers at a range of sizes including the region $d \approx \lambda$ which is not possible using Rayleigh

Channel	Illumination	Detection
1	Linear (Horizontal)	Linear (Horizontal)
2	Linear (Horizontal)	Linear (Vertical)
3	Circular (Right)	Circular (Right)
4	Circular (Right)	Circular (Left)

Table 3.1: *Polarization discrimination detection scheme.*

models[3] which are tailored to very small particles. The implementation of Mie theory also includes determining the rigorous mathematical solution of the electromagnetic field interacting with the scattering particle. This provides a detailed scattering phase function characterising scattered field with scattering angle. Such a detailed solution is not provided by the Henyey-Greenstein solution[34] which provides an approximation to the result provided by Mie theory.

3.3 The Polarization Detection Regimes

The techniques throughout this thesis use both linear and circular polarization states to illuminate the samples due to their different behaviour with scattering as discussed in section 3.2. To allow analysis of the behaviour of the polarization state of scattered light, a detection regime is required to provide analysis of light emerging in different states. To achieve this, a four channel detection scheme is used as outlined in table 3.1. This shows that for each of the different illuminating polarization states, linear and circular, both the co-polar and cross-polar intensities are detected. The reason for this selection is to allow discrimination between light that may have maintained its initial polarization state to some degree, which would fall into the co-polar detection channel, and that which has had this property randomised which would therefore be detected either in the orthogonal cross-polar or parallel co-polar channel.

For the investigations performed in this thesis it is necessary to be able to perform this discrimination both experimentally, using optical components, and theoretically, via manipulation of the Stokes' parameters to allow analysis of simulated data[39].

To achieve the illumination state required for channels 1 and 2 from table 3.1 it is clear that only a linear polarizer is required. On detection these channels also only require a single linear polarizer aligned along the plane of polarization to produce the co-polar channel 1 and orthogonal to this plane to yield the cross-polar channel 2.

Additional components are required for experimental implementation of the circularly polarized channels (3 and 4). A quarter wave retardation component is required between the first linear polarizer and sample, with its fast-axis aligned at 45 degrees to the plane of linear polarization. This produces circularly polarized illumination[86]. On detection, a quarter wave retardation is also required to unwrap the emerging circular polarizations into the co-polar and cross-polar channels. Discrimination is therefore achieved by a following linear polarizer, aligned to the illuminating linear polarization plane for channel 3 or orthogonal to the plane for channel 4.

To derive the process required to extract these channels mathematically it is necessary to consider the Mueller matrices used to represent the theoretical components in the system[39]. Using the standard notation for the Stokes' parameters, the four channels are therefore defined by equations 3.1 to 3.4.

$$I_{ch1} = \frac{I}{2} + \frac{Q}{2} \tag{3.1}$$

$$I_{ch2} = \frac{I}{2} - \frac{Q}{2} \tag{3.2}$$

$$I_{ch3} = \frac{I}{2} - \frac{V}{2} \tag{3.3}$$

$$I_{ch4} = \frac{I}{2} + \frac{V}{2} \tag{3.4}$$

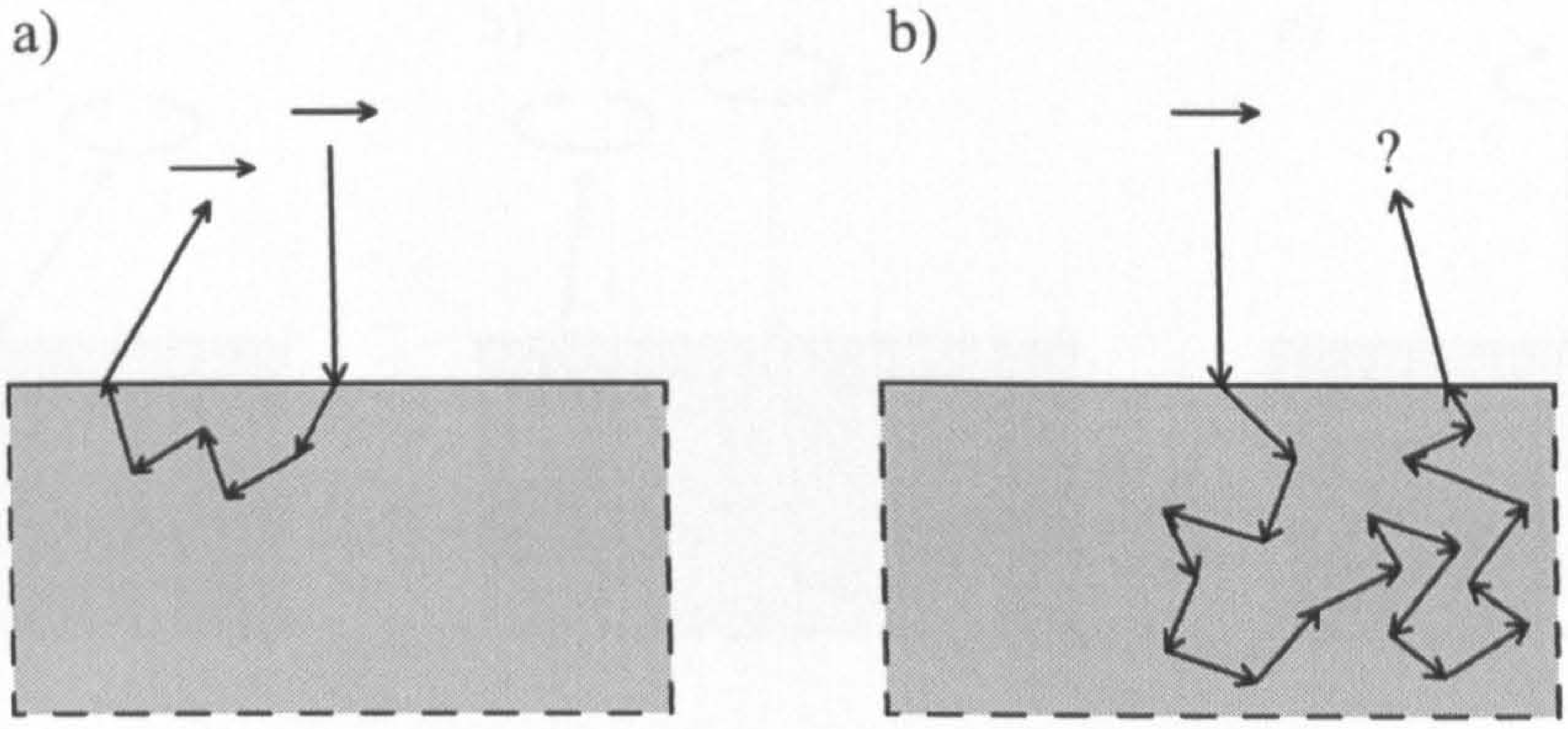

Figure 3.4: *Illumination with linearly polarized illumination results in two general categories of backscatter: a) polarization maintaining due to a low number of scattering events and b) polarization randomising multiple scatter.*

Contained within the defined polarization channels are different categories of light, the understanding of which may enable investigation of different sample volumes. It has been discussed in section 3.2 that light maintains its initial polarization state to an extent if the number of scattering events is not too large. Therefore, for linearly polarized illumination, the backscattered light falls into two broad categories as illustrated in figure 3.4. Here it can be seen that the two categories are polarization maintaining light, probing superficial regions of the medium, and multiple scatter which has probed deeper regions and hence has undergone many scattering events.

The case for circularly polarized illumination does not result in such a simple solution as the helicity of the polarization state must also be considered. The different types of light emergent in backscatter from a scattering sample are represented in figure 3.5. Here it can be seen that light which has propagated deep into the sample has once again had its polarization randomised. However, for shallow penetrating light a discrimination must be made. Light which is returned from the sample by a single scattering event will have its polarization helicity reversed due to an effective mirror reflection, whereas light which has been subjected to a forward scattering sequence before backscatter will have maintained

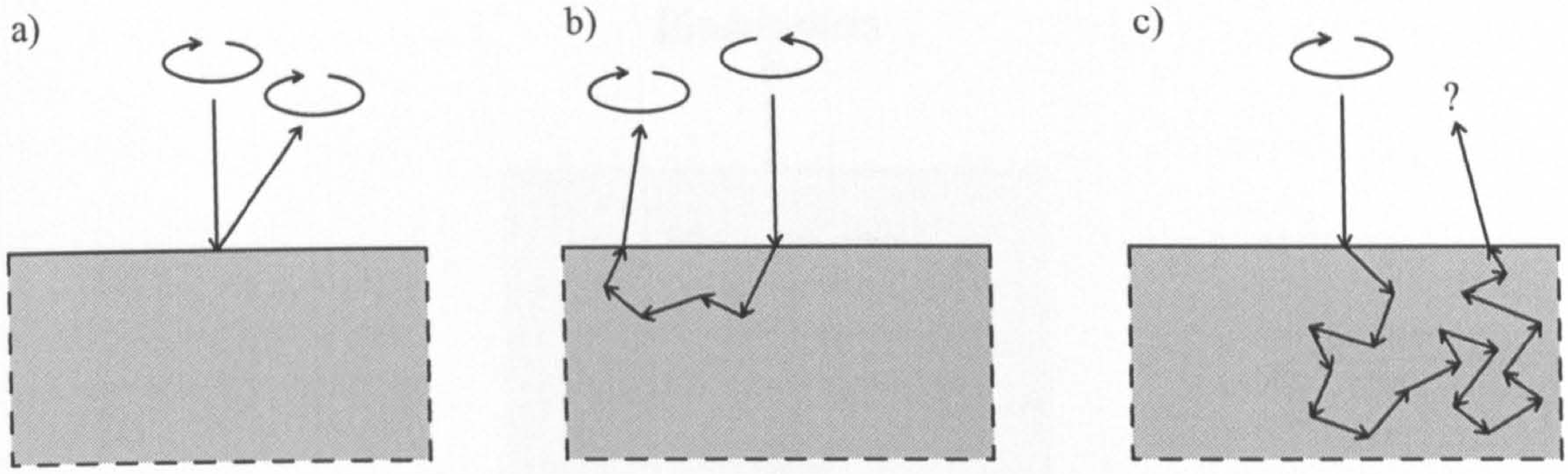

Figure 3.5: *Illumination with circularly polarized illumination results in three general categories of backscatter: a) helicity flipping singles scatter return, b) forward scattering polarization maintaining scattering sequence and c) multiple scatter polarization randomising sequence.*

its polarization state and will emerge in the orthogonal state to single scatter.

3.4 Monte Carlo Simulation

As stated previously, the technique used during the early work to examine the behaviour of polarized light propagating in, and being backscattered from, scattering media is a fully polarized Monte Carlo simulation. This model simulates illumination of a medium with a pencil beam of polarized light perpendicular to its surface and models individual photons (or light packets) propagating through a layered scattering medium composed of Mie scattering particles[3]. The details of the basic Monte Carlo engine extended here to represent layered media have been discussed elsewhere[38] and is therefore addressed only briefly here.

Photons are individually tracked through the layered scattering medium and, at each photon-particle collision, the direction and polarization are modified via adjustment of the photon's directional cosines and Stokes' parameters. The propagation distance before the next possible particle collision is then selected from a distribution weighted around the mean free path (MFP). Several characteristics of photons backscattered from the medium

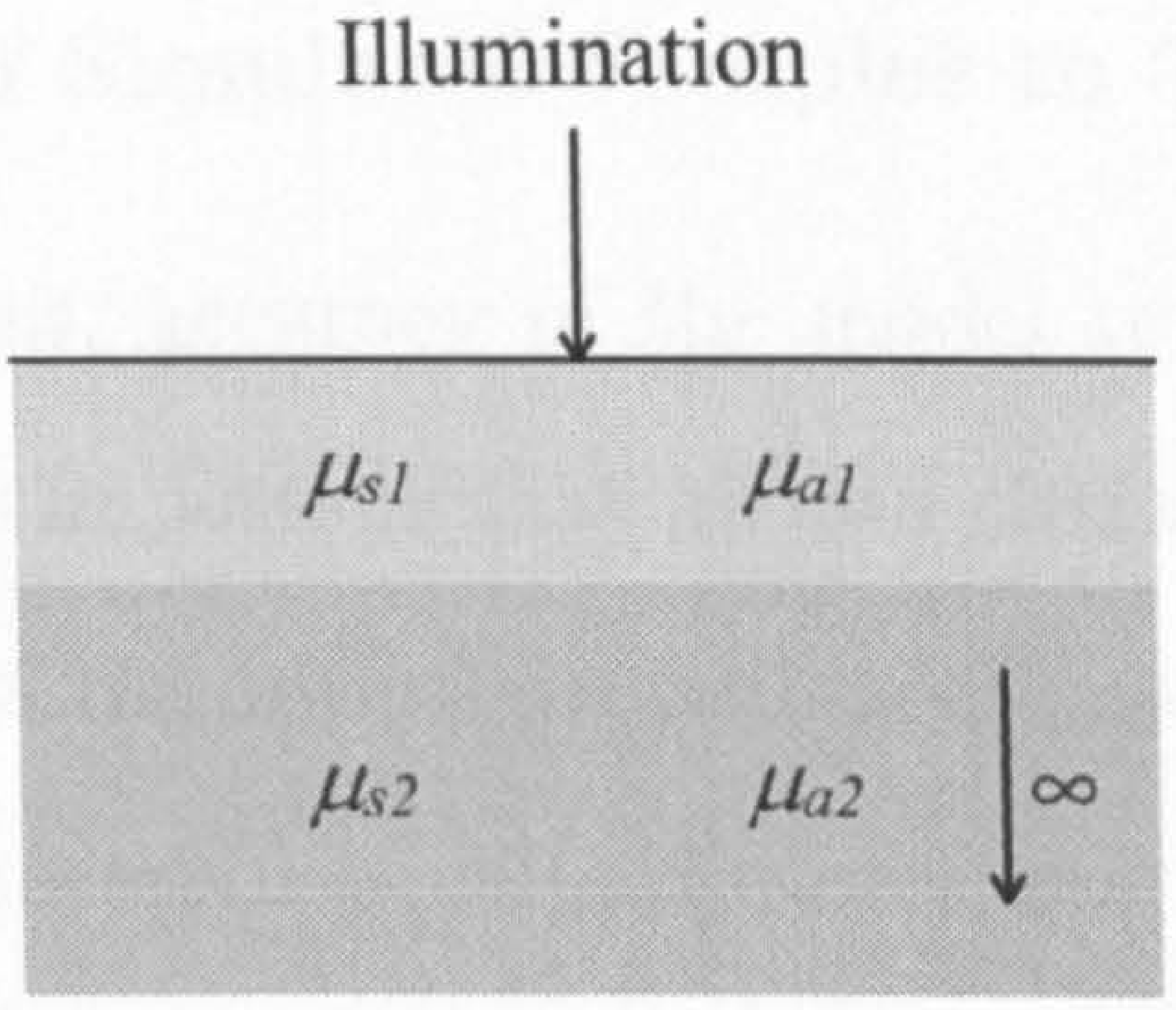

Figure 3.6: *General simulated sample geometry.*

are recorded, including: resulting Stokes' parameters, emerging directional cosines, mean and maximum depth penetrations, emergence location and absolute distance traveled in each internal layer.

3.4.1 Sample Structures and Variable Parameters

Figure 3.6 shows the general form of a sample under investigation. The model is capable of simulating multiple layers each infinite in the x-y plane with a lower layer which is semi-infinite in the z direction. However, for simplicity we generally consider a two layer medium in this study, as this is deemed sufficient to model the structure of the superficial regions of the skin. Approximation of this model to the properties of human tissue is discussed further in section 3.4.2. Each layer can have different scattering parameters, μ_s and g[2]. The values of absorption coefficient, μ_{a1} and μ_{a2}, can also be independently varied for each layer.

---

[2] Variation of the anisotropy factor, g, is achieved by adjusting the size parameter, x, associated with the illuminated particle (equation 1.1) and refractive index mismatch between the particle and its surrounding medium.

3.4.2 Approximation of Simulated Samples to Tissue Parameters

During the early investigations, accuracy of the model to represent human skin tissue is not essential, however, it is important that certain characteristics mirror those in real biological tissue. Evaluation of the optical properties of human skin tissue has formed the subject of a large amount of research [4, 27]. However, one common feature fundamental to the behaviour of polarized light in scattering media is that the scattering events have a high forward tendency. For the purposes of this early research therefore $g = 0.92$. The selection of a realistic value of surrounding refractive index ($n = 1.4$) fixes the value of size parameter defined in equation 1.1 as $x = 13.896$ at $\lambda = 633$nm.

This forms only a first approximation to tissue properties, but should provide indication of any trends resultant from a heavily forward scattering medium such as the skin.

3.4.3 Addition of Absorption

As discussed in section 1.2.2, the degree to which light is absorbed by a material, and the subsequent effect on the intensities of light with different wavelengths, is determined by the absorption coefficient, $\mu_a(\lambda)$. Lambert-Beer's law was defined in equation 1.3 for light propagating a known path length. Provided the absolute path length of a photon is carefully tracked by the model as it travels between scattering centres this expression still holds. Therefore, with the path length data being recorded, absorption effects can be added post-simulation. This allows the modelling of different levels of absorption for different layers, providing the propagation distance in each layer is also stored.

3.5 Preliminary Polarization Investigation

It has been suggested previously [25, 82] and discussed in section 3.2 that initially linearly and circularly polarized light behave in different ways as they propagate through scattering media in terms of the rate at which the light depolarizes. This fundamental property forms the basis for much of the early research performed in this study, therefore, it is necessary to confirm the occurrence of this property for bulk scattering. To enable a theoretical analysis, the Monte Carlo technique outlined in section 3.4 has been used to model the propagation of polarized light in a single layer scattering sample of varying thickness and constant scatterer concentration. Simulated results for linearly and circularly polarized illumination, detected in-line with the channels defined in table 3.1, for a sample of varying thickness are shown in figures 3.7 and 3.8. The thickness is defined in terms of the MFP for the medium. Also included in these figures for reference is a plot of the difference between the two detected channels. The significance of this will become apparent in section 3.6. The properties of this initial scattering medium were an absorption coefficient of zero, MFP of unity and an anisotropy factor, g, equal to 0.92.

The first feature that is clear from figures 3.7 and 3.8 is that for all channels the intensity increases with sample thickness. This is due to the fact that, for thinner samples, more light is transmitted through the medium and is therefore not detected in the backscatter. Alternatively for thicker samples more scattering events are experienced when trying to propagate through the medium and thus, the probability of the scattering causing a photon to be returned in backscatter is increased. However, these trends are prevalent irrespective of polarization state and consequently give no indication of the effectiveness of applying such discrimination; to achieve this the subtleties of the variations must be analysed.

Considering first the linearly polarized channels, it is clear that at all thicknesses the co-polar channel (channel 1) results in a higher backscattered intensity than channel 2, the cross-polar channel. Reasoning for this stems from the fact that it takes a number of scattering events for the polarization state of light to be randomised. Therefore, if the path of a photon results in it being backscattered from the sample before being subjected to this number of scattering events it will still maintain some level of tendency to the initial illuminating state of polarization. Photons which have undergone many scattering

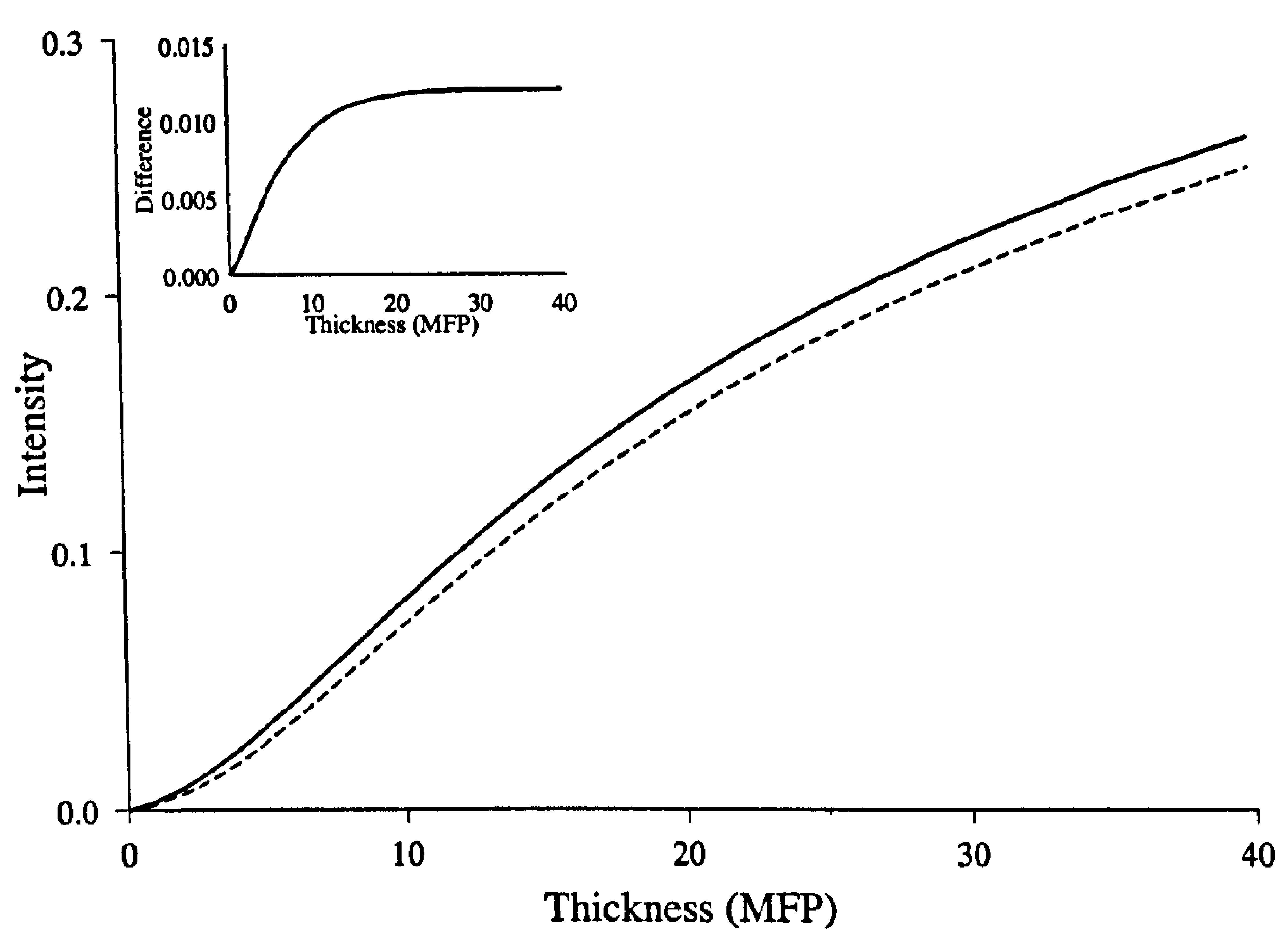

Figure 3.7: *Simulated levels of backscattered intensity for linearly polarized illumination in the co-polar channel 1 (solid line) and cross-polar channel 2 (dashed line) for varying sample thicknesses. The inset shows the difference between the two channels.*

events will have had their polarization state randomised and therefore the contribution of such a photon will, on average, contribute equally to channels 1 and 2. Any difference in the variation of the two channel intensities with sample thickness can therefore be assigned to the contribution of photons which, to some level, have maintained their initial polarization state. It can be seen that the difference between the two channels reaches a constant level at a thickness of around 12MFPs. This indicates that for samples thinner than this, some light which has maintained its polarization has propagated all the way through the medium. Therefore, for an increase in thickness for samples thicker than 12MFPs, any increase in channel intensity can be mainly attributed to multiple scatter.

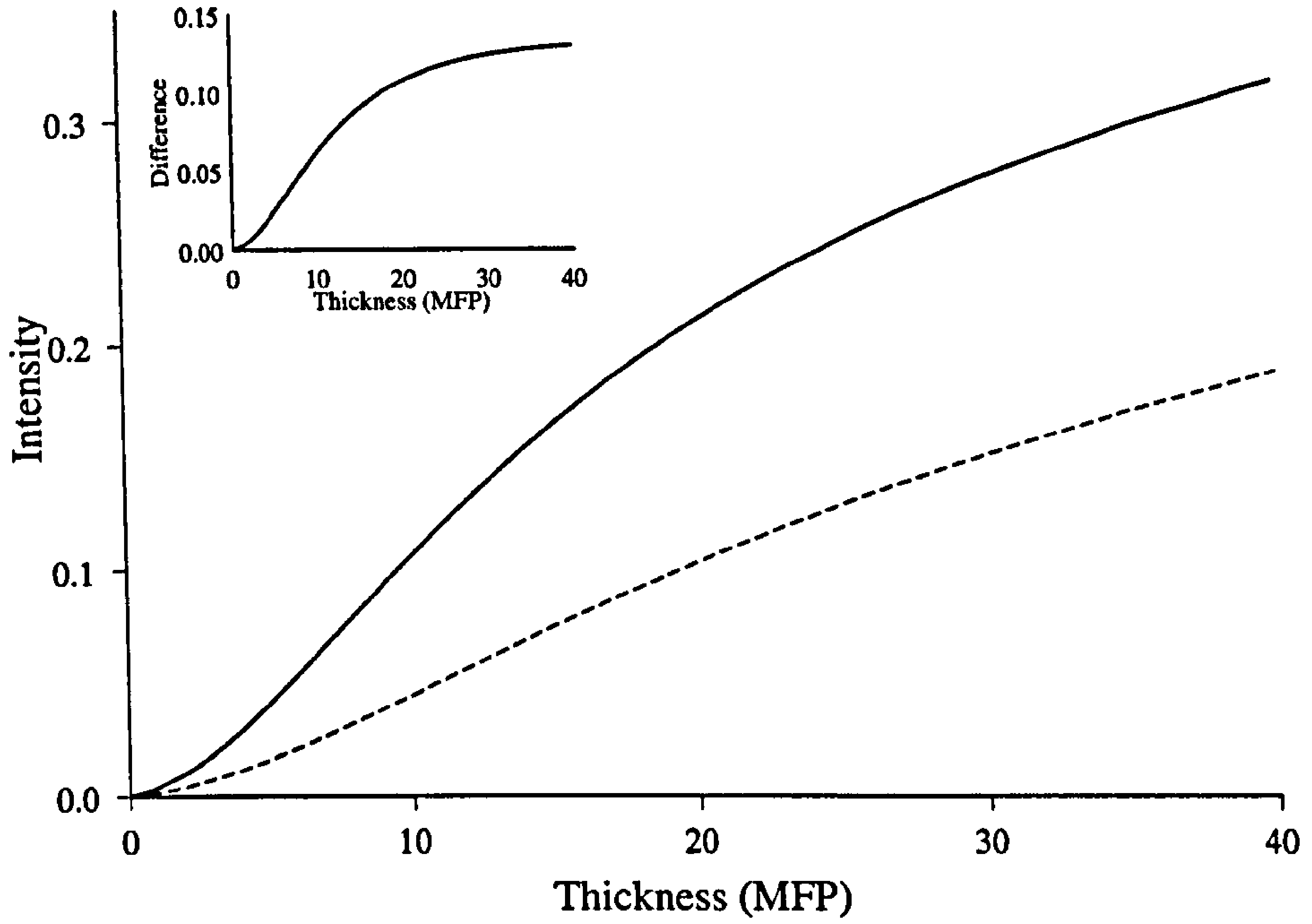

Figure 3.8: *Simulated levels of backscattered intensity for circularly polarized illumination in the co-polar channel 3 (solid line) and cross-polar channel 4 (dashed line) for varying sample thickness. The inset shows the difference between the two channels.*

To provide a better indication of the polarization maintenance properties of the backscattered light, a degree of polarization (DOP) can be defined (equation 3.5).

$$DOP_l = \frac{I_{ch1} - I_{ch2}}{I_{ch1} + I_{ch2}} \tag{3.5}$$

The variation of this value with sample thickness, calculated from the plots in figure 3.7 can be seen in figure 3.9. This plot reiterates the previous point clearly showing that for thin samples, a high proportion of the backscattered light has maintained, to some degree, its initial polarization state. As the sample thickness increases more multiple scattered light is detected, increasing the intensity of both channels. This indicates that

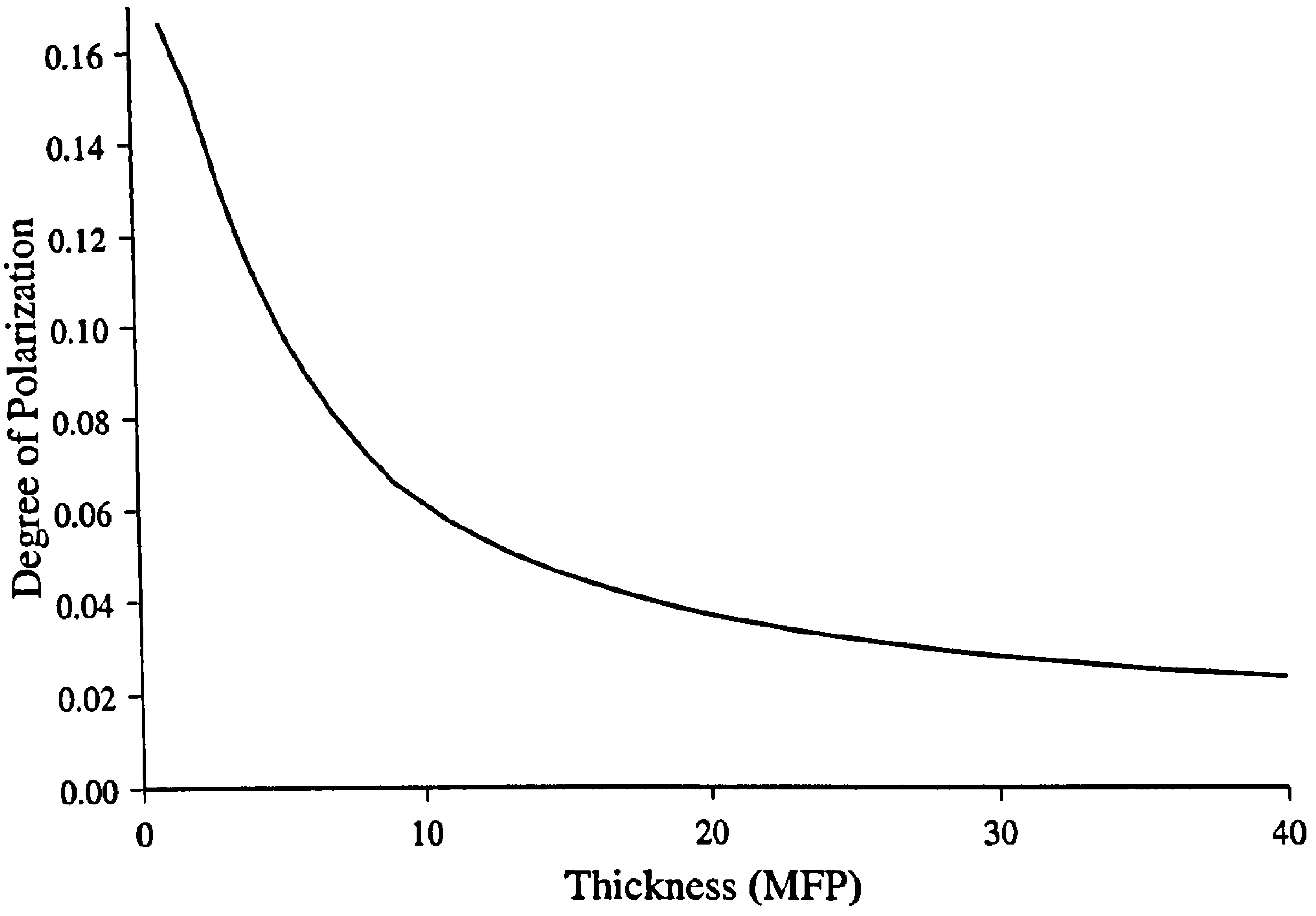

Figure 3.9: *Degree of linear polarization calculated from the variations in figure 3.7 for varying sample thickness.*

the polarization maintaining component in channel 1 forms a lower percentage of the backscattered light, which reduces the overall degree of linear polarization.

The circularly polarized channels represented in figure 3.8 clearly indicate that the intensity of the co-polar channel 3 is greater than the intensity detected in the cross-polar channel 4 for all sample thicknesses. The arguments for linearly polarized light maintaining its initial polarization state also hold for circular polarizations. The anisotropy factor of the scattering particles present in the medium has a large effect on the ratio of the two circular channels. This is due to particles promoting direct backscatter increasing the occurrence of photons emerging in channel 4 and with forward scattering particles increasing the weighting of channel 3. For the simulations presented here, the properties of the individual particles in the medium are heavily forward scattering, suggesting that few photons are returned directly from their first scattering event, which would contribute to the cross-polar circular polarization channel. The tendency is for photons to travel in a forward direction, maintaining the initial helicity of the circular polarization. For this reason the intensity of channel 3 containing the forward scattered component has a higher intensity than the cross-polar equivalent. It is clear that the two plots are tending to become parallel, indicating that the multiple scatter component, which contributes equally to both co-polar and cross-polar channels, is increasing at a higher rate than the polarization maintaining circular polarization. The DOP for circular polarizations is defined in equation 3.6 and its variation with sample thickness plotted in figure 3.10.

$$DOP_c = \frac{I_{ch3} - I_{ch4}}{I_{ch3} + I_{ch4}} \tag{3.6}$$

When comparing figures 3.7 and 3.8, it is clear that the linear polarization channels become parallel sooner (in terms of sample thickness) than in the circular case. This suggests that the circularly polarized illumination is maintaining its initial polarization to greater depths. This can be further investigated by analysis of the DOP for the circular polarization channels as shown in figure 3.10.

Here it can be seen that not only is the overall DOP much greater than the linearly polarized equivalent, but the rate of decay is clearly much less, indicating a better maintenance of initial polarization state. Another interesting feature that is prevalent in the variation of DOP for circular polarizations is that, rather than the DOP decreasing monotonically, there is a small increase in value between 0 and 7MFPs. This effect is explainable after reviewing the mechanism of a forward scattering sequence resulting in polarization maintaining circularly polarized light as illustrated in figure 3.11. For a photon to be backscattered from a purely forward scattering sequence there must be certain depth of medium available in which to scatter, otherwise the sequence will be transmitted through the sample. This implies that these forward scattering sequences are suppressed for thin

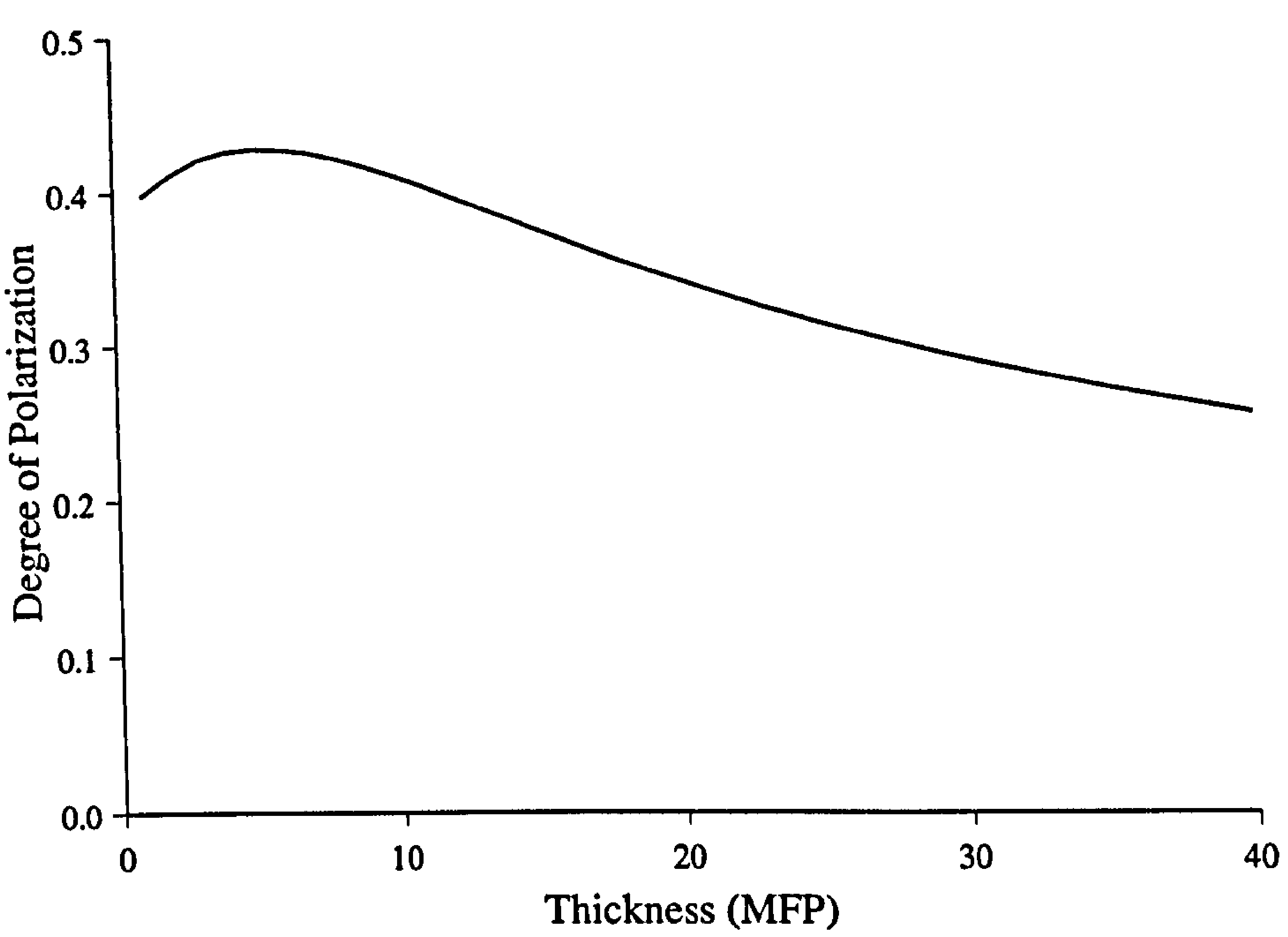

Figure 3.10: *Degree of circular polarization calculated from the variation in figure 3.8 for varying sample thickness.*

samples, resulting in a reduced DOP until at a thickness of around 7MFPs where similar sequences are included in the backscattered intensity.

3.6 Extraction of Polarization Maintaining Light

It has been mentioned in the above discussion that there are crudely two distinct categories of backscattered light; that which has maintained its initial polarization state and that which has had its initial polarization randomised due to a large number of scattering events. Generally speaking the light which has maintained its initial state has probed only the superficial volumes of the sample, which are the regions of interest in skin tissue

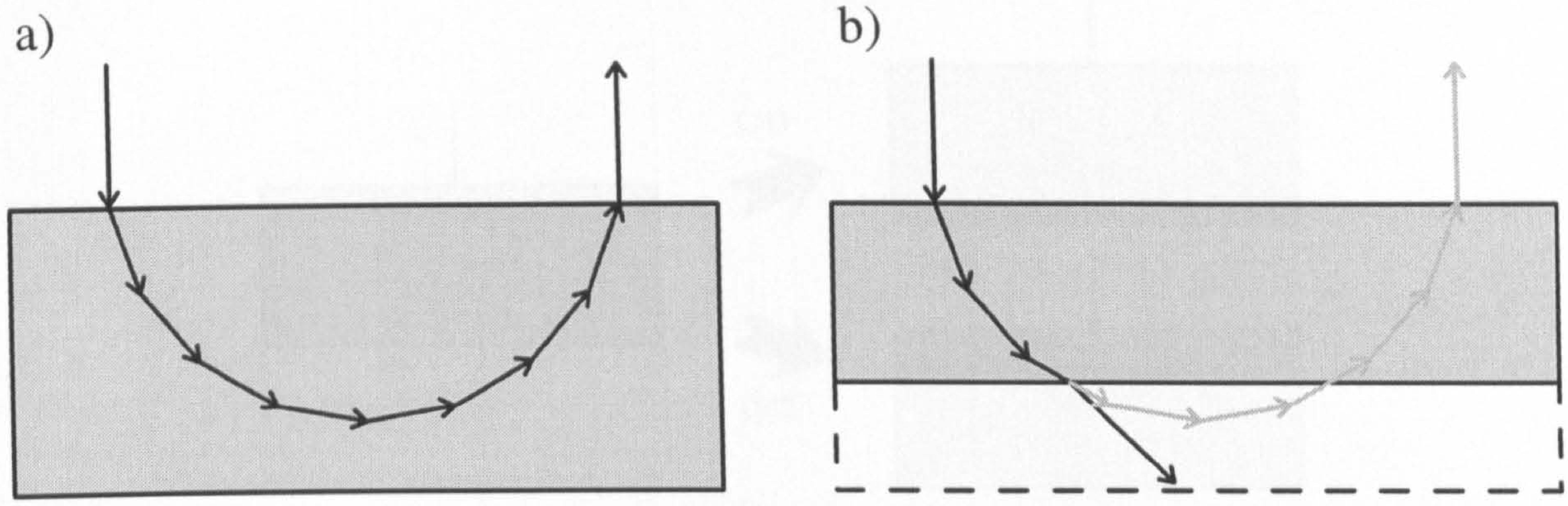

Figure 3.11: *a) A hypothetical perfect forward scattering sequence resulting in a polarization maintaining circularly polarized photon requires a certain sample depth to be possible. For thinner samples b) such a sequence allows the photon to escape due to propagation through the medium.*

imaging. For this reason it would be highly desirable if the component of light which had maintained its initial polarization state could be extracted for examination. Figures 3.7 and 3.8 illustrate that the differences due to polarization state are subtle. This implies that the polarization maintaining light is dominated by that which is multiply scattered. Therefore, the removal of this multiple scattered background will enable more effective analysis of the light which has probed the more useful depths.

To investigate the possibility of extracting this polarization maintaining component, the different categories of light emerging in the different polarization detection channels should be examined. For linearly polarized illumination this is done with the aid of figure 3.12.

Channel 1 is the co-polar channel for linearly polarized illumination. Therefore, it will contain light which has penetrated only to shallow depths and therefore has a tendency to this initial state which forms the component of light that we are interested in extracting. Alongside this is a large component due to multiple scatter containing light with a random polarization state, some of which will have linear components in the same plane as the

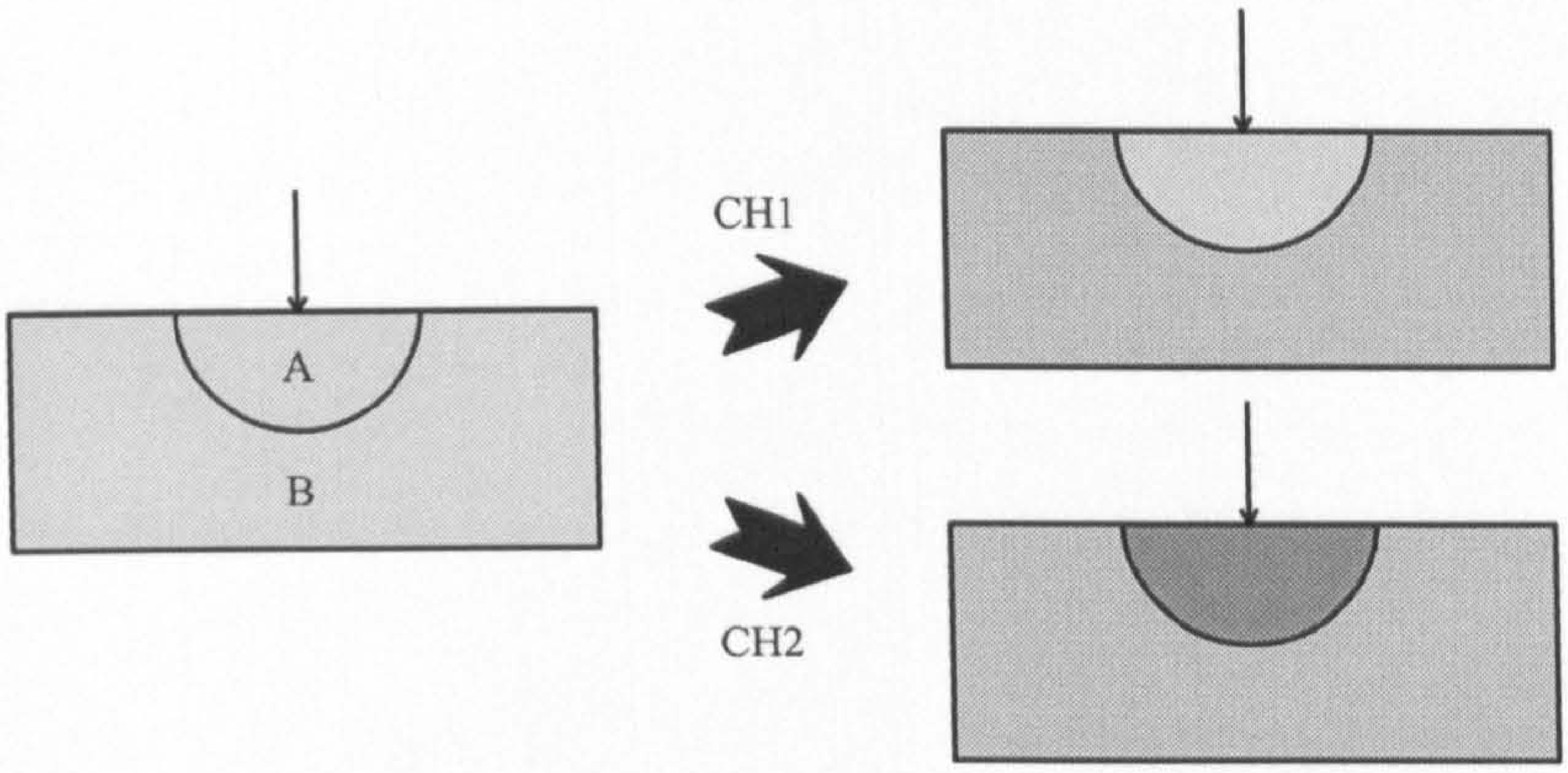

Figure 3.12: *Light backscattered from a sample after linearly polarized illumination divides in to two very general categories: A - light which had maintained the initial polarization and B - multiply scattered light with randomised polarization state. Discrimination into channel 1 results in light from category A and statistically 50% of the light from region B. Channel 2 contains the other 50% from category B.*

illuminating plane of polarization. In considering the cross-polar channel 2, all of the shallow penetrating light which has maintained its polarization state is optically removed. This leaves the other half of the multiple scattered light, which randomly has components in a direction orthogonal to the illumination polarization plane.

Due to the random nature of the multiple scattered light, the intensity attributed to this component is divided equally between channels 1 and 2. Therefore, if the two channels are subtracted, the remaining component will be the light which has maintained its polarization state. As stated above, this light has probed the regions of interest. Extraction of this component is clarified by the following expressions:

$$\begin{aligned} I_{lsub} &= I_{ch1} - I_{ch2} \qquad (3.7) \\ I_{lsub} &= (I_{maintain} + I_{multiple}) - I_{multiple} \\ I_{lsub} &= I_{maintain} \end{aligned}$$

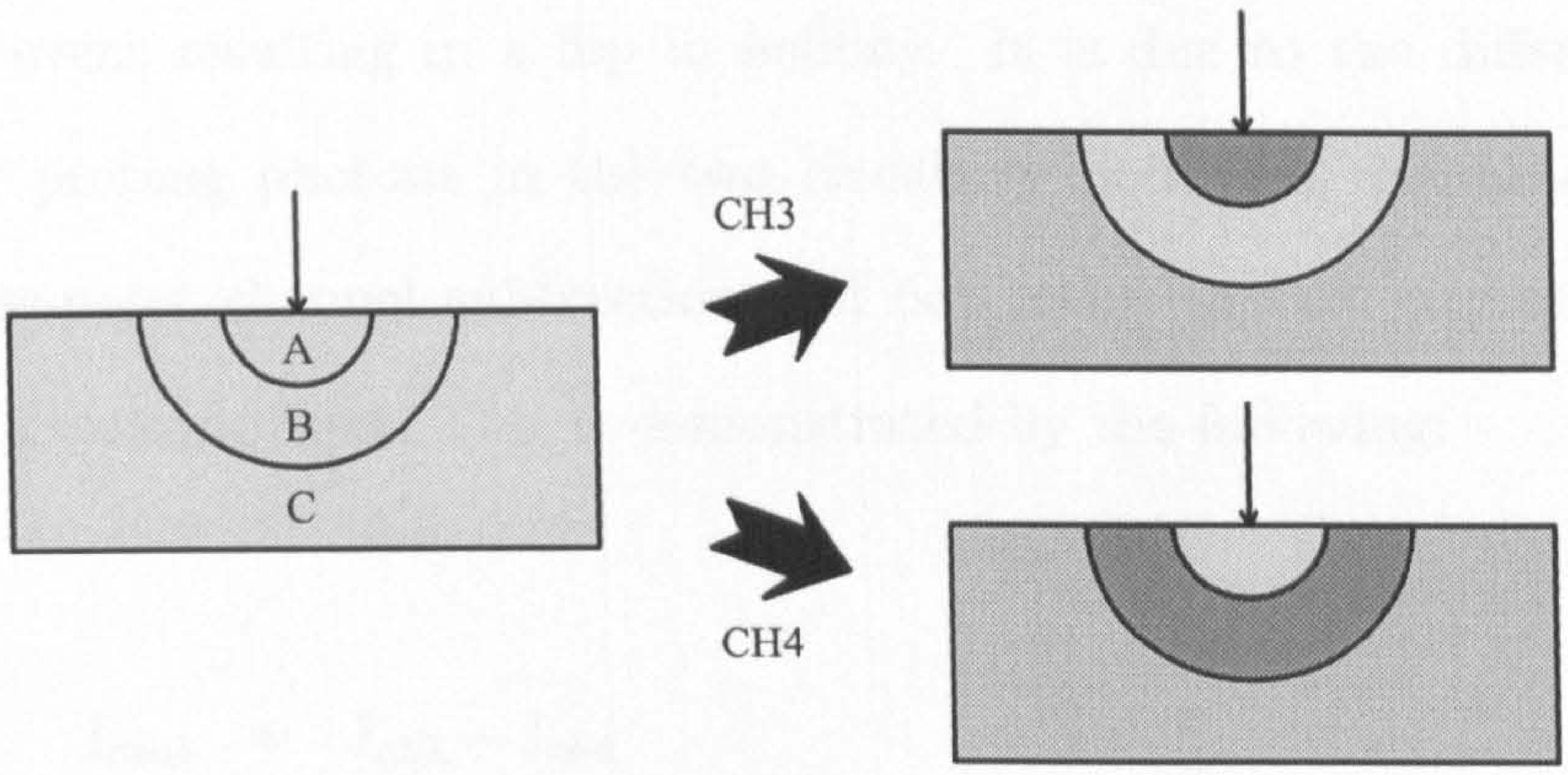

Figure 3.13: *Light backscattered from a sample after circularly polarized illumination divides in to three very general categories: A - singly scattered light resulting in a flip in helicity of polarization, B - polarization maintaining light resulting from a forward scattering sequence and C - multiply scattered light with randomised polarization state. Discrimination into channel 3 results in light from category B and statistically 50% of the light from region C. Channel 2 contains the other 50% from category C and the helicity flipped singly scattered light from region A.*

This is a standard technique which has been applied extensively elsewhere [50, 85, 120, 121, 122].

Extraction of circularly polarized illumination which has maintained this initial state is not so trivial. The different categories of light backscattered into channels 3 and 4 are illustrated in figure 3.13.

When illuminating with circularly polarized light, the output polarization channels are slightly more complex than for the case involving linear polarization states. In reference to the previous discussion, a sequence of forward scattering events will result in a photon maintaining its initial polarization state and will contribute only to channel 3. Along with this contribution, half of the polarization randomised multiple scatter will also be detected here. For the cross-polar circular channel the other half of this randomised light will be detected along with light which has undergone a mirror reflection due to a direct backscattering event resulting in a flip in helicity. It is due to the different properties of superficially probing photons in the two circularly polarized channels that indicate a co-polar/cross-polar channel subtraction will not result in the extraction of circular polarization maintaining light. This is demonstrated by the following:

$$\begin{aligned} I_{csub} &= I_{ch3} - I_{ch4} \\ I_{csub} &= (I_{forward} + I_{multiple}) - (I_{reflected} + I_{multiple}) \\ I_{csub} &= I_{forward} - I_{reflected} \end{aligned}$$

To avoid this unwanted cross term, the approximation is made that the multiple scattered, initially linearly polarized light, is equal to the multiply scattered light due to initially circularly polarized light. This implies that subtraction of channel 2, which is composed solely of multiple scattered light, from the circular co-polar channel, will result in the extraction of the circularly polarized maintaining state as demonstrated below. The effect of this approximation is examined in appendix A.

$$\begin{aligned} I_{xsub} &= I_{ch3} - I_{ch2} \\ I_{xsub} &= (I_{forward} + I_{Cmultiple}) - (I_{Lmultiple}) \\ I_{Cmultiple} &\approx I_{Lmultiple} \\ I_{xsub} &= I_{forward} \end{aligned} \tag{3.8}$$

Performing the subtractions described in equations 3.7 and 3.8 results in the variations of polarization maintaining light with sample thickness shown in figure 3.14. It is clear from this figure that at a thickness of around 20MFPs almost all of the linearly polarized light which has maintained its polarization has been backscattered whereas for circularly polarized light there is still an increase in polarization maintaining light for thicknesses approaching 40MFPs.

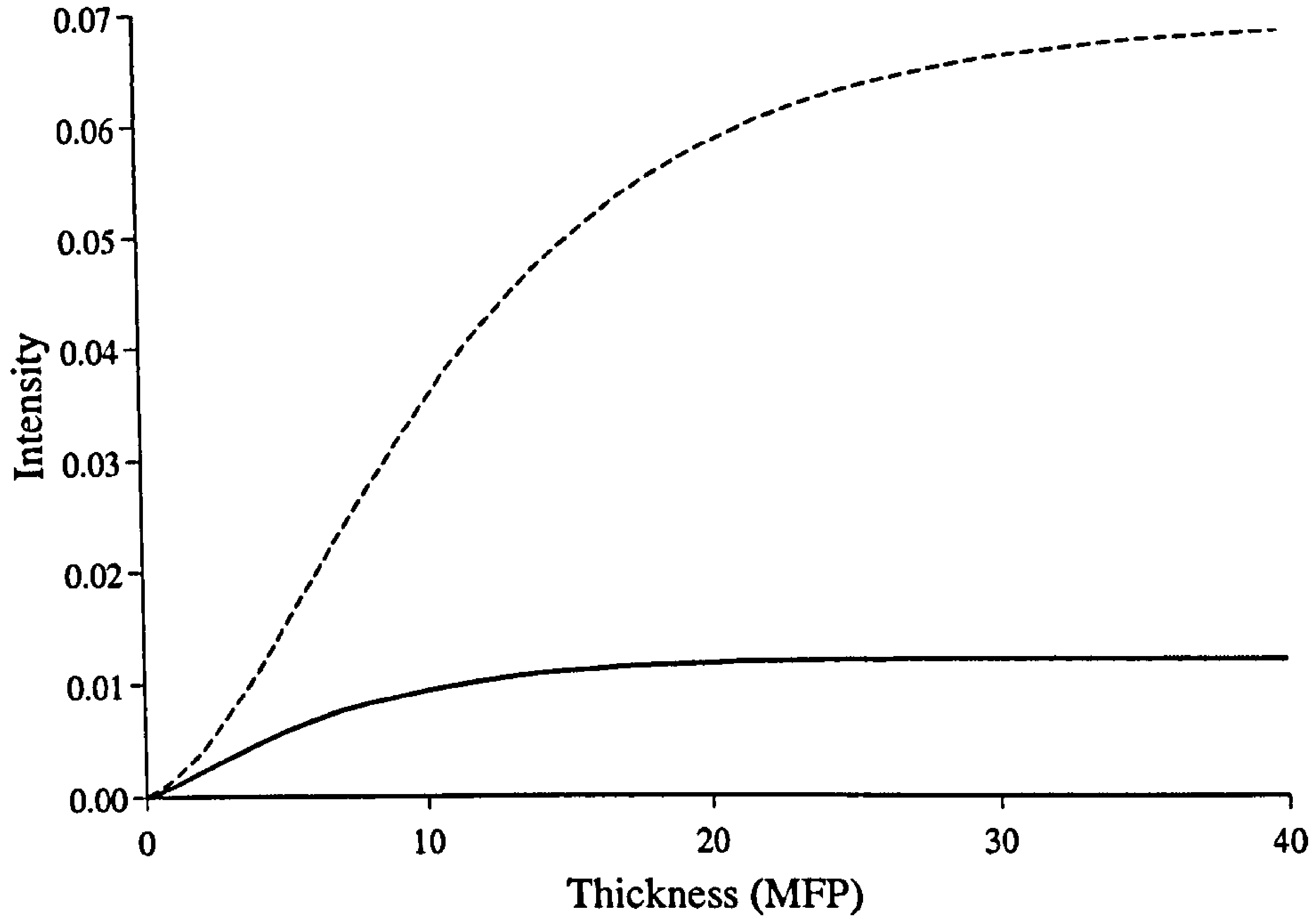

Figure 3.14: *Variation linear polarization maintaining light (solid line) (channel 1 - channel 2) and circular polarization maintaining light (dashed line) (channel 3 - channel 2) with sample thickness.*

3.7 Spatial Analysis

It has been shown in the previous section that there are differences between the behaviour of linearly and circularly polarized light in terms of its maintenance of initial polarization state. To investigate the sensitivity of the different polarization channels to different layers within a medium, the radial distribution of the backscatter in the different channels can be assessed. Dependency on spatial emergence is widely used in many systems as address in section 2.3.5. Such analysis takes advantage of the interdependence of radial emergence distance and depth probed.

The spatial intensity distributions produced here, $I(r)$, are obtained by collecting emerging photons into radial bins of width 0.25MFPs. The frequency of photons emerging within annuli centered on the source is measured and normalized by the area of the detector annulus. Mathematically, the intensity detected in the i^{th} radial bin, I_i, is determined as in equation 3.9.

$$I_i = \frac{\int_{r=r_i}^{r_{i+1}} n_r dr}{\pi(r_{i+1}^2 - r_i^2)}, \tag{3.9}$$

where r_i is the radius of the lower boundary of the i^{th} bin and n_r is the photon count detected at radial distance r.

Initially, a single layer semi-infinite homogeneous medium is investigated in terms of the spatial distribution of the emerging light in the different polarization channels. The scattering properties of the medium under test are identical to those examined in section 3.5. The distributions for the four polarization channels are shown in figure 3.15 with the corresponding radial DOP distributions displayed in figure 3.16.

Considering first the linearly polarized channels, it can be seen that for radial distances up to 15MFPs from the source, channel 1 is greater in intensity than channel 2. As discussed in section 3.5 both channels contain equal amounts of multiple scattered light, but channel 1 contains an additional component that has maintained the original polarization. At high radial distances there is no polarization maintaining light and so the DOP (figure 3.16) tends to zero. It is interesting to note that the peak in the linearly polarized DOP is positioned away from the source. At positions close to the source there is a high proportion of single scattered light. Approximately 40% of photons in the first radial bin are returned by a single scatter and, due to this, the intensity distribution can be seen to have a tendency to the Mie scattering footprint of a single scatterer, resulting in an intensity peak removed from the point of illumination. Further discussion of this is performed in appendix C. By performing the simple channel subtraction described in section 3.6, the shallow probing light can be observed. The results of this subtraction are

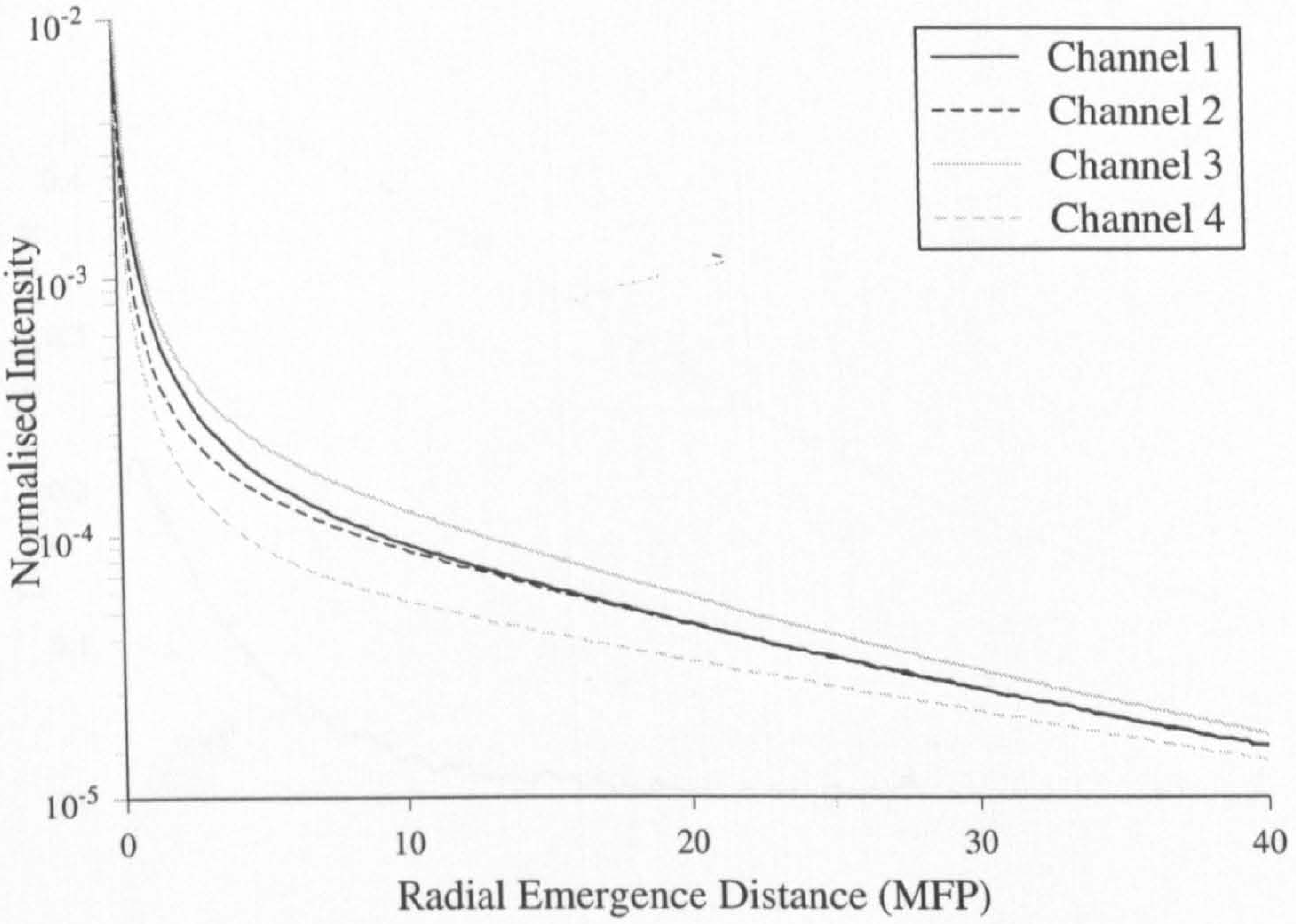

Figure 3.15: *Backscattered intensity radial distributions in the four polarization channels emergent from a single layer semi-infinite homogeneous medium.*

shown in figure 3.17. This demonstrates an apparent improvement in lateral resolution achieved by the removal of multiple scatter, however, it should be noted that this occurs due to the reduction in the depth probed by the light which inherently improves the spatial confinement of the light.

The subtraction has negligible affect on the $1/e$ width of the distributions. This is primarily is due to the high intensity very close to the source and the fact that the majority of light in this region has maintained its initial polarization. It is therefore present in both channel 1 and the resultant subtraction. However, the tail of the distribution has been significantly suppressed due to the exclusion of multiply scattered light.

Figure 3.15 shows that there is a difference between channels 3 and 4 for all radial

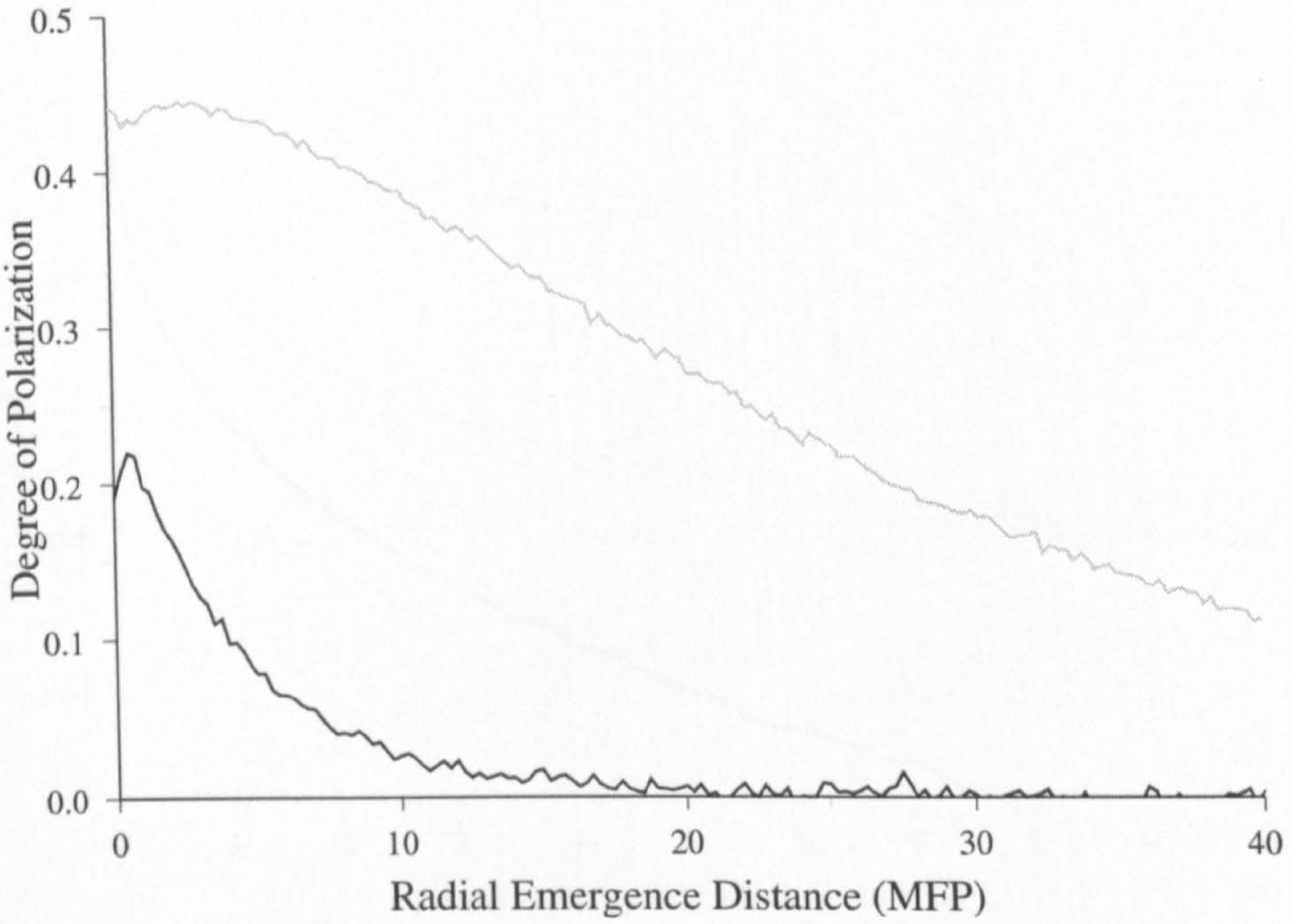

Figure 3.16: *The degree of polarization plots for linearly (black line) and circularly (grey line) polarized illuminations calculated from the spatial distribution curves presented in figure 3.15.*

positions considered. The peak in this DOP plot is away from the source at around $r =$ 2.75MFP. This is due to the mirror reflected contribution present in the cross channel that is concentrated in areas close to the point of illumination in combination with the nature of the mean path taken to establish a forward scattering sequence. Circular polarization maintaining light can also be extracted using the channel subtraction described in section 3.6. The resulting spatial distribution can be seen in figure 3.18. It can be seen that this subtraction also reduces the tail of the radial distribution, indicating an improvement in spatial confinement of circular polarization maintaining light over multiple scatter.

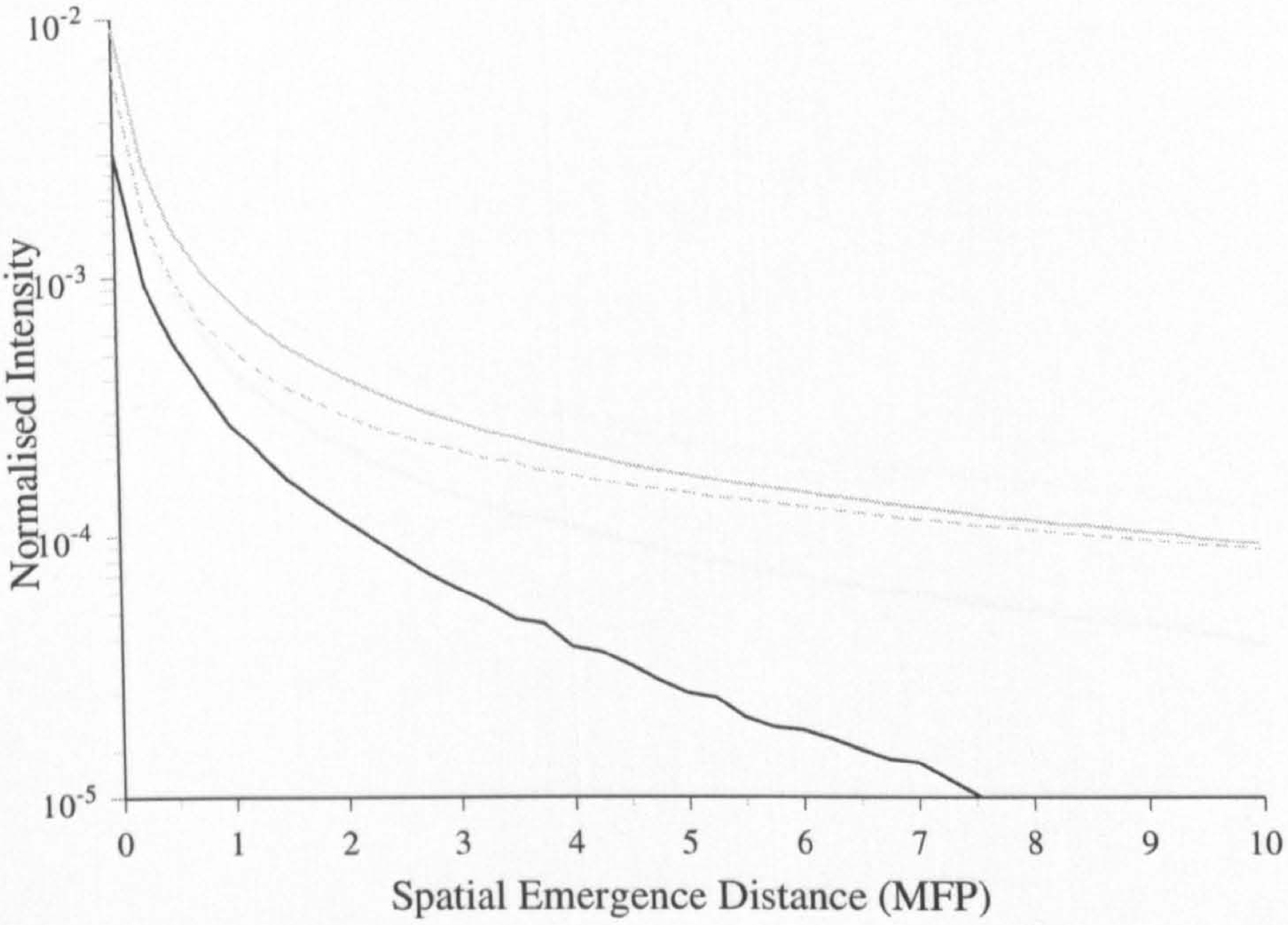

Figure 3.17: *Lateral localisation obtained by extracting linear polarization maintaining light (channel 1 - channel 2) (black line) in comparison to the detected channel 1 (grey solid line) and channel 2(grey dashed line) distributions.*

3.7.1 Depth Analysis

The analysis of the spatial distributions indicate the different initial polarizations probe different volumes of sample. As the data presented is simulated and the path of each photon is tracked it enables the recording of statistics concerning the volumes of sample which have been probed. The maximum visitation depth into the sample can be recorded for each photon, allowing formation of a depth profile directly showing the photon visitation for different polarization states.

Figure 3.19 shows the visitation depths for the four polarization channels. Differences between these trends can be noted, not only in the difference in overall intensities which

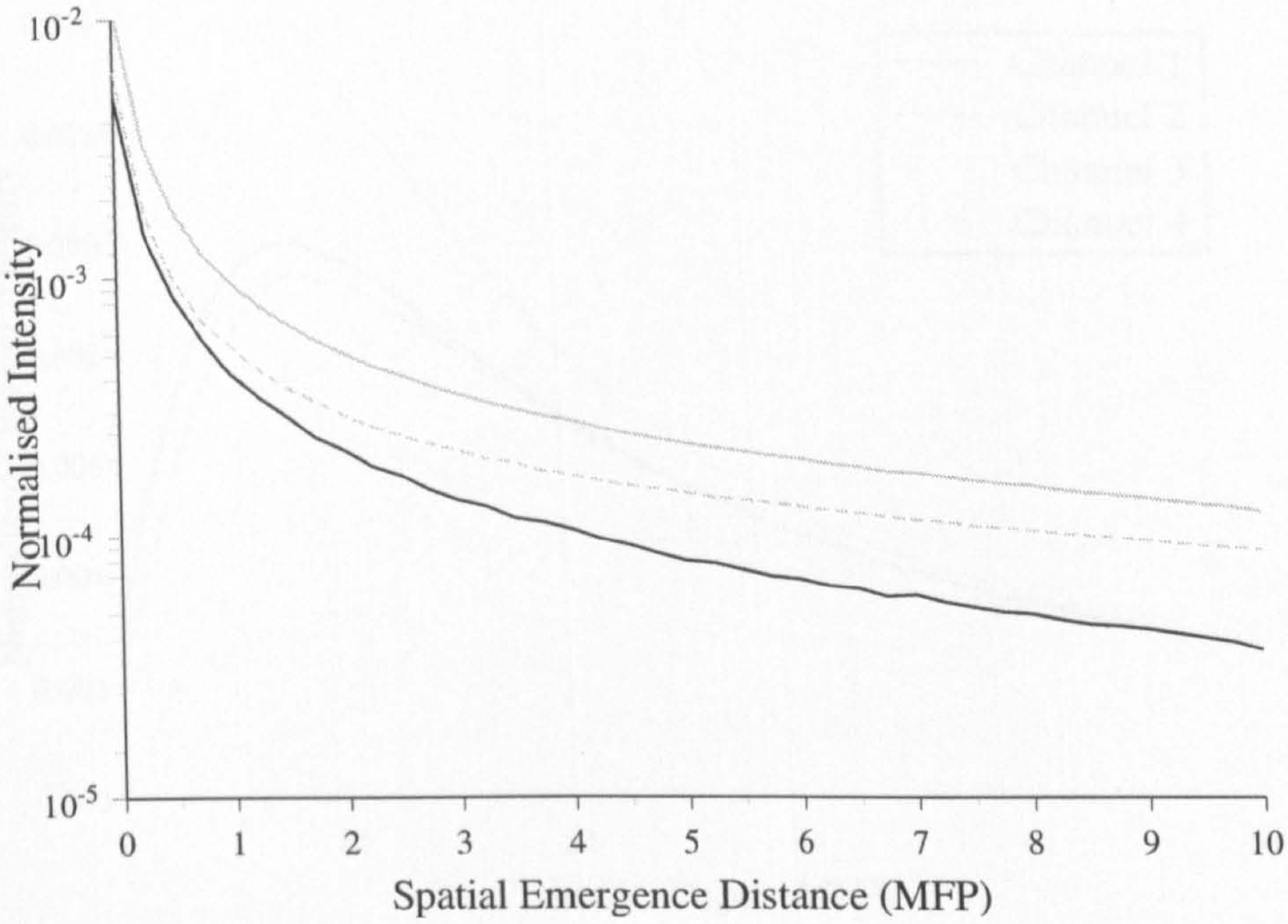

Figure 3.18: *Lateral localisation obtained by extracting circular polarization maintaining light (channel 3 - channel 2) (black line) in comparison to the detected channel 3 (grey solid line) and channel 2 (grey dashed line) distributions.*

have been addressed earlier, but the position of the intensity peaks. However, the clarity of these results in terms of the performance of different polarization maintaining components is not good. By performing the extraction of polarization maintaining light using channel subtraction the result forms the most significant so far.

Shown in figure 3.20 are the intensity depth profiles for polarization maintaining light in the different initial states, normalised to peak intensity. It is clearly shown that the extraction of the different maintained polarizations provides interrogation of different depths. The peak in the linear maintaining distribution occurs at 2MFPs into the sample and 7MFPs for circular polarization maintaining illumination. These are compared to the

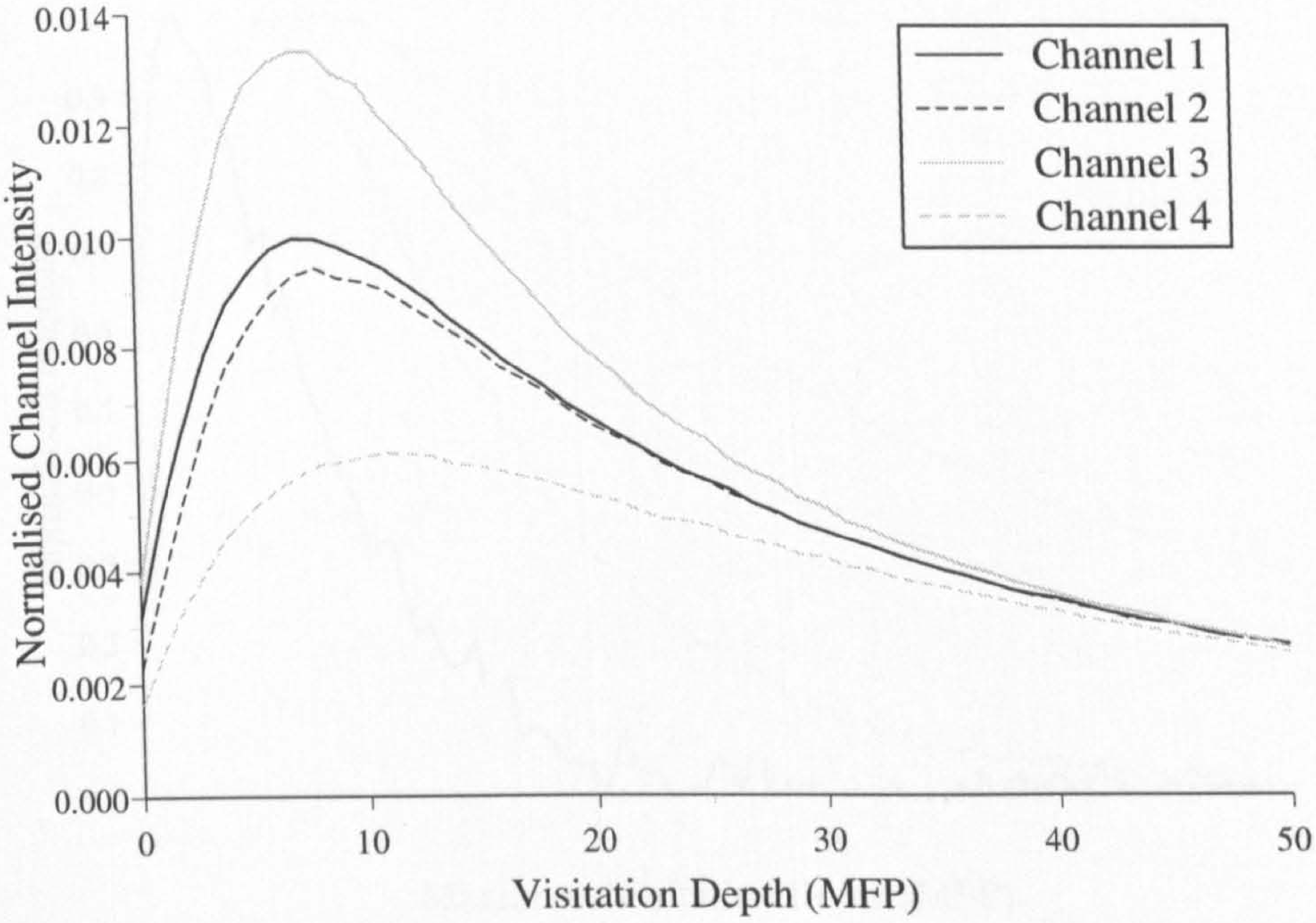

Figure 3.19: *Maximum visitation depth of photons discriminated into the four polarization channels.*

peak location for multiple scattered light which falls at 10MFPs. This property suggests that different polarization states can be used to characterise different depths and therefore different layers within the medium. This is investigated in the following sections.

It should be re-emphasised at this point that the depth properties and hence all resultant trends presented here are valid only for the scattering properties specified. Any significant adjustment in the properties which results in an adjustment of anisotropy factor, may result in these depth properties being significantly altered up to the point where the relative positions of linear maintaining and circular maintaining light are reversed for heavy backward scattering[25].

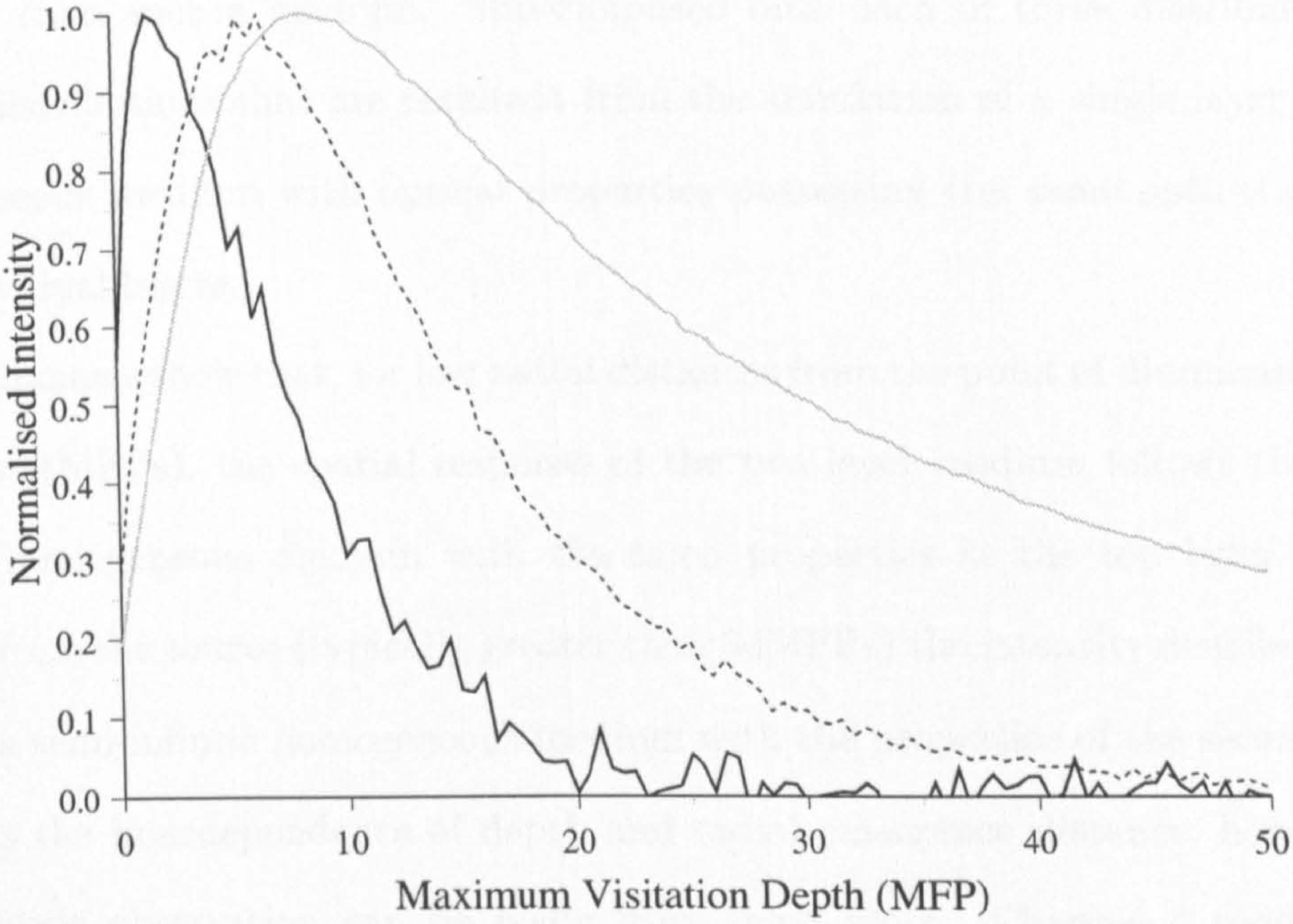

Figure 3.20: *Intensity depth profile, normalised to peak intensity, of extracted linearly polarized light (solid black line), circularly polarized light (dashed black line) and multiple scatter (grey line).*

3.7.2 Two Layer Medium Simulation

The difference in volumes probed by the different polarization states has been illustrated. However, determination of whether these differences are observable in the properties of the backscattered light require examination. To investigate the sensitivity of these different polarizations to different depths within a medium, in terms of their optical response, a two layer structure can be used. A medium with a top layer MFP of 1.0 and semi-infinite bottom layer with a MFP of 2.0 is simulated to provide a mis-match between the layer properties. The thickness of the top layer is set to 10MFPs (relative to the top layer[3])

---

[3] All measures of thickness and absorption are made relative to the MFP of the top layer.

and for this initial case the absorption coefficient for both layers is set to zero.

Shown in figure 3.21 are the spatial distributions resultant in the four polarization channels from such a medium. Superimposed onto each of these distributions are the spatial distributions that are resultant from the simulation of a single layer semi-infinite homogeneous medium with optical properties possessing the same optical properties as the individual layers.

All channels show that, for low radial distances from the point of illumination (typically less than 4MFPs), the spatial response of the two layer medium follows that of a semi-infinite homogeneous medium with the same properties as the top layer. Conversely, further from the source (typically greater than 30MFPs) the intensity distribution tends to that of a semi-infinite homogeneous medium with the properties of the second layer. This confirms the interdependence of depth and radial emergence distance, however, another more subtle observation can be made from these plots. Channel 4 tends toward the response of the second layer at a slower rate than channel 3. This slight difference is due to channel 4 containing a component of light which has propagated a shorter distance, since being returned by a single scattering event, and is therefore more representative of the top layer.

These simple results illustrate that differences in the depths probed by the different polarizations result in a variation in the backscattered light due to optical property variation in the depth direction. To further investigate these sensitivities, variation of the absorption coefficients and layer thickness will now be considered.

Using an approach described previously[82], we have modelled varying top layer thickness by using a single layer medium of finite thickness. This has the effect of modelling a variable thickness top layer sitting on a totally absorbing bottom layer. The advantage of this is that a single Monte Carlo simulation can be performed and different top layer thicknesses simulated by recording the maximum visitation depth of a photon and discarding those absorbed in the second medium. This improves the efficiency of the simulations

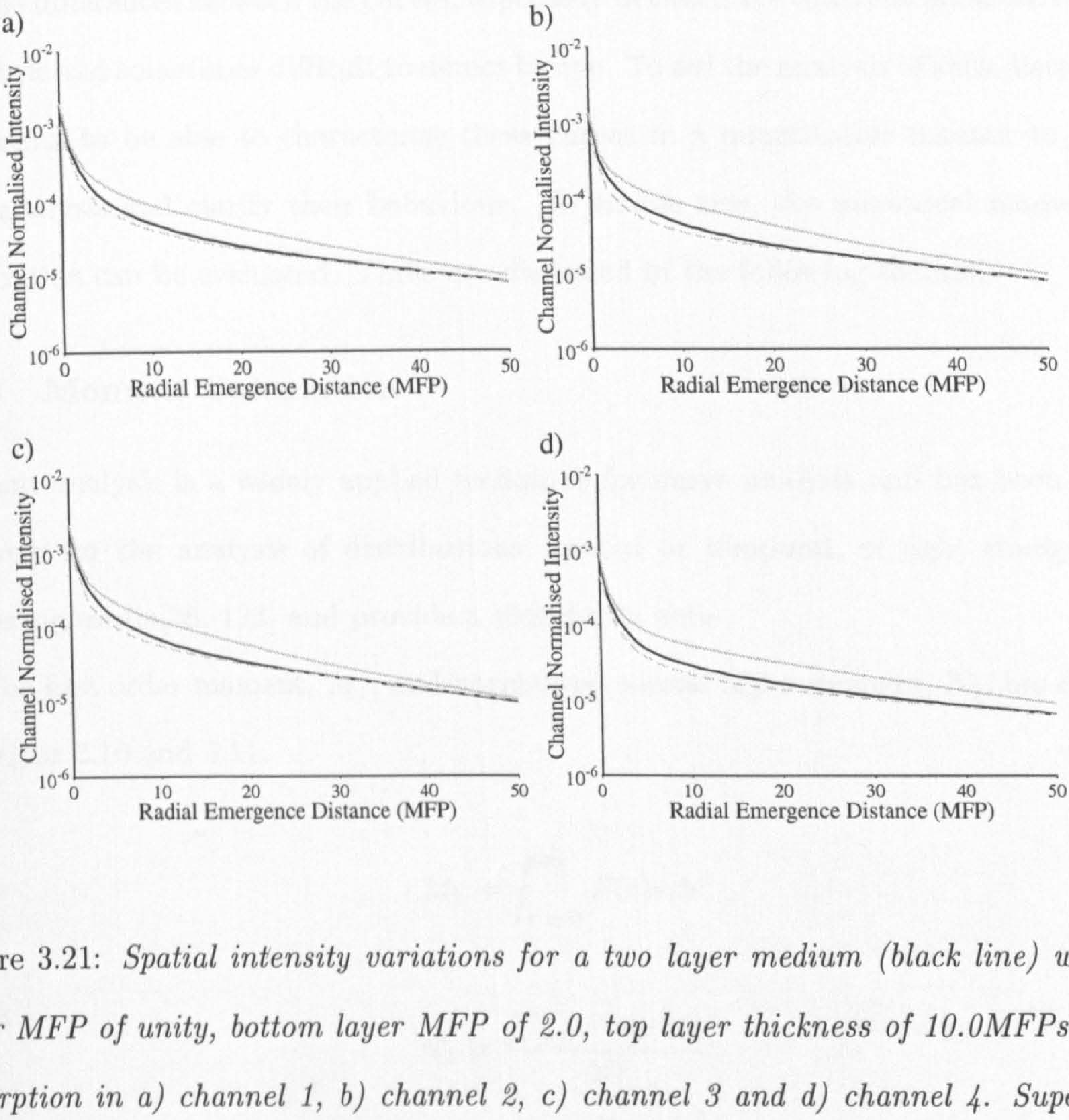

Figure 3.21: *Spatial intensity variations for a two layer medium (black line) with a top layer MFP of unity, bottom layer MFP of 2.0, top layer thickness of 10.0MFPs and zero absorption in a) channel 1, b) channel 2, c) channel 3 and d) channel 4. Superimposed onto all these curves are measurements for semi-infinite media with optical properties of the top layer (solid grey line) and bottom layer (dashed grey line).*

and makes performing a run with a large number of photons (1×10^8) feasible, but is also necessary due to the low light levels returned for very thin top layer thicknesses. It should be noted that these results represent the extreme contrast for a two layer sample.

It is clear from the figures presented thus far containing radial emergence distributions, that the differences between the curves, especially between the different polarization states are subtle and sometimes difficult to detect by eye. To aid the analysis of such distributions it is useful to be able to characterise these curves in a quantitative manner to simplify their analysis and clarify their behaviour. To enable this, the numerical moments of a distribution can be evaluated. These are discussed in the following section.

3.7.3 Moment Calculation

Moment analysis is a widely applied technique for curve analysis and has been used extensively for the analysis of distributions, spatial or temporal, of light emerging from scattering media[28, 123] and provide a useful tool here.

The first order moment, M_1, and normalised second order moment, N_2, are defined in equations 3.10 and 3.11.

$$M_1 = \int_{r=0}^{\infty} P(r) r dr \tag{3.10}$$

$$N_2 = \frac{\int_{r=0}^{\infty} P(r) r^2 dr}{M_1^2} \tag{3.11}$$

where $P(r)$ is a probability density function estimated by normalizing the area under the photon frequency histogram, $I(r)$, to unity ($I(r)$ is obtained through the method described at the beginning of section 3.7). From the calculations it can be seen that M_1 represents a measure of the width of the distribution and N_2 is characteristic of the shape if the distribution in terms of its standard deviation and due to its r^2 dependence is more heavily influenced by photons measured further from the source.

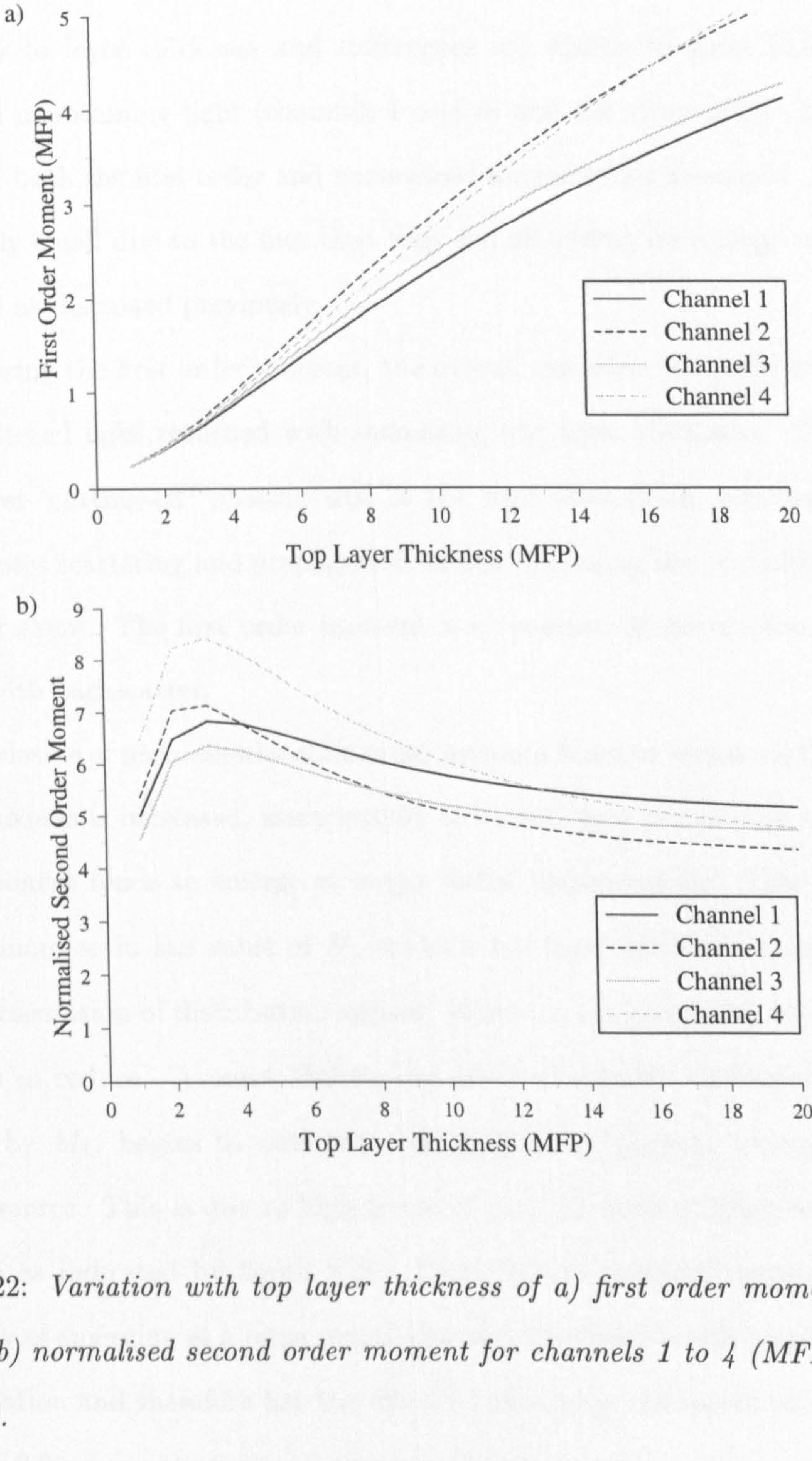

Figure 3.22: *Variation with top layer thickness of a) first order moment for channels 1 to 4 and b) normalised second order moment for channels 1 to 4 (*$MFP_1 = 1.0$*,* $\mu_{a1} = 0$*,* $\mu_{a2} = \infty$*).*

3.7.4 Top Layer Thickness Variation

Shown in figure 3.22 are the variations of the first and normalised second order moments for the four polarization channels with top layer thickness. All channels demonstrate a sensitivity to layer thickness and differences are visible to some extent between the polarization maintaining light (channels 1 and 3) and the cross-polar channels (channels 2 and 4) for both the first order and normalised second order moments. These differences are relatively small due to the fact that they are all sitting on a large multiply scattered background as discussed previously.

Considering the first order moment, the overall variation is clearly due to the increase in backscattered light returned with increasing top layer thickness. This is due to the bottom layer 'cutting-off' photons due to the high absorption, whereas the thicker top layer promotes scattering and propagation, hence increasing the probability of a successful backscatter event. The first order moment is a measure of mean intensity and therefore increases with backscatter.

The variation of normalised second order moment is not as simple as the first order case. As the thickness is increased, more heavily scattered light is included in the backscatter. This component tends to emerge at larger radial displacements. This therefore leads to an initial increase in the value of N_2 up to a top layer thickness of around 3MFP, due to its representation of distribution spread. However, for increasing top layer thicknesses, N_2 begins to reduce. Around 3MFPs the effect of rapidly increasing overall intensity, indicated by M_1, begins to dominate the increase in photons emerging at a distance from the source. This is due to high levels of multiple scatter being returned for thicker top layers as indicated by figure 3.20. Even though multiple scatter has an increased probability of emerging at a large radial distance, the trend is still biased toward the point of illumination and therefore has the effect of narrowing the distribution.

Figure 3.23 shows the first and normalised second order moments for extracted linearly and circularly polarized light along with those resultant from multiple scatter (channel 2) for reference. As demonstrated in figure 3.20 the majority of linearly and circularly polarized light is maintained within the top 15 and 30MFPs respectively, therefore, the moment calculations are insensitive to thicker layers greater than this for the two polarizations. The elimination of the multiply scattered light enhances the differences between the moments of the different polarizations and potentially may be better conditioned for any inversion.

It has been stated previously that this is the extreme case for contrast in absorption between the top and bottom layers. However, due to the fact that the polarization maintaining light extraction will remove a large contribution from the second underlying layer, the effect of the selection of these extreme conditions is not as drastic as they may at first seem. This should result in variations for more realistic properties, tending toward those illustrated in figure 3.23, as the presence of the bottom layer will become undetectable for the thicker top layer arrangements.

3.7.5 Layer Absorption Variation

The levels of optical absorption present within a sample are also of great relevance to this study due to melanin and blood being the main absorbers within human tissue and their concentrations being of diagnostic interest to clinicians.

To examine the effect of optical absorption, for the experiments presented here, the MFP for both layers has been set to unity to remove any influence due to a scattering mismatch between layers. The top layer thickness is fixed at 10MFPs and the absorption coefficients of the top and bottom layers varied independently. The first and normalised second order moments of the different polarization channels are presented in figure 3.24 using contour plots to show the variation of both layer absorptions simultaneously. Featured on these plots are lines of constant value of moment. It is apparent from these plots that if these two moment values are known, the absorptions for the two sample layers can be independently determined showing that the problem is well-conditioned. Practi-

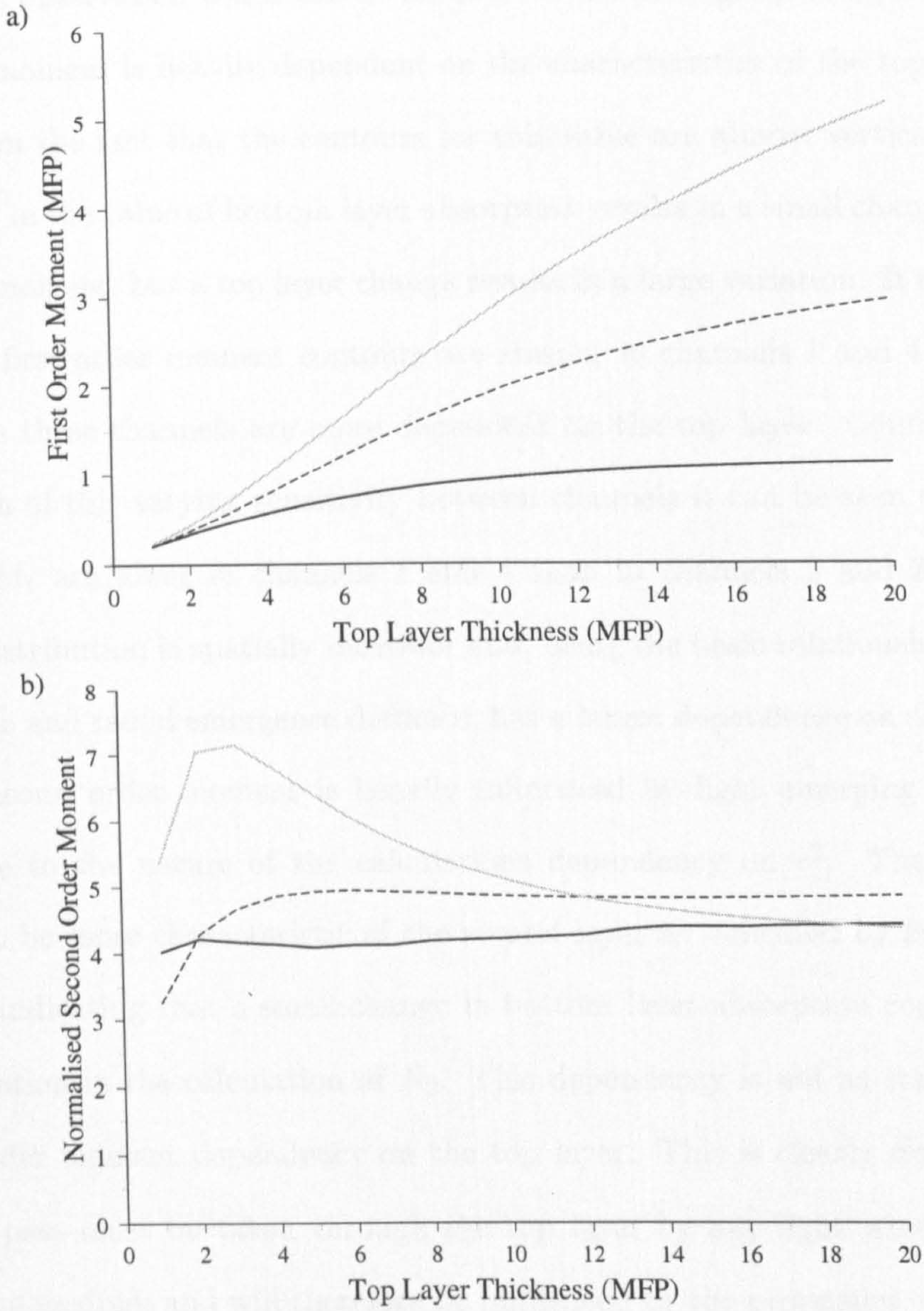

Figure 3.23: *Variation with top layer thickness of a) first order moment and b) normalised second order moment for linear polarization maintaining (black solid), circular polarization maintaining (black dashed) and multiple scattered light (grey)* ($MFP_1 = 1.0$, $\mu_{a1} = 0$, $\mu_{a2} = \infty$).

cal application of such a technique indicates that the more perpendicular the two sets of contours, the greater the tolerance to noise on either calculated value of moment[123].

The first observation which can be made from the plots given in figure 3.24 is that the first order moment is heavily dependent on the characteristics of the top layer. This can be seen from the fact that the contours for this value are almost vertical. Therefore, an adjustment in the value of bottom layer absorption results in a small change in the value of first order moment, but a top layer change results in a large variation. It can also be noted that these first order moment contours are steeper in channels 1 and 4 than in channel 2 and 3, as these channels are more dependent on the top layer. Confirming this as an explanation of this varying sensitivity between channels it can be seen that the absolute values of M_1 are lower in channels 1 and 4 than in channels 2 and 3. This indicates that the distribution is spatially narrower and, using the basic relationship between depth penetration and radial emergence distance, has a larger dependence on shallower volumes.

The second order moment is heavily influenced by light emerging further from the source due to the nature of the calculations dependency on r^2. Therefore, this value appears to be more characteristic of the second layer as indicated by its more horizontal tendency indicating that a small change in bottom layer absorption coefficient leads to a large variation in the calculation of N_2. This dependency is not as stark as for the case of first order moment dependency on the top layer. This is clearly due to the fact that a double pass must be taken through the top layer by any light which has propagated deep in the medium and will therefore be influenced by the properties of this region. This becomes more evident for larger values of μ_{a1} where it can be seen that the contours tend to be more vertical hence depending more heavily on the top layer properties.

One interesting feature that occurs in the variation of normalised second order moment with top and bottom layer absorption is that the channels dependent on more shallow regions (channels 1 and 4) provide a more horizontal contour. On first consideration this would appear to go against expectation due to the deeper regions being probed by

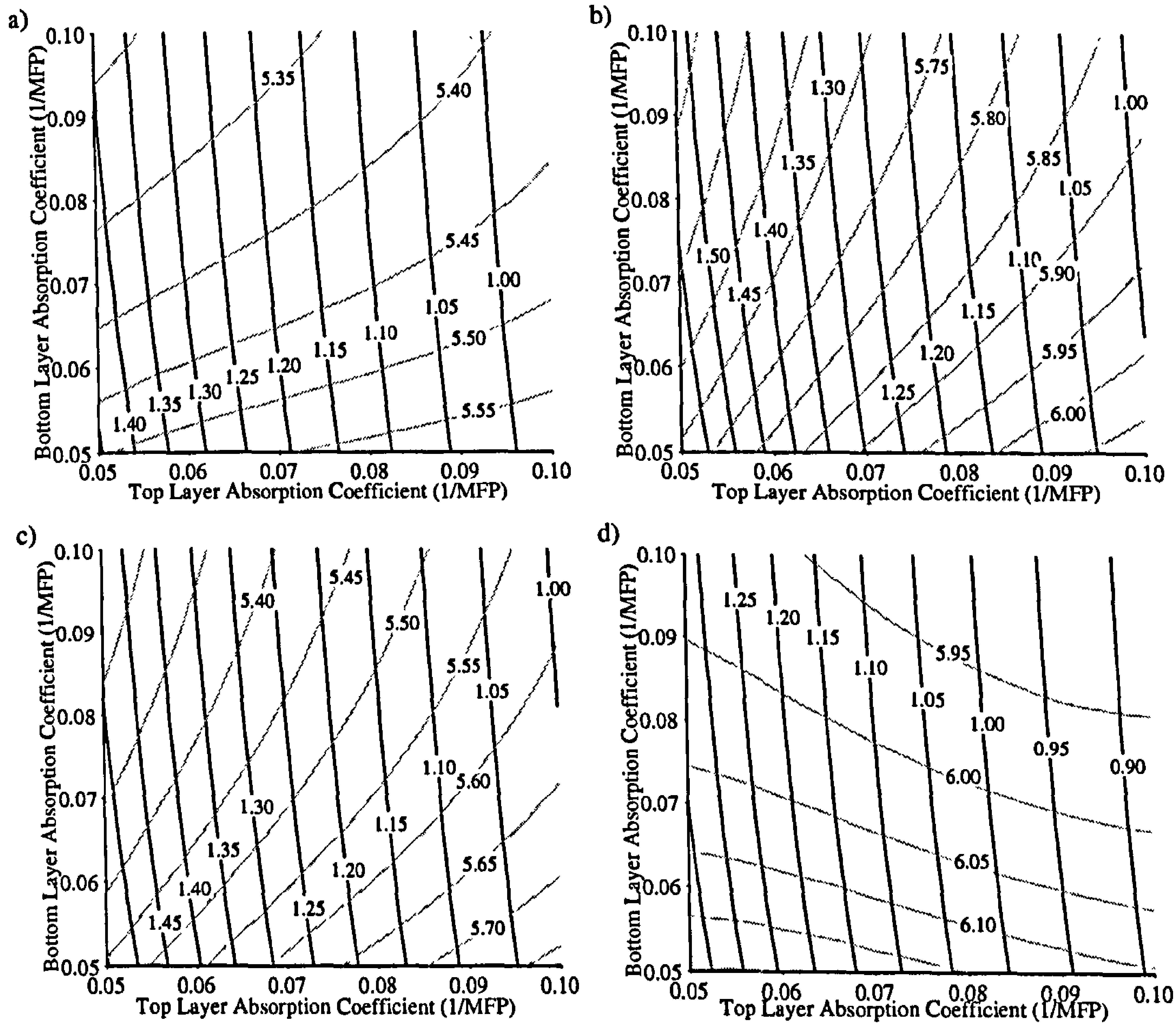

Figure 3.24: *Contour plots of the first order (black) and normalised second order (grey) moments for different top and bottom layer absorption coefficients in a) channel 1, b) channel 2, c) channel 3 and d) channel 4.*

channels 2 and 3. This effect can be explained when considering what the value N_2 represents and how it is calculated. As stated in section 3.7.3, this value represents the standard deviation or spread of the spatial distribution. Considering first the effects of an increase in μ_{a2} on the deeply penetrating channels 2 and 3. It is clear that all components of these channels will be greatly affected by an increase in this value therefore reducing this value at a steady rate as shown in figure 3.24. However, when considering channels 1 and 4 the shallow penetrating components strangely have a significant effect on the variation of N_2 with bottom layer absorption coefficient. This is due to the variation in the bottom layer absorption having no effect on the large component which has only undergone a few scattering events in these superficial regions, but affecting only the deeper component significantly. The evaluation of standard deviation is, by definition, dependent on the relative levels of well confined data to that which has a wide spread. Therefore, as the value of μ_{a2} increases, the well confined component which has probed shallow regions is not reduced in line with the deep penetrating light which is more considerably reduced with an increase in absorption. This results in the value of N_2 reducing more rapidly in channels 1 and 4 than for channels 2 and 3 resulting in an apparent increased dependence on bottom layer properties for channel 1 and 4.

3.8 Summary

Presented thus far have been results illustrating the sensitivity of polarization maintaining light to superficial regions of simulated scattering media. These sensitivities have been investigated by firstly considering polarization channel intensities backscattered from a simple single layer medium, of varying thickness, and by performing channel subtraction to extract polarization maintaining light leading to enhanced sensitivity. This was followed by demonstration of a sensitivity to depth through analysis of the radial distributions of emerging light in the different polarization states, moving on to direct analysis of the visitation depth of photons. These initial simulations indicated that, for a heavily forward scattering sample such as this, linear polarized light which emerged from the sample had, on average, penetrated 2MFPs into the medium, circular polarizations had penetrated to 7MFPs and the depth profile for multiple scatter peaked around 10MFPs.

These investigations were then extended to two layer media where sensitivities to top layer thickness and absorption coefficients of the top and bottom layers were analysed through the variation of the numerical moments determined from the emerging spatial intensity distributions. These showed that sensitivity to the two separate layers within the sample can be achieved by discriminating for polarization state.

Chapter 4

Polarization Imaging

4.1 Introduction

A large proportion of the investigation performed in the previous chapter involved evaluation of a scattering medium's properties from the spatial distribution of the emerging light in different states of polarization. However, this property is difficult to extract experimentally due to the large dynamic range of detector required. Nevertheless, it has been attempted previously[73] with limited success on single layer homogeneous tissue phantoms. Another problem with such a technique is that it is dependent on illumination at a single point. Therefore, it would be necessary to scan the illumination over an area to provide information concerning the properties of an extended region of tissue. For implementation in the biomedical field it is highly desirable to apply full field analysis of tissue, as this greatly reduces examination time making it easier for clinicians and reducing movement artifacts. To allow full field analysis, the intensities detected in the four polarization channels can be detected over an extended region. Such systems have been applied previously using linearly polarized light [84, 85] and have been discussed in section 2.3.6.

The fundamental investigations performed in the previous chapter, and experiments performed in [82], indicate that there are clear differences between the behaviour of initially linearly and circularly polarized light interacting with a scattering medium composed of uniform scattering centres. This chapter seeks to extend these ideas from single point to full-field illumination and provide further evaluation of the performance of these different states with a view to implementation of a polarized light imaging system. This is provided through the simulation of full field illumination of a sample composed of uniform scatterers coupled with the imaging results provided by a similar experimental regime to examine the localisation achieved by polarization discrimination. To advance the techniques away from uniform scattering samples and toward a more clinical application, preliminary polarization images are recorded, using the same experimental system, from *in-vivo* skin tissue. The majority of these imaging results are as presented in [124].

4.2 Full Field Depth Discrimination

To examine the localisation abilities of the polarization discrimination and subtraction techniques in an imaging regime it is desirable to perform the simulations and experimental analysis on samples with known properties. To perform the assessment of the lateral resolution available, a thin totally absorbing target can be submerged in the scattering medium. This target can then be scanned in the depth direction, through the polarization gates predicted by the results presented in chapter 3. This allows assessment of the performance of the different polarization states for different sample volumes.

4.2.1 Simulation Methodology

To perform simulation of full field illumination using the Monte Carlo model, results from single point illumination simulations can be used, providing certain information is stored concerning the position of photons as they propagate. The x co-ordinate can be translated to compensate for each different illuminating position for all occurrences of x displacement in the photon migration model. Therefore, any variation in sample property along this axial direction can be assessed. The emerging photons can then also be compensated for

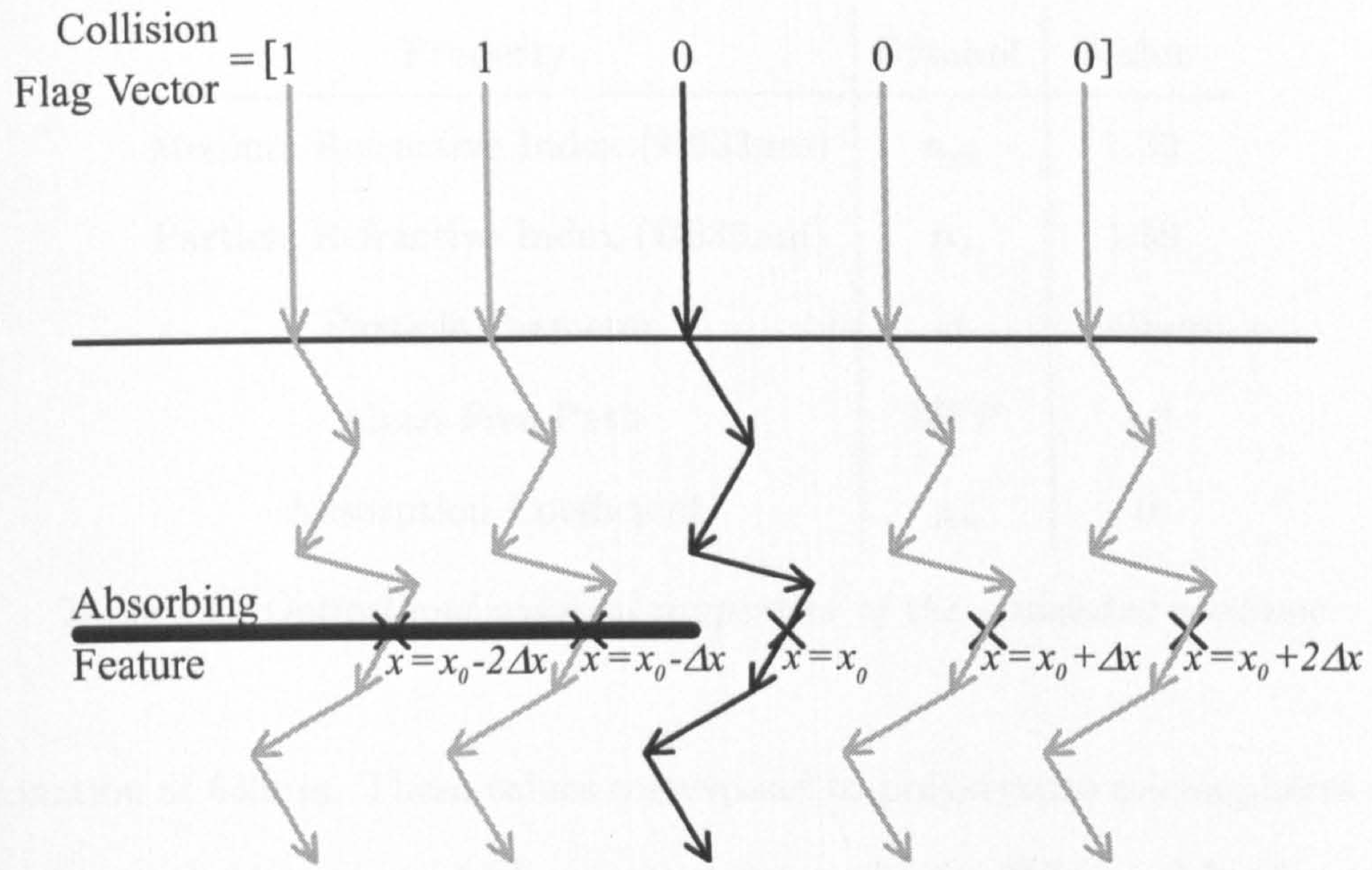

Figure 4.1: *Simulation of full field illumination through translation of simulated photon position.*

illumination location to simulate full field imaging of a sample with variation along a single lateral direction. Effectively the results are formed by the superposition of results obtained by scanning the illumination along x. Application of this technique to image an absorbing edge is shown in figure 4.1. Due to the overlaying of simulated data at each illumination point and the lateral binning of backscattered photons the number of simulated photons can be significantly reduced to 2.56×10^5, whilst still providing an acceptable signal-to-noise ratio. Illumination is applied at 0.25MFP intervals along the x-direction with a lateral detection bins 1.0MFP wide. For the medium properties described in the next paragraph, this results in a signal-to-noise ratio of 1011.9 for non-absorbing regions before polarization discrimination.

A single layer medium is used for the analysis to ensure that any trends are due to the absorbing edge and not effects due to sample property variation. The properties of the medium are defined in table 4.1.

These parameters yield a size parameter of $x = 13.896$ and anisotropy factor, $g = 0.903$

Property	Symbol	Value
Medium Refractive Index (@633nm)	n_m	1.33
Particle Refractive Index (@633nm)	n_s	1.59
Particle Diameter	d	1.40μm
Mean Free Path	MFP	1.0
Absorption Coefficient	μ_a	0

Table 4.1: *Optical and physical properties of the simulated medium.*

for illumination at 633nm. These values correspond to polystyrene microspheres of diameter 1.4μm suspended in water, which represent those which will be used for the experimental verification presented in section 4.2.3. It should be noted that the simulated results presented here do not account for the geometry of the imaging optics in a system's detection arm (through angular filtering), but seeks to identify the fundamental performance due solely to the interaction of polarized light with the sample.

4.2.2 Simulated Results

Shown in figure 4.2 are the emerging channel intensities, varying along the x-direction, for simulated absorber depths of 2, 5, 10, 15, 20 and 25MFPs. The values of intensity quoted correspond to unity at each point of illumination for linearly and circularly polarized light. It is clear from these plots that as the absorbing target is submerged deeper into the scattering medium the edge sharpness (lateral resolution) is reduced, as expected when relating back to the transmission case represented in figure 1.1.

For all target depths the relative channel intensities emerge as illustrated using the parameters quoted in chapter 3, with the linear and circular co-polar channels having a higher intensity than their cross-polar equivalents for all lateral displacements. Also, channel 3 is higher in intensity than channel 1 indicating that circular states are maintaining their polarization to a greater extent. The intensities at large negative x are the same for

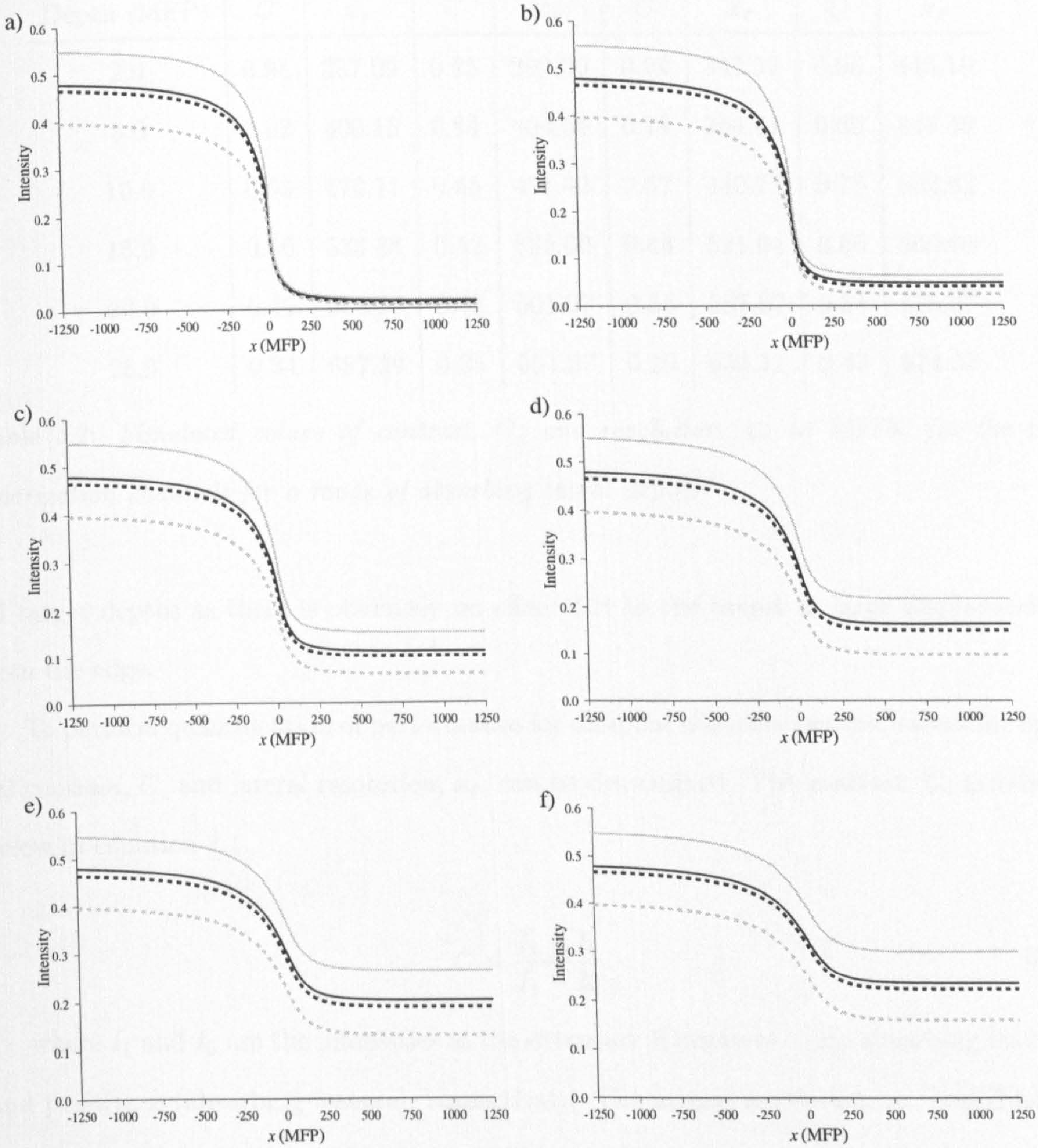

Figure 4.2: *Intensity variation of the four polarization channels in the x-direction due to a thin totally absorbing feature covering all positive x at a) 2MFPs, b) 5MFPs, c) 10MFPs, d) 15MFPs, e) 20MFPs and f) 25MFPs depth. Channel 1 - black solid line, channel 2 - black dashed line, channel 3 - grey solid line and channel 4 - grey dashed line.*

Target	Channel 1		Channel 2		Channel 3		Channel 4	
Depth (MFP)	C	x_r	C	x_r	C	x_r	C	x_r
2.0	0.94	387.09	0.95	392.30	0.94	343.57	0.96	445.19
5.0	0.82	400.15	0.84	404.56	0.79	364.61	0.89	449.48
10.0	0.63	470.11	0.65	471.42	0.57	440.73	0.73	502.63
15.0	0.50	533.38	0.52	538.00	0.44	521.04	0.60	560.63
20.0	0.40	604.95	0.42	601.97	0.35	587.97	0.51	615.87
25.0	0.34	657.39	0.35	654.37	0.29	653.11	0.43	674.57

Table 4.2: *Simulated values of contrast, C, and resolution, x_r in MFPs, for the raw polarization channels for a range of absorbing target depths.*

all target depths as there is obviously no effect due to the target at large displacements from the edge.

To perform quantification of performance for different absorber depths, values for optical contrast, C, and lateral resolution, x_r, can be determined. The contrast, C, is defined below in equation 4.1.

$$C = \frac{I_1 - I_0}{I_1 + I_0} \tag{4.1}$$

where I_1 and I_0 are the intensities at the extremes of negative x (no absorbing feature) and positive x (absorbing feature), respectively. The lateral resolution, x_r, is defined as the displacement between the values of 90% and 10% peak intensity of the transition. These two values are quantified for the different polarization channels in table 4.2.

It is clear from the variations in table 4.2 that, as shown in figure 4.2, both the contrast and the lateral resolution are reduced by the increase in submergence depth of the absorbing feature. Considering first the values of x_r for linearly polarized illumination it can be seen that the multiple scattered channel 2 performs worse than the co-polar channel in terms of its localisation. This is evidently due to the light which has maintained its initial polarization state. The polarization maintaining component present in channel 1 slightly increases the sensitivity to the superficial regions, and therefore to the target. This leads to a more narrow transition and hence lower value of x_r. When considering the levels of contrast however, it can be seen that the performance of the cross-polar channel is better than that of the co-polar equivalent. This difference is clearly once again due to a proportion of the shallow penetrating polarization maintaining light present in channel 1 which propagates to such superficial regions that the absorbing feature has not been reached. This therefore results in an increased intensity in the positive x region compared with channel 2.

Considering the circularly polarized channels it is apparent that channel 3 has an improvement in x_r performance for the same reasons as the case for linear polarizations. However, the difference in performance is greater than for the linearly polarized case due higher intensity of polarization maintaining circular polarizations compared to the linear case. This provides a higher contribution from photons with a better defined path. The optical contrast is better in channel 4 than channel 3 for the same reasons as the linear polarization maintaining light. The greater difference between these two channels compared to channels 1 and 2 is solely due to the improved maintenance of circularly polarized light therefore more light which is returned before striking the absorber has maintained its initial state.

For a more complete investigation it is desirable to discriminate between light which is absorbed whilst propagating in a forward direction and that which is absorbed when back-illuminating the target. The breakdown of the line scans into these two components is shown for target depths of 5 and 20MFPs in figure 4.3.

From here it can be seen that, in the positive x region, the low intensity (providing the contrast) can be almost completely attributed to absorbing events by forward propagating photons. This is evidently due to photons not being able to reach depths past the absorber without first being absorbed. At regions far from the edge of the feature (large negative

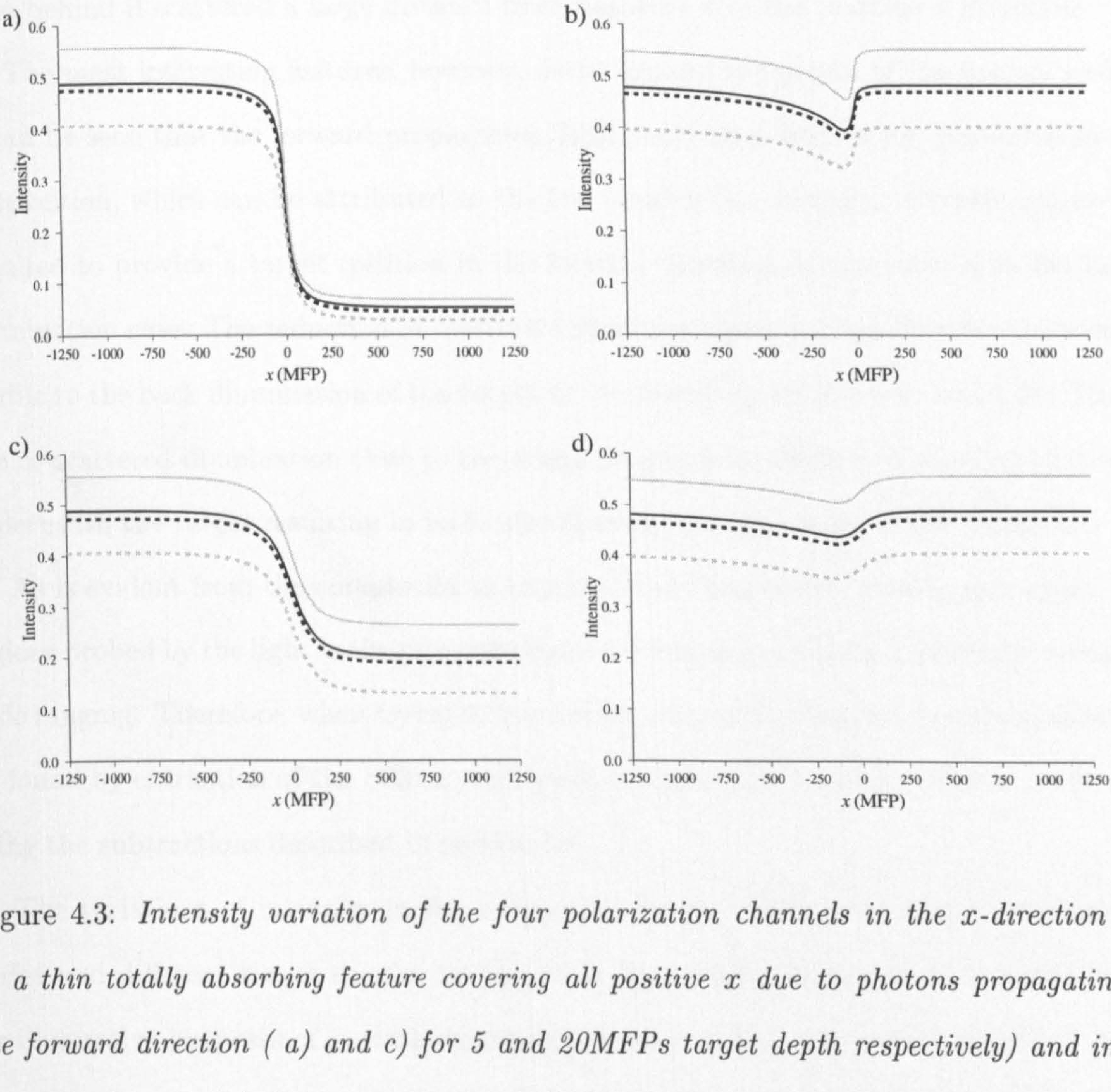

Figure 4.3: *Intensity variation of the four polarization channels in the x-direction due to a thin totally absorbing feature covering all positive x due to photons propagating in the forward direction (a) and c) for 5 and 20MFPs target depth respectively) and in the backward direction (b) 5MFP and d) 20MFP). Channel 1 - black solid line, channel 2 - black dashed line, channel 3 - grey solid line and channel 4 - grey dashed line.*

x) the response mirrors that of back-illuminating light. Clearly, for light to be affected by the target in this region it must propagate a large radial distance and, from the interdependence of radial emergence and visitation depth confirmed in the previous chapter, will be statistically more likely to have probed deeply. This will lead to the target being struck from behind if scattered a large distance from negative x in the positive x-direction.

The most interesting features, however, occur around the region of the feature's edge. It can be seen that the forward propagating light provides a very sharp transition in the distribution, which can be attributed to the low number (on average) of scattering events required to provide a target collision in the forward direction in comparison to the back-illumination case. The reduction in resolution shown in figure 4.2 can therefore be seen to be due to the back illumination of the target as illustrated by figures 4.3b and 4.3d. This is due to scattered illumination close to the origin propagating shallow depths but tunneling underneath the target resulting in back-illumination and a blurring of the transition.

As is evident from the complexity in explanation of the above trends, once again, the regions probed by the light in the raw polarization channels are poorly defined and spatially wide ranging. Therefore, when trying to localise regions within samples, improvements can be found by extraction of the different polarization maintaining states. This is performed using the subtractions described in section 3.6.

The variations of intensity in the x-direction for the different extracted polarization states and different target depths are shown in figure 4.4. These curves are normalised for illustrative purposes of x_r with emergent intensity at the extreme of negative x set to unity and positive x to zero. The absolute values presented in table 4.3 determined from the un-normalised data. Also shown are the resultant values of C.

It is clear from both the line plots and numerical values in table 4.3 that there is a significant improvement in the localisation provided by polarization maintaining light as opposed to the raw channels. This is due to the removal of the multiple scattered component which has an ill-defined propagation path leading to a lack of localisation. The

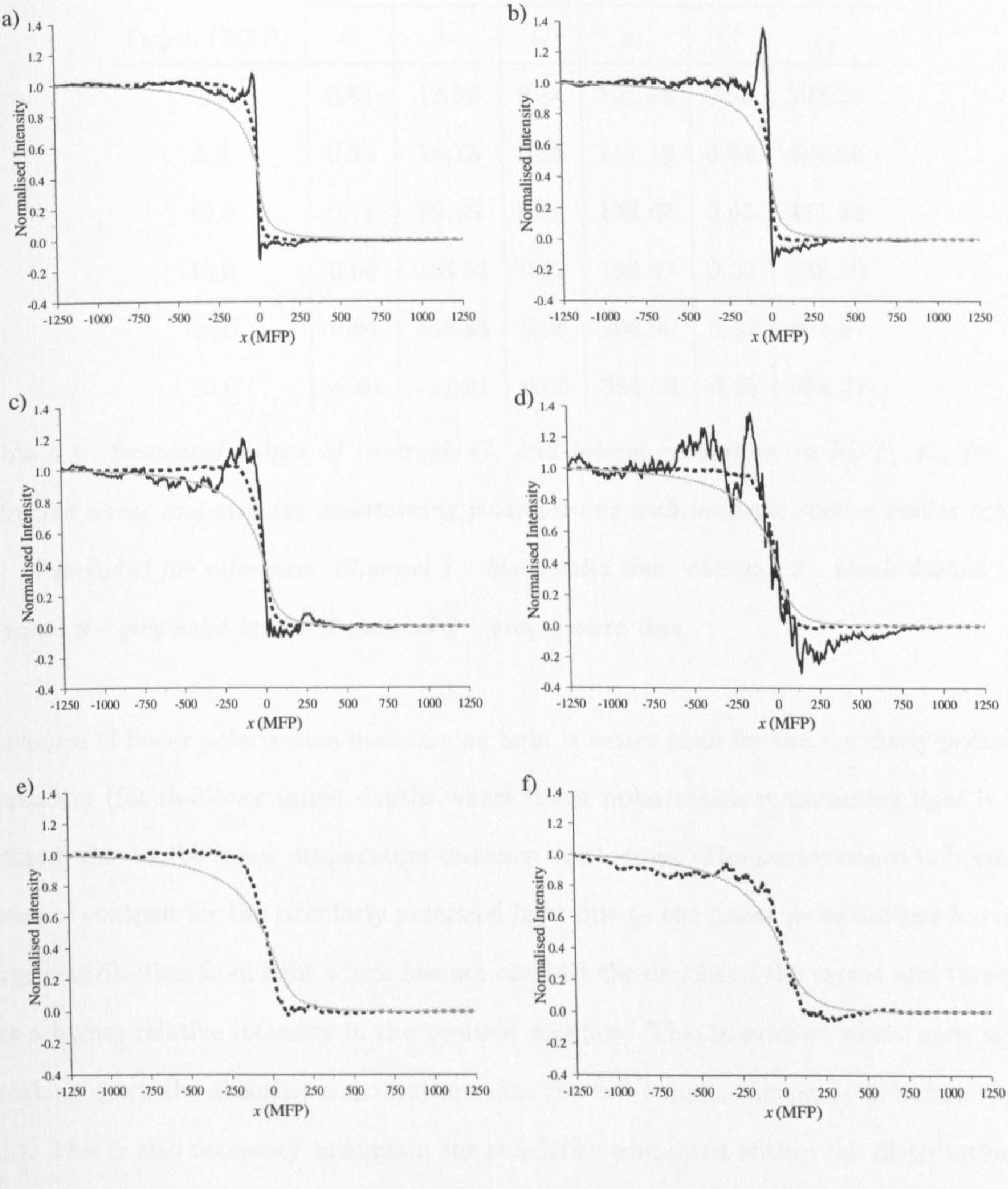

Figure 4.4: *Intensity variation of linearly maintaining (black solid) and circularly maintaining (black dashed) polarizations along with multiple scatter (grey) in the x-direction due to a thin totally absorbing feature covering all positive x at a) 2MFPs, b) 5MFPs, c) 10MFPs, d) 15MFPs, e) 20MFPs and f) 25MFPs depth. These curves have been normalised to illustrate the variation of lateral resolution.*

Target	Linear		Circular		Multiple	
Depth (MFP)	C	x_r	C	x_r	C	x_r
2.0	0.61	12.56	0.84	102.68	0.95	392.30
5.0	0.25	18.73	0.56	111.18	0.84	404.56
10.0	0.11	59.88	0.24	148.65	0.65	471.42
15.0	0.05	243.53	0.12	193.67	0.52	538.00
20.0	0.04	765.36	0.06	204.90	0.42	601.97
25.0	-0.01	751.91	0.03	384.03	0.35	654.37

Table 4.3: *Simulated values of contrast, C, and lateral resolution in MFP, x_r, for the extracted linear and circular maintaining polarizations with multiple scatter values (channel 2) included for reference. Channel 1 - black solid line, channel 2 - black dashed line, channel 3 - grey solid line and channel 4 - grey dashed line.*

sharpness of linear polarization maintaining light is better than for the circularly polarized equivalent (for shallower target depths where linear polarization maintaining light is well defined) due to the lower propagation distance of photons. The performance is better in terms of contrast for the circularly polarized light due to the linear polarizations having a large contribution from light which has not reached the depths of the target and therefore has a higher relative intensity in the positive x region. This is evident when, once again, breaking down the absorber contributions into the two constituent parts as before (figure 4.5). This is also necessary to explain the subtleties contained within the distributions.

It is apparent from the line scans presented in figure 4.4 that the lateral variation of intensity is not as simple as for the raw detected channels. This discrimination between the direction of propagation at the point of absorption greatly aids the understanding of these distributions. Plotted in figure 4.5 are the components of forward- and back-illumination for an absorbing feature submergence depth of 5MFPs.

Considering the linear polarization maintaining backscatter, the overall trend (figure

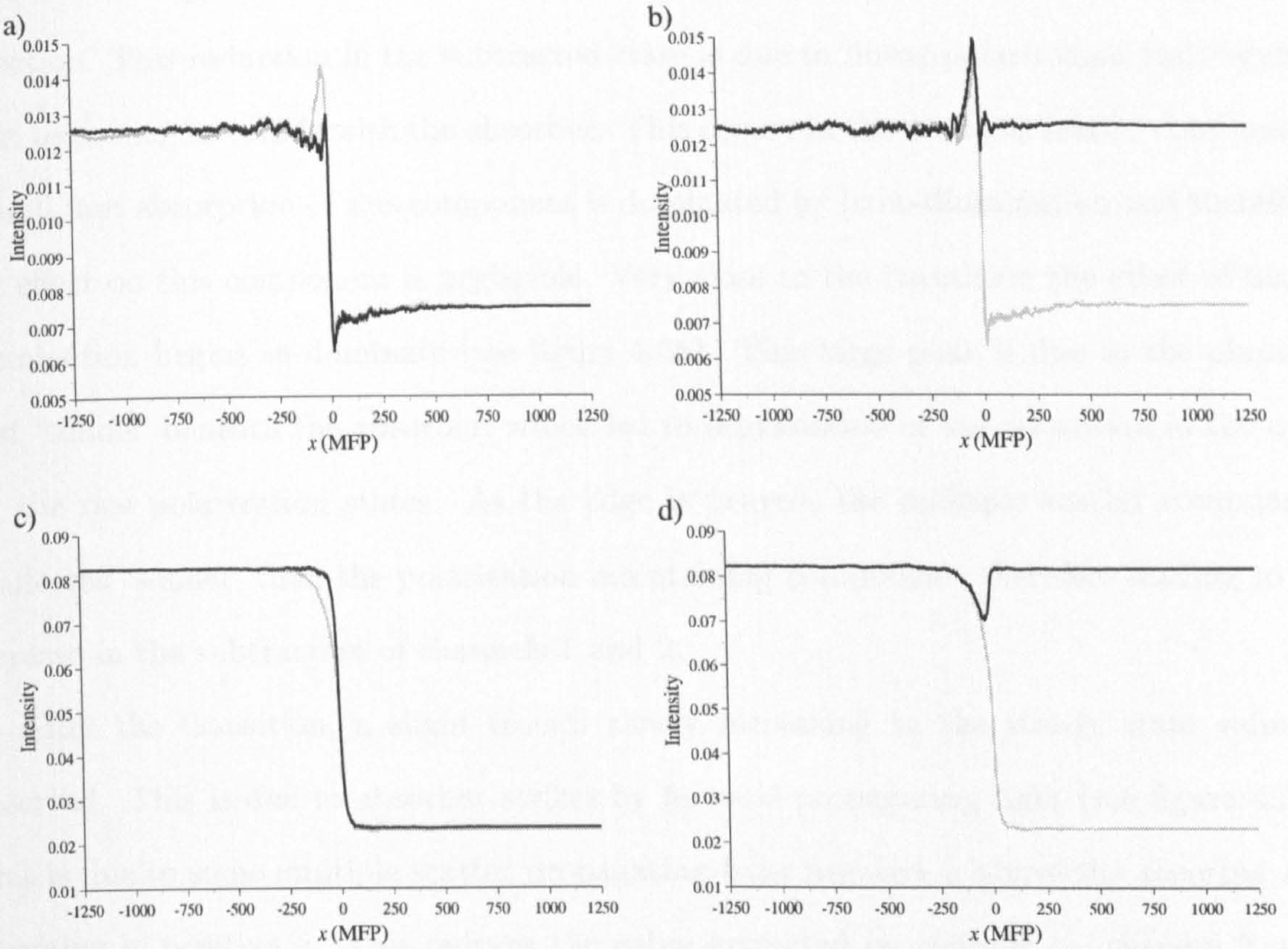

Figure 4.5: *Intensity variation of linearly maintaining and circularly maintaining polarizations in the x-direction due to a thin totally absorbing feature covering all positive x due to photons propagating in the forward direction (a) and c) for linear and circular polarization maintaining light respectively) and in the backward direction (b) and d)) for an absorber depth of 5MFPs. The combination of forward and backward target collisions is plotted in grey on each plot.*

4.4b and plotted in grey in figures 4.5a and 4.5b) can be divided into several distinct regions. In the first region, at large negative x, it can be seen that the absorbing edge has no effect. However, as the absorbing edge is approached the intensity can be seen to reduce. From figure 4.5a it can be seen that this is due to absorber collisions in the forward direction. This reduction in the subtracted state is due to linear polarization maintaining light beginning to collide with the absorber. This occurs in the multiple scatter component as well, but absorption of this component is dominated by back-illumination and therefore the effect on this component is negligible. Very close to the transition the effect of back-illumination begins to dominate (see figure 4.5b). This large peak is due to the photons that 'tunnel' beneath the absorber, which led to degradation of the transition in the case for the raw polarization states. As the edge is neared, the multiple scatter component is affected 'sooner' than the polarization maintaining component, therefore leading to an increase in the subtraction of channels 1 and 2.

After the transition, a slight trough slowly increasing to the steady state value is observed. This is due to absorber strikes by forward propagating light (see figure 4.5a). This is due to some multiple scatter propagating from negative x above the absorber and emerging in positive x. This reduces the value extracted by channel 1 - channel 2 until the contribution becomes negligible at large positive x.

For the circular polarization maintaining channel such subtle effects are not evident due to combined factors of deep penetration of polarization maintaining light (for shallow absorber submergence) and trend blurring due to scattering (for deeper absorbers where the trend subtleties would be otherwise prevalent).

To confirm the effects presented thus far and their dependence on the polarization gating, correlation between the variations of C and x_r for extracted polarization maintaining light can be plotted with varying absorber depth alongside the depth profiles of the three different polarization gates. The variations of C and x_r are plotted in figures 4.6 and 4.7 respectively with the maximum visitation depth of photons in the simulated medium given

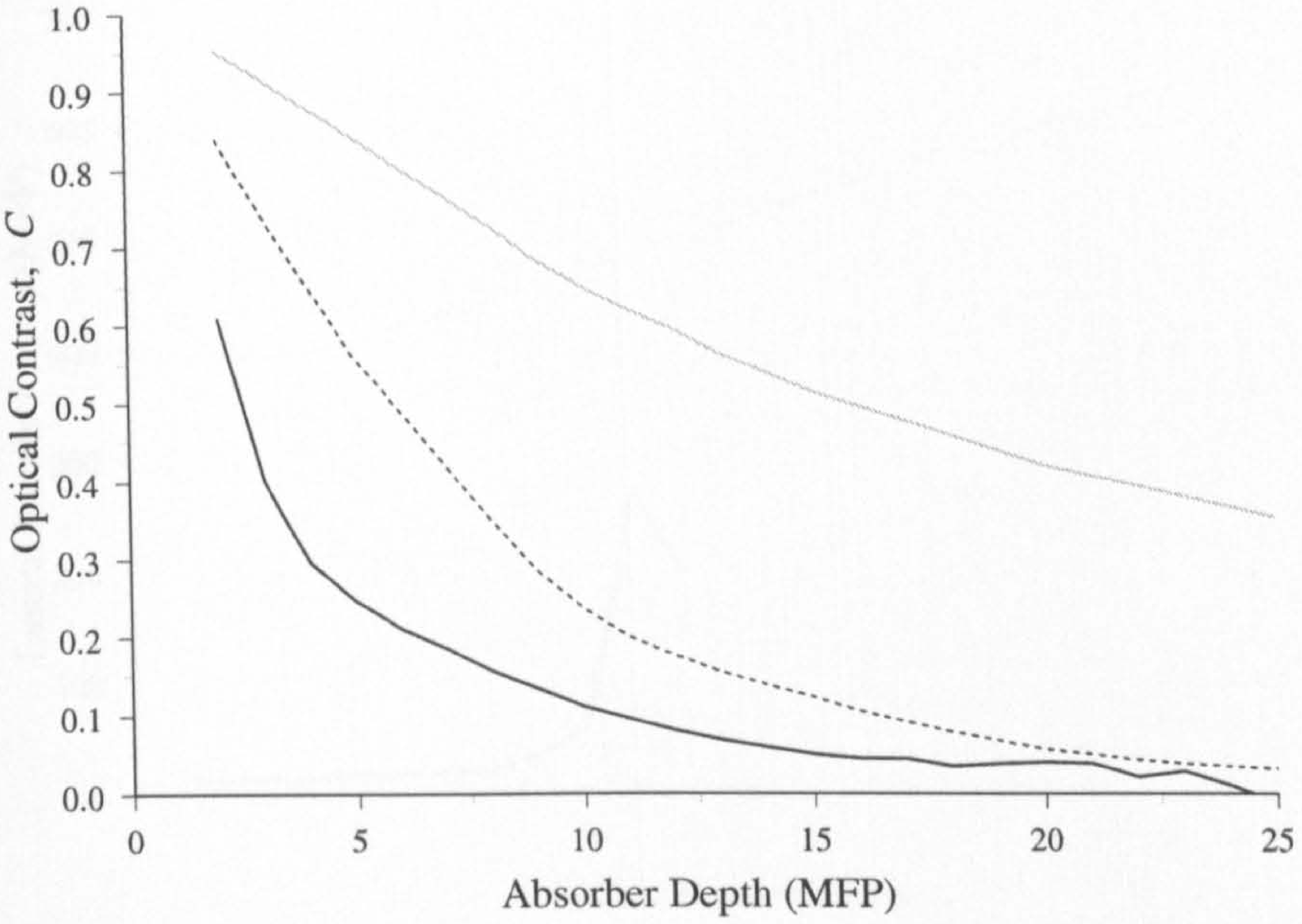

Figure 4.6: *Variation of the optical contrast, C, with absorbing target depth for linear (black) and circular (dotted) maintaining polarization states along with multiple scatter (grey).*

in figure 4.8.

It is clear for both of these plots that the improved performance and stability of these values is confined to an absorber submerged within the corresponding polarization gate. The value of contrast for linearly polarized light (figure 4.6) can be seen to be nearing a constant level at an absorber depth of 10MFPs, whilst the value of x_r becomes highly unstable around this value of feature depth. It can be seen from figure 4.8 that this corresponds to a depth after the peak in the depth distribution for linear polarization maintaining light. A similar trend is emergent due to circularly polarized backscatter with the flattening of the contrast curve and de-stabilisation of the lateral resolution determination occurring for a submergence depth of 13MFPs. Even the low noise multiple

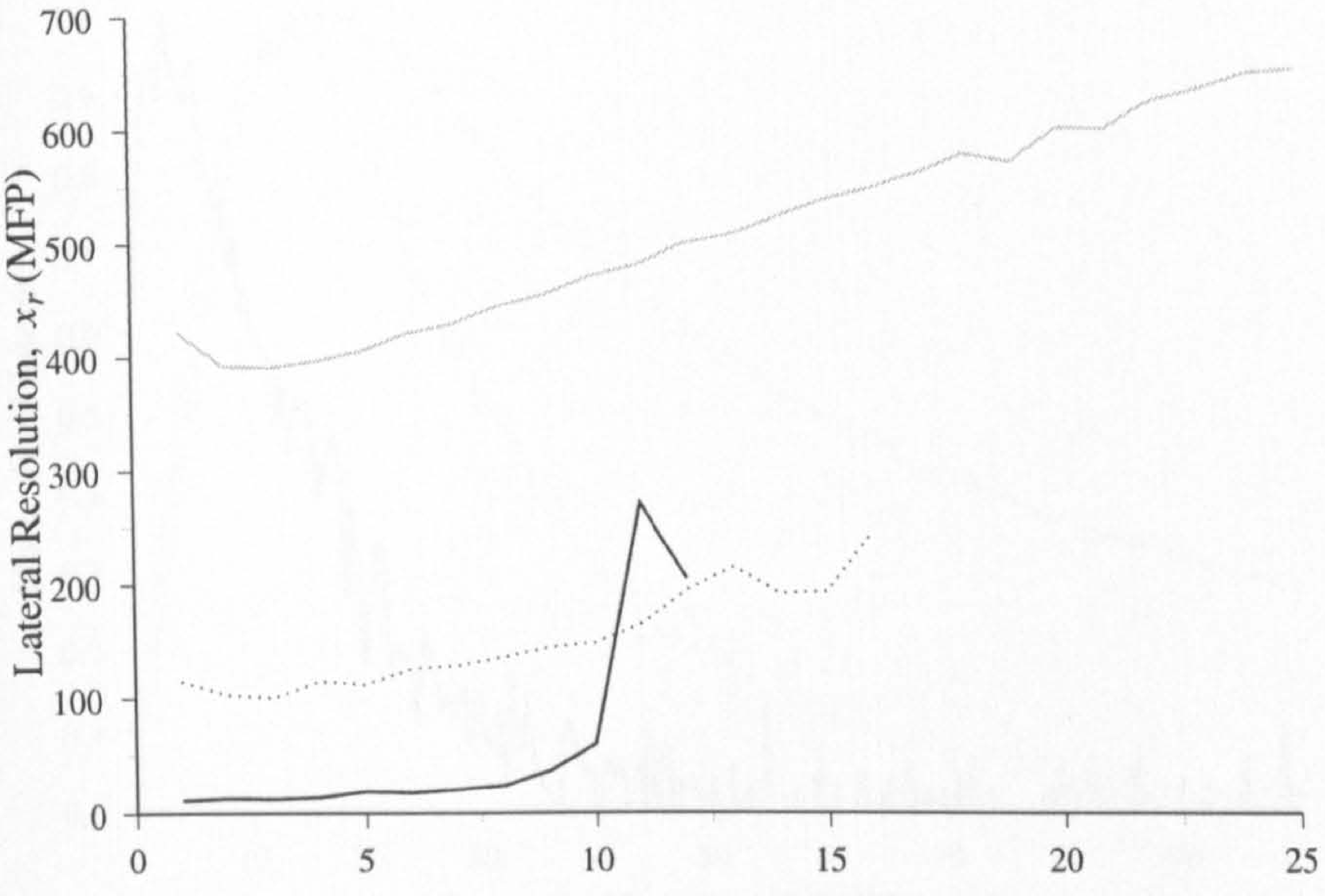

Figure 4.7: *Variation of the lateral resolution, x_r, with absorbing target depth for linear (black) and circular (dotted) maintaining polarization states along with multiple scatter (grey).*

scatter component can be seen to de-stabilise slightly in the calculation of x_r for an absorber submerged at depths greater than 18MFPs, which corresponds to a depth just following the distribution's peak. These trends tend to de-stabilise in their determination of x_r sooner than C due to the ability to perform significant signal averaging in the calculation of contrast that is not available in assessment of the transition width.

4.2.3 Experimental Investigation

Thus far the focus has been on the analysis of results derived from numerical simulations. It is clearly necessary to verify the simulated trends in an experimental context. To allow this, the system shown in figure 4.9 is used to provide the required illuminating

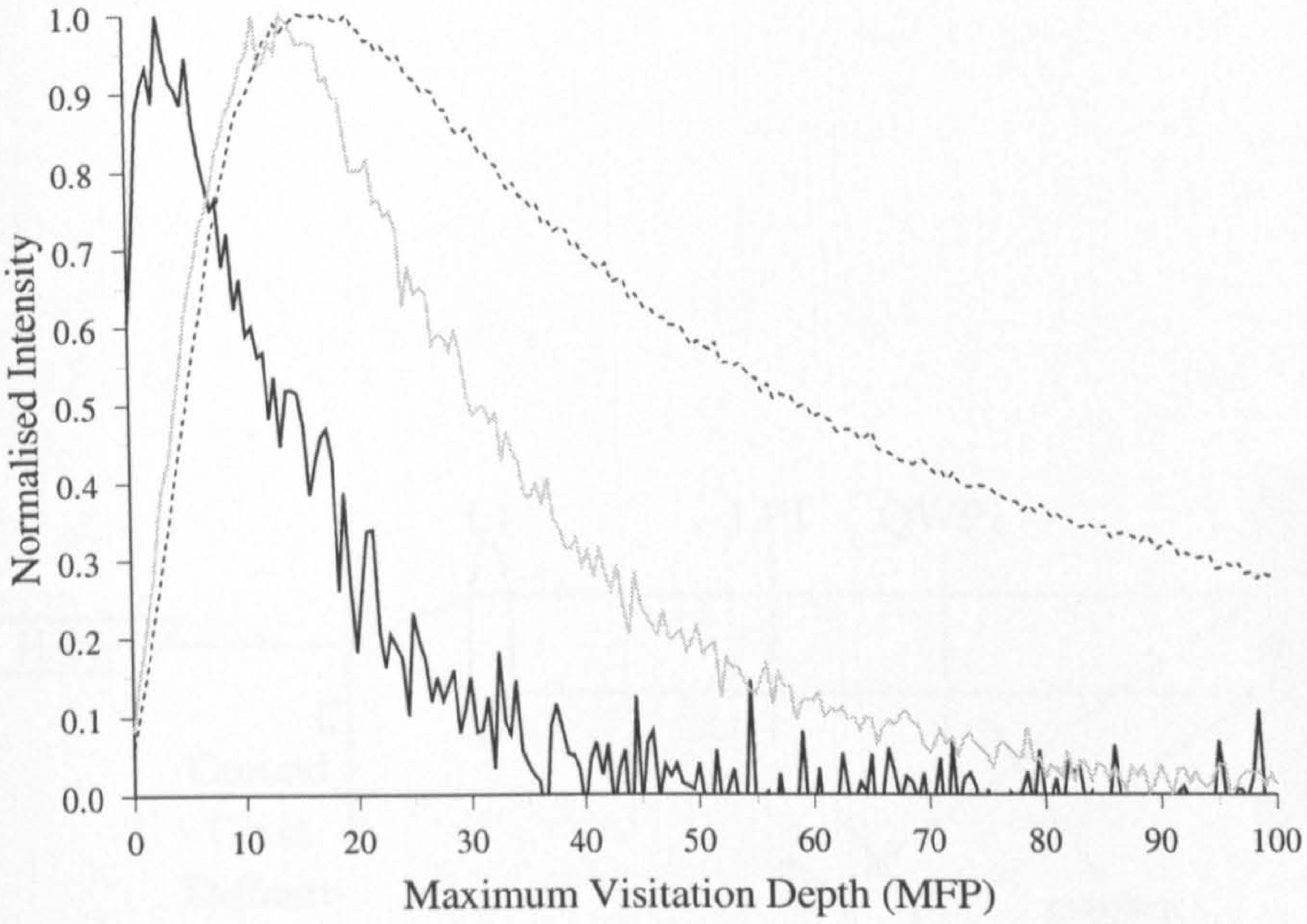

Figure 4.8: *Intensity depth profile, normalised to peak intensity, of extracted linearly polarized light (solid black line), circularly polarized light (dashed black line) and multiple scatter (grey line) calculated from simulations representing 1.4μm polystyrene microspheres suspended in water.*

polarizations and analyse the backscattered light.

The source used is a polarized 10mW helium-neon laser illuminating at 632.8nm. To eliminate the problem of laser speckle on the image due to the coherence of the source, a spinning ground glass disc is then used to diffuse the light before it is collimated ready for projection onto the sample. To achieve the required polarization state a linear polarizer (LP1), aligned along the plane of polarization from the source, is used to ensure linearly polarized light reaches the quarter waveplate (QWP1). For the two linearly polarized detection channels (channels 1 and 2), QWP1 has its fast-axis aligned with the plane of polarization of the incident linear polarization, hence having no effect and allowing the

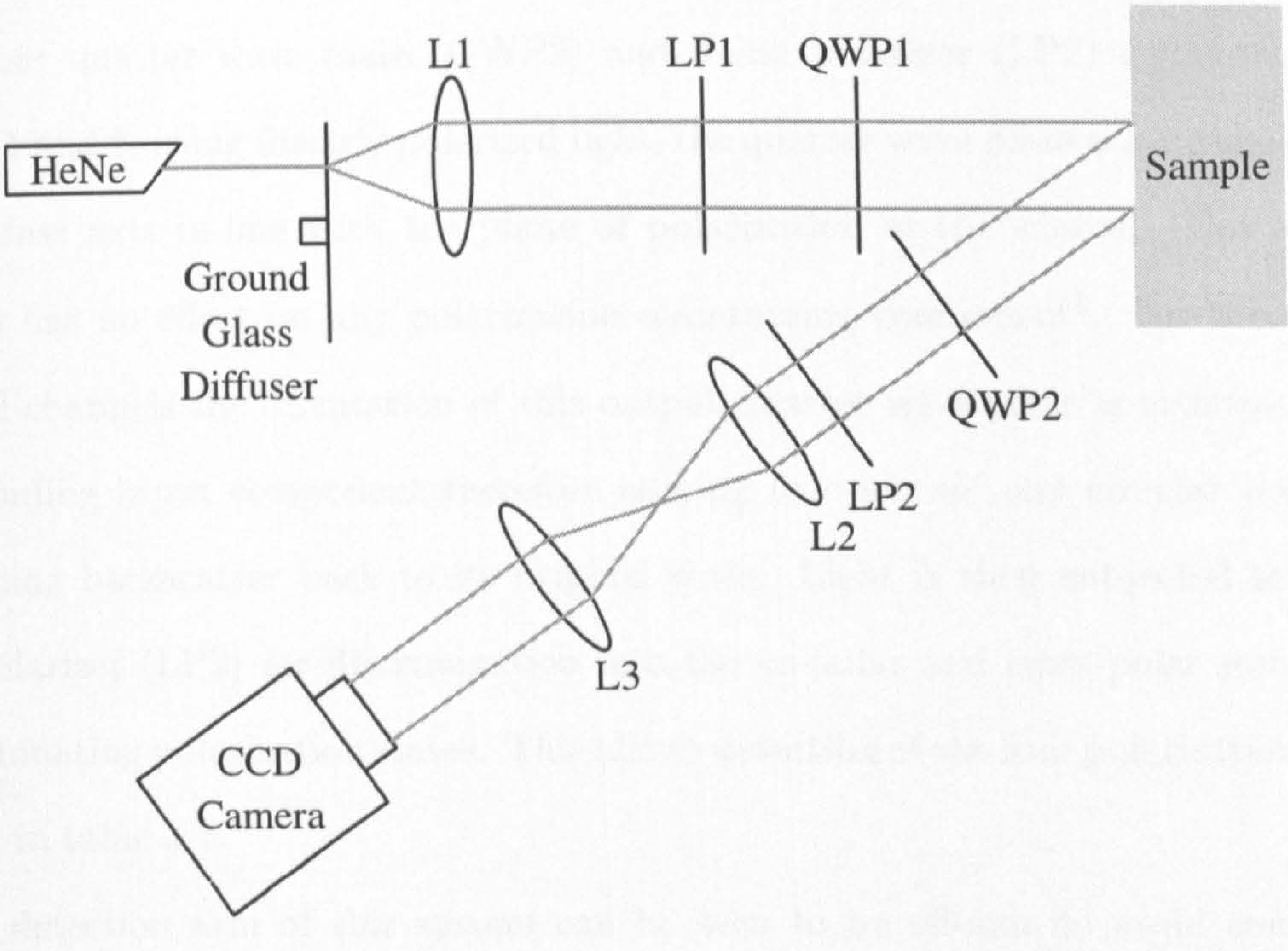

Figure 4.9: *Off-axis polarization imaging system using linearly and circularly polarized light.*

linearly polarized illumination to enter the scattering medium. For the two detection channels requiring circularly polarized illumination the quarter wave plate is rotated so as the fast axis is at 45 degrees to the plane of linear polarization resulting in a circular state[39].

Once the light is returned from the sample it is detected away from the optical axis of the illumination so to direct the surface reflections from the cuvette's surface away from the detection arm. To achieve analysis of the polarization state, detection is performed via another quarter wave plate (QWP2) and linear polarizer (LP2) combination. For channels 1 and 2, using linearly polarized light, the quarter wave plate is once again aligned with its fast axis in-line with the plane of polarization of the source. This alignment therefore has no effect on any polarization maintaining component[1]. For the circularly polarized channels the orientation of this output quarter wave plate is orthogonal to the corresponding input component therefore seeking to 'unwrap' any circular polarization maintaining backscatter back to its original state. Light is then subjected to the final linear polarizer (LP2) for discrimination into the co-polar and cross-polar states for the two illuminating polarization states. This allows detection of the four polarization channels outlined in table 3.1.

The detection arm of this system can be seen to be off-axis to avoid contributions from surface reflections as in [85] and [125]. A more complete consideration of surface reflections from samples is given in section 4.3.

The samples under examination for these experiments mirror those used in the simulations discussed in section 4.2.1. The properties found in table 4.1 are therefore applicable with one notable difference. For simulation, the selected unitless MFP for the simulations was set to unity. For the purposes of these experiments the microspheres were suspended to provide an MFP of 0.05mm ($\mu_s = 20mm^{-1}$) for 633nm illumination in a glass cuvette

---

[1] A consideration of the effects of other emerging linearly polarized states which would have planes of polarization away from that of the fast-axis, hence resulting in elliptical or circular polarization states, is discussed in appendix B.

Target	Channel 1		Channel 2		Channel 3		Channel 4	
Depth (MFP)	C	x_r	C	x_r	C	x_r	C	x_r
2.0	0.81	41.4	0.86	43.4	0.82	37.0	0.85	46.4
10.0	0.53	48.8	0.59	48.0	0.45	48.6	0.68	51.4
22.0	0.27	62.4	0.30	61.4	0.15	58.2	0.45	62.2

Table 4.4: *Experimentally recorded values of contrast, C, and resolution in MFP, x_r, for the raw polarization channels for a range of absorbing target depths.*

of dimensions 10mm × 47mm × 42mm. This level of scattering was selected to allow demonstration of all three polarization gates within the limited thickness of the cuvette. The target used is a highly absorbing black Perspex disk, 3mm in diameter, attached to a transparent Perspex rod and is scanned through from 0 to 30MFPs in the depth direction. The images shown in 4.10 are for object depths of 0.1mm (2MFP), 0.5mm (10MFP) and 1.1mm (22MFP) in channels 1 to 4 with a CCD camera exposure time of 64ms.

Once again, in line with intuition, the absorbing target becomes less visible as it is scanned in the depth direction. However, the differences apparent between polarization channels are seeming only in the overall intensity and provide no detailed information concerning the volumes of sensitivity. This is due to the large multiple scatter contribution present in all channels, once again illustrating the need for channel subtraction to extract polarization maintaining light to achieve localisation.

To aid comparison with the simulated data line scans from these images are shown in figure 4.11 for absorber depths of 0.1, 0.5 and 1.1mm. The corresponding values of C and x_r are given in table 4.4. These line scans have been corrected for non-uniform illumination through normalisation by the illumination profile and the values of C and x_r determined by extrapolating the trend into negative x in-fitting with the shape of the distribution.

It is apparent from these obtained values that the resultant trends mirror those pro-

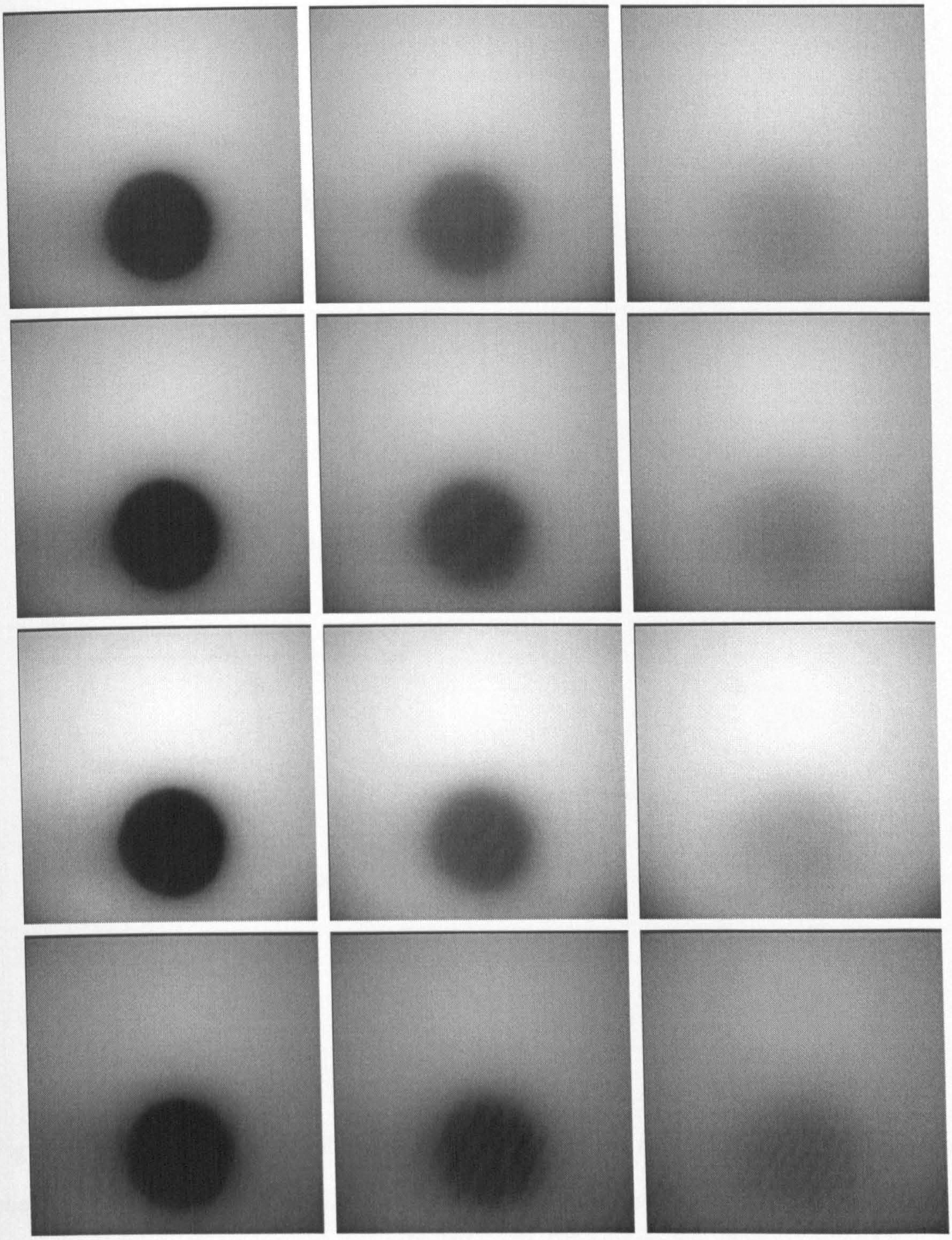

Figure 4.10: *Raw polarization images detected at target depths of 0.1mm (first column), 0.5mm (second column) and 1.1mm (third column), in channel 1 (top row), channel 2 (second row), channel 3 (third row) and channel 4 (bottom row).*

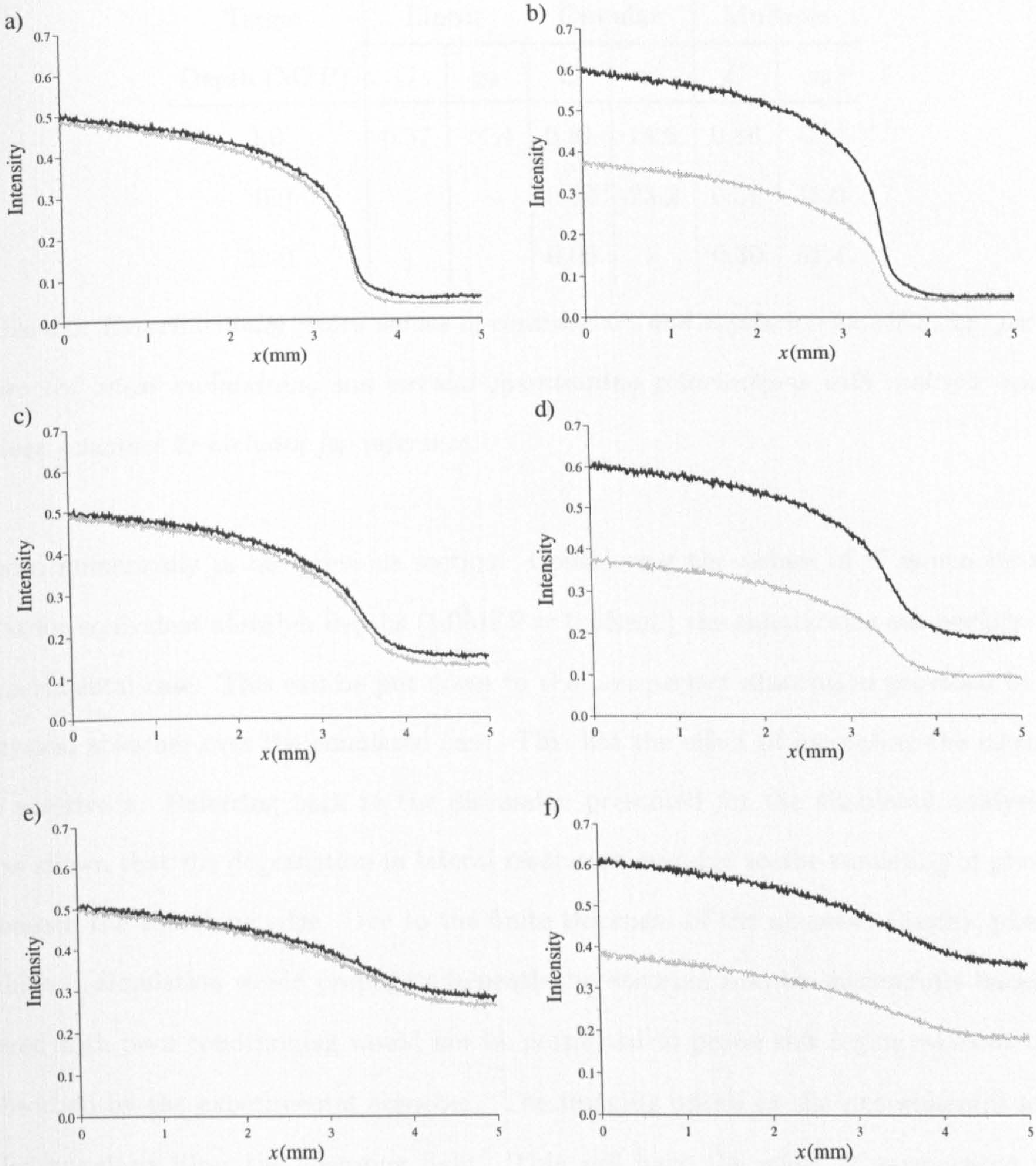

Figure 4.11: *Line scans recorded from the images in figure 4.10 in the four polarization channels for absorbing feature depths of 0.1mm (top row), 0.5mm (middle row) and 1.1mm (bottom row). The left hand column (images a), c) and e)) are obtained from the linearly polarized images (black line - channel 1, grey line - channel 2) and the right hand column (images b), d) and f)) are represent the circularly polarized states (black - channel 3, grey - channel 4).*

Target	Linear		Circular		Multiple	
Depth (MFP)	C	x_r	C	x_r	C	x_r
2.0	0.37	14.4	0.81	14.6	0.86	43.4
10.0	-	-	0.32	23.2	0.59	48.0
22.0	-	-	0.06	-	0.30	61.4

Table 4.5: *Experimentally record values of contrast, C, and resolution in MFP, x_r, for the extracted linear maintaining and circular maintaining polarizations with multiple scatter values (channel 2) included for reference.*

duced numerically in the previous section. Considering the values of C is can be seen that for equivalent absorber depths (1.0MFP = 0.05mm) the simulations out perform the experimental case. This can be put down to the non-perfect absorption provided by the physical absorber over the simulated case. This has the effect of increasing the intensity in positive x. Referring back to the discussion presented for the simulated analysis, it was shown that the degradation in lateral resolution was due to the tunneling of photons beneath the absorbing edge. Due to the finite thickness of the absorber (3mm), photons which in simulation would propagate beneath the absorber and be successfully backscattered with poor conditioning would not be permitted to probe this region without being absorbed by the experimental absorber. The imaging optics in the experimental set-up also angularly filter the emerging light. This will have the effect of suppressing more heavily scattered light increasing the dependence on superficially probing photons.

The images resultant from the polarization image subtractions, hence containing polarization maintaining light are shown in figure 4.12. Extracted line scans from these images are shown in figure 4.13 with the measured values of resolution and contrast given in table 4.4, noise permitting.

The first object depth (2MFPs) clearly falls within the linear polarization gate. As this is the shallowest of the polarization gates (see figure 4.8) the absorber is therefore visible

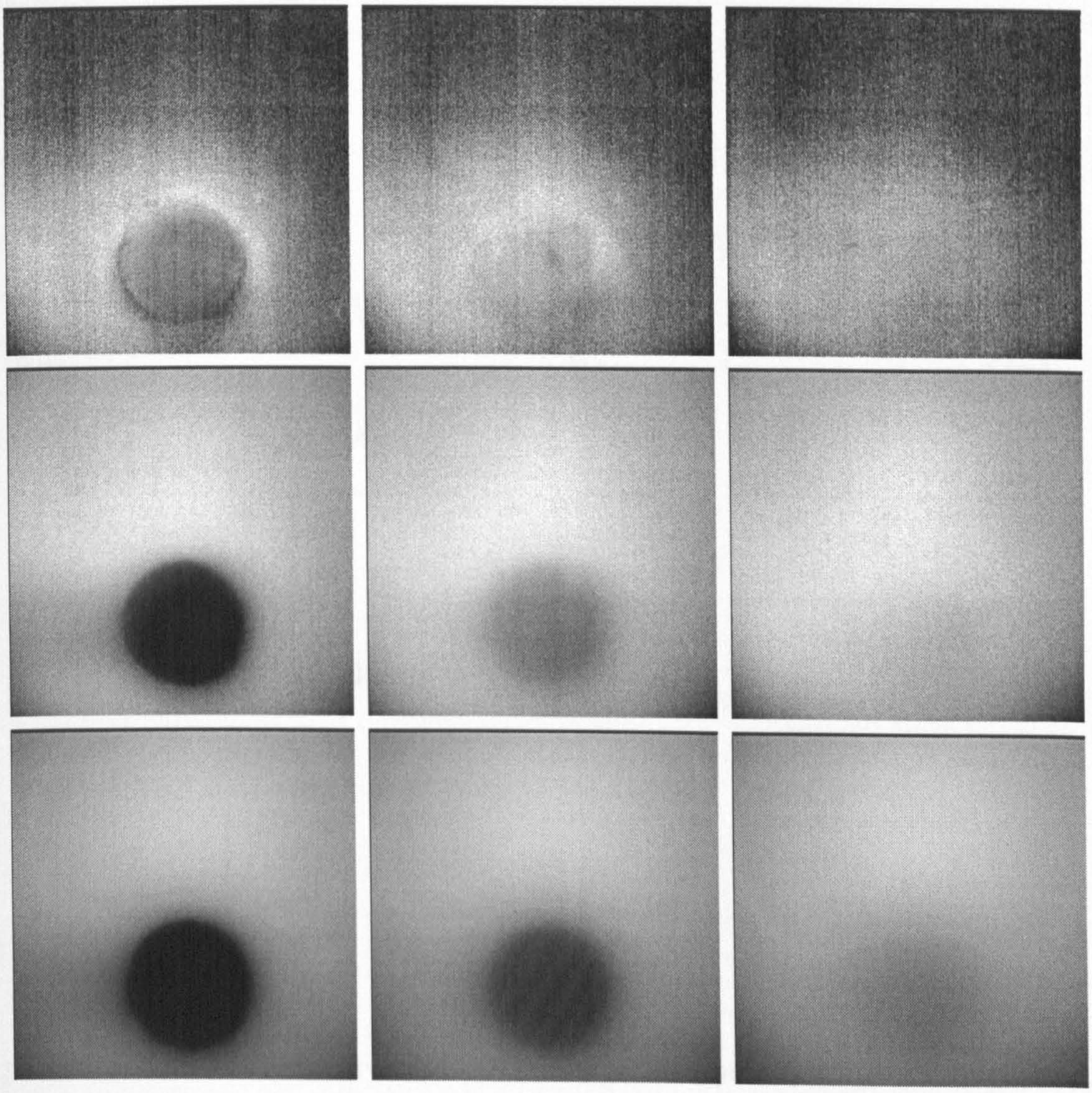

Figure 4.12: *Images of the absorbing feature located at 0.1mm (first column), 0.5mm (second column) and 1.1mm (third column) for different polarization gates (row 1, linear polarization maintaining; row 2, circular polarization maintaining; row 3, multiple scattered light.*

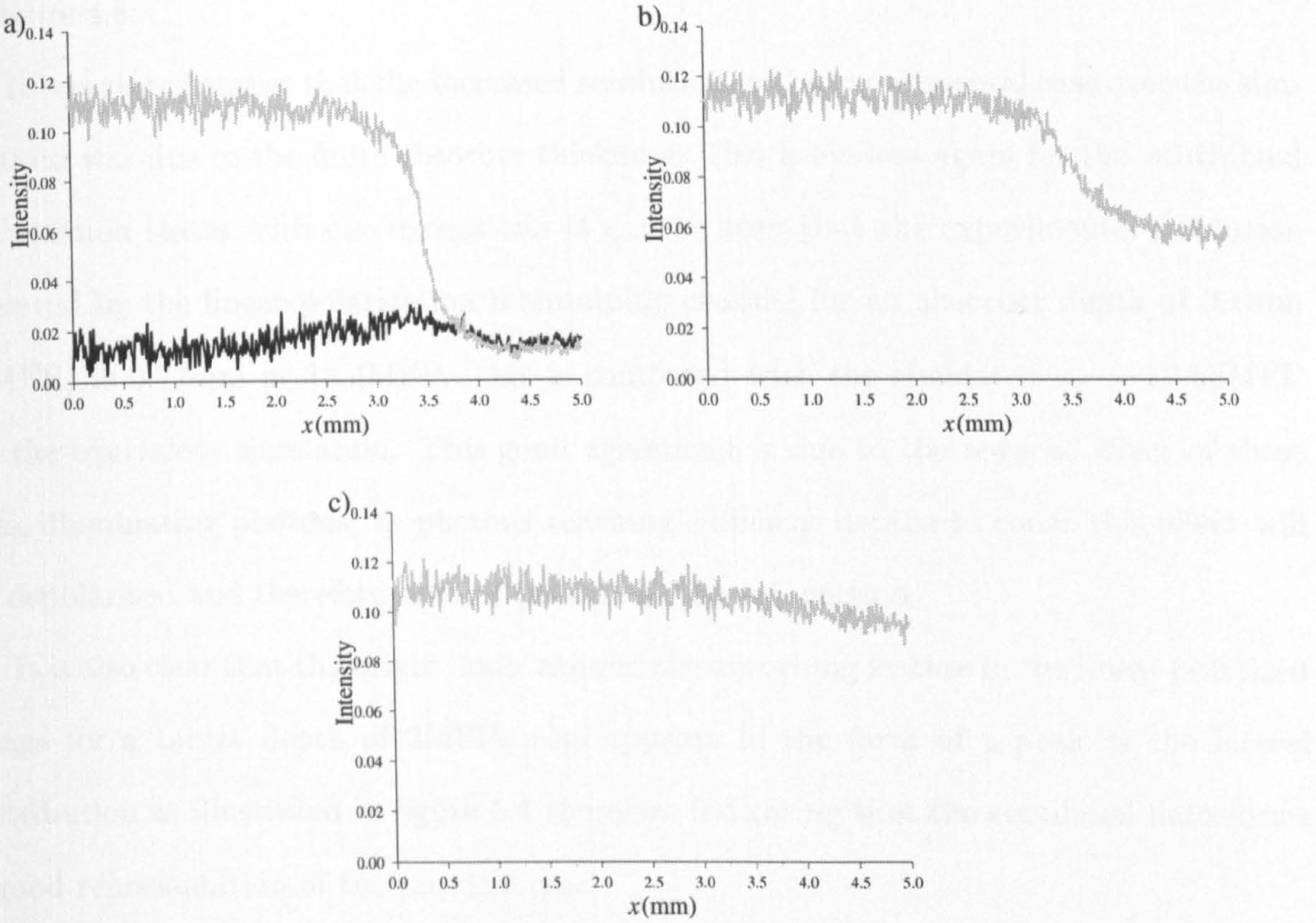

Figure 4.13: *Line scans recorded from the images in figure 4.12 for linear (black) and circular (grey) maintaining polarizations for absorbing feature depths of a) 0.1, b) 0.5 and c) 1.1mm.*

in all polarization gates. For an absorber depth of 10MFPs the object has moved outside the linear polarization gate and is therefore no longer visible in this image. However, it remains present in the other two states. At the third object position of 22MFPs depth, the absorber is barely visible in the circularly polarized channel, but still remains in the multiple scatter image due to the prominent tail still present at this depth as can be seen in figure 4.8.

It was stated earlier that the increased resolution in the experimental case over the simulations was due to the finite absorber thickness. This is evident again for the subtracted polarization states with one exception. It can be seen that the experimental resolution achieved by the linear polarization maintaining channel for an absorber depth of 0.1mm (2MFP) is 0.72mm or 14.4MFP. This is compared with the simulated x_r = 12.65MFP for the equivalent simulation. This good agreement is due to the reduced effect of these back-illuminating photons, as photons reaching sufficient depths to cause this effect will be depolarized and therefore are not present in the subtraction.

It is also clear that the bright 'halo' around the absorbing feature in the linear polarized image for a target depth of 2MFPs also appears in the form of a peak in the lateral distribution as illustrated in figure 4.4 therefore indicating that the simulated data forms a good representation of the physical case.

Considered thus far for both simulated and experimental analysis have been media containing scatterers that are very uniform in terms of both size and shape. In the context of human tissue as a scattering medium this is clearly not the case due to the skin complex structure. It is clear however that, due to the wide range of scattering centres, irregularity in shape and dense scatterer packing, their scattering properties will also vary. Presented in figures 3.20 and 4.8 were the intensity depth profiles for media composed of uniform scatterers, but it would be panglossian to suggest these would hold for biological tissue. Therefore, it is necessary to consider the enhancement provided by the use of circularly polarized light over those currently implemented techniques using only linear states. This is discussed in the following section.

4.3 Surface Reflection Considerations

The results presented above were concerned with the illumination of a sample contained within a cuvette with optically flat surfaces, combined with an 'off-axis' detection system (figure 4.9). Due to these factors, any reflections from the surface of the sample were directed away from the imaging optics and were therefore not detected. Problems occur during the optical imaging of skin, as the reflections emanating from the surface of tissue are not highly directional due to the irregular surface structure. This suggests that surface reflections from skin samples are detected irrespective of the angle of detection. This contribution can dominate the detected light and can therefore distort the extraction of information from light which has penetrated the samples surface and therefore carries information concerning the more useful sub-surface regions. For this reason it is clear that removal of such a component would be highly desirable. Previous attempts to remove this surface component have generally involved the application of a flat glass plate and refractive index matching fluid to the surface of the skin. This allows redirection of any specular reflection away from the instrument's detection arm as shown in 4.14. Such an arrangement is also applied in [85] and [125].

For applications such as those considered in this study and discussed in section 1.3 this solution is far from ideal as the process of application may cause irritation to the area under examination due to the necessary contact. Any pressure exerted on the surface of the skin due to the slide being pushed onto the skin's surface may also adjust the structural and hence optical properties of the underlying tissue through the evacuation of blood or the distortion of the collagen architecture. This is in addition to the inconvenience of an increase in the time taken to perform the examination process.

A widely used technique which can be applied to remove these surface contributions is to simply detect the cross-polar linear component[83, 126] (channel 2) which removes

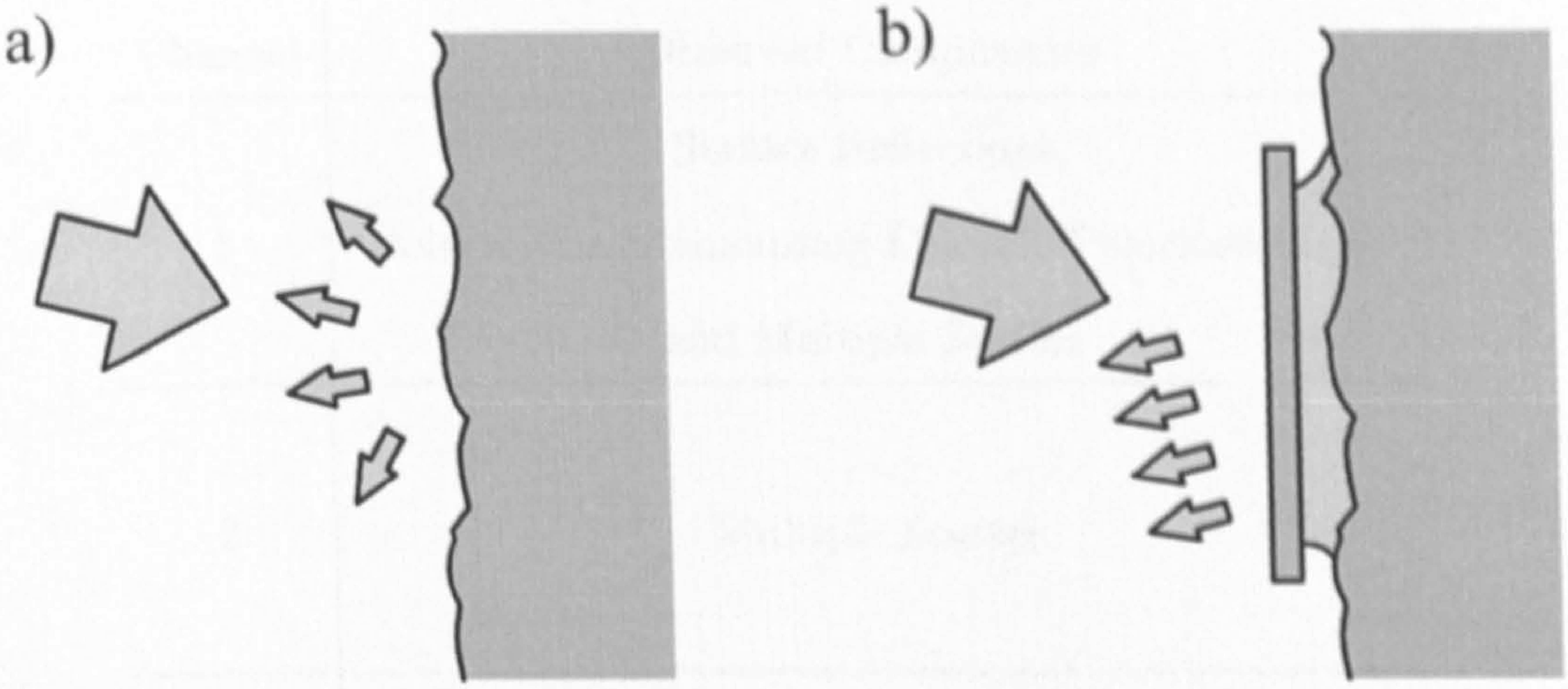

Figure 4.14: *Reflection from the irregular surface of a skin sample as shown in a) are not confined to a narrow range of angles. However, these reflections can be controlled as in b) through the application of a flat glass plate coupled with matching fluid.*

the need for application of the glass plate and matching fluid. This scheme will include only light which has had its polarization state randomised by many scattering events and will therefore not include any surface component. As is clear from figure 3.20 this component has a high sensitivity to deeper sample regions and is also poorly localised in both the lateral and depth directions leading to uncertainty concerning the volumes probed. Also, for an application where the superficial regions of a sample are of interest, as they are here, the sensitivity to this depth region will be detrimented by the large multiple scattered background. Therefore, should removal of both surface reflections and multiple scatter be possible using non-contact methods, enhanced sensitivity to a localised sub-surface region should be achieved.

The solution to the removal of these unwanted components can be seen from further analysis of the technique presented in section 3.6. Presented in this section were the origins of the light backscattered into the different polarization channels, graphically represented in figures 3.4 and 3.5, for linearly polarized and circularly polarized light respectively. One practically occurring component omitted from these representations is the surface

Channel	Observed Components
1	Surface Reflections, Polarization Maintaining Linearly Polarized Light and Multiple Scatter
2	Multiple Scatter
3	Polarization Maintaining Circularly Polarized Light and Multiple Scatter
4	Surface Reflections, Single Scattered (Flipped Helicity) Light and Multiple Scatter

Table 4.6: *Categories of light backscattered into the four polarization channels from tissue samples.*

reflection contribution discussed here. A surface reflection event will appear on detection with the same properties as a directly returned single backscatter event and will therefore form a contribution to channels 1 and 4. The components emerging from tissue samples in the different polarization channels are summarised in table 4.6.

Techniques applied previously to remove the multiple scatter component using polarized light illumination have been concerned with linearly polarized illumination and channel subtraction (channel 1 - channel 2) [50, 51, 80, 85, 122]. However, such techniques require the use of channel 1 which contains a contribution from the surface and will therefore influence the extracted polarization maintaining component. The key to the successful removal of both surface reflection and multiple scatter is to note that the use of circularly polarized light discriminates between weakly scattered light (emergent in channel 3) and surface reflections (detected in channel 4). The linear polarized case does not make this discrimination and both components would be backscattered into the linear co-polar channel. As channels 2 and 3 contain no surface component the extraction of circular polarization maintaining light through their subtraction, as discussed in section 3.6, should result in an image localised in depth and containing no surface reflection component.

4.4 Preliminary Tissue Imaging

Using the same system as described in section 4.2.3, the sequence of polarized light images shown in figure 4.15 have been recorded from a lentigo on the arm of a 31-year-old caucasian male.

It can be seen from the images for channels 1 and 4 (figures 4.15a and 4.15d) that there is a significant contribution detected due to surface reflections. These surface reflections are not detected in channels 2 and 3 (figures 4.15b and 4.15c) in keeping with the considerations presented in the previous section. In accordance with the discussion in chapter 3 the difference between these two images is due to weakly scattered circular polarization maintaining light.

The two subtractions discussed in the previous section and in section 3.6 can be performed to extract the polarization maintaining components and are presented in figure 4.16. It is clear from these images formed from polarization maintaining light that the linearly polarized image (figure 4.16a) is dominated by surface reflections and provides no discernible information concerning the underlying tissue.

Figure 4.16b is composed of circular polarization maintaining backscatter. As expected this is free from any surface reflection component. This provides an image consisting solely of light which has probed localised sub-surface regions of tissue. The brighter area near the top of the image is due to some non-uniformity in the illuminating beam coupled with the curvature of the forearm. This indicates the potential for non-contact polarized light

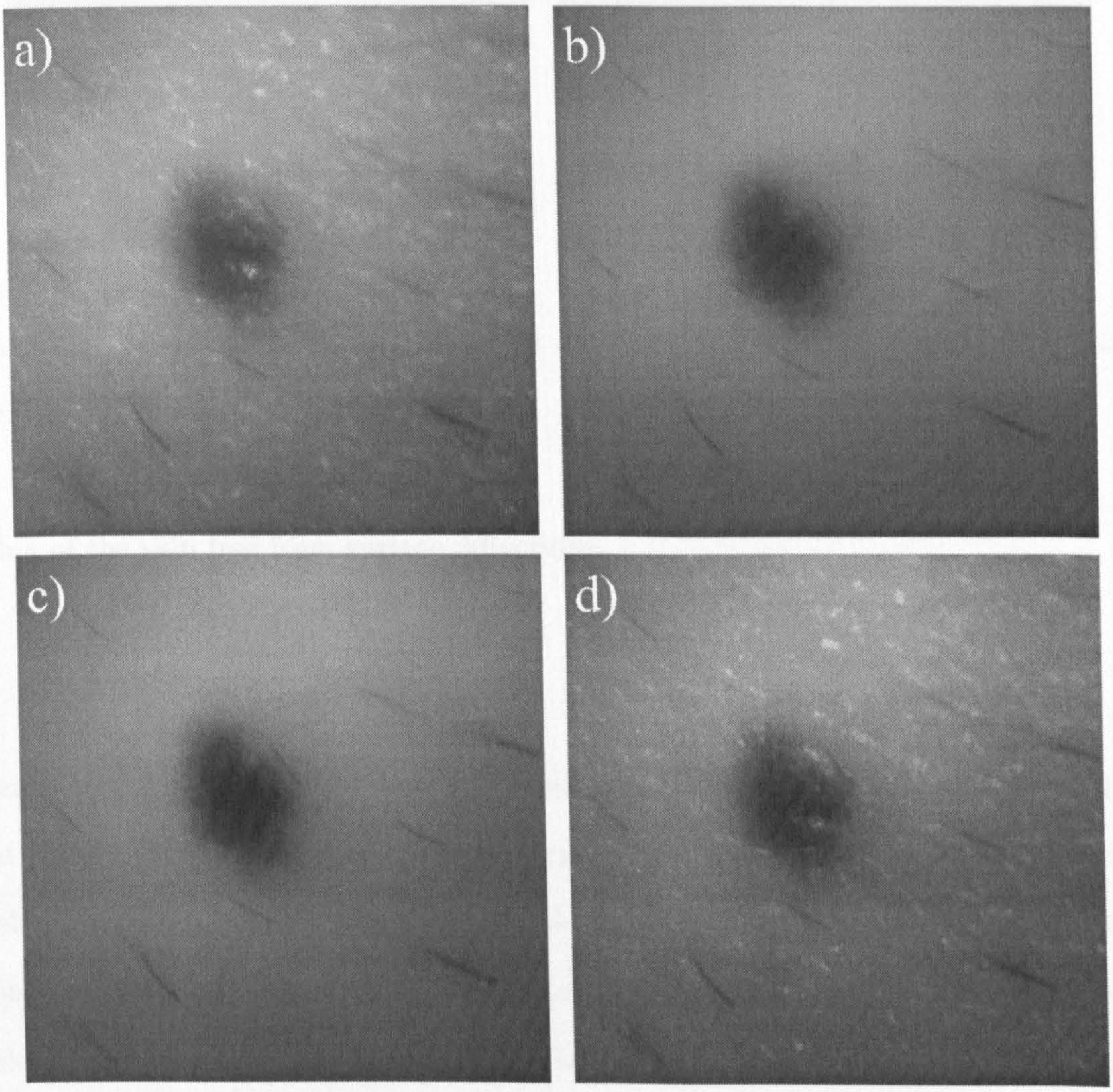

Figure 4.15: *Polarization images of a lentigo in a) channel 1, b) channel 2, c) channel 3 and d) channel 4.*

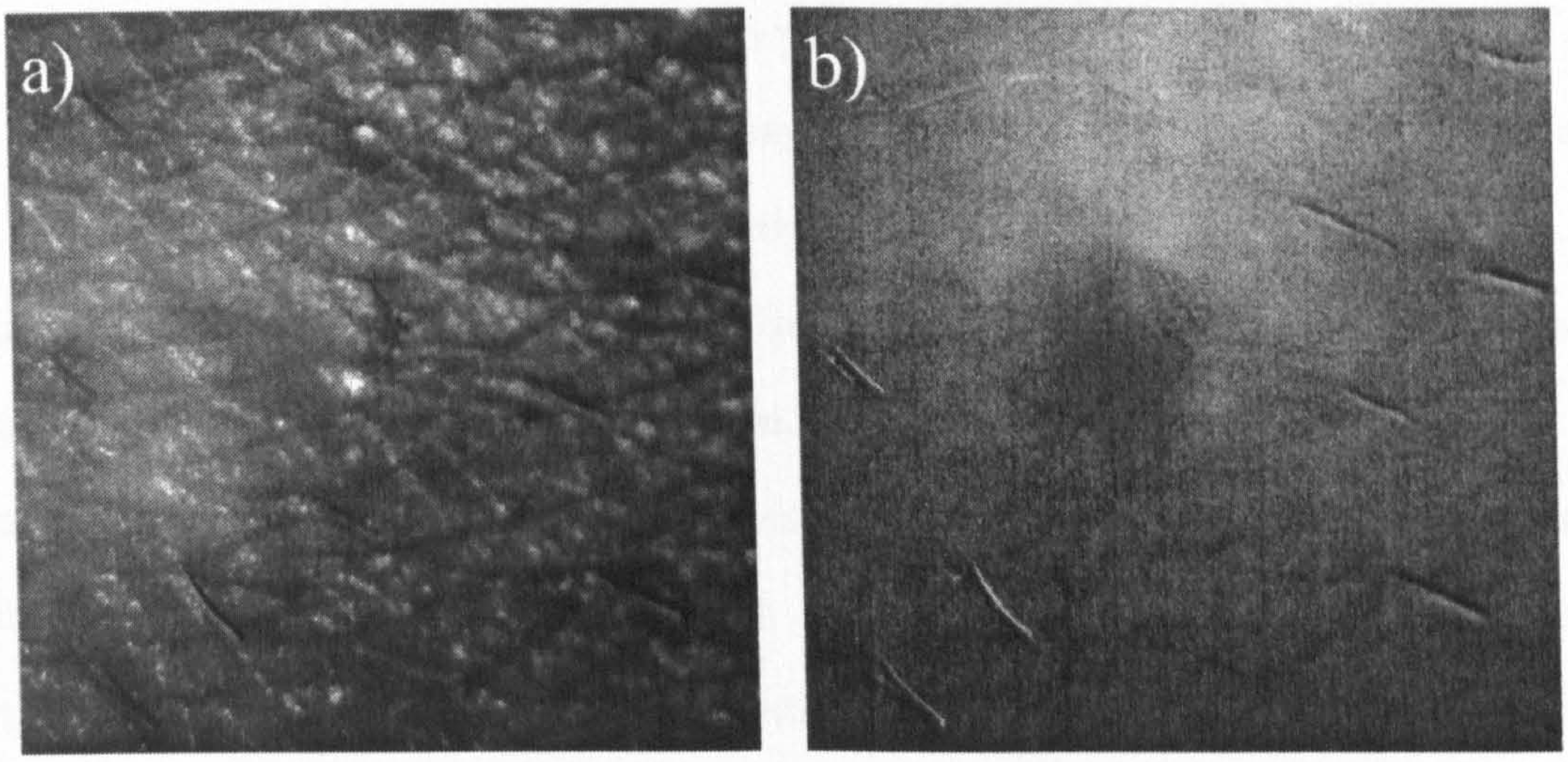

Figure 4.16: *Subtracted polarization images of a lentigo due to a) linear and b) circular polarization maintaining light.*

imaging of the skin free from surface reflections.

4.5 Summary

Presented in this chapter have been line scans resultant from simulations of full field illumination of a sample containing a depth varying absorbing feature. The interdependence of polarization gate and volume sensitivity has also been demonstrated through analysis of contrast and lateral resolution. These simulated results have then been extended to a simple, laser based, bench-top polarization imaging system. Images have been retrieved from scattering microsphere suspensions containing an absorbing object. These results illustrate the depth gating properties and that coarse optical sectioning can be achieved by polarization discrimination, also showing good correlation with the anticipated depth response predicted from Monte Carlo simulations.

The system has also been used to image an *in-vivo* lentigo. These results demonstrate the presence of a large surface contribution present in polarization channels 1 and 4 due to surface reflection and single scatter events. These contributions can be seen to be absent from the linear cross-polar and circular co-polar channels allowing construction of an image due to circular polarization maintaining light which is free from specular reflection whilst also removing the contribution of multiple scatter from deep within the tissue. This polarization image subtraction method has been demonstrated to be an effective method to image the superficial regions of skin tissue.

One feature resultant when analysing visitation depth profiles similar to those presented in figures 3.20 and 4.8 is that with the addition of a small amount of optical absorption the properties of circular polarization maintaining light and multiple scattered light are very similar due to the large effect on long propagation length photons. This effect is illustrated by the visitation profiles in figure 4.17. This suggests that the improvements provided by the use of circularly polarized light over the simple detection of cross-polarized linearly polarized light are removed by the presence of absorption. However, as mentioned previously, the depth properties resultant in skin tissue are not as simple as those from uniform microspheres. The fact that there is significant signal present in the circular polarization maintaining light component (figure 4.16b) indicates that for tissue samples, there is a clear distinction between circular polarization maintaining light and the multiple scatter component.

The images recorded in this chapter for different polarization states are taken sequentially at different rotations of quarter-wave plates and linear polarizers. This makes the technique susceptible to movement artifacts as it requires the manual rotation of components to the correct orientation. Effects due to movement artifacts can be seen to be present in figure 4.16b by the misalignment of hairs on the arm. Automation of the set-up to reduce this effect and form a more practical system is considered in the following chapter.

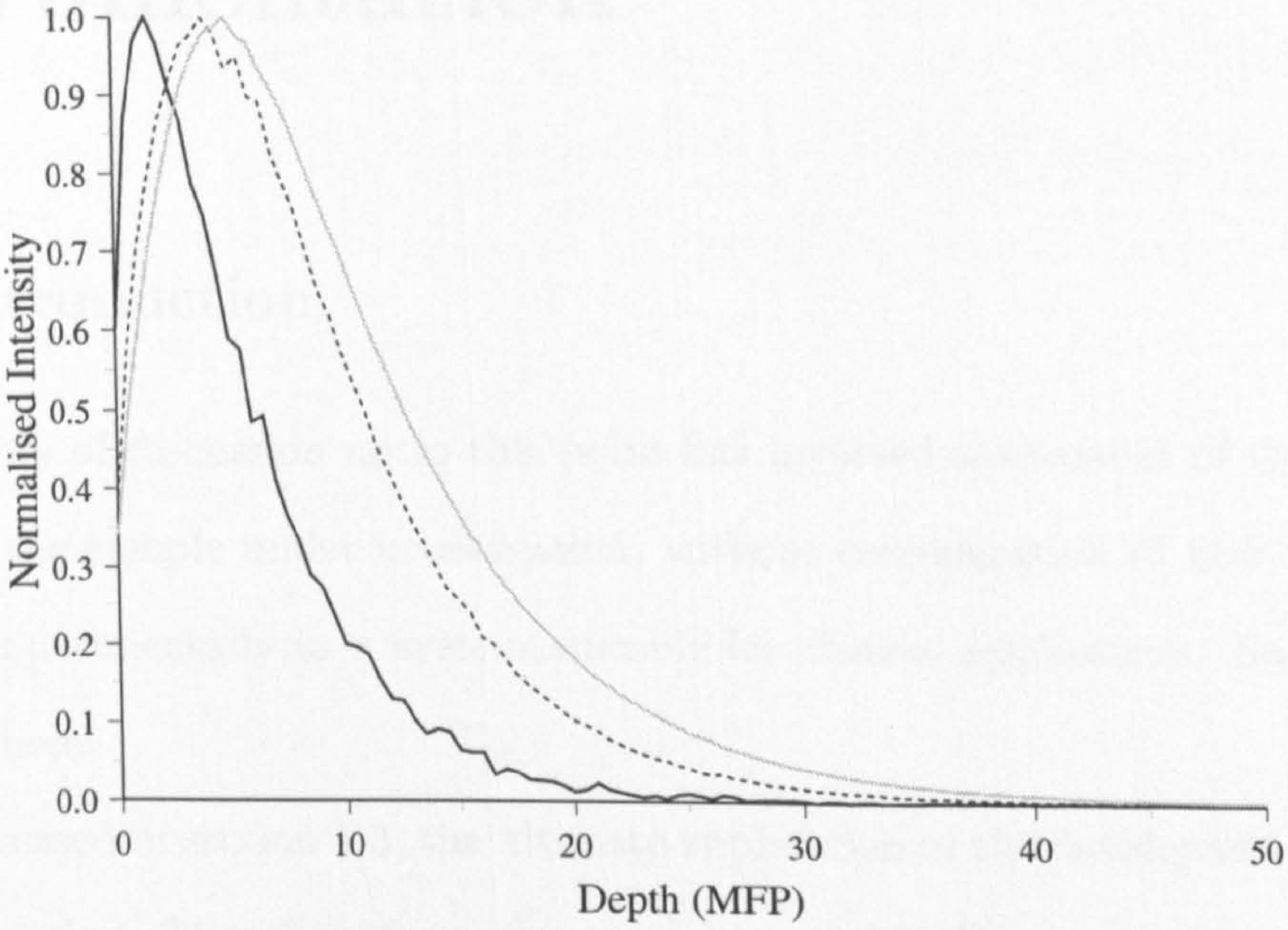

Figure 4.17: *Normalised plot of the visitation depths of photons in the linear polarization maintaining channel (black), circular polarization maintaining channel (dotted) and multiple scatter (grey) channels with* $\mu_a = 0.01 MFP^{-1}$.

Chapter 5

Instrumentation

5.1 Introduction

The majority of discussion up to this point has involved assessment of the interaction of light with the sample under investigation, without consideration of how such analysis is achieved experimentally in a system suitable for clinical application. Such discussion is presented here.

As discussed in section 1.3, the ultimate application of the developed techniques are in medical imaging. Therefore, for a system to be a viable diagnostic aid it must fit certain criteria in terms of simplicity and hence ruggedness, safety, usability and of course cost, if it is to be suitable for widespread implementation. This chapter includes a discussion of these practical considerations, with the aim of producing a system that is appropriate as a prototype for use in a dermatology clinic. Discussion here provides the reasoning behind the selection of the different illuminating wavelength sources along with a brief discussion of several design characteristics of the system. The chapter concludes with the characterisation of the final system along with a discussion of the system automation, software control and photographs of the developed instrument.

5.2 Proposed System

A bench top system has already been used for experimental analysis in this thesis, and a discussion of this can be found in section 4.2.3. In the system developed here, a fundamental change is made to the system layout.

The basic layout of the laboratory set-up involved the backscattered light being detected at an angle removed from the optical axis of the illumination arm. This arrangement ensured that any surface reflections from the flat front surface of the sample were reflected away from the imaging arm and were not detected. This allowed the linearly polarized co-polar channel, channel 1, and the mirror reflected circularly polarized cross-polar channel, channel 4, to be viewed with reduced distortion from these reflections. The off-axis detection system is shown in figure 4.9. As discussed in section 4.3 problems arise in tissue imaging due to the high levels of light specularly reflected from the surface of the skin. It has already been discussed how these effects can be removed using the cross-polar linearly polarized channel and the co-polar circularly polarized channel (see sections 3.6 and 4.3). However, to fully take advantage of such a technique, on-axis detection can be applied. Such a system unlocks the possibility for a technique to be applied in an endoscopic arrangement giving greater flexibility in the range of possible applications. This modified arrangement becomes possible as it combines the functionality of the two quarter wave retarders into a double pass through a single component in illumination and detection. This is discussed further in section 5.2.2. The combination of QWP1 and QWP2 from figure 4.9 means that the number of quarter wave plates can be halved. This becomes increasingly important in the multiple wavelength system. Not only does this reduce cost, but it also removes problems with component performance matching. The layout of the proposed system (illustrated here for a single wavelength) is shown in figure 5.1.

From looking at the system it can be seen that there are three main functions that are performed: sample illumination by light of a chosen wavelength and polarization state (performed by the source, LP1 and QWP), polarization analysis of the light backscattered

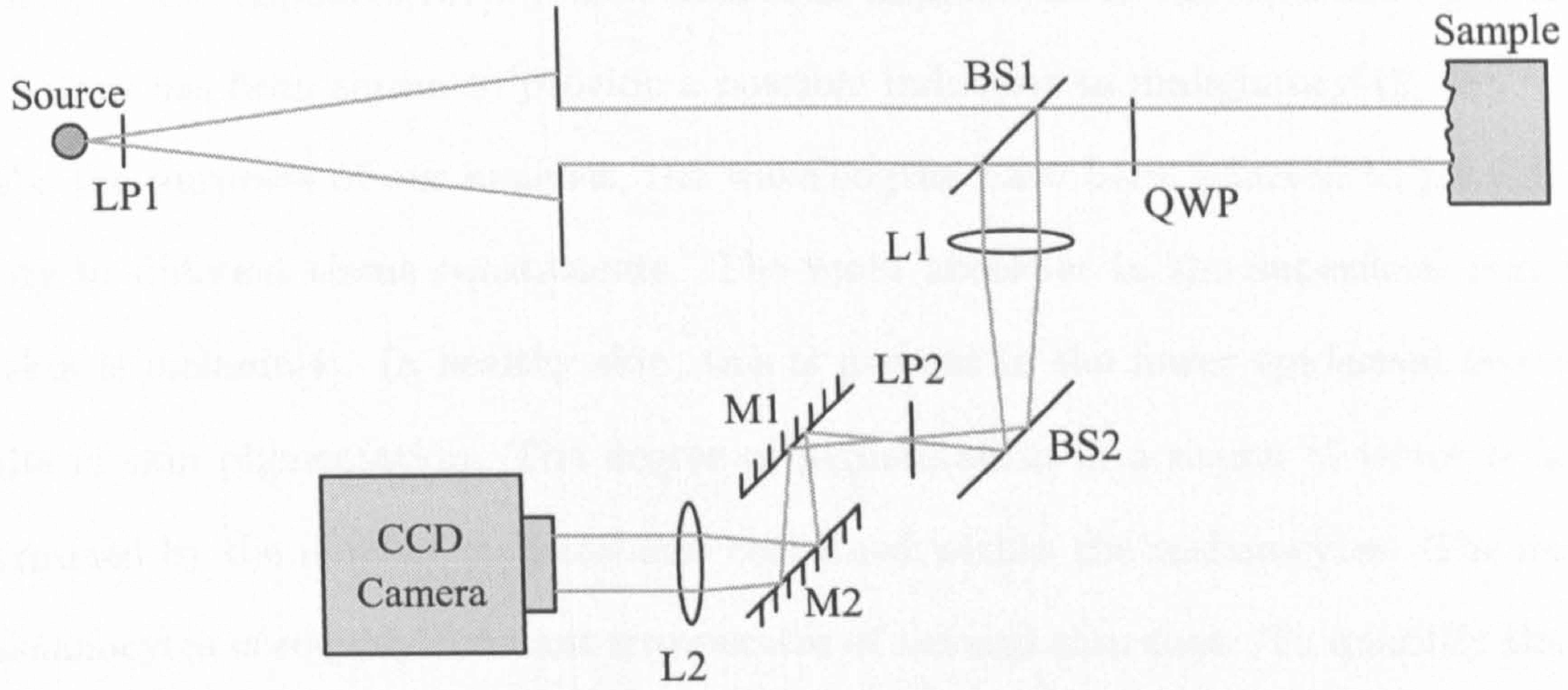

Figure 5.1: *The basic layout of the proposed system for a single wavelength source.*

from the sample (QWP and LP2) and imaging and detection of the analysed light (L1, L2 and the CCD camera).

The backscatter is reflected for detection by a pellicle beamsplitter, BS1. Such a device is selected over a regular cube beamsplitter due to problems with component imperfections. The illumination passes through BS1 before reaching the sample and, therefore, a large component is reflected away. This light, when using a cube beamsplitter, would have to pass through a glass/air interface on exit, leading to low levels of reflection entering the detection arm. In many systems this does not prove problematic, however, due to the very low light levels being backscattered from the sample, this unwanted reflection would dominate the detected image. This is clearly not an issue when using a pellicle beamsplitter. The functions of BS2, M1 and M2 are described in section 5.2.3.

5.2.1 Illumination

When selecting the sources of illumination used in the system a key factor to consider are the wavelengths used. In previous studies, the spectral properties of tissue has been used extensively when analysing the skin[42, 46] to determine the presence and concentration of different chromophores[127]. This is of special importance as the 'spectral signature' of skin lesions has been shown to provide a possible indicator to malignancy[42, 48].

For the purposes of our analysis, the wavelengths have been selected to provide sensitivity to different tissue constituents. The main absorber in the superficial regions of the skin is melanin[4]. In healthy skin, this is present in the lower epidermal layers and results in skin pigmentation. The degree of pigmentation in a region of tissue is largely determined by the number melanosomes contained within the melanocytes. The number of melanocytes is roughly constant irrespective of natural skin tone. To quantify the level of melanin, a volume fraction, V_{fmepi}, can be defined, which is the percentage of volume occupied by the melanosomes in the epidermal layer. The variation of skin tone with epidermal melanin volume fraction is considered more fully in section 7.3.2, but shown in figure 5.2 is the absorption spectrum for an epidermal layer with $V_{fmepi} = 10\%$. Contained within this spectrum, and indicated separately on the plot, is the contribution to absorption due to epidermal tissue that is free from the influence of melanin. This absorption is due to keratin, keratinocytes and cytoplasm and has a much lower influence than the presence of melanin (note the logarithmic scale), however it is included for completeness.

Due to the shape of this spectrum it is clear that the selection of a short wavelength should provide high sensitivity to the presence and concentration of melanin. For this reason the wavelength of the first source was selected in the 450-480nm band. This high level of absorption will also suppress the 'tail' of the depth profile (presented in section 3.7.1) and therefore should be greatly influenced by the epidermal layers. The extraction of polarization maintaining light through subtraction should therefore result in an improved resolution map of epidermal melanin. This would prove to be a useful diagnostic measurement as border irregularity can be used as an indicator of melanoma malignancy[12, 13].

In the healthy dermis there is no melanin present to provide optical absorption. However, a large contributor to optical absorption in this region is the presence of blood and more specifically hæmoglobin. The absorption spectra for oxy- and deoxy-hæmoglobin are

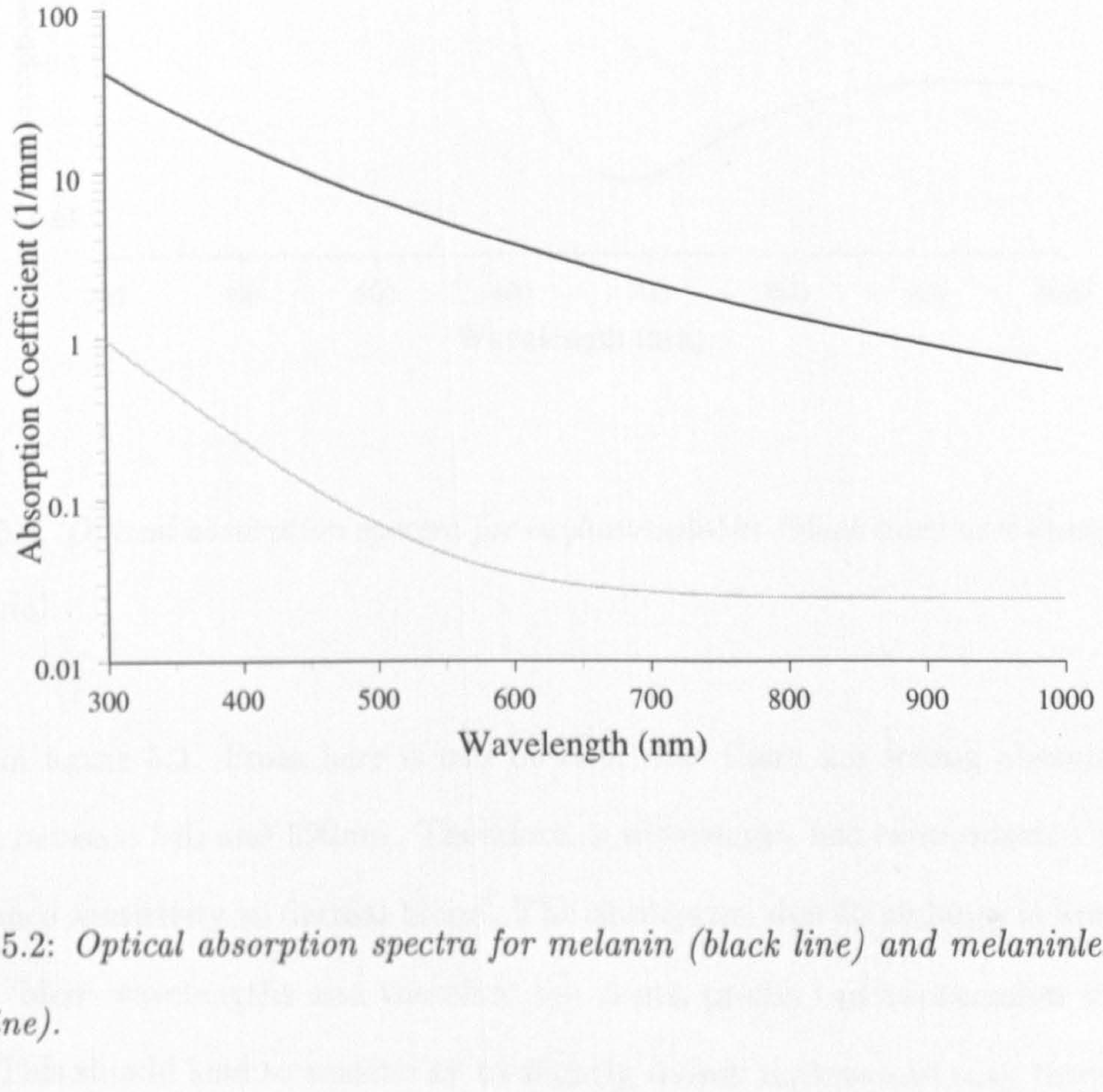

Figure 5.2: *Optical absorption spectra for melanin (black line) and melaninless epidermis (grey line).*

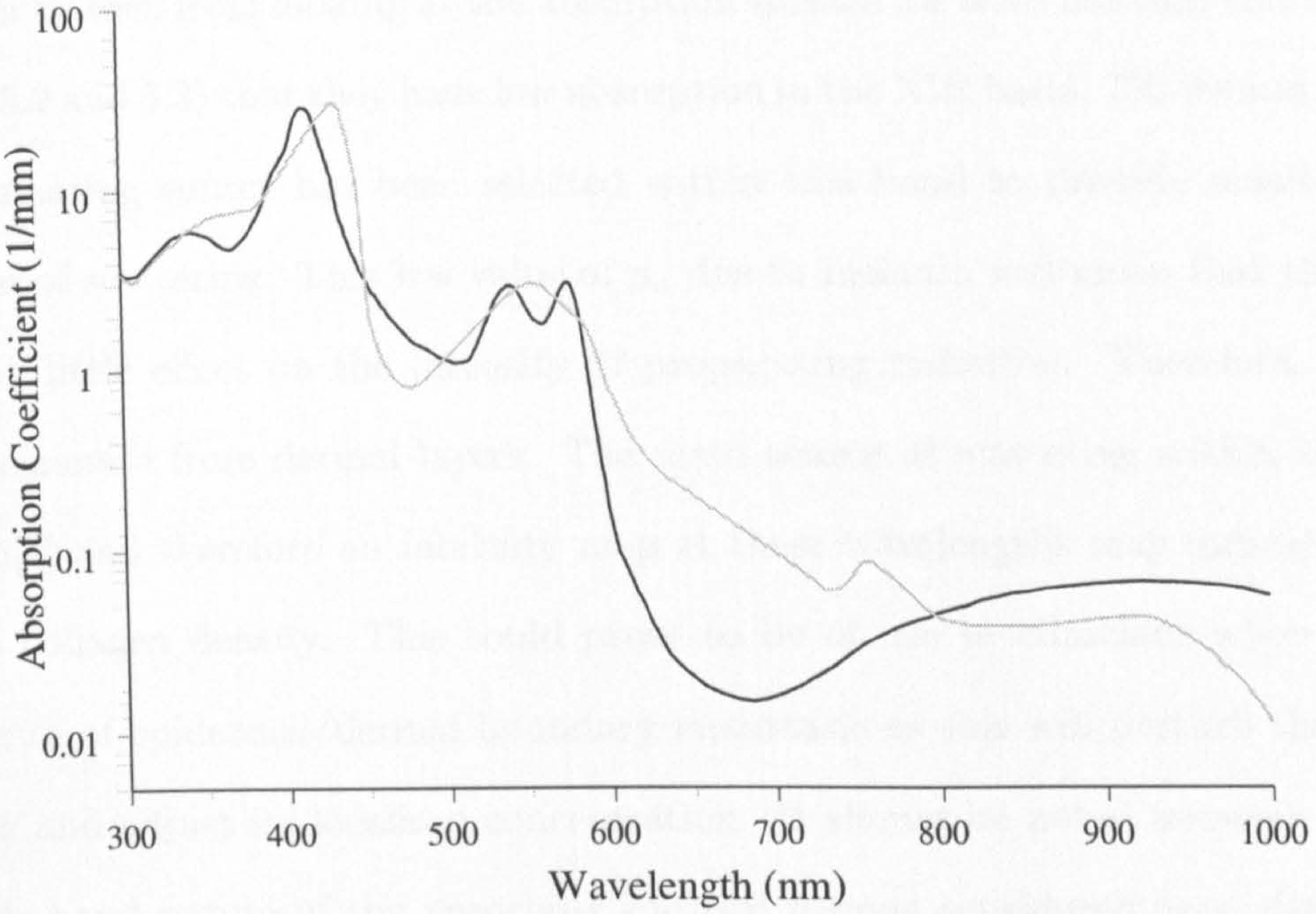

Figure 5.3: *Optical absorption spectra for oxyhæmoglobin (black line) and deoxyhæmoglobin (grey line).*

shown in figure 5.3. From here it can be seen that there are strong absorption peak(s) located between 540 and 590nm. Therefore, a wavelength has been selected in this range to enhance sensitivity to dermal blood. The absorption due to melanin is lower here than for the 'blue' wavelengths and therefore the depth profile tail suppression will not be as great. This should lead to sensitivity to slightly deeper regions and may therefore provide sensitivity to capillaries in the papillary dermis.

The selection of a wavelength in the 620-680nm band relates to a region of reasonably low optical absorption due to melanin and a trough in the (oxy)hæmoglobin spectrum. Therefore, the peak of the intensity depth profiles will be located at still greater depths than for shorter wavelength illumination. This wavelength is therefore intended to provide sensitivity to deeper volumes of melanin which may have compromised the epidermal/dermal boundary.

It can be seen from looking at the absorption spectra for both melanin and hæmoglobin (figures 5.2 and 5.3) that they have low absorption in the NIR band, 700-900nm. Therefore, an illuminating source has been selected within this band to provide sensitivity to the variation of scattering. This low value of μ_a due to melanin will mean that the epidermis will have little effect on the intensity of propagating radiation. Therefore, backscatter should emanate from dermal layers. The main source of scattering within skin tissue is collagen[4] and therefore an intensity map at these wavelengths may indicate properties such as collagen density. This could prove to be of use to clinicians when seeking the occurrence of epidermal/dermal boundary metastasis as this will perturb the underlying collagen and adjust its localised concentration. It should be noted however, that due to the wide band nature of the absorbing spectral regions considered here, direct mapping from intensity to choromphore concentration is not trivial.

Consideration must also be made of the type of device used for illumination. In the laboratory based system (figure 4.9), a 10mW helium-neon laser was used. However, for use in a prototype for clinical use there are limitations on the application of such devices. The aim of this system is to investigate whether the principles outlined in this study are worthy of further consideration. Therefore, fast realisation of a cheap and safe device is key. When applying a system in a clinical setting patient safety is clearly of major concern. The application of lasers in such a system opens up many restrictions on the mechanical and optical construction, along with complicating the ethical approval process. In addition to safety, the system cost can be reduced through the selection of alternative devices. To fit in with these specifications LEDs of different wavelengths can be used. These fit all the criteria outlined above. Due to their low levels of coherence such devices avoid issues such as image speckle and safety issues, whilst also being available at a wide range of wavelengths at extremely low cost.

Wavelength (nm)	Intensity	Spectral Width (nm) (FWHM)
470	1575mcd	35
574	5000mcd	11
660	3500mcd	20
865	80mW/sr	41

Table 5.1: *Basic specification for the selected LEDs*

For these reasons outlined above, coupled with the availability of devices and the wavelength sensitivities of the selected CCD camera, the chosen wavelengths are 470, 574, 660 and 865nm. A brief summary of the LED specifications are given in table 5.1, accompanied by the emission spectra of the selected devices, recorded using a spectrometer, in figure 5.4.

5.2.2 Polarization Selection

A further component selection which is required is the choice of quarter wave retardation device. Selected here are zero-order quartz wave plates. These are available at a wide range of wavelengths and, being zero-order, are robust in terms of performance in the presence of finite band sources and finite angle of transition.

The basic layout of the polarization components applied in the modified system is shown in figure 5.5. The illumination and return paths are separated for illustrative purposes only.

The setting of the illumination polarization state is performed by light being passed through a linear polarizer (LP1) to produce a single linear polarization state. For the two linearly polarized detection channels (channels 1 and 2) the quarter wave retardation component is switched out of position (as will be discussed in section 5.3). The backscattered light passes, via a beamsplitter, through the second linear polarizer (LP2), where the discrimination is made between the co-polar or cross-polar states.

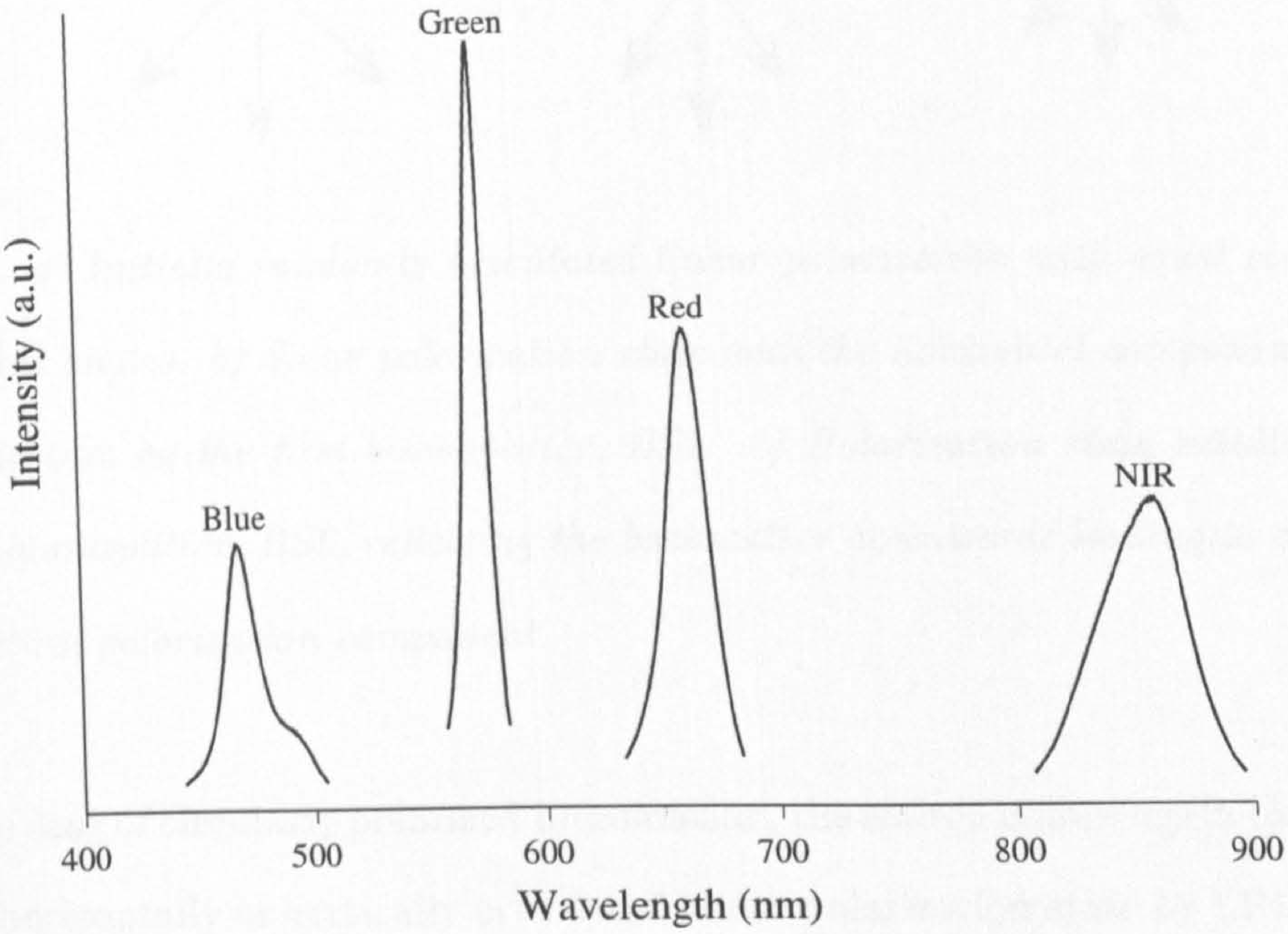

Figure 5.4: *LED radiation spectra.*

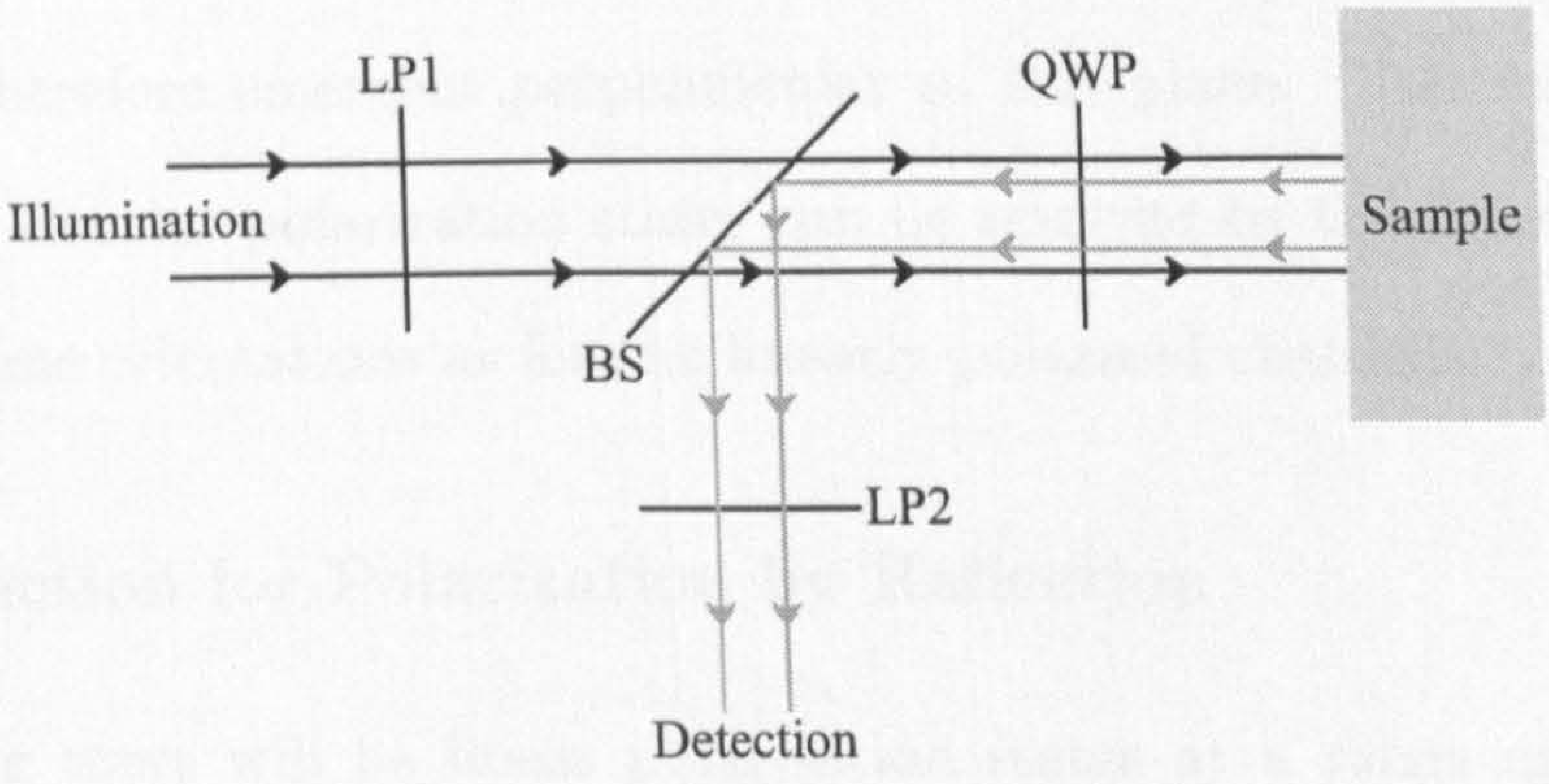

Figure 5.5: *The layout of the polarization components in the final implementation.*

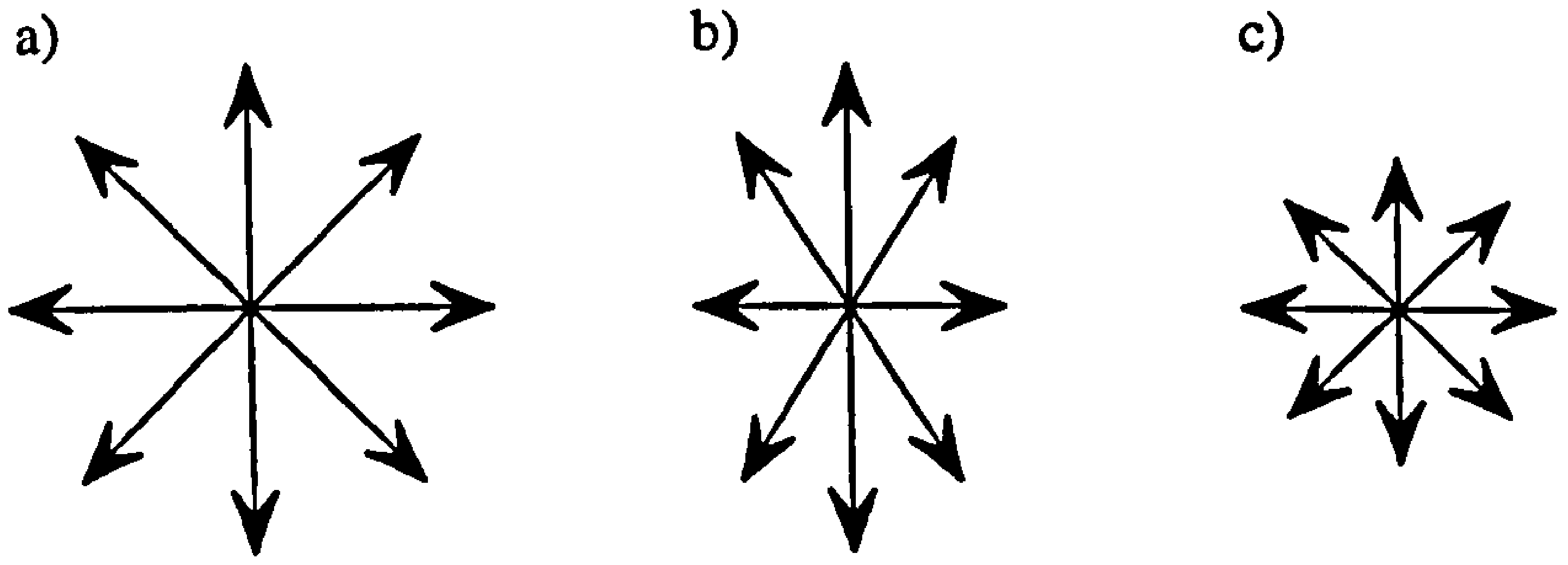

Figure 5.6: *a) Initially randomly orientated linear polarization with equal components at all azimuthal angles. b) Same polarization state with the horizontal component suppressed due to reflection by the first beamsplitter, BS1. c) Polarization state resultant from the correcting beamsplitter, BS2, reflecting the backscatter downwards leading to a suppression of any vertical polarization component.*

For the case of circularly polarized illumination, the source is once again cleaned up into an initial horizontally or vertically orientated linear polarization state by LP1 before being passed through the retardation component (QWP), which is orientated at 45 degrees to the plane of linear polarization. This results in the circular polarization state. The backscatter then passes through this same component which is now orientated at -45 degrees relative to the plane of incident polarization. This results in any emerging polarization maintaining light being rotated parallel to the initial plane of linear polarization. Any mirror reflected component is therefore emergent perpendicular to this plane. This means the co-polar and cross-polar circular polarization states can be resolved by the same output polarizer (LP2) in the same orientations as for the linearly polarized channels.

5.2.3 Correction for Polarization by Reflection

After scattering there will be linear polarization states at a range of azimuthal angles being reflected by the 45 degree beam splitter (BS1). Therefore, the overall polarization state will be affected due to a variation in reflection coefficient with azimuthal angle at the dielectric surface.

To counteract this polarization by reflection which results in the suppression of the horizontal component, and hence would affect the ratio of co-polar to cross-polar light, a downwards reflection can be introduced immediately before discrimination by the output linear polarizer, LP2. This is the function of BS2 in figure 5.1. A qualitative representation of the correction process is given in figure 5.6. The first mirror in the detection arm (M1) is used to produce a horizontal path after the downwards reflection from BS2. The second mirror (M2) reflects the backscatter onto the detector and is used to allow flexibility in the positioning of the CCD camera, leading to a more compact system.

5.2.4 Detection

The final function performed by the system is the detection and imaging of the backscattered light. The main design decision to be made here is concerning the specifications of the CCD camera onto which the light shall be imaged. The main factor is that we are interested in is the polarization maintaining light, which is extracted through image subtraction, from the raw images. However, the magnitude of the polarization maintaining component is generally expected to be much smaller than the multiple scattered background on top of which it sits. It is therefore necessary to ensure that there are enough grey levels available to represent the component resultant from the image subtraction without quantisation noise becoming too great a factor. For this reason a 12 bit CCD camera (offering 4096 grey levels) has been implemented in this system. It has been previously estimated that around 3% of light backscattered from tissue has maintained its initial polarization state. Using this as an approximation more than 100 levels are available to form the subtracted image. Another factor that must be considered in the selection of camera is the spectral sensitivity of the detector. This is due to the selection of an illuminating source in the NIR region.

Taking all of these above design considerations into account the chosen CCD camera was the Hamamatsu ORCA ER. The detector has 1344 × 1024 pixels which are 6.45μm square. The well capacity of a single pixel is 18000 electrons.

5.3 System Automation

There are several components within the system that only operate efficiently at a single wavelength or limited range of wavelengths. To allow utilisation of such components in a multiple wavelength system such as this, some level of automation is required to switch the required component into the beam path for the corresponding illuminating wavelength and possibly adjust its orientation. To achieve this, a bipolar stepper motor control system has been constructed that allows full control of the system through the parallel port of a standard PC, allowing full software control. Custom made mounts have been designed and fabricated to allow the most efficient and practical method of component switching and orientation selection. The four channel motor controller is used to select the correct LED, switch in the corresponding quarter wave plate, control the orientation of the quarter wave plate and select the relevant output linear polarizer. Once the desired LED is rotated into position it can be switched on and off by software through an additional parallel port connection and interfacing electronics as necessary.

The CCD camera is also controlled through the PC using a Firewire interface card via supplied driving hardware. This allows adjustment of many aspects of the camera functionality including the exposure time and sub-array pixel binning of the detector array. These values can be adjusted for the different wavelengths to ensure that the maximum number of levels are used in forming the detected image.

The interconnection and layout of the component parts of the system is shown in figure 5.7.

Clinical implementation of an instrument requires some form of user friendly interface to be used by the clinician. To achieve this, keeping usability in mind, a Windows based GUI was designed and implemented using Microsoft Visual C++. A presentation of the designed software can be found in appendix E.

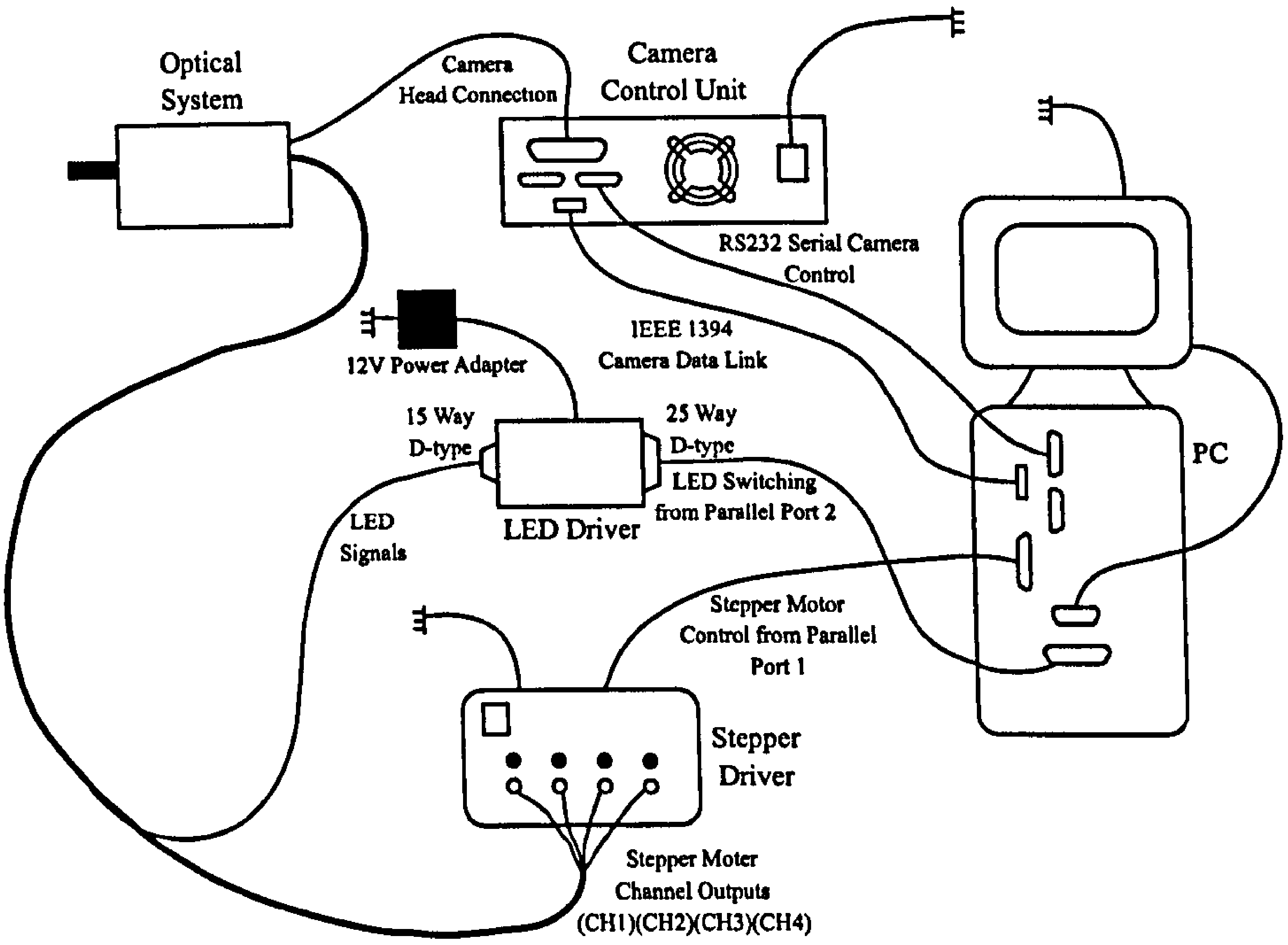

Figure 5.7: *System schematic showing the components required for system automation.*

5.4 System Mechanics

A major part of the system development has been concerned with the design and fabrication of the mounts used to select and rotate the required optical component. Shown in figure 5.8 is the motor driven rotary mount, made to select the required LED. Mounted along with each LED is the input linear polarizer (LP1) aligned to be vertically polarizing when the source is switched into the selected position. These were separate for each source as different components were required for the visible and NIR wavelengths.

Figure 5.9 shows the developed mount used to select the quarter wave plate appropriate to the input illumination and orientate it to the correct angle. This requires two channels from the stepper motor driver.

To provide the discrimination of linear polarization states on the output, four different polarizers were used: two for the visible wavelengths and two for the NIR, with co-polar and cross-polar orientations for each band. The mounting of these components can be seen

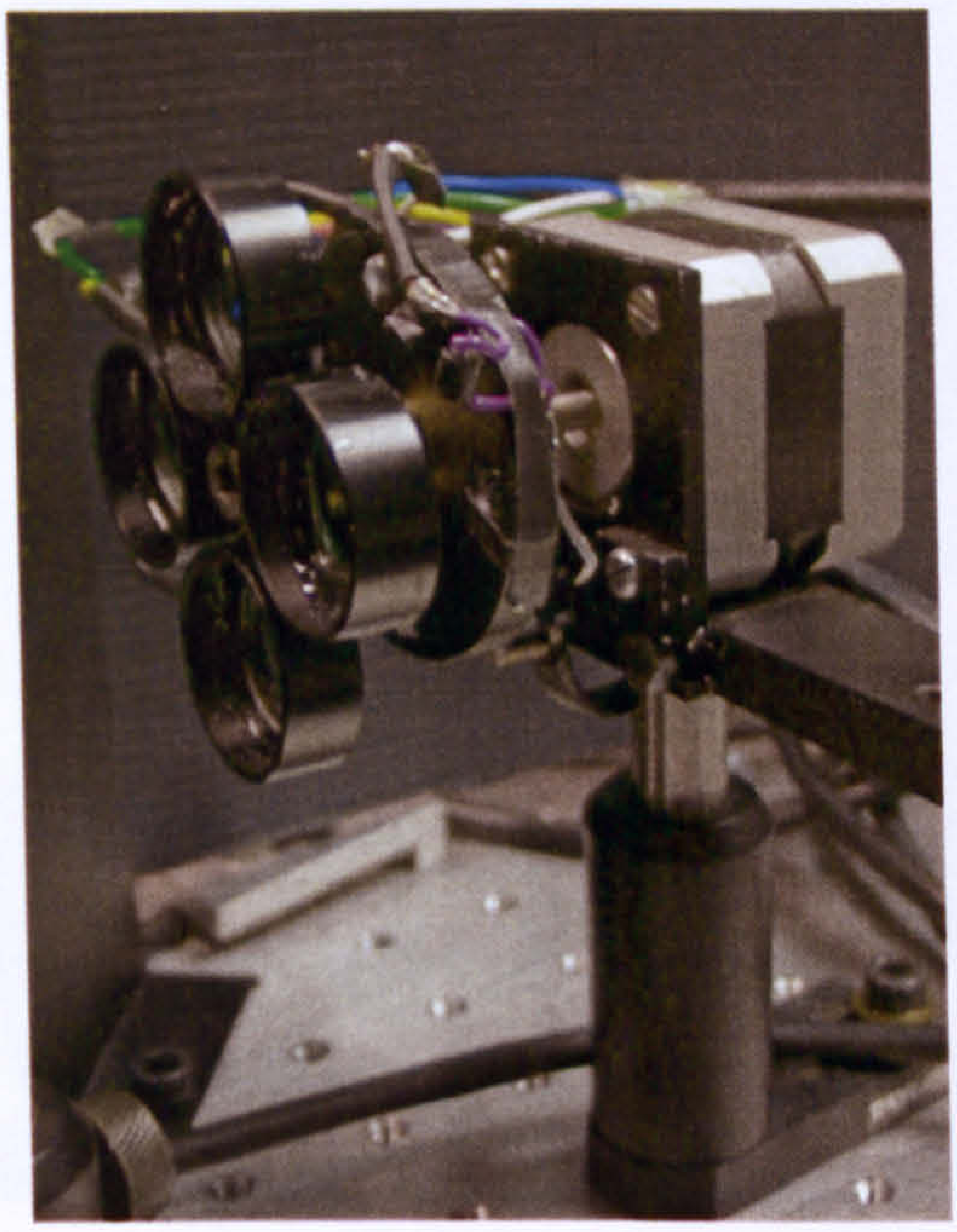

Figure 5.8: *Stepper motor controlled rotary mount for the four sources and input linear polarizers.*

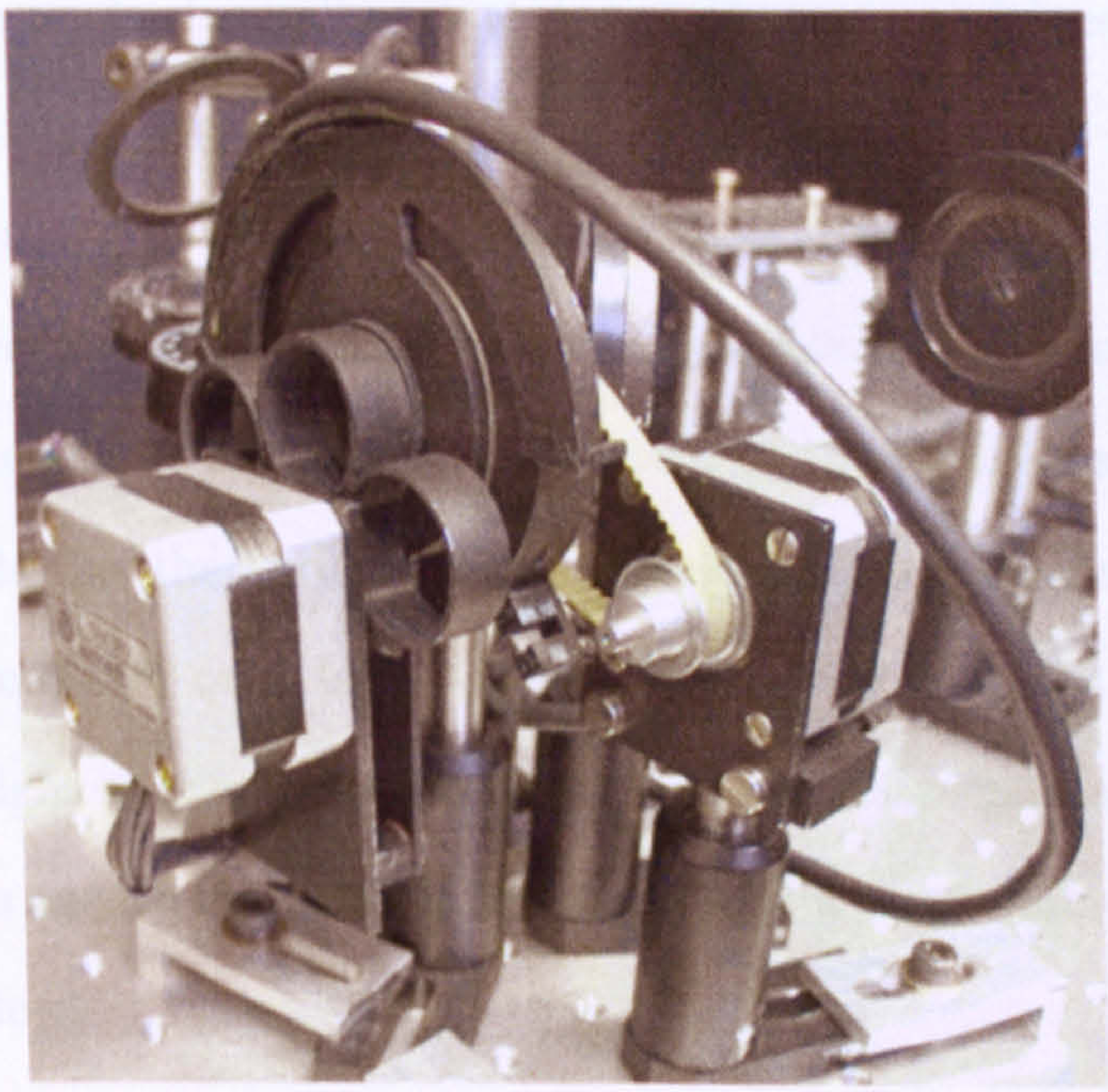

Figure 5.9: *Dual-stepper motor controlled QWP mount allowing both component selection and rotation.*

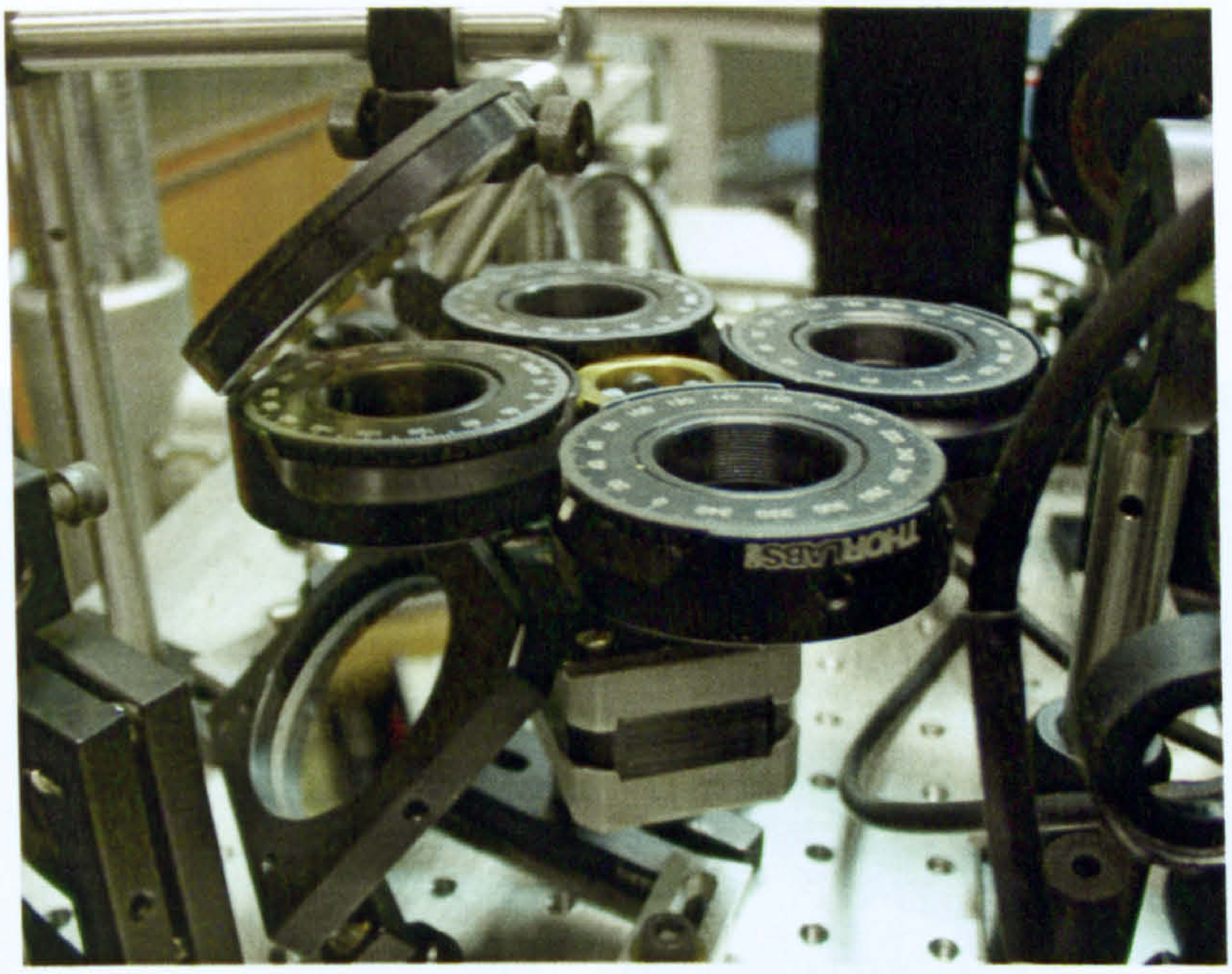

Figure 5.10: *Stepper motor controlled rotary mount allowing selection of the pre-aligned output linear polarizers.*

in figure 5.10. These are horizontally orientated as they are positioned directly following the downward reflecting beamsplitter (BS2) as pictured. The full arrangement of the optical system with these mounts in position can be seen in figure 5.11.

To enable the system to be used as easily as possible by the clinician it is necessary to allow flexibility in the positioning of the system to image lesions on various areas of the body. To provide this the optical system was assembled on a metal plate (400mm × 740mm) and then mounted on a large adjustable stand as pictured in figure 5.12. This stand allows the height of the system to be adjusted mechanically along with the tilting of the instrument to ensure that the patient can adopt a comfortable position during the examination procedure.

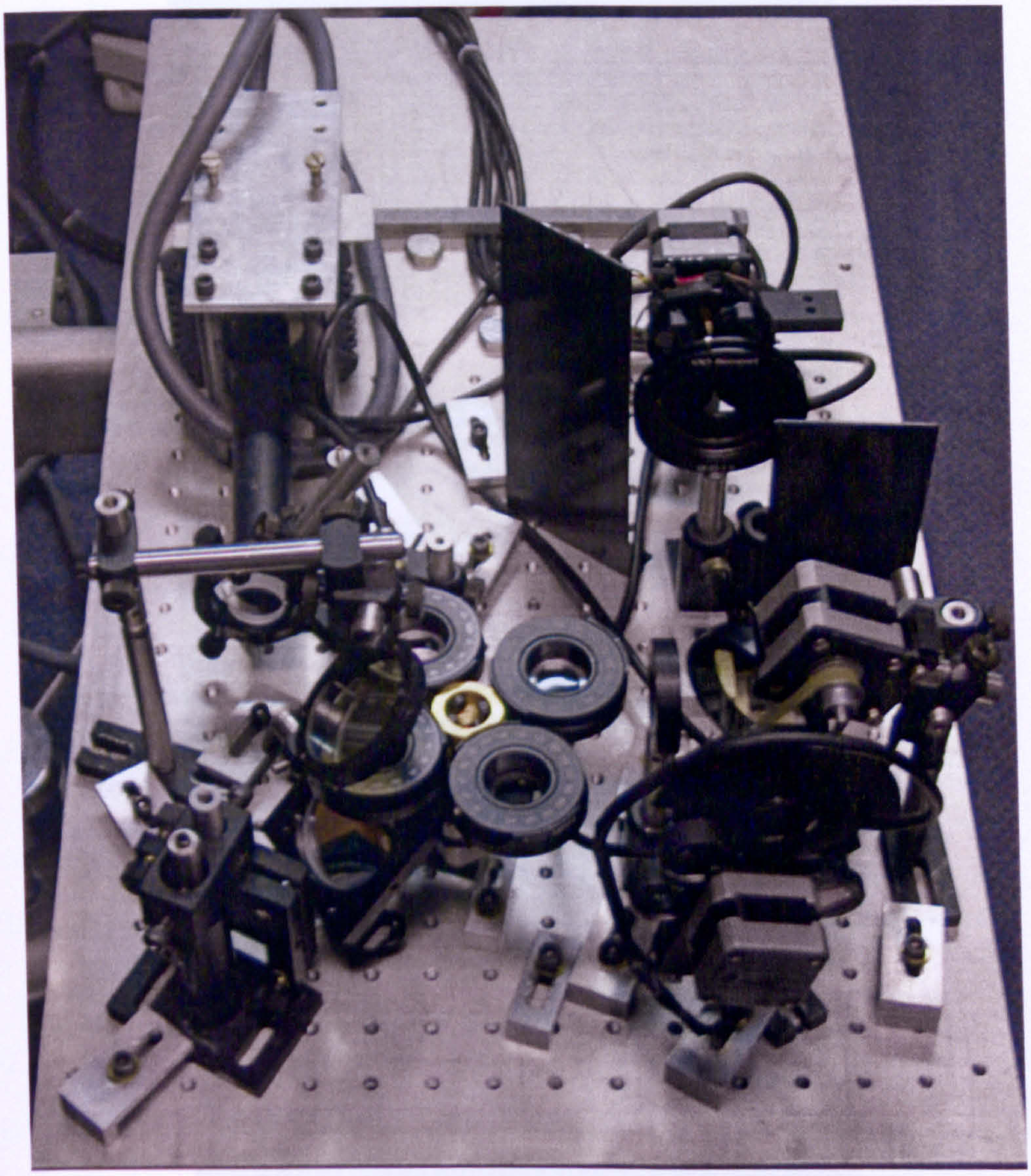

Figure 5.11: *The automated optical system.*

Figure 5.12: *The optical system mounted on an adjustable stand for flexible system positioning.*

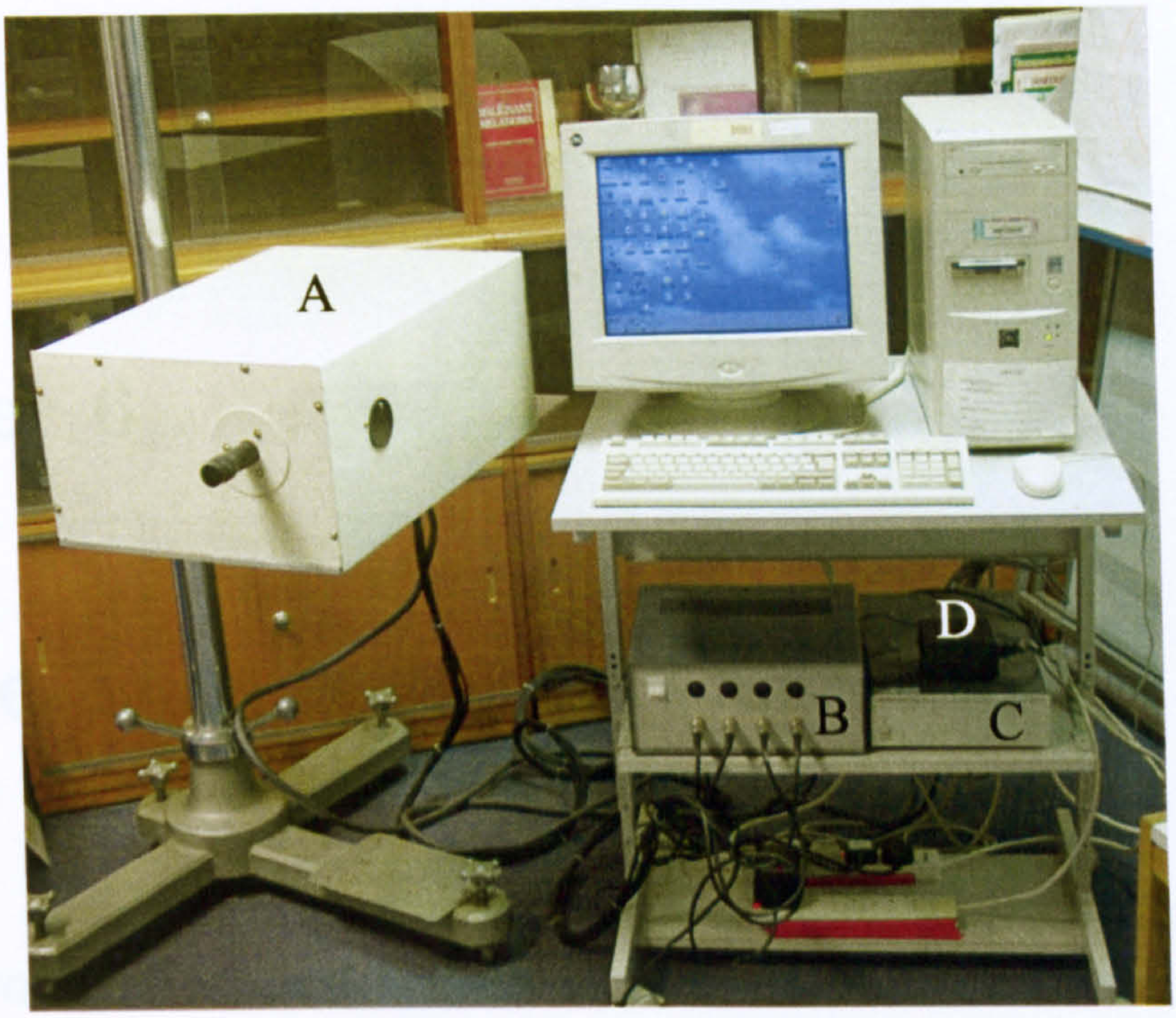

Figure 5.13: *The full developed system including A) the optical system, B) stepper motor control electronics, C) CCD camera control hardware and D) LED switching electronics.*

5.5 Summary

Presented in this chapter has been the proposed system for application in a dermatology clinic. This has included a redesign of the laboratory based system to allow more flexible on-axis detection, selection of multiple illuminating wavelengths to provide sensitivity to different chromophores and tissue volumes, full automation of the system to allow the use of standard optical components and practical considerations required for implementation in a clinic. Ergonomic and practical issues have also been addressed resulting in the development of the full system which is pictured in figure 5.13.

Following the development of the system outlined here ethical approval has been sought and obtained for testing of the prototype system in the Dermatology Clinic at the Queen's Medical Centre, Nottingham. A presentation of some preliminary tissue results to demonstrate the technique can be found in the following chapter.

Chapter 6

Tissue Images

6.1 Introduction

Presented in this chapter are the preliminary tissue images which have been recorded from a benign melanocytic lesion using the prototype system described in the previous chapter. The aim of this chapter is to illustrate further the effectiveness of the extraction of circular polarization maintaining light techniques to localise sub-surface regions of tissue. This is with a view to showing the improvement of applying the polarization discrimination techniques proposed in this study over conventional surface reflection and multiple scatter removal techniques as discussed in section 4.3. This work also aims to illustrate the sensitivity of the different wavelength sources to different optical absorbers within the tissue along with long and short term improvements which can be made to the system.

6.2 Improvement on Current Techniques

Two techniques are commonly used to remove the surface reflections from tissue samples. The first technique considered involves the removal of surface reflections through the application of a flat glass plate and matching fluid to the surface of the skin. The surface of the glass plate can then be used to direct the reflected light away from the detection arm of the imaging system. Polarization channel subtraction using linearly polarized light is then frequently applied to provide removal of multiple scatter[50, 51, 85]. Improvement on this technique is shown here using the extraction of circularly polarization maintaining light.

To mimic the results obtained using the above technique, a glass plate and matching fluid can be applied to the surface of an *in-vivo* benign lesion for imaging using the prototype system. Due to the design of the imaging system employing on-axis detection (figure 5.1), the glass plate must be slightly angled away from the plane perpendicular to the optical axis so as to not reflect directly into the imaging arm. Illumination at this stage is only supplied at the 470nm wavelength to provide high levels of contrast to melanin. The four polarization images recorded are shown in figure 6.1.

It can be seen from these images that the glare due to surface reflections from the tissue is largely removed from the image as they are reflected away from the detection arm. These would otherwise be detected in polarization channels 1 and 4 as indicated in table 4.6. It is clear however, that there are still contributions from the surface texture of the skin. Channels 2 and 3 provide images free from surface reflections, but all of the images provide a low resolution representation of the pigmented region due to the large contribution from multiply scattered light.

To remove the contribution due to the poorly confined multiple scatter, the linear polarization maintaining light can be extracted by subtraction of channels 1 and 2 (section 3.6). The result of this subtraction using the images in figure 6.1 is shown in figure 6.2. It can be seen from this that the definition of the borders of the pigmented region has improved from that observed in the raw polarization images. Still observable on this image however is the textured surface contribution which greatly distorts the underlying region of interest.

To compare this result obtained using existing techniques with those obtained using the circular polarization maintaining light, images were recorded of the same lesion without

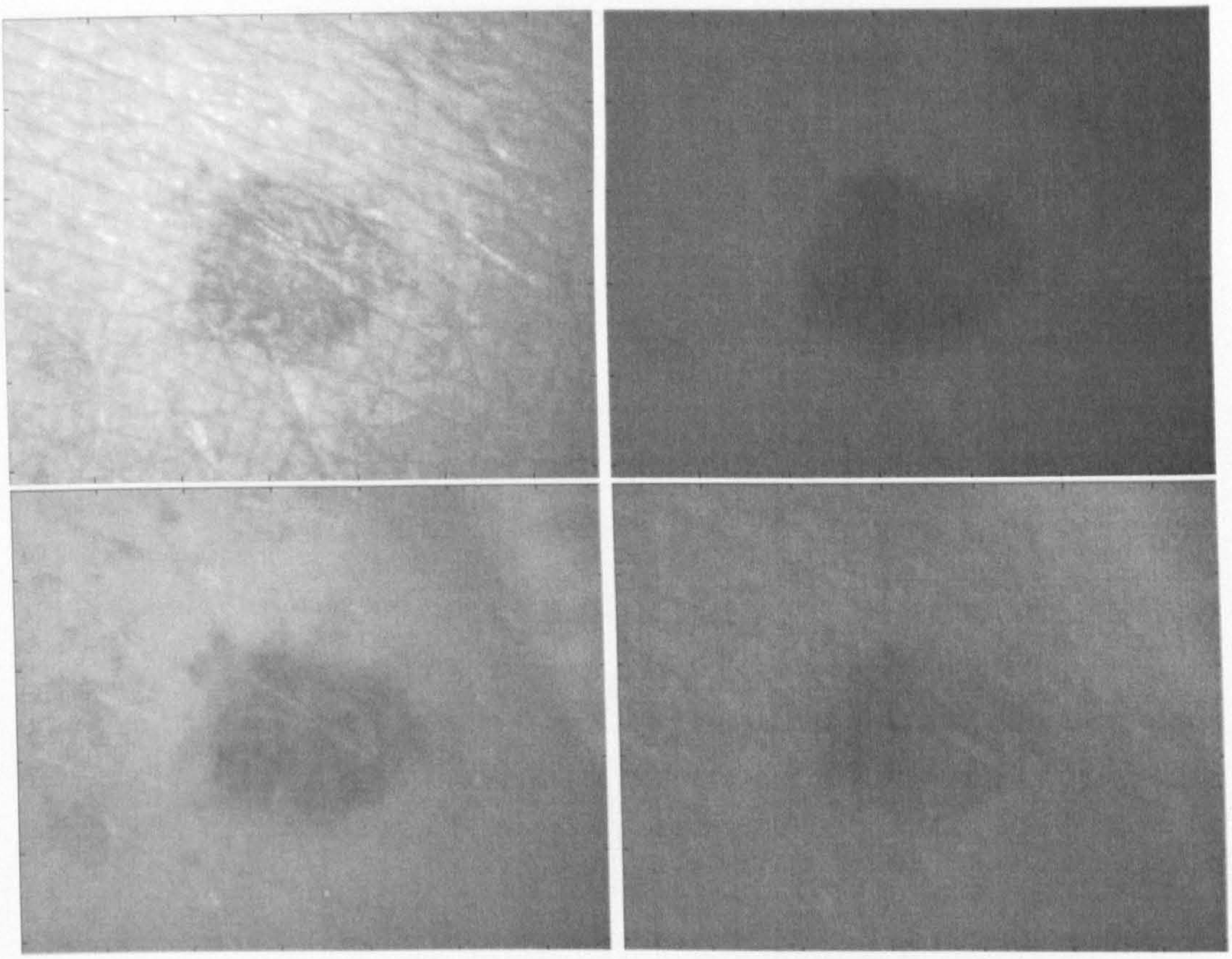

Figure 6.1: *Lesion images recorded with* $\lambda = 470nm$ *channel 1 (top left), channel 2 (top right), channel 3 (bottom left) and channel 4 (bottom right) using a flat glass plate and matching fluid to reduce surface reflections.*

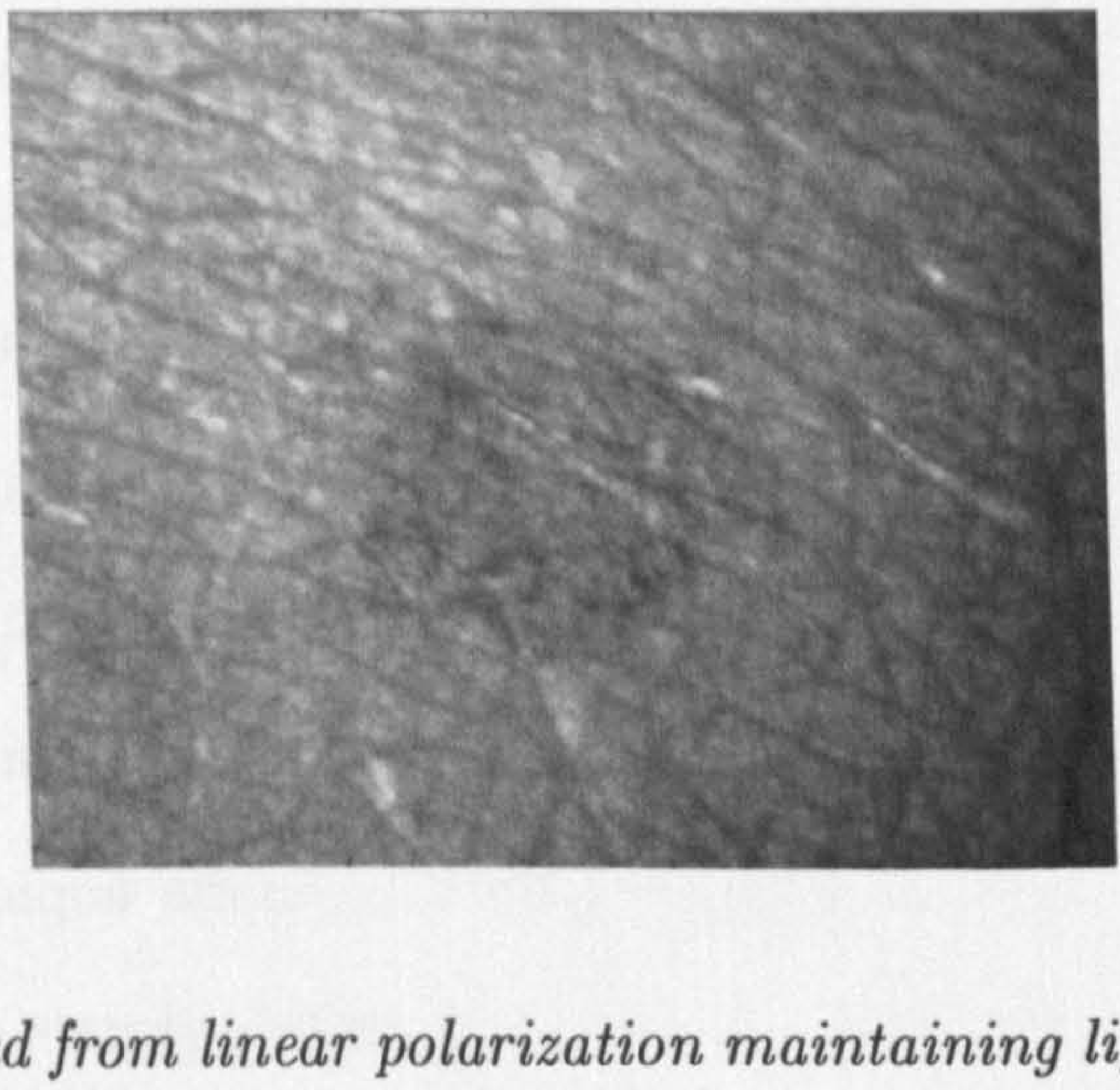

Figure 6.2: *Image formed from linear polarization maintaining light using a flat glass plate and matching fluid to reduce surface reflections.*

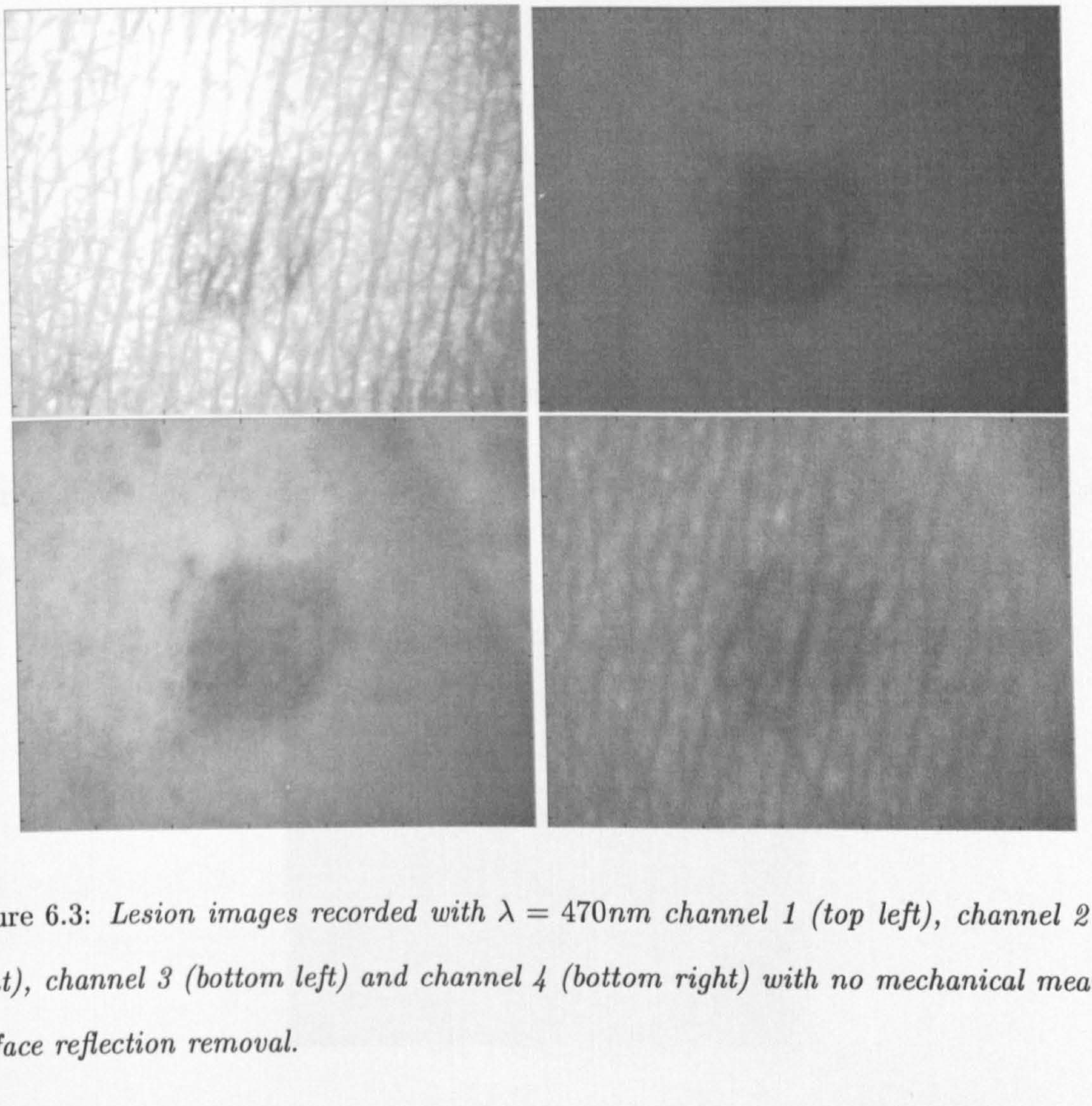

Figure 6.3: *Lesion images recorded with* $\lambda = 470nm$ *channel 1 (top left), channel 2 (top right), channel 3 (bottom left) and channel 4 (bottom right) with no mechanical means of surface reflection removal.*

the glass plate and matching fluid. The raw polarization images recorded in the four channels in this arrangement are shown in figure 6.3.

It can be seen from these images that the surface reflections observed in channels 1 and 4 are much larger than those observed in figure 6.1. These levels of surface reflections would render the use of these images useless as can be seen from the attempts to extract the polarization maintaining linearly polarized light in figure 6.4.

An alternative technique which is widely applied to remove the contribution of the surface reflections is to simply detect the linearly polarized channel orthogonal to the plane of illumination (channel 2), as mentioned above. The result of such discrimination

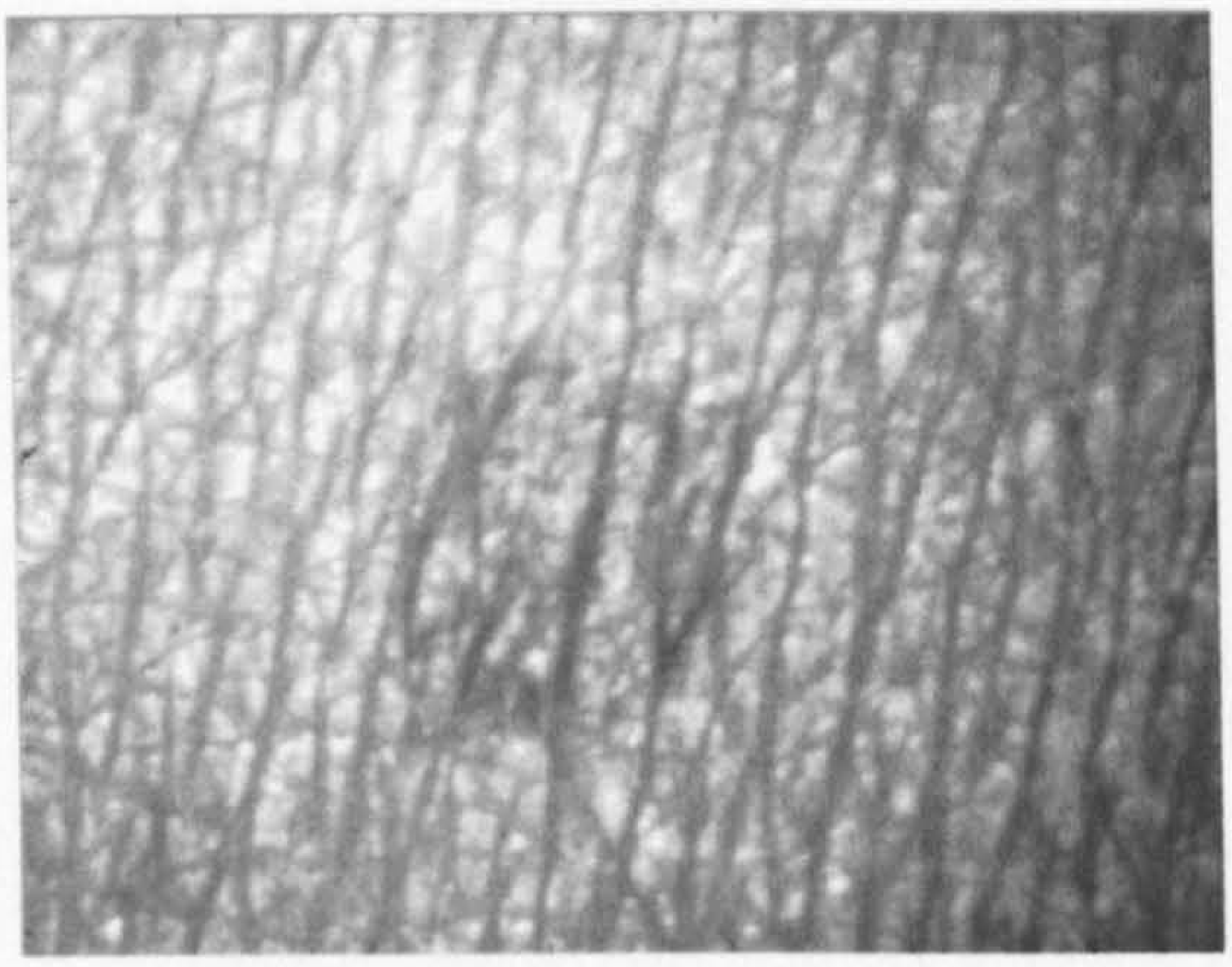

Figure 6.4: *Image formed from linear polarization maintaining light with no means of surface reflection removal.*

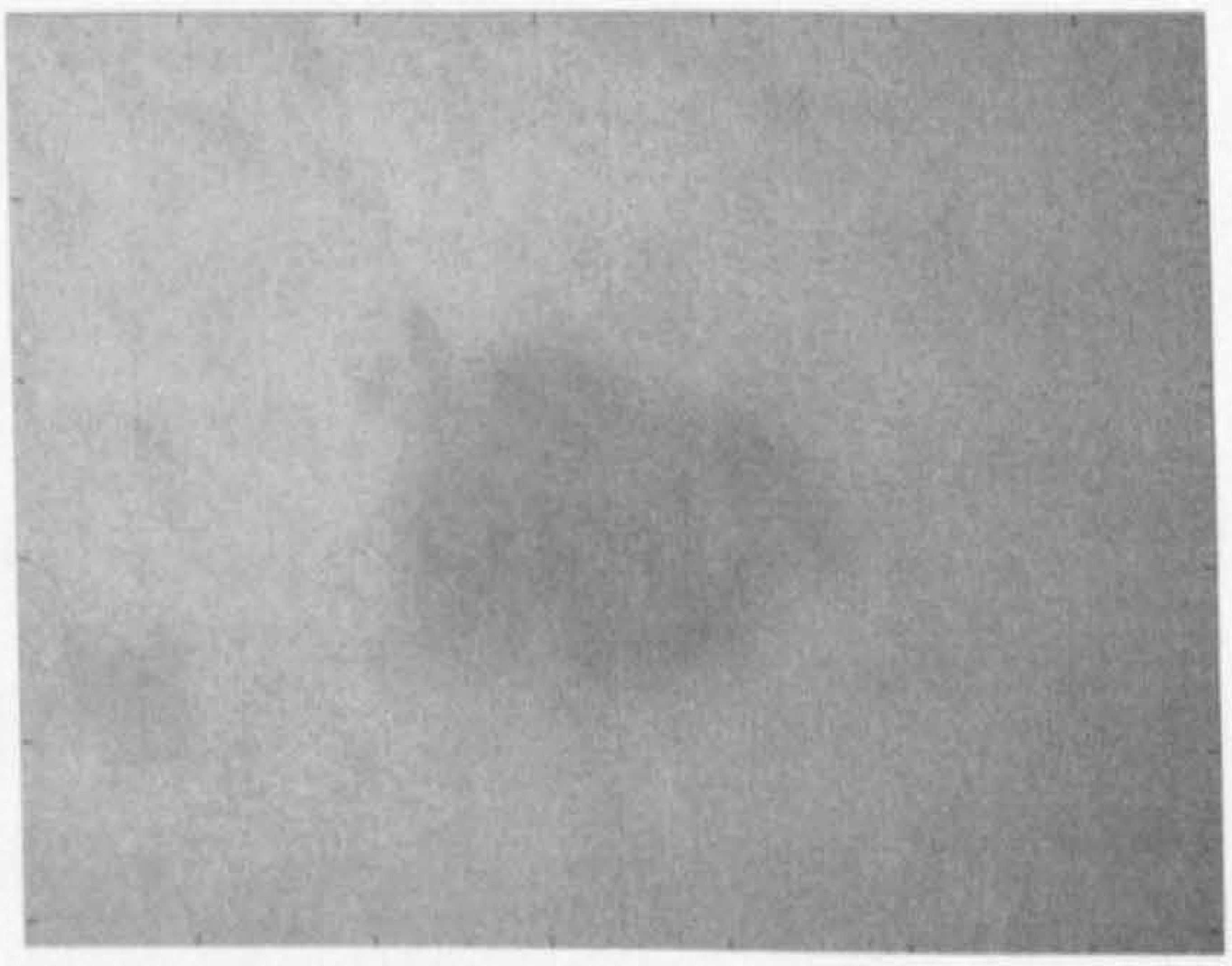

Figure 6.5: *Image resultant from multiple scatter with* $\lambda = 470nm$.

results in the image shown in figure 6.5, which is repeat of that presented in figure 6.3 with gain applied.

It can be seen from this image that the pigmented region can be viewed without distortion from surface contributions. The short fall of this discrimination technique is that the resolution is poor due to the poorly defined paths of propagation of multiply scattered light. Extraction of the circular polarization maintaining light seeks to remove all contributions from the surface of the skin (therefore improving on figure 6.2) whilst maintaining good resolution due to the removal of multiply scattered light resulting in

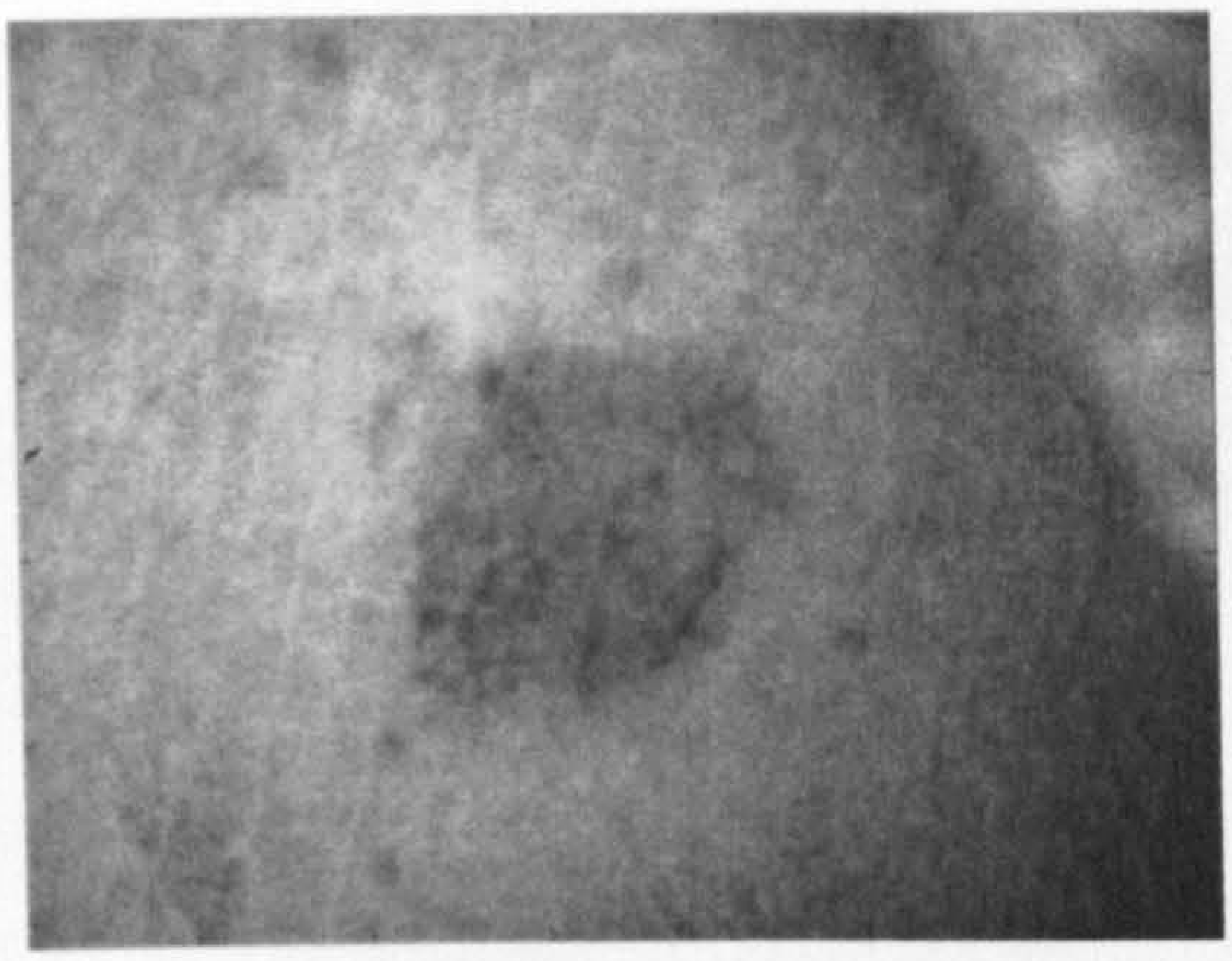

Figure 6.6: *Image formed by circular polarization maintaining light with no mechanical means of surface reflection removal.*

a sub-surface localised image (improving on figure 6.5). To achieve this, the circular polarization maintaining image is formed by performing the subtraction of the images recorded in polarization channels 3 and 2. The result is shown in figure 6.6.

It can be seen that this technique for imaging sub-surface regions of tissue, free from surface reflections, outperforms those generated using existing techniques. The improved resolution provides the ability to resolve many of the small spots of melanin surrounding the main area of pigmentation. Varying levels of melanin can also be observed within the region of pigmentation.

During the automated analysis of pigmented lesions, tissue images undergo numerical processing to attempt extraction of information concerning its properties (see section 2.4). Improvements in image quality will allow more accurate and efficient application of such techniques especially those concerned with border regularity which has proved to be a good diagnostic indicator. It can be seen from this image that the definitions of the margins of the lesion are vastly improved over the image recorded in the cross-polar linearly polarized image due to the improved resolution. Compared to figure 6.2 improvement to these techniques will be provided as due to the absence of surface texture would obscure the observation and hence automated definition of the margins of pigmentation.

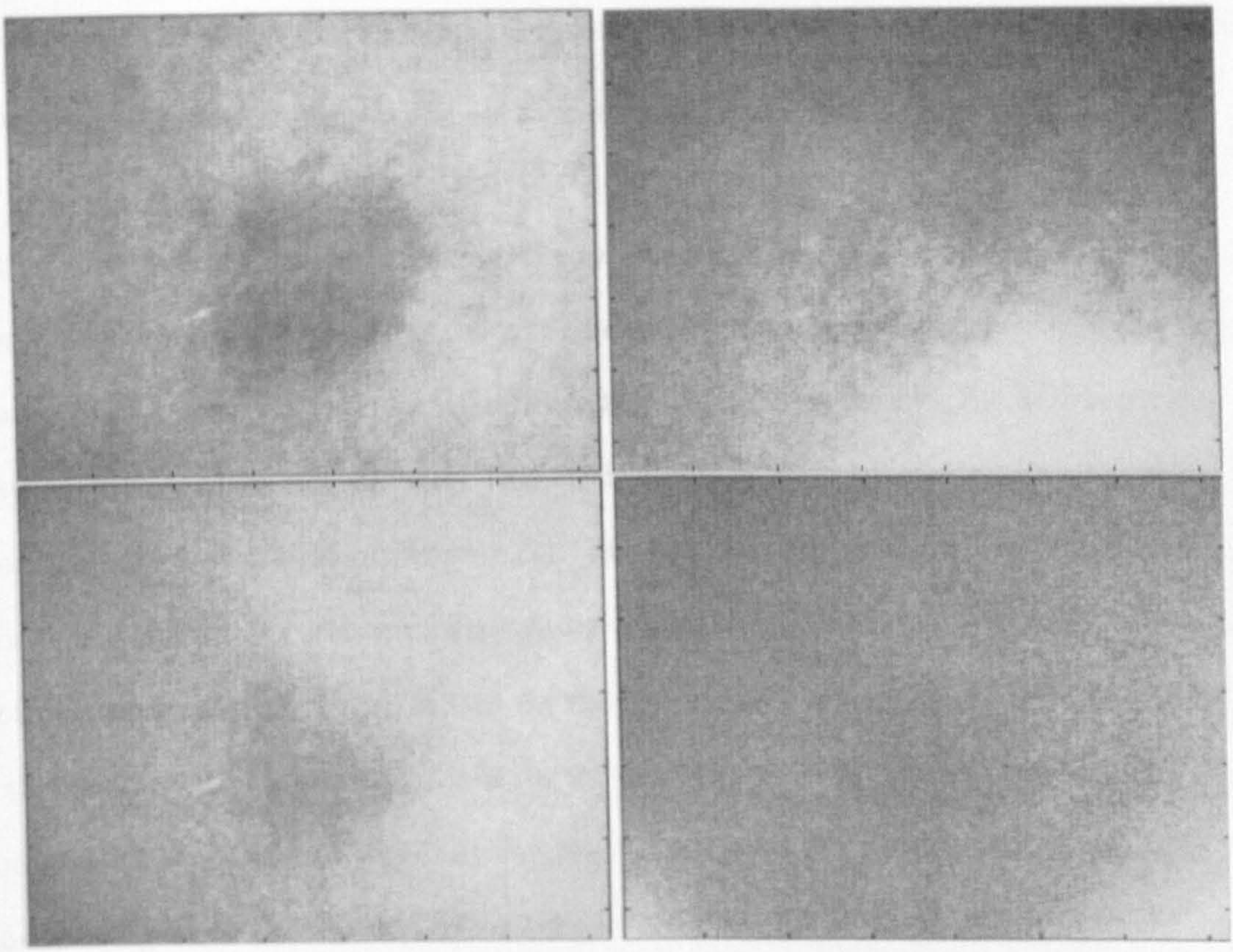

Figure 6.7: *Lesion images detected in polarization channel 3 with* $\lambda = 470nm$ *(top left), 574nm (top right), 660nm (bottom left) and 865nm (bottom right) illumination.*

6.3 Multi-Spectral Images

To explore the sensitivity of the different wavelengths to the absorbers within tissue samples for which they were designed, as described in section 5.2.1, the full four wavelength prototype was used to image the same lesion as considered in the previous section.

Shown in figure 6.7 are the images detected in channel 3 using 470nm, 574nm, 660nm and 865nm illumination.

After consultation with a clinician, it can be assumed for the purposes of the analysis here, that the absorption present in the images is due to melanin in the epidermis and uniformly distributed hæmoglobin in the dermis. These images are recorded using eight-by-eight pixel binning on the CCD camera to reduce the required exposure times.

This reduces the time required for examination and therefore, reduces problems due to movement artifacts.

It is apparent from figure 6.7 that the image recorded using 470nm wavelength illumination provides high sensitivity to the epidermal melanin, as discussed in the previous section. This should allow enhanced processing of border regularity and asymmetry as discussed in the previous section. The illumination at 574nm is intended to provide sensitivity to blood as it can be seen that this wavelength corresponds to a peak in the hæmoglobin spectrum shown in figure 5.3. Before reproduction the quality of this image is poor due to the highly non-uniform nature of the illumination which will be discussed in the following section. However, it can be seen from the more central regions of the image that the contrast to the melanin is reduced in comparison to the image recorded at the 470nm wavelength. The absorption spectrum for an epidermal layer containing melanin is shown in figure 5.2. It is difficult to demonstrate the sensitivity of this wavelength to hæmoglobin due to its expected uniformity across the imaged area. However, an indicator that the images recorded using 574nm and 660nm wavelength illumination are sensitive to hæmoglobin and melanin respectively can be provided by comparison of the two images. It can be seen that the sensitivity to the pigmented region for $\lambda = 660$nm is greater than for $\lambda = 574$nm. The absorption coefficient for melanin at $\lambda = 574$nm is 1.5 times that for 660nm light. Therefore, it can be assumed the high absorption at 574nm is due to another absorber, namely hæmoglobin. Illumination at 660nm corresponds to a trough in the hæmoglobin spectrum and therefore some sensitivity appears to be available to areas containing melanin. Until further testing is performed, as discussed below, it is unclear to what depth within the tissue this sensitivity is produced.

It is observable from the image recorded using 865nm that the lack of absorption due to melanin and hæmoglobin in this range results in an image clear from almost all of the pigmented features. Due to the lack of dermal melanin and, therefore collagen perturbation, the variation across the region appears to be solely down to the non-uniform illumination.

To confirm the sensitivity and performance of the system at different wavelengths the subtraction of polarization states is required at each wavelength. The images reported above 6.7 do not provide reliable information in the subtracted channels due to problems with the non-uniform illumination. Removal of this factor is discussed in the next section. Phantom studies are also required to confirm the performance of the subtraction for different wavelengths in the presence of an absorber with specific properties sensitive to that wavelength. However, once testing of the system begins in the clinic, malignant lesions will be imaged followed by excision to determine their histopathology. Comparison of this with the *in-vivo* images recorded pre-excision will allow assessment of what information is available from the system.

6.4 Future System Improvements

Future work concerned with improvements to the system should seek to improve the the image quality provided. It has been shown that the image at $\lambda = 574$nm is influenced by the variation of the illumination across the surface of the tissue. Therefore, a modification to improve the uniformity of illumination should be investigated. One possibility involves coupling the LEDs into a fibre and collimation being provided by an aspherical lens.

A more fundamental change to improve the performance of the technique involves detection using a recently developed modulated light camera[128] rather than CCD detection. It can be observed from the results presented throughout this study that the levels of light extracted through polarization channel subtraction are low and are therefore more vulnerable to noise. Modulation of the polarization state of illumination or detection can be performed, using either mechanical rotation of a polarization component[81] or use of photoelastic modulators. This would provide a varying intensity polarization maintaining component on top of the constant intensity multiple scattered background. This allows lock-in detection of the modulated component using the on-chip processing and will allow all quantisation levels to be assigned to this component on digitisation. The current device is only 64 × 64 pixels over a 3.0mm × 2.5mm area, however the solution has the potential to be scaled to larger detector arrays.

6.5 Summary

It has been shown conclusively in this chapter that the extraction of circularly polarized light which has maintained its initial state of polarization due to a series of forward scattering events provides an improvement over current techniques. Compared to the case of illumination and detection in orthogonal linearly polarized states the developed technique has shown to provide enhanced resolution when imaging the superficial regions of interest. Existing techniques applied to remove the contribution due to this large multiple scatter contribution use linearly polarized light image subtraction coupled with a flat glass plate and matching fluid to remove the surface reflections. The polarization subtraction technique proposed here has be seen to provide much better rejection of surface features allowing clearer observation of the region of interest and opening up the potential for more effective image processing.

The sensitivity of the different wavelengths of light used to illuminate the sample to the expected tissue absorbers has also been indicated from a preliminary result however, further confirmation is required. Also presented has been possible improvements which can be made to the system to enhance the noise performance and image quality.

Chapter 7

Feasibility of Numerical Inversion

7.1 Introduction

Up to this point the discussion has been concerned with the behaviour of polarized light under scattering conditions and its use to achieve sensitivity to either different depths of sample in microsphere suspensions or different sources of backscattered light in tissue imaging. To fully achieve the aims of this study it is necessary to consider the ability to determine the medium's optical properties. The proposed technique is to analyse the intensity detected in different polarization channels using the system proposed in chapter 5. These optical properties are linked to the physical properties of the sample and therefore their determination is required to allow evaluation of the tissue's histology.

The proposed method to perform the inversion from detected polarization intensities to the optical properties of the examined medium is based around reference to data produced from numerical simulations. A data set can be produced containing results using varying sample properties for use, in the first instance, as a 'look-up' table. The main aim of this chapter is to examine the appropriateness of the proposed detection regime to determine sample properties. This is achieved by assessing the condition of the simulated data space in terms of its ability to deduce a unique solution from the detected measurables under ideal conditions (in the absence of noise). Once this is performed, refinements to the developed algorithms to achieve more accurate inversion from detected system measurables to sample parameters are presented. This is along with any approximations and assumptions which may be required to improve the performance of the processing.

Before this, the structure of the samples under examination is presented, along with the reasoning behind the selection of the variable sample parameters. Alongside this is an outline of the simulations which must be performed to allow construction of the data space for use in the inversion process.

7.2 Sample Structures

Before simulating the required data set, it is necessary to define the variable parameters that are to be extracted by the inversion process. For the purposes of this evaluation, the skin will once again be modelled as a two layer structure; the top layer representing the epidermis and the lower, the dermis. From this model there are four parameters which are considered as being of relevance to analysis of skin tissue for diagnostic purposes. The general structure of the samples, marked with the variable parameters, is given in figure 7.1.

The selected inversion parameters are top layer thickness, t, bottom layer scattering coefficient, μ_{s2}, and top and bottom layer absorption coefficients, μ_{a1} and μ_{a2} respectively. The reasons behind the selection of these variables are presented in sections 7.3.1 and 7.3.2. It is assumed by this model that the scattering concentration of the upper (epidermal) layer is constant but finite, as is the anisotropy factor which is common to both layers for a given wavelength.

7.3 Sample Parameter Considerations

To produce the look-up table it is necessary to perform simulations of samples over a range of the variable parameters. To determine the range of parameter variation, approx-

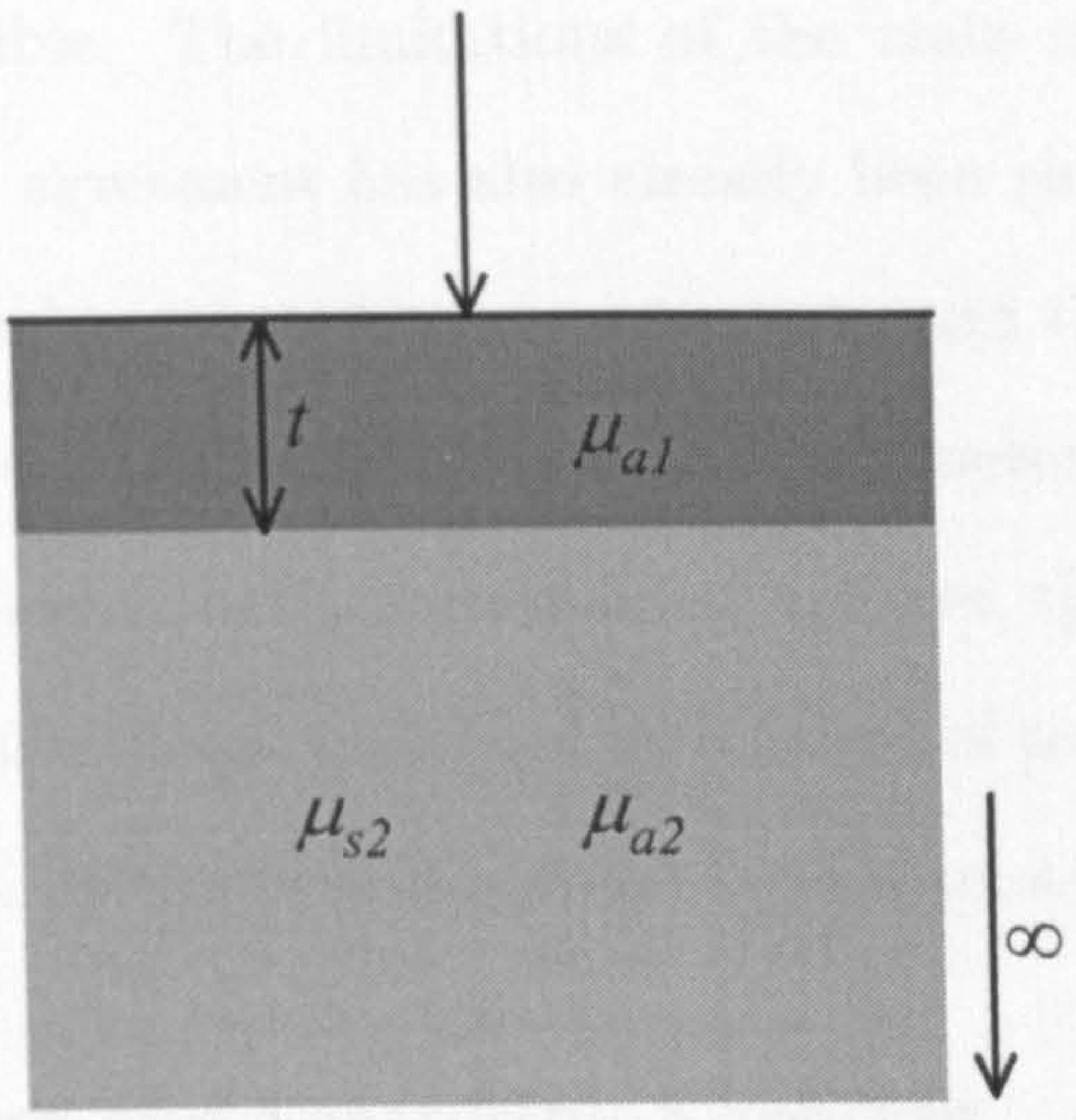

Figure 7.1: *Proposed sample structure indicating the variable parameters to be extracted by the inversion process.* μ_{s1} *is constant.*

imation to parameters occurring in tissue samples is required to ensure the results are as relevant and representative as possible. However, the initial experiments performed to test the performance of different inversion algorithms will be performed on layered scattering phantoms with known properties. Therefore, the simulations performed should correspond directly to the proposed methods of phantom construction but, as the following sections discuss, are heavily based around skin tissue properties.

Two methods of phantom production have been investigated here. The first involves forming solid tissue phantoms composed of polystyrene microspheres suspended in glycol methacrylate resin. This allows easy construction of multiple layered media, which can be machined as required. The construction of such samples is discussed in more detail in appendix D. The second method for sample production is the suspension of polystyrene microspheres in water, contained within a two layer tank. The method selected on which to base the simulations and therefore experimental inversion beyond the scope of this study is microsphere suspension in water rather than resin. This method was selected as the scattering and absorption properties of the water based microsphere solutions are more stable and reproducible. The limitations of the resin samples are discussed further in appendix D. Good agreement has also already been shown in chapter 4 between experimental results with microsphere-water suspensions and the Monte Carlo model.

To approximate as closely as possible to tissue parameters whilst, maintaining the producibility and reducing errors in the formation of samples, the approximate dimensions and optical properties for skin tissue are scaled by a factor of ten to provide the properties required for the phantoms. Selection of the simulated parameter values is presented here.

7.3.1 Layer Thickness and Scattering Selection

The thickness of the epidermis varies depending on the selected skin site[7] and this forms part of the reason for its selection as a parameter for inversion. The thickness of this layer is generally of the order of 100μm[7] and therefore the selected range of variation is between 40μm and 200μm, which corresponds to a phantom top layer thickness range of 0.4mm to 2mm.

The second parameter to be considered is the bottom layer scattering coefficient. This value has been selected as a variable parameter due to the event of metastasis which occurs in more advanced cases of malignant melanoma, as discussed in section 1.3.2. The discussion of skin histology given in section 1.3.1 stated that melanocytes are generally confined to the epidermis. However, in advanced malignant melanoma these can penetrate the epidermal/dermal boundary and perturb the underlying collagen, which forms the main source of scattering in skin tissue. This may then lead to a local variation in the scattering properties of the dermis. Standard values quoted for the MFP in the dermis are in the order of 100μm at $\lambda = 633$nm[5], which corresponds to $\mu_{s2} = 10\text{mm}^{-1}$ at 633nm. Therefore, the simulated data space uses μ_{s2} values between 1mm^{-1} and 3mm^{-1} (10mm^{-1} and 30mm^{-1} in tissue). It is worth noting at this stage that, due to the wavelength dependence of μ_{s2}, it is more appropriate to refer to the levels of scattering as scatterers per unit volume, N, and to use this value as the inversion parameter. However, μ_{s2} at

Wavelength, λ (nm)	Anisotropy Factor, g	Scattering Coefficient, μ_{s1} (mm^{-1})
470	0.8023	0.571
574	0.8844	0.844
660	0.9155	1.079
865	0.9347	1.203

Table 7.1: *Variation of anisotropy factor and top layer scattering coefficient with illuminating wavelength.*

λ = 633nm is used here due to the more manageable numerical values. Table 7.1 provides an indication of the extent to which the scattering coefficient and anisotropy factor vary between the selected illuminating wavelengths as discussed in section 1.2.

The value of top layer scattering is of less interest in a clinical context and is therefore not varied here. However, its value will affect the variation of the other parameters. Holding this value constant reduces the problem from five variables to four and although this may affect the final accuracy it is a valid assumption for this initial consideration. The range of scattering coefficients quoted for this layer is greatly variable, but it is universally agreed that the levels of scattering are low (some even set to zero[17]) and therefore this value is set to 1.0mm^{-1} for 633nm illumination.

7.3.2 Layer Absorption Selection

The presence of optical absorption in tissue samples is clearly important as the variation of pigmentation can be great, not only between different skin samples, but across a single pigmented lesion and may hold the key to successful diagnosis. When considering the levels of absorption it is necessary to analyse the source of the absorption in the different layers.

Considering first the epidermis, it is known that the main absorber is melanin[4].

Discussed in section 1.3.1, present in the lower layers of the epidermis are melanocytes responsible for the production of melanin, resulting in skin pigmentation. Stated previously (section 5.2.1), the degree of pigmentation in a region of tissue is determined by the value of V_{fmepi}, which represents the number of melanosomes contained within the melanocytes. The number of melanocytes has low variability irrespective of skin tone. For lightly pigmented skin, the volume fraction in the epidermis, V_{fmepi}, can be as low as 1% and up to around 45% for very dark skin. Due to the wavelength dependence of the absorption coefficient it is more appropriate to invert the levels of absorption into V_{fmepi}, as this is a physical parameter and is therefore wavelength insensitive.

Consideration of the absorption in the dermis will determine the values of μ_{a2} used in the model. In healthy tissue the main absorber is blood or more specifically hæmoglobin[129]. The absorption spectra for oxy- and deoxy-hæmoglobin have been given in figure 5.3. In the same way that a volume fraction can be defined to indicate melanin levels in the epidermis, an equivalent, V_{fhae}, can be defined for blood saturation in the dermis and can reach up to 15%.

The levels of absorption in the dermis are complicated here due to the possibility of melanin appearing in the papillary dermis due to metastasis in cancerous tissue. Such an occurrence is accounted for in the range of possible bottom layer absorption values with levels of dermal melanin, V_{fmder}, varying between 2% and 30%.

A summary of the above information concerning the selected absorption coefficients, along with the values of t and μ_{s2} discussed in section 7.3.1, is given in table 7.2 for clarity. This table appears to indicate that the number of parameters which are to be extracted is five (t, N, V_{fmepi}, V_{fhae} and V_{fmder}). However, the two components which define μ_{a2} can be treated as one. This is due to an approximation being applied that if the determined bottom layer absorption is above a given threshold the absorption is dominated by dermal melanin rather than hæmoglobin. This thresholding forms the first assumption that is made concerning the sample properties.

Optical Property	Inversion Parameter	Lower Limit	Upper Limit	Interval	Data Points
-	t (mm)	0.4	2.0	0.4	5
μ_{s2}	N (mm^{-3}) or μ_{s2}(633nm) (mm^{-1})	185768 or 1.0	557304 or 3.0	74307 or 0.4	6
μ_{a1}	V_{fmepi}	1%	45%	1%	45
μ_{a2}	V_{fhae}	0.5%	15%	0.5%	30
	V_{fmder}	0%	0%	-	
	V_{fhae}	5%	5%	-	15
	V_{fmder}	2%	30%	2%	

Table 7.2: *Summary of simulated parameter values.*

The reasons behind the selection of the quoted intervals, and therefore the number of simulated data points along each dimension, is discussed in section 7.4.

Using the absorption spectra for melanin and hæmoglobin, table 7.3 provides a conversion from the defined physical properties (V_{fmepi}, V_{fhae} and V_{fmder}) to the optical properties (μ_{a1} and μ_{a2}) used for simulation.

7.4 Simulation of the Data Space

The disadvantage of the use of Monte Carlo modelling is the extensive time required to simulate the number of photons required to achieve an acceptable SNR. However, when performing simulations to represent the variation of the four selected parameters only the top layer thickness, t, and the bottom layer scattering coefficient, μ_{s2}, need to be adjusted. This is because the variation of absorption coefficients can be performed post-simulation using Lambert-Beer's law (equation 1.3) providing the path length in each layer is tracked,

Wavelength (nm)	Parameter	Lower Limit (mm^{-1})	Upper Limit (mm^{-1})	Interval (mm^{-1})
-	V_{fmepi}	1%	40%	1%
	V_{fhae} and V_{fmder}	0.5% and 0%	15.0% and 0%	0.5% and 0%
	V_{fhae} and V_{fmder}	5.0% and 2.0%	5.0% and 30.0%	0% and 2.0%
470	μ_{a1}	9.301×10^{-2}	3.761	8.336×10^{-2}
	μ_{a2}	1.610×10^{-2}	2.032×10^{-1}	6.452×10^{-3}
	μ_{a2}	2.505×10^{-1}	2.585	1.667×10^{-1}
574	μ_{a1}	4.679×10^{-2}	1.932	4.285×10^{-2}
	μ_{a2}	1.392×10^{-2}	3.033×10^{-1}	9.980×10^{-3}
	μ_{a2}	1.934×10^{-1}	1.393	8.570×10^{-2}
660	μ_{a1}	2.976×10^{-2}	1.214	2.692×10^{-2}
	μ_{a2}	2.944×10^{-3}	5.721×10^{-3}	9.576×10^{-5}
	μ_{a2}	6.049×10^{-2}	8.141×10^{-1}	5.383×10^{-2}
865	μ_{a1}	1.338×10^{-2}	4.940×10^{-1}	1.092×10^{-2}
	μ_{a2}	3.046×10^{-3}	2.009×10^{-2}	5.877×10^{-4}
	μ_{a2}	3.264×10^{-2}	3.385×10^{-1}	2.184×10^{-2}

Table 7.3: *Absorption coefficient variation with volume fractions:* V_{fmepi}, V_{fhae} *and* V_{fmder}.

as discussed in section 2.2.3.

To build up full knowledge of the variation of these parameters, simulations are performed for all combinations of t and μ_{s2} at the four different wavelengths using both linearly and circularly polarized illumination. This results in a required 240 simulations[1]. The time taken to perform a single simulation of 5×10^6 photons is around twelve hours on a PC with a 1GHz Pentium processor. The post-simulation analysis applying all combinations of μ_{a1} and μ_{a2} require a further six hours per simulation for forty-five different absorption values along each of these dimensions. This large number of absorption values compared to t and μ_{s2} (see table 7.2) is possible due to the ability to apply their effect post-simulation in this manner. This proves convenient due to the high levels of sensitivity to μ_{a1} and μ_{a2} as will be demonstrated in section 7.6. Resultant from these simulations and absorption analysis runs are 60,750 data points per measurable.

7.5 Detection Regime

The proposed detection regime is to use the backscattered intensity of a polarization maintaining component, extracted through subtraction of raw polarization channels (section 3.6), along with the intensity in the linearly polarized multiple scatter channel (polarization channel 2). This provides a two channel detection scheme with the different polarizations providing sensitivity to different regions of sample. The general structure of the samples has been defined in section 7.2 as being variable in four parameters. Therefore, the use of only two measured intensities does not provide enough information to uniquely define the four variables. It has been discussed in section 5.2.1 that illumination in the experimental system will be provided at four different wavelengths. This provides two measurables (polarization maintaining and multiple scatter intensities) for each wavelength, resulting in eight measurables to define the four sample variables.

As discussed previously, it is highly desirable to use the circular polarization main-

---

[1] 5(t values)×6(μ_{s2} values)×2(polarization states)×4(wavelengths) = 240 simulations

taining light to provide sensitivity to superficial skin regions, as this is more useful for the imaging of skin samples. However, it has was shown in section 4.5 that, for the scattering properties of the applied microspheres, the visitation depth of linearly polarized multiple scatter is almost identical to that of polarization maintaining circularly polarized light for low levels of absorption. It has been shown however that clear differences can be observed between these two components for *in-vivo* skin tissue (indicated by figures 4.15b and 4.16b). Therefore, to provide a more representative investigation of the ability to invert from detected measurables to sample parameters in tissue, linear polarization maintaining light is used here due to the improved contrast between the visitation depths. This is viable due to the absence of problems due to surface reflections in the numerical simulations.

7.6 Analysis of the Simulated Data Space

Presented in this section is a review of the sensitivity of the detected measurables to variations in the sample parameters. This is performed in reference to the simulated data space. An exhaustive analysis of the trends is not necessary here as many similar trends have been reported in chapter 3. The function of this section is to begin to indicate any possible problems in the unique determination of sample parameters from the detected measurable set.

7.6.1 Measurable Variation with Absorption

Variation of the intensity backscattered from the media considered here will be solely down to the presence of absorption in the two layers. This is due to the bottom layer being semi-infinite in the z-direction and, therefore with no absorption, all illumination will eventually be backscattered with no attenuation. The variation of the measurables due to t and μ_{s2} will therefore be highly dependent on the values of μ_{a1} and μ_{a2}; with no absorption there would be no variation in the emerging total intensity.

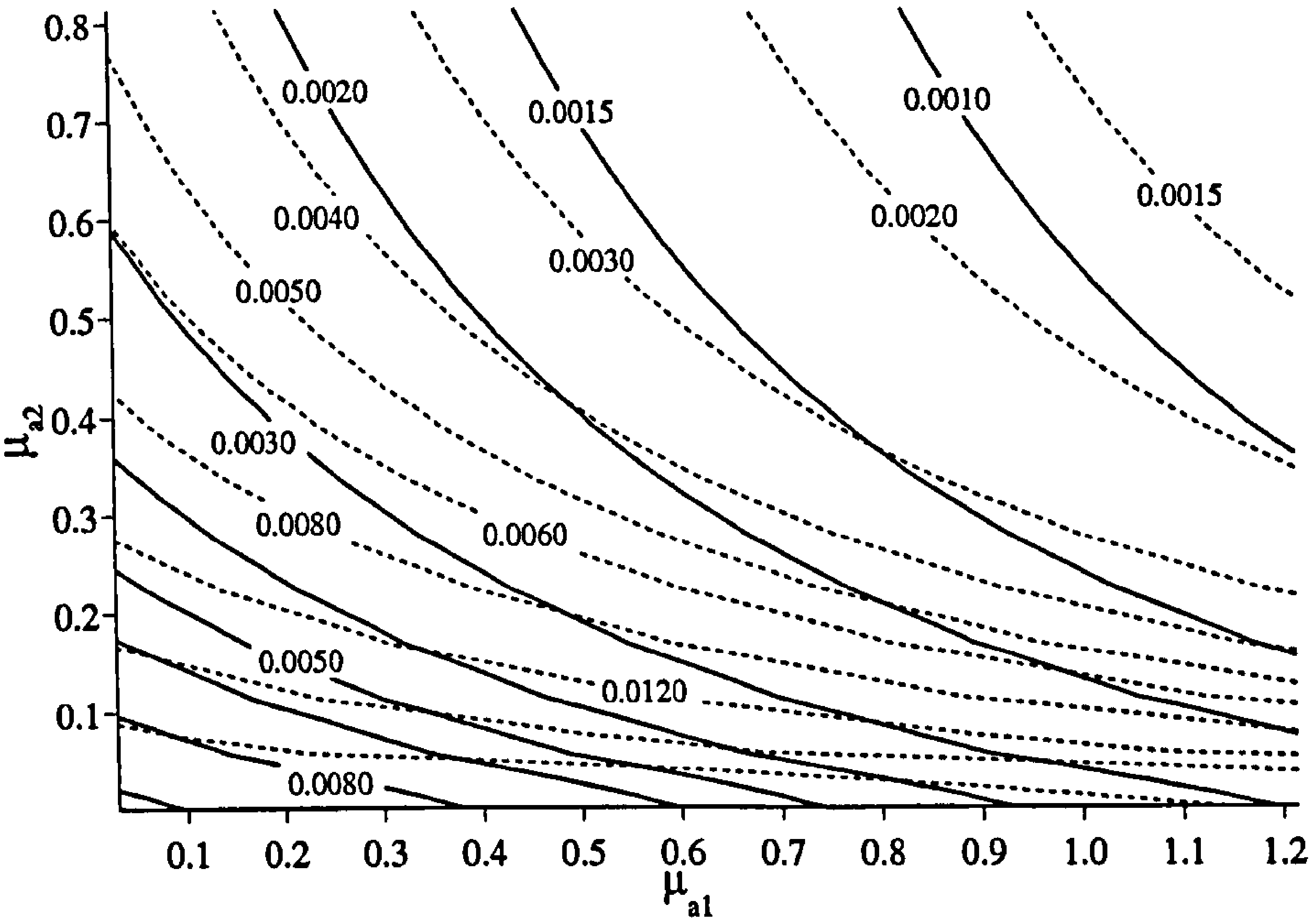

Figure 7.2: *Detected intensity in the linear polarization maintaining component (solid) and the multiple scatter channel (dashed) for varying top and bottom layer absorption coefficient.* $\lambda = 660nm$, $\mu_{s2} = 1.8mm^{-1}$ *and* $t = 0.8mm$.

To provide an indication of how μ_{a1} and μ_{a2} affect the measurables, contour plots of constant intensity are plotted for two of the proposed eight measurables. The variation of the measurables due to μ_{a1} and μ_{a2} is shown in figure 7.2 for $\lambda = 660$nm, $t = 0.8$mm and $\mu_{s2} = 1.8\text{mm}^{-1}$.

It can be seen from these contours that each combination of absorption coefficients corresponds to a unique pair of measurables and vice-versa. This trend is mirrored throughout the data space for varying values of t and μ_{s2}. It should therefore be theoretically possible to extract the values of μ_{a1} and μ_{a2} for any given combination of t and μ_{s2} using only these two detected measurables. However, it can be seen that in some regions of the plot the contours become increasingly parallel. In practice therefore, error free extraction is not a realistic achievement. This is due to any noise on the detected measurable translating to an error in the determined variable parameter value. A consideration of the influence of noise on data conditioning of the four dimensional problem is presented in section 7.10. To determine the sensitivity to noise, two factors must be taken into account. The first measure is the local orthogonality of the contours. Highly orthogonal contours will provide a more robust inversion in the presence of noise, whereas near-parallel contours indicate that a small change in measurable value (possibly due to noise) will cause great variation in the extracted parameter value. The second factor to consider is the local rate of change of the measurable. A 'steep' variation of measurable value will mean that a large change of measurable is required to provide considerable change in the determined parameters and is therefore less sensitive to noise. In summary, the gradients of the two data sets should be large and orthogonal to achieve the optimum performance of a system in the presence of noise[28]. To transform from the measurable space defined by the detected measurables to values of absorption coefficient, the Jacobian, J_{2D}, can be defined as shown in equation 7.1. This translation also provides an indication of the magnitude and orthogonality of the gradients of the two data sets and therefore provides an indication of the performance of the system in the presence of noise[28].

$$J_{2D} = \det \begin{pmatrix} \frac{\partial M_1}{\partial \mu_{a1}} & \frac{\partial M_1}{\partial \mu_{a2}} \\ \frac{\partial M_2}{\partial \mu_{a1}} & \frac{\partial M_2}{\partial \mu_{a2}} \end{pmatrix} = \frac{\partial M_1}{\partial \mu_{a1}} \frac{\partial M_2}{\partial \mu_{a2}} - \frac{\partial M_1}{\partial \mu_{a2}} \frac{\partial M_2}{\partial \mu_{a1}} \tag{7.1}$$

where M_1 and M_2 are the detected measurables.

The local variation of J_{2D} across the contour plots presented in figure 7.2 is given in figure 7.3. This is along with a direct evaluation of contour orthogonality.

It can be seen from these plots that the contours can be divided into two regions in terms of sensitivity. For high levels of μ_{a2}, the contours become more parallel and also have a low rate of change indicated by widely spaced contours[2] rendering them highly

---

[2] It should be noted that the variation of the contour levels plotted in figure 7.2 is not uniform. Therefore this does not provide an obvious graphical representation of the difference in contour spacing between low and high levels of μ_{a2}.

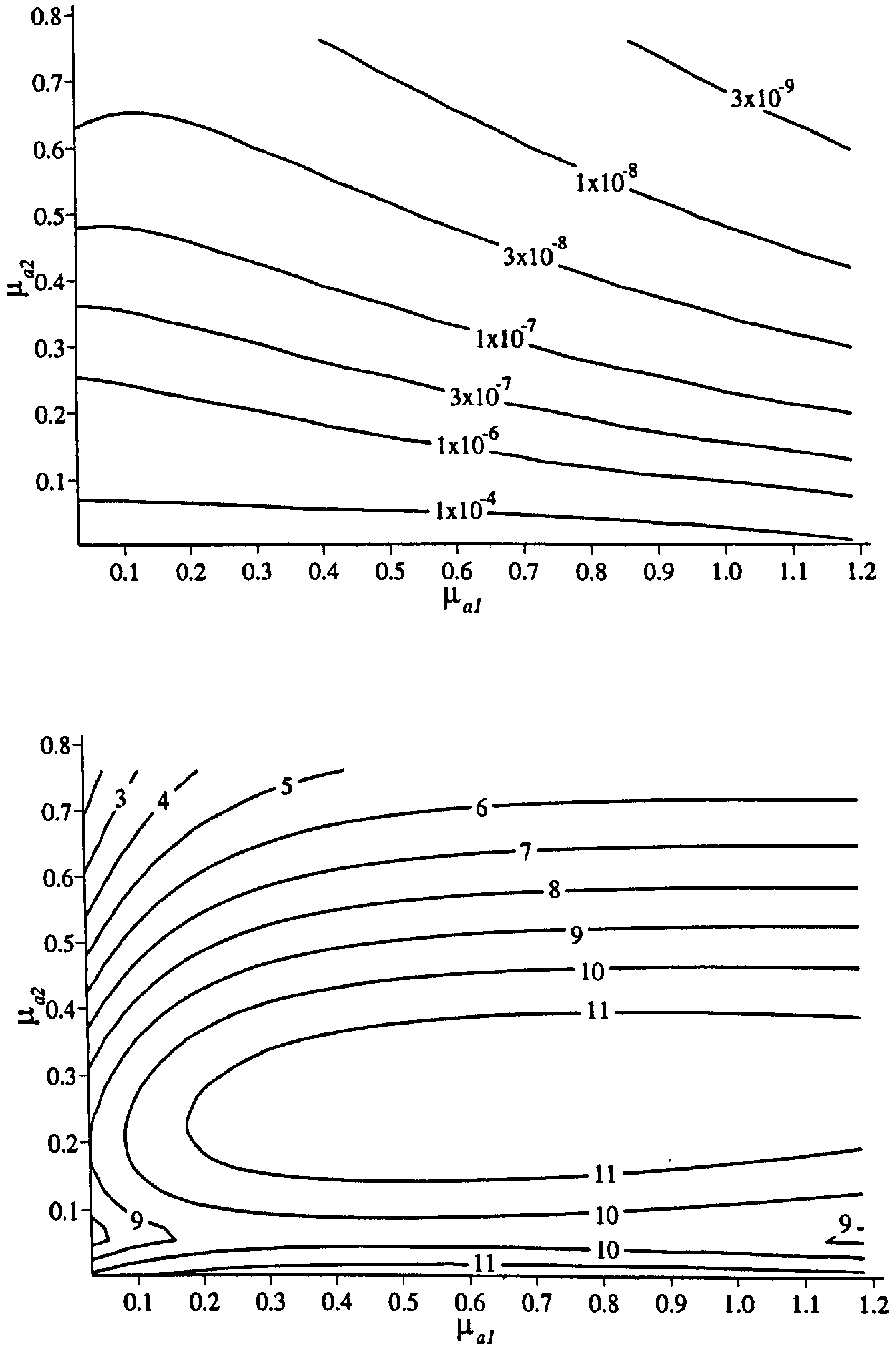

Figure 7.3: *Variation of a)* J_{2D} *and b) contour orthogonality with* μ_{a1} *and* μ_{a2}. *The illustrated variations are for* $\lambda = 660nm$, $t = 0.8mm$ *and* $\mu_{s2} = 1.8mm^{-1}$.

influenced by the presence of noise. This is due to similarity between the two different polarizations and is caused by the deeply penetrating photons, which account for the difference in measurable in low absorption, becoming highly attenuated by the high levels of absorption. This renders both the intensity depth profiles (similar to those shown in figure 3.20) confined to similar regions resulting in similar dependency. For lower levels of bottom layer absorption, the contours become more closely spaced and have increasing orthogonality due to the increased contrast between the depths probed by the different polarization states.

7.6.2 Measurable Variation with Layer Thickness and Scattering

As mentioned previously, the variation of the remaining two parameters, t and μ_{s2}, is determined largely by the values of absorption coefficient selected for the different layers. Therefore, the dependency of the output measurables on their variation is expected to be much more subtle.

Shown in figure 7.4 are four contour plots for varying t and μ_{s2} at a selection of μ_{a1} and μ_{a2} values for $\lambda = 660$nm illumination. It is apparent from the variation of these contour values that, as expected, the variation of the outputs due to change in these properties is not as great as with the changes in absorption. However, this is also largely down to the reduced range of variation of these values compared with the levels of absorption. Figure 7.4 also shows that, not only are the contours largely parallel and slow varying indicating a high sensitivity to noise, but also observable are multiple crossings of two contours. This indicates the presence of non-unique solution to the two variable problem. Such an issue may be resolved through the integration of this result with those from measurables for other wavelengths. Conditioning of the four-dimensional problem using all eight measurables is evaluated in the following section.

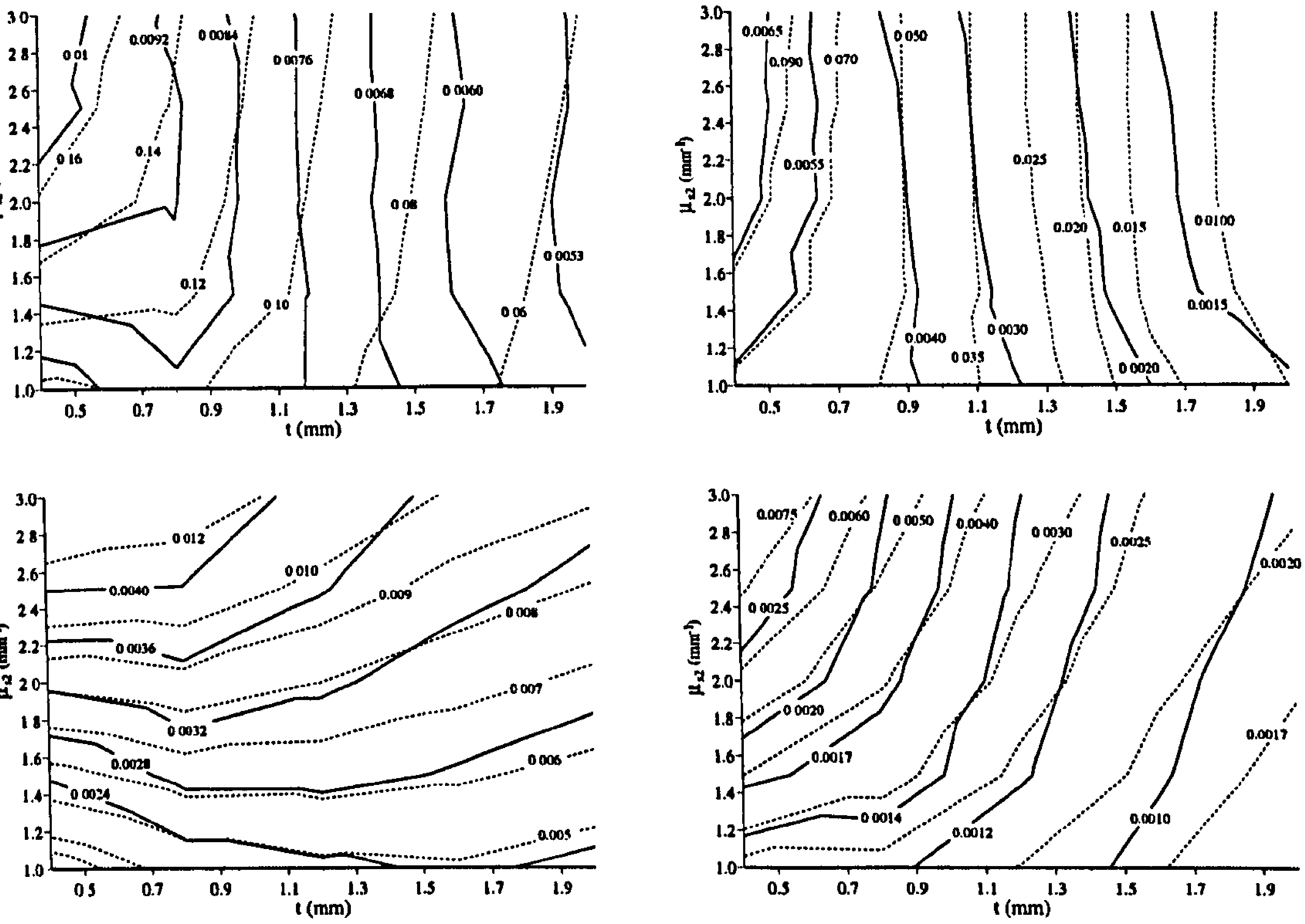

Figure 7.4: *Contours of constant measurable intensity plotted for varying t and* μ_{s2} *with a)* $V_{fmepi} = 10\%$, $V_{fhae} = 5\%$ *and* $V_{fmder} = 0\%$, *b)* $V_{fmepi} = 30\%$, $V_{fhae} = 5\%$ *and* $V_{fmder} = 0\%$, *c)* $V_{fmepi} = 10\%$, $V_{fhae} = 5\%$ *and* $V_{fmder} = 10\%$ *and d)* $V_{fmepi} = 30\%$, $V_{fhae} = 5\%$ *and* $V_{fmder} = 10\%$.

7.7 Data Conditioning

It has been discussed in the previous sections of this chapter how simulations of samples with different combinations of parameters can be used to construct a look-up table. This produced data set of measurables is now used to assess the conditioning of the problem. The definition of a well-conditioned problem is one where a given set of measurables corresponds to a unique set of the sample parameters which are to be determined and vice versa. As well as acting as the look-up table, the performed simulations also provide realistic sets of the eight measurables, defined in section 7.5, which can be used as an input to an inversion algorithm to attempt determination of the sample parameters. If these known measurable sets can produce a unique solution of sample parameters, and more importantly the correct combination of parameters, this will prove that the inversion problem is well-conditioned. However, it is intuitive to expect that the measurable sets resulting from different combinations of sample parameters will have varying levels of conditioning. For this reason all measurables across the full range of the simulated data space are used as inputs to assess under what circumstances the problem is well-defined.

The proposed process of measurable simulation and then inversion from these measurables back to sample properties is outlined in figure 7.5. In a practical system the measurables M_1 to M_8 will be determined experimentally.

7.7.1 The Search Algorithm

To determine the conditioning of the problem, the first stage of the inversion process illustrated in figure 7.5, transforming from measurables to a set of possible solutions, can be performed. To look-up the value of a measurable within its corresponding simulated data space a search algorithm is required. Each set of inputs to the search is composed of eight measurables which correspond to values of t, N, V_{fmepi}, V_{fhae} and V_{fmder} provided as inputs at the simulation stage. A measurable is only searched for within the simulated measurable data space corresponding to that detected channel. To find the desired value,

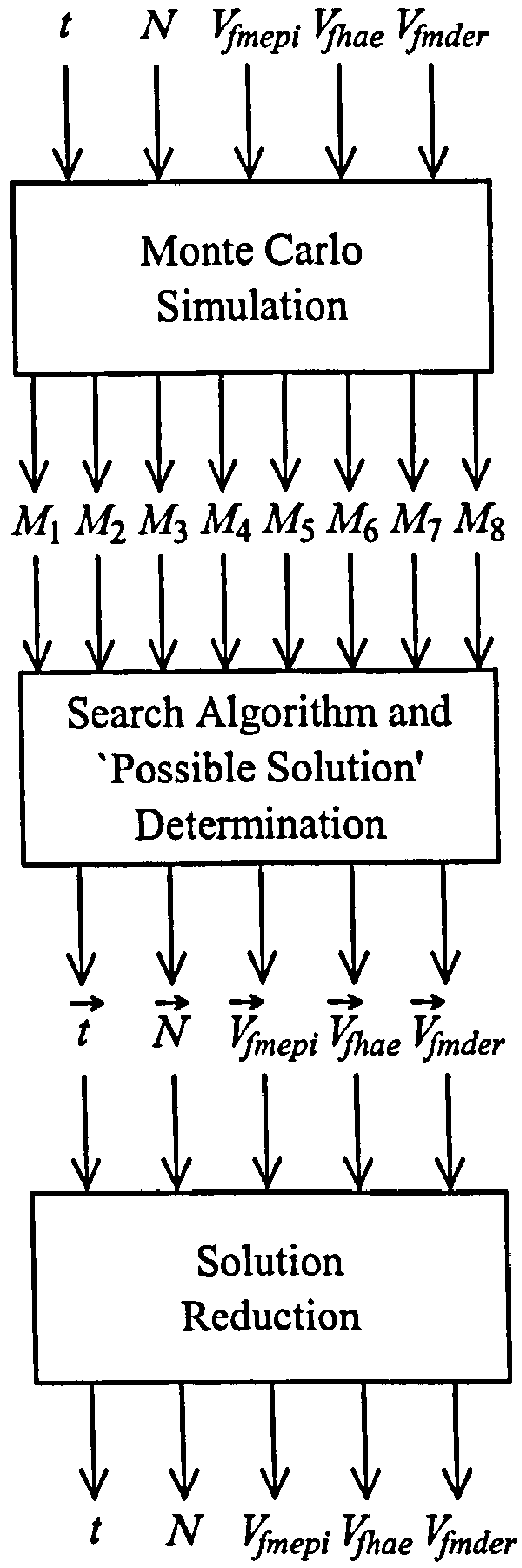

Figure 7.5: *To simulate the determination of the sample properties from detected measurables the first stage is to simulate the detected measurables (M_1 to M_8) resultant from a sample with given properties t, μ_{s2}, V_{fmepi}, V_{fhae}, and V_{fmder} as described in section 7.4. These measurables are then input into the first stage of the inversion process. This involves a search to determine a set of possible values for the sample parameters. The final stage of the proposed inversion is to determine a solution set consisting of single values for t, N, V_{fmepi}, V_{fhae} and V_{fmder}.*

a search is performed along the μ_{a1} and μ_{a2} directions. This involves selection of a value in the data space and detection of whether the measurable value for which is being searched can be found within the region bounded by the adjacent points in the μ_{a1} and μ_{a2} directions. If an occurrence of the search value is found within this region, the central value is 'flagged' as a possible solution[3] before moving onto the next point in the μ_{a1}-μ_{a2} plane. This is more easily represented graphically in figure 7.6[4], however only a three dimensional representation is clearly possible in place of the actual four dimensional data space. Both graphical and intuitive representation of the data space is complicated by its four dimensional nature, however, due to properties of the data space it can be considered as a set of thirty planes varying in the μ_{a1} and μ_{a2} directions for different combinations of t and μ_{s2}. This is viable due to the slow variation of data along the t and μ_{s2} directions (see section 7.6.2) with the general μ_{a1}-μ_{a2} trends occurring, with slightly varying characteristics, at each combination of t and μ_{s2}. A search in the μ_{a1}-μ_{a2} plane is acceptable rather than in all four dimensions due to this increased rate of variation along these axes.

7.7.2 Single Measurable Conditioning

Attempting to solve a four parameter problem such as this using a single measurable is clearly not viable. However, assessment of the number and location in the data space of flagged possible solutions for a single measurable provides a good indication of the improvement achieved by the later combination of measurables and therefore, indicates their performance. To perform assessment of the data, each of the 55,470 measurable sets[5],

---

[3] The data points flagged by the search algorithm, corresponding to a set of the four sample parameters, are not strictly 'possible solutions' as the results will not always fall directly onto the nodes of the data space. However, they provide an indicator to the location of a possible solution for processing by the solution reduction algorithms proposed in section 7.8 (defined by a unique combination of sample parameters).

[4] In this figure the search value is represented as a single point in space for simplicity. In reality a constant value will map a contour plane varying in four dimensions.

[5] This corresponds to five t values, six values of μ_{s2} and forty-three μ_{a1} and μ_{a2} values. Due to the nature of the search, use of the first and last absorption values in each dimension are omitted.

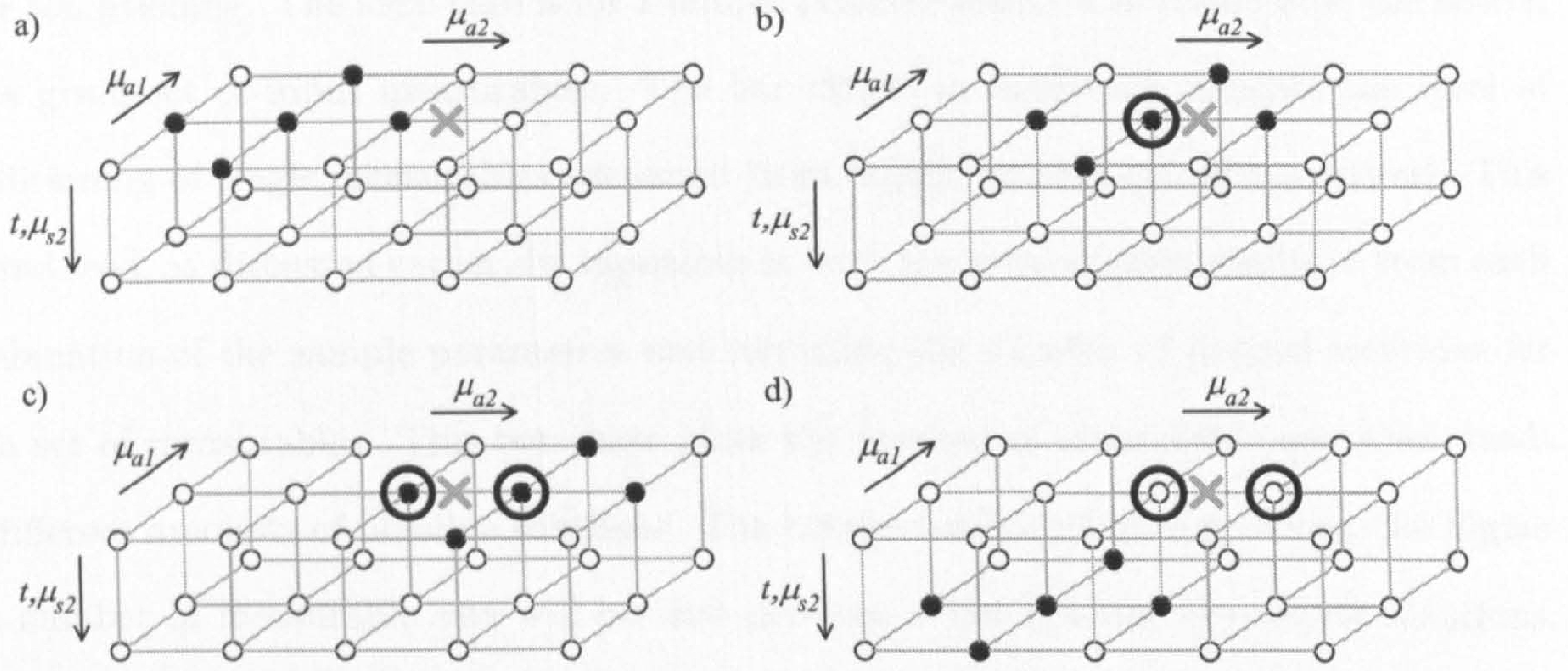

Figure 7.6: *The search procedure involves a) selection of a data point within the measurable space and detection of whether the search value (represented by the cross) is encountered within the region bounded by adjacent values of* μ_{a1} *and* μ_{a2}*, b) if the search value is found the central point of the region is flagged. c) The flagged data positions are stored for later processing and d) once the current* $\mu_{a1}=\mu_{a2}$ *plane is completely searched the plane corresponding to the next combination of* t *and* μ_{s2} *is searched.*

defined by the simulations for different sample property combinations, is used as an input to the search algorithm. The number and position of the possible solutions flagged by the routine are recorded. For each of the eight individual measurables, the mean number of values flagged per input measurable set is shown in table 7.4. For each set of measurables input to the search algorithm a four dimensional array of data points, flagged as possible solutions, will result. If a large number of possible solutions are produced then this implies poor conditioning. The ideal case is for a unique possible solution to result from the search for a given set of input measurables. The bar charts in figure 7.7 indicate the level of conditioning of single measurables (detected from 660nm wavelength illumination). This is produced, as discussed earlier, by inputting in turn the measurables resultant from each combination of the sample parameters and recording the number of flagged solutions for each set of measurables. This bar chart plots the number of measurable sets that result in different amounts of possible solutions. The better conditioned the problem, the higher the number of measurable sets will be that produce a low number of possible solutions. The plots show that for both of the illustrated measurables, the conditioning, as expected, is poor with over 70% of the input measurable sets resulting in more than 2,000 possible solutions.

Upon analysis of the array of flagged possible solutions produced by the search algorithm it can be seen that the marked nodes in the data space map a four dimensional plane through the data space which surround the searched measurable value.

7.7.3 Conditioning at a Single Wavelength

To attempt improvement of the conditioning of the data space, the number of measurables used to define the sample parameters is increased. If information produced by the different polarization states at a single wavelength are combined, the contrast between polarization states can hopefully be utilised to improve the conditioning. The combination of measurable information is achieved by overlaying the two arrays of possible solutions for the two

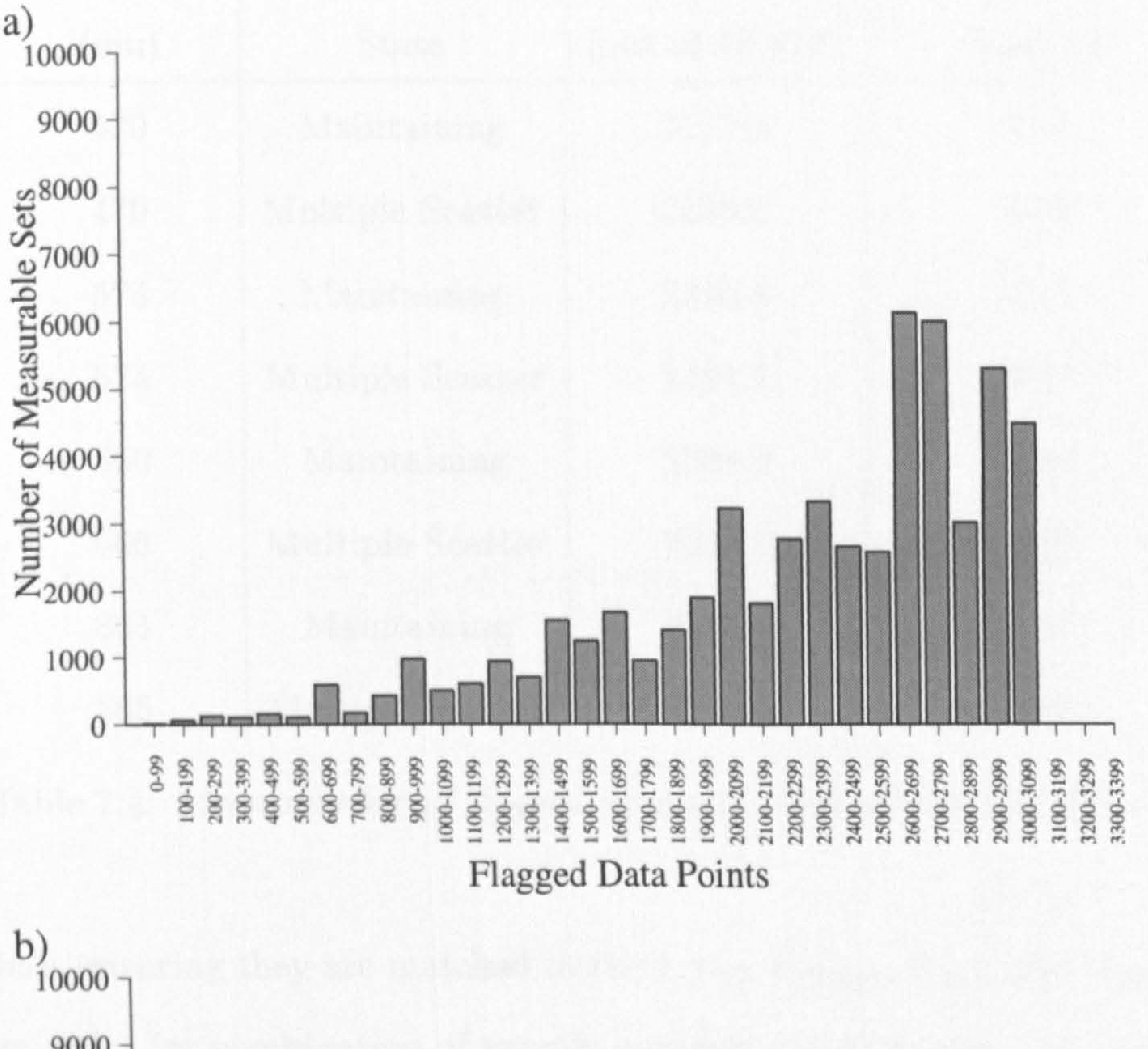

Figure 7.7: *Number of values flagged as possible values for a) the polarization maintaining measurable and b) the multiple scatter measurable, both recorded for* $\lambda = 660nm$.

Wavelength (nm)	Polarization State	Mean Flags (out of 55,470)	% of Data Points 'Flagged'
470	Maintaining	2182.5	3.91
470	Multiple Scatter	2255.6	4.05
574	Maintaining	2326.5	4.17
574	Multiple Scatter	2491.7	4.47
660	Maintaining	2308.3	4.14
660	Multiple Scatter	2335.0	4.19
865	Maintaining	2290.2	4.11
865	Multiple Scatter	2163.1	3.88

Table 7.4: *Mean number of flagged values in each measurable data space.*

measurables, ensuring they are matched in the t, μ_{s2}, V_{fmepi}, V_{fhae} and V_{fmder} directions. For a data point (or combination of sample parameters) to remain a possible solution, it must be flagged up by both measurables.

Shown in table 7.5 is the improvement provided by the combination of polarization states at each wavelength. This is along with the bar charts in figure 7.8, representing the number of possible solutions flagged over the range of input measurable sets. The polarization information has significantly reduced the number of possible solutions. However, the problem is still under defined for each wavelength with only two measurables being used to define the four variable problem.

7.7.4 Multiple Wavelength Performance

To assess the conditioning resultant from the full set of measurables, the possible solutions must be combined for the different illuminating wavelengths which were resultant from the combination of polarization states discussed in the previous section. This can be achieved in a similar manner to the combination of polarization channels by overlaying the flagged

Wavelength (nm)	Mean Flags (out of 55,470)	% of Data Points 'Flagged'
470	702.1	1.26
574	803.0	1.44
660	611.7	1.10
865	370.9	0.67

Table 7.5: *Mean number of flagged values for each wavelength.*

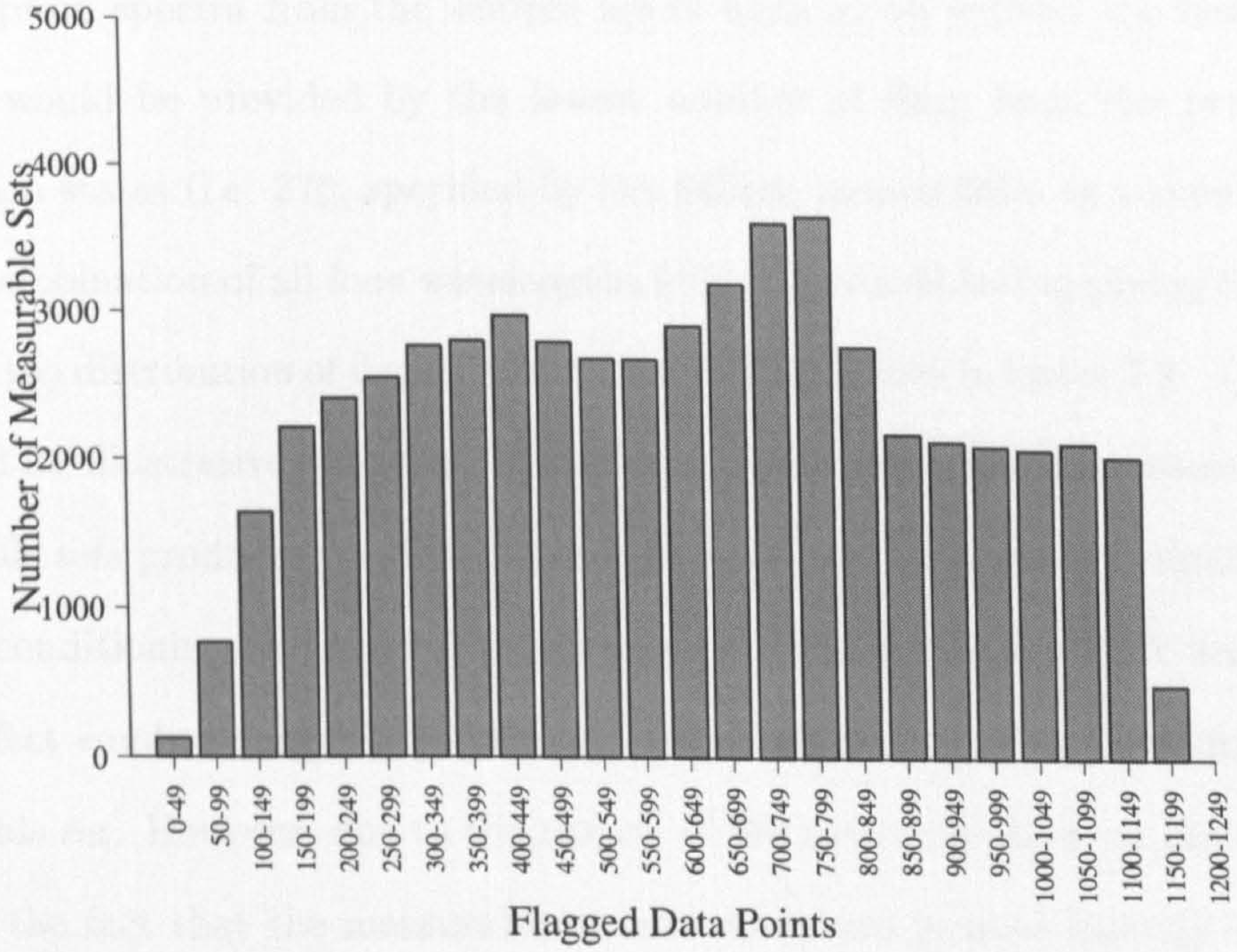

Figure 7.8: *Number of values flagged as possible values for at $\lambda = 660nm$ by combining the polarization maintaining and multiple scatter channels.*

solution arrays. However, the integration of cross-wavelength data is not as trivial as it was for different polarization states at a single wavelength. The overlaying of data between wavelengths requires one to assume knowledge of the spectra of the dominant absorbers in the tissue. The data space has been defined by the wavelength insensitive values, t, N (or μ_{s2} at $\lambda = 633$nm), V_{fmepi}, V_{fhae} and V_{fmder}. Therefore, overlaying the possible solution flags for corresponding values of these parameters at different wavelengths will integrate the effect of the contrast between illuminating wavelengths. Although the values of V_{fmepi}, V_{fhae} and V_{fmder} are wavelength insensitive, their value has been used to select the optical absorption for a given layer based on the expected absorption spectrum for that layer (section 7.3.2). Therefore, even though the overlaying of data matching in terms of the V_{fmepi}, V_{fhae} and V_{fmder} values appears to be valid without assumption, the assumptions are inherently employed at the point of simulation. If no knowledge of the absorption spectra from the sample layers were to be applied the best performance available would be provided by the lowest number of flags from the overlaying of the polarization states (i.e. 370, specified by the 865nm measurables as shown in table 7.5).

The combination of all four wavelengths (eight measurables) applying this assumption produces the distribution of flagged possible solutions shown in figure 7.9. The plot as been truncated for illustrative purposes. There are very low numbers of the most ill-conditioned measurable sets producing up to 183 possible solutions. This shows a significant improvement in conditioning by reducing the number of possible solutions. It was stated earlier that perfect conditioning will produce a unique set of sample parameters from a single measurable set. However, due to the nature of the search method, as illustrated in figure 7.6, and the fact that the measurable search values are located directly on the nodes of the data space, the ideal solution will provide five flagged data points. The data in figure 7.9 shows that 21.5% of the measurable sets applied result in this level of conditioning and 59.7% provide 12 or less possible solutions.

The result in figure 7.9 is only promising if two conditions are met concerning the

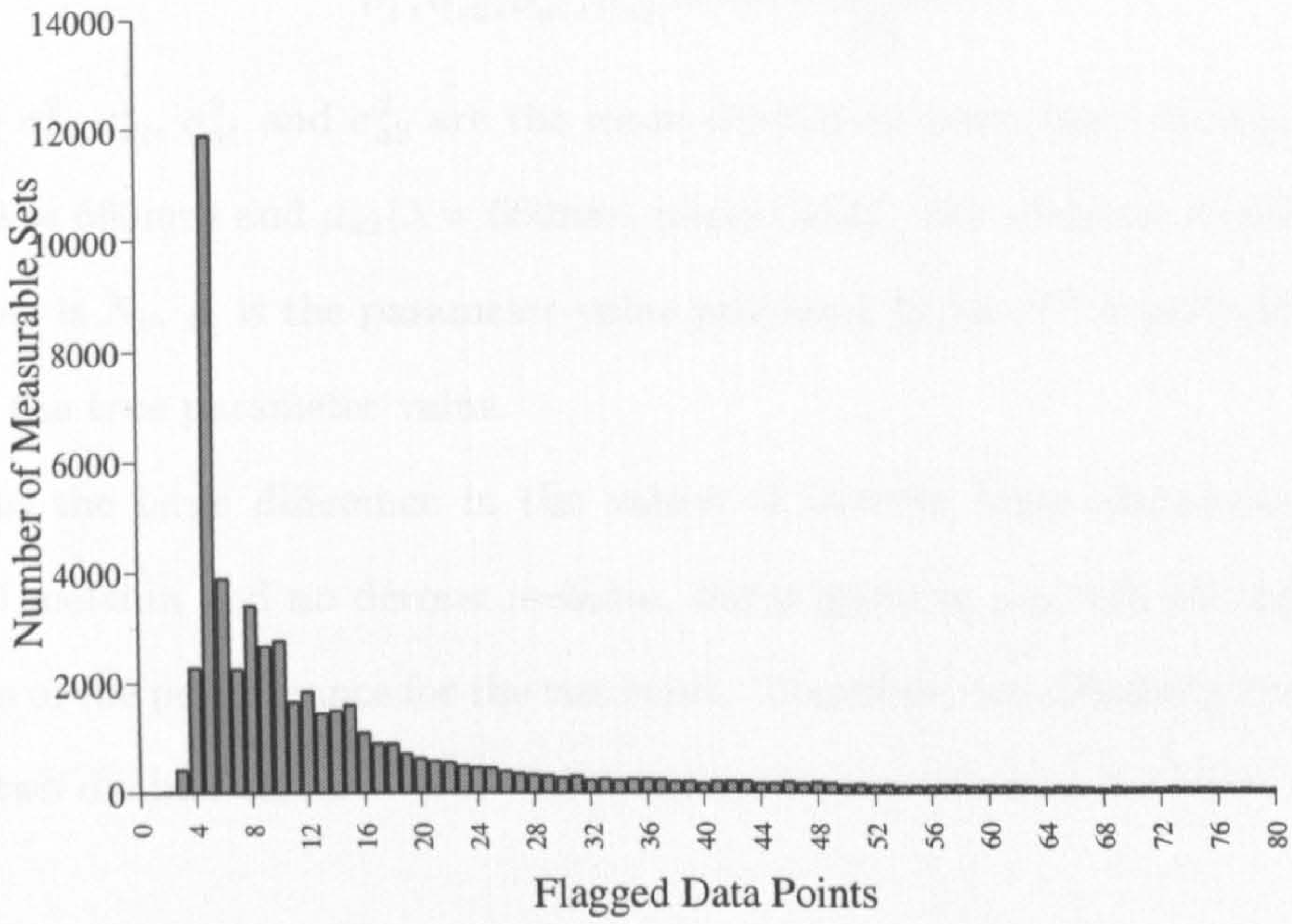

Figure 7.9: *Distribution of the possible solutions after combination of all eight measurables.*

location of the data points flagged as solutions. Firstly, the correct solution which was used to simulate the input measurable set to the algorithm must be among the data points flagged as possible solutions. Furthermore, the incorrectly flagged possible solutions must be reasonably confined to a region around the correct value. This would ensure that the error on any parameter values derived from these flagged values would be much lower than if the incorrect flags were erratically spread across the data space. As the data up to this point has been free from noise there is no problem in ensuring that the first condition is met and the 'correct' data point is flagged for all measurable sets. This suggests that the grouping of the incorrect possible solutions is of interest. It is clearly impractical to assess directly the location of the incorrect values resultant from application of each of the 55,470 measurable sets. Therefore, the spread of flagged solutions is assessed by determining the variance of the proposed solution away from the correct value. This is defined for each sample parameter in equation 7.2.

$$\sigma_t^2, \sigma_{s2}^2, \sigma_{a1}^2, \sigma_{a2}^2 = \frac{\sum_{i=1}^{N_e}(\rho_i' - \rho_0)^2}{N_e} \tag{7.2}$$

where σ_t^2, σ_{s2}^2, σ_{a1}^2 and σ_{a2}^2 are the mean deviations away from the correct value of t, μ_{s2}, $\mu_{a1}(\lambda = 660\text{nm})$ and $\mu_{a2}(\lambda = 660\text{nm})$ respectively. The number of incorrectly flagged data points is N_e, ρ_i' is the parameter value proposed by the i^{th} incorrectly flagged point and ρ_0 is the true parameter value.

Due to the large difference in the values of bottom layer absorption for the cases of dermal melanin and no dermal melanin, linear plots in μ_{a2} will not provide sufficient indication of the performance for the two cases. Therefore, the following analysis is divided into the two distinct cases.

7.7.5 No Dermal Melanin

To represent the results of applying equation 7.2 for the four sample parameters, figure 7.10 shows the variation of σ_t^2, σ_{s2}^2, σ_{a1}^2 and σ_{a2}^2 with V_{fmepi} and V_{fhae} across a plane of constant t and μ_{s2} in the region of the data space modelling hæmoglobin as the major dermal absorber.

To aid understanding of these trends, figure 7.11 plots the number of flagged possible solutions for each of the measurable sets on a plane of constant t and μ_{s2}. The range of input measurable sets considered in both figures correspond to those resultant from simulation of the parameter values $\mu_{s2} = 1.4\text{mm}^{-1}$, $t = 1.2\text{mm}$, $V_{fmder} = 0\%$, $2\% \leq V_{fmepi} \leq 44\%$ and $1.0\% \leq V_{fhae} \leq 14.5\%$. It should be noted that these values of sample parameter, along with those marked on the axes in figures 7.10 and 7.11, are representative of the parameters used to generate the specific measurable set and not on the result of any inversion.

The first tendency to be observed from comparison of figures 7.10 and 7.11 is that the regions of high parameter value variation (large σ^2) correspond to measurable sets which produce a large number of values are flagged as possible solutions. This may seem

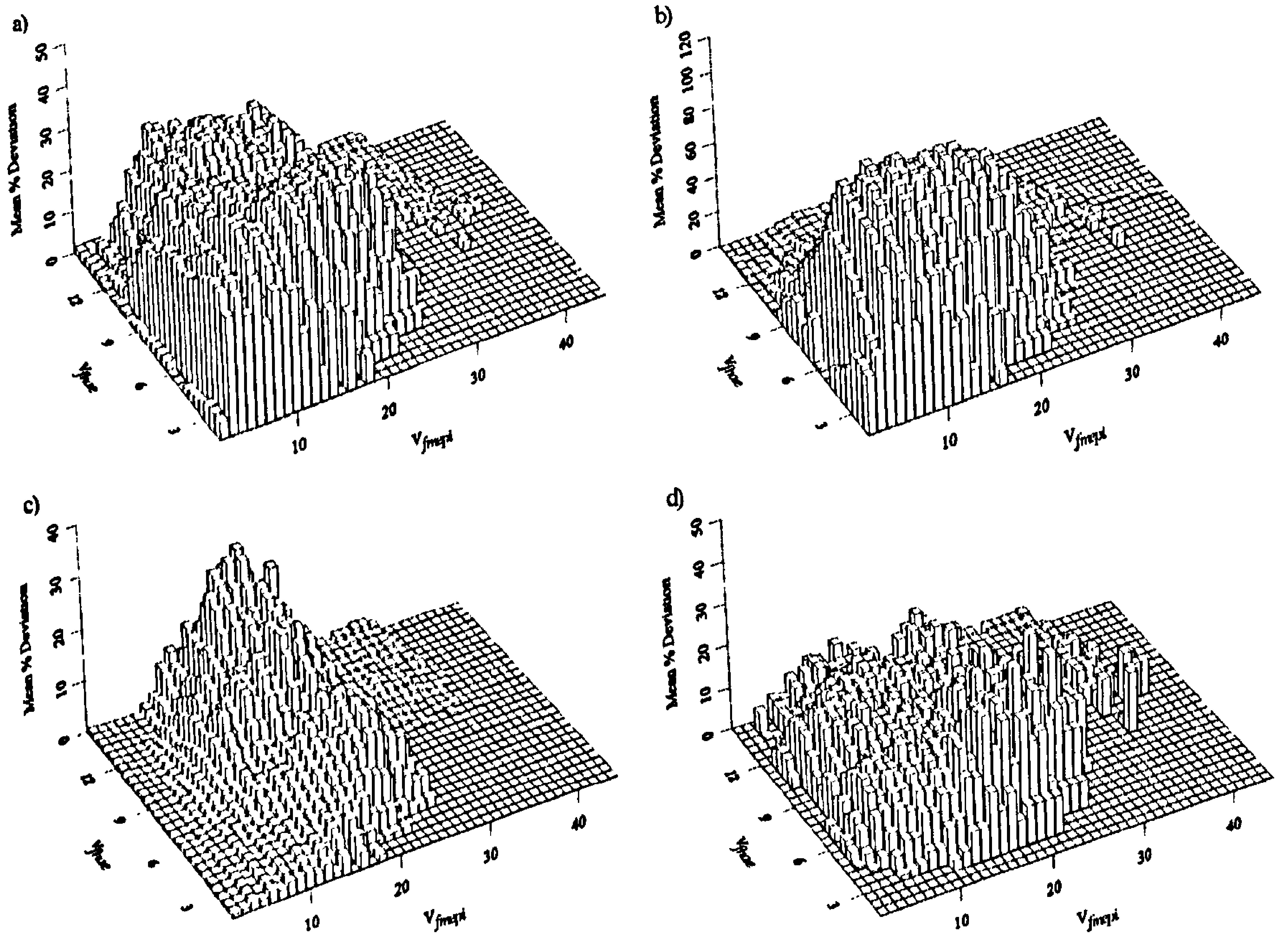

Figure 7.10: *Plots of a)* σ_t^2*, b)* σ_{s2}^2*, c)* σ_{a1}^2 *and d)* σ_{a2}^2 *across the region modelling hæmoglobin as the main dermal absorber (*$V_{fmder} = 0\%$*,* $2\% \leq V_{fmepi} \leq 44\%$ *and* $1.0\% \leq V_{fhae} \leq 14.5\%$*) for* $t = 1.2mm$*,* $\mu_{s2} = 1.4mm^{-1}$.

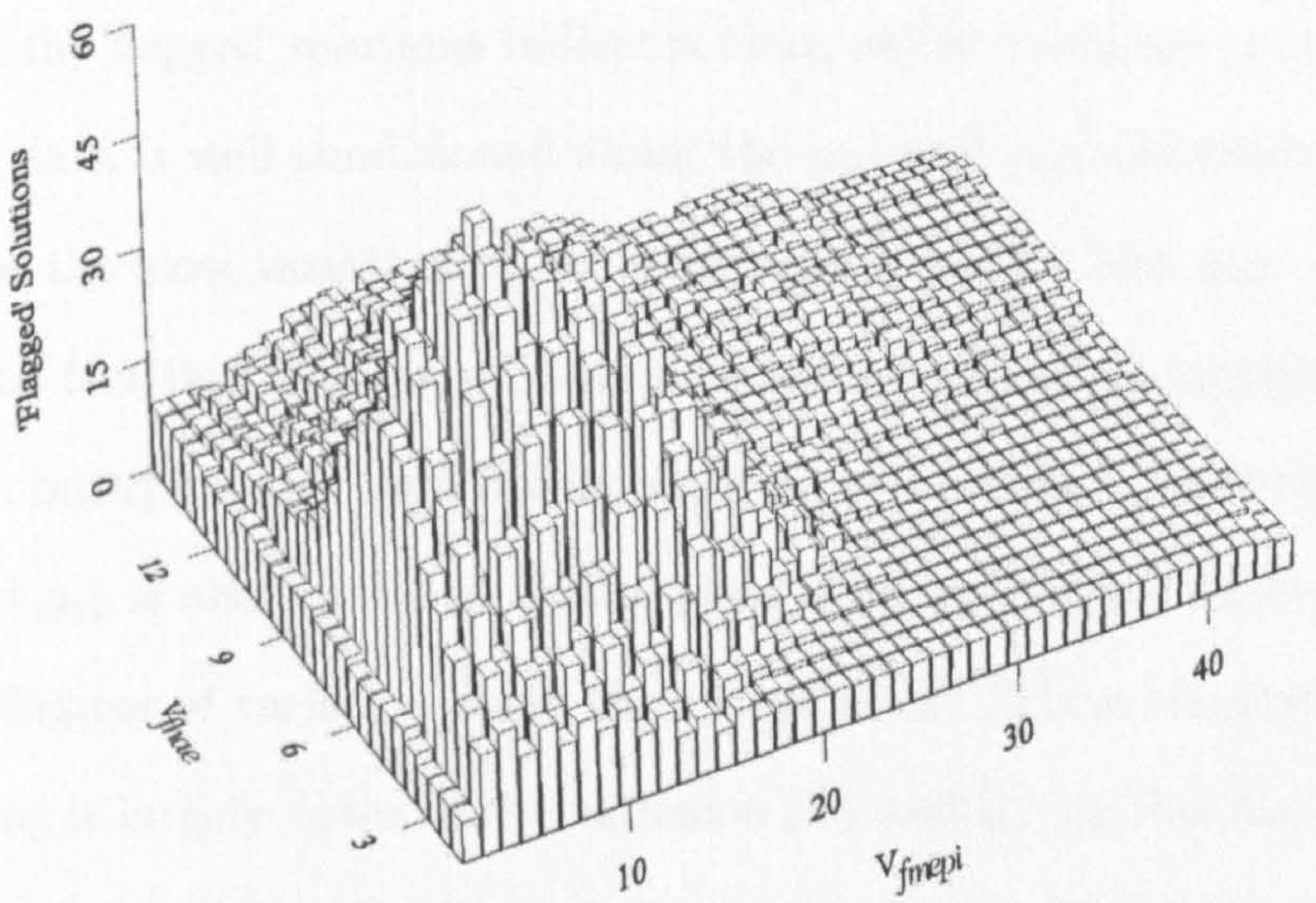

Figure 7.11: *Bar chart representing the number of possible solutions flagged for measurable input sets across the region modelling hæmoglobin as the main dermal absorber* ($V_{fmder} = 0\%$, $2\% \leq V_{fmepi} \leq 44\%$ *and* $1.0\% \leq V_{fhae} \leq 14.5\%$) *for* $t = 1.2mm$, $\mu_{s2} = 1.4mm^{-1}$.

a logical result, but it implies that the proposed solutions resultant from measurable sets that yield a low number of possible solutions, are restricted to a small region of the data space. Therefore, explanation of the large variation of parameter values can be found within explanation of why the range of data points have remained flagged as possible solutions.

It is clear from figure 7.11 that the poorest region of the data space in terms of conditioning (i.e. measurable sets that result in a high number of possible solutions) occurs for low values of top and bottom layer absorption. This trend is mirrored across the full range of μ_{s2}-t combinations. To examine the reasoning behind the levels of conditioning for different regions of the data space, the flagged solutions resultant from the input of a measurable set, selected from the region of interest, can be analysed.

The measurable set selected at random from the region of poorest conditioning corresponds to simulated input parameters of t = 1.2mm, μ_{s2} = 1.4mm^{-1}, V_{fmepi} = 14%,

$V_{fhae} = 5.5\%$ and $V_{fmder} = 0\%$, which produces forty-eight possible solutions. Reviewing the location of the flagged solutions indicates that, as the contours in figures 7.2 and 7.4 suggested, the data is well conditioned along the μ_{a1} and μ_{a2} directions. Problems arise however due to the slow variation of the measurables with t and μ_{s2}. These trends are indicated by the fact that the flagged data points are confined to localised patches on the μ_{a1}-μ_{a2} planes, but spread through the data space in the t and μ_{s2} directions. Such dependency on t and μ_{s2} is also indicated by the plots of σ_t^2 and σ_{s2}^2 in figures 7.10a and 7.10b showing high degrees of variation along these directions[6]. These suggest that problems in the conditioning is largely down to the variation of t and μ_{s2} in this region. The spread of the data in the μ_{a1} and μ_{a2} directions indicated by figures 7.10c and 7.10d is due to the contour slowly moving across the μ_{a1}-μ_{a2} plane for different combinations of t and μ_{s2}.

Problems resolving the value of μ_{s2} for low absorptions is partly the reason for reduced conditioning of the data in these regions. This is illustrated by observing the extreme case of no sample absorption. As stated earlier the measurable values are highly dependent on the values of absorption as they supply the main contrast mechanism. For zero absorption there will be no variation of backscattered intensity with μ_{s2}. Therefore, low absorption implies a low sensitivity to μ_{s2} A similar problem occurs for the thickness parameter. The contrast between wavelengths is low, therefore relying on the more subtle variation of the scattering properties to achieve inter-wavelength contrast. In summary, the multiple wavelength combination of possible solutions does not reject enough solutions as it tends to the case of trying to solve a four dimensional problem with only two measurables.

An apparent flaw in this reasoning is indicated by the peak in figure 7.11 being located away from the origin. This improved performance is due to fact the measurable sets in this region are close to the edge of the data space. Therefore, the contour representing the search value 'falls off' the data space sooner than for higher levels of absorption. The number of flagged data points is reduced the nearer a measurable set is positioned relative

---

[6] Note the differences in z-axis scale in figure 7.10.

to the edge of the data space.

It can be seen that, for higher levels of μ_{a1} (V_{fmepi}) and μ_{a2} (V_{fhae}), the conditioning of the data is vastly improved. Analysis of the solutions flagged by the search algorithm for a randomly selected input measurable set in this region shows a small group of flagged data points around the search value, confined to a single μ_{a1}-μ_{a2} plane. The performance is vastly improved due to the increased levels of absorption providing significant contrast between the intensities backscattered at the different wavelengths.

7.7.6 Dermal Melanin

Shown in figure 7.12 are the variations of σ_t^2, σ_{s1}^2, σ_{a1}^2 and σ_{a2}^2 in the region for high bottom layer absorption due to the simulated presence of dermal melanin. This is once again accompanied in figure 7.13 by the number of possible solutions, this time extracted for the the measurable sets produced to represent the parameter range: $t = 1.2$mm, $\mu_{s2} = 1.4\text{mm}^{-1}$, $V_{fhae} = 5\%$, $2\% \leq V_{fmepi} \leq 44\%$ and $4\% \leq V_{fmder} \leq 30\%$.

Once again it can be seen for this region of measurables that the area indicating poor conditioning relates to the region of high deviation of the possible parameter values away from the expected results. To examine the reason behind the poor conditioning, a measurable set is selected for analysis within this region. The input measurable set selected corresponds to $t = 1.2$mm, $\mu_{s2} = 1.4\text{mm}^{-1}$, $V_{fmepi} = 10\%$, $V_{fhae} = 5\%$ and $V_{fmder} = 6\%$ and results in ninety-three data points being flagged. Once again the flagged values track through various combinations of t and μ_{s2}, mapping a localised patch of flagged values in the μ_{a1} and μ_{a2} directions. However, in the previous case, representing the region with no dermal melanin, the cluster of data points was well localised in the absorption directions and consisted of only four or five data points on each μ_{a1}-μ_{a2} plane. The problems in conditioning were solely down to variation with t and μ_{s2} for low μ_{a1} and μ_{a2}. Here, this trend is extended with the cluster of flagged solutions becoming extended in the μ_{a1} direction, indicating that the measurables have reduced sensitivity to this value.

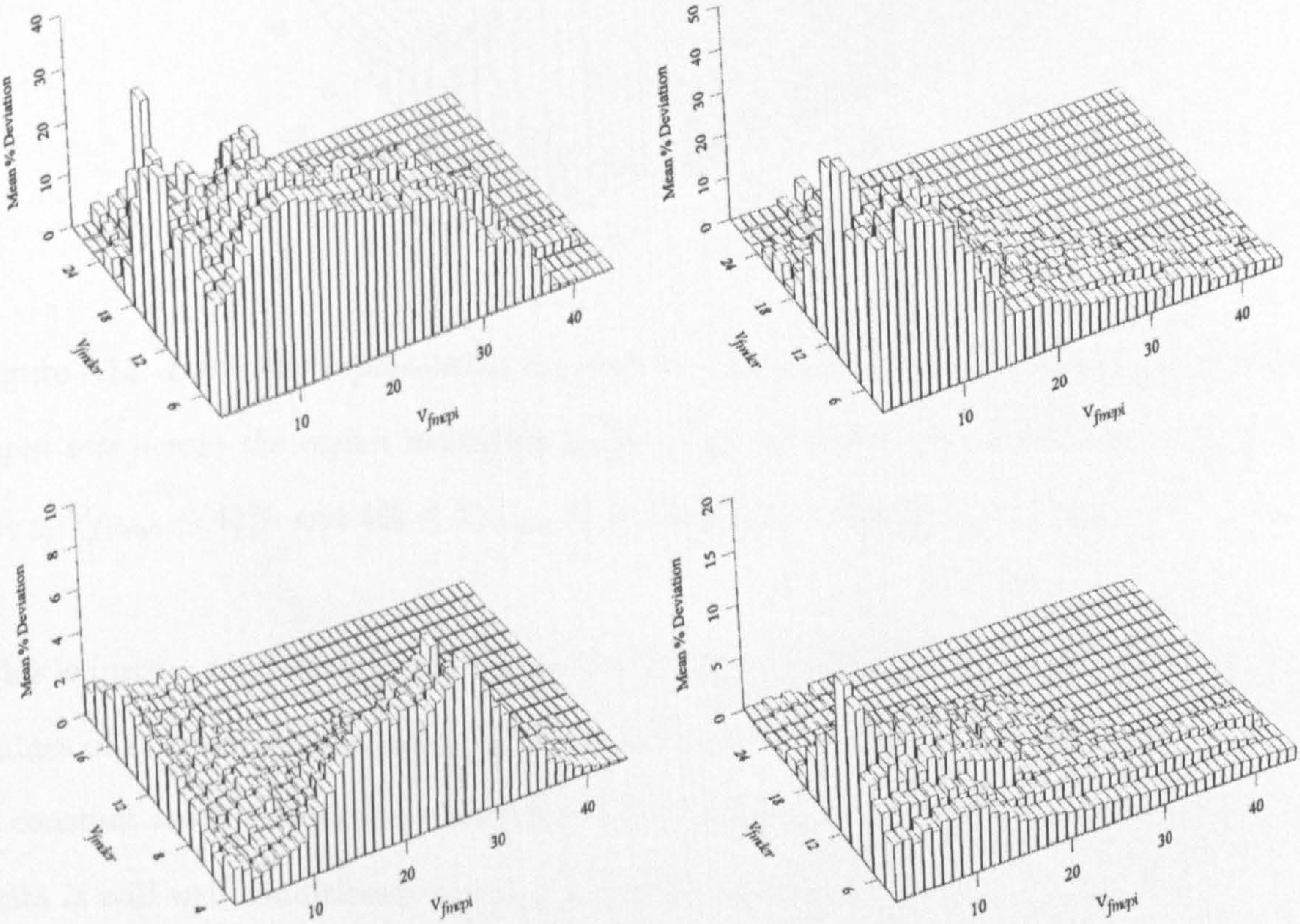

Figure 7.12: *Plots of a) σ_t^2, b) σ_{s2}^2, c) σ_{a1}^2 and d) σ_{a2}^2 across the region modelling melanin as the main dermal absorber ($V_{fhae} = 5\%$, $2\% \leq V_{fmepi} \leq 44\%$ and $4\% \leq V_{fmder} \leq 28\%$) for $t = 1.2mm$, $\mu_{s2} = 1.4mm^{-1}$.*

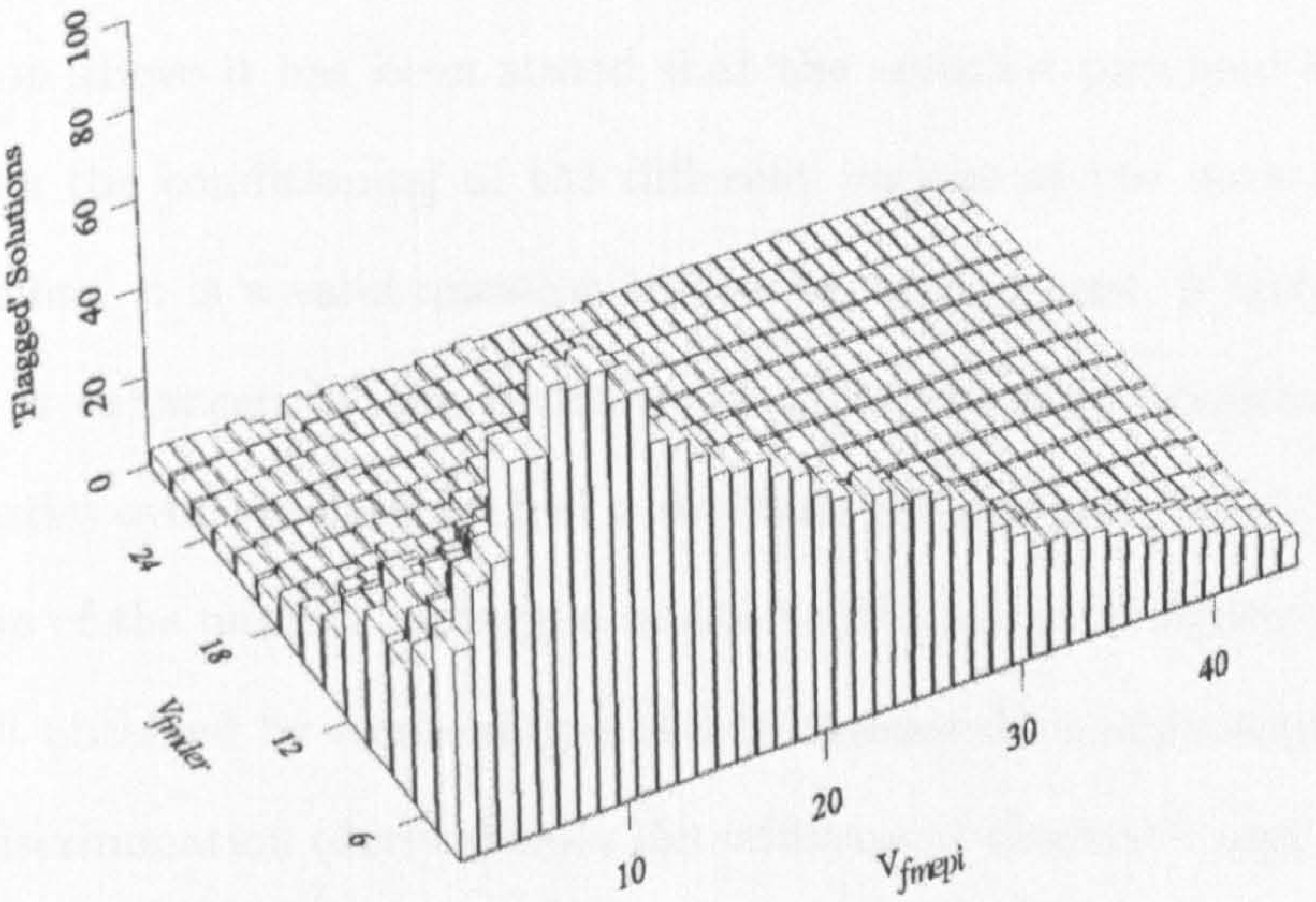

Figure 7.13: *Bar chart representing the number of possible solutions flagged for measurable input sets across the region modelling melanin as the main dermal absorber* ($V_{fhae} = 5\%$, $2\% \le V_{fmepi} \le 44\%$ *and* $4\% \le V_{fmder} \le 28\%$) *for* $t = 1.2mm$, $\mu_{s2} = 1.4mm^{-1}$.

This is further confirmed by the region becoming increasingly 'stretched' along μ_{a1} for low values of t. However, the mean number of flagged solutions on a single μ_{a1}-μ_{a2} plane for a constant t-$\mu s2$ combination for the selected measurable input is 6.9 indicating that the data is still well conditioned in the μ_{a1} and μ_{a2} directions.

Problems with the localisation of μ_{s2} follows on from the previous consideration for high values of V_{fhae} (which provide less absorption than the low levels of V_{fmder} observed for the case of dermal melanin). Determination of μ_{s2} proves problematic due to the high bottom layer absorption meaning low levels of the backscatter represent this region.

It can be seen from both figures 7.12 and 7.13 that the conditioning of the data improves for increasing values of V_{fmepi} and V_{fmder}. This is due to the nearing of the edge of the data space as was the case for low levels of absorption in the case for no dermal melanin. The effect in this region however is much more exaggerated than for the previous case due to the general shape of the measurable variation with μ_{a1} and μ_{a2} observed in figure 7.2.

7.7.7 Spectral Analysis

In the discussion above it has been stated that the contrast provided by the absorption spectrum affects the conditioning of the different regions of the data space to different extents. Therefore, it is a valid question to ask to what extent, if any, the conditioning of the system is enhanced by the inclusion of polarization information along with the spectral properties over the case for just a multiple wavelength system. To examine this, the distribution of the number of flagged solutions illustrated in figure 7.9 is compared to a similar result obtained by combination of four measurables representing the absence of polarization discrimination (derived from the addition of channel 1 and channel 2) at each of the illuminating wavelengths.

A comparison of the two cases is plotted in figure 7.14. The more appropriate bar chart has been replaced by a discrete line plot to aid illustration and comparison. It can be seen from these plots that the number of data points flagged as possible solutions is much improved when the polarization information is included.

7.8 Solution Reduction Techniques

Once the range of possible solutions has been determined it is necessary to derive a solitary solution which is a close to the actual sample properties as possible.

It has been shown in the previous sections that for the majority of the data space the flagged possible solutions are confined to a restricted region, either in all four dimensions or in the two absorption directions. Therefore, a primitive but valid method of derivation of a single solution is to average the parameter values along the four dimensions. The result of this method however, will not produce reliably accurate results and will produce large errors for values close to the edge of the data space in any of the four dimensions.

It has been discussed in section 7.7 that the first stage in the proposed inversion process involves determination of possible solution locations through use of the look-up

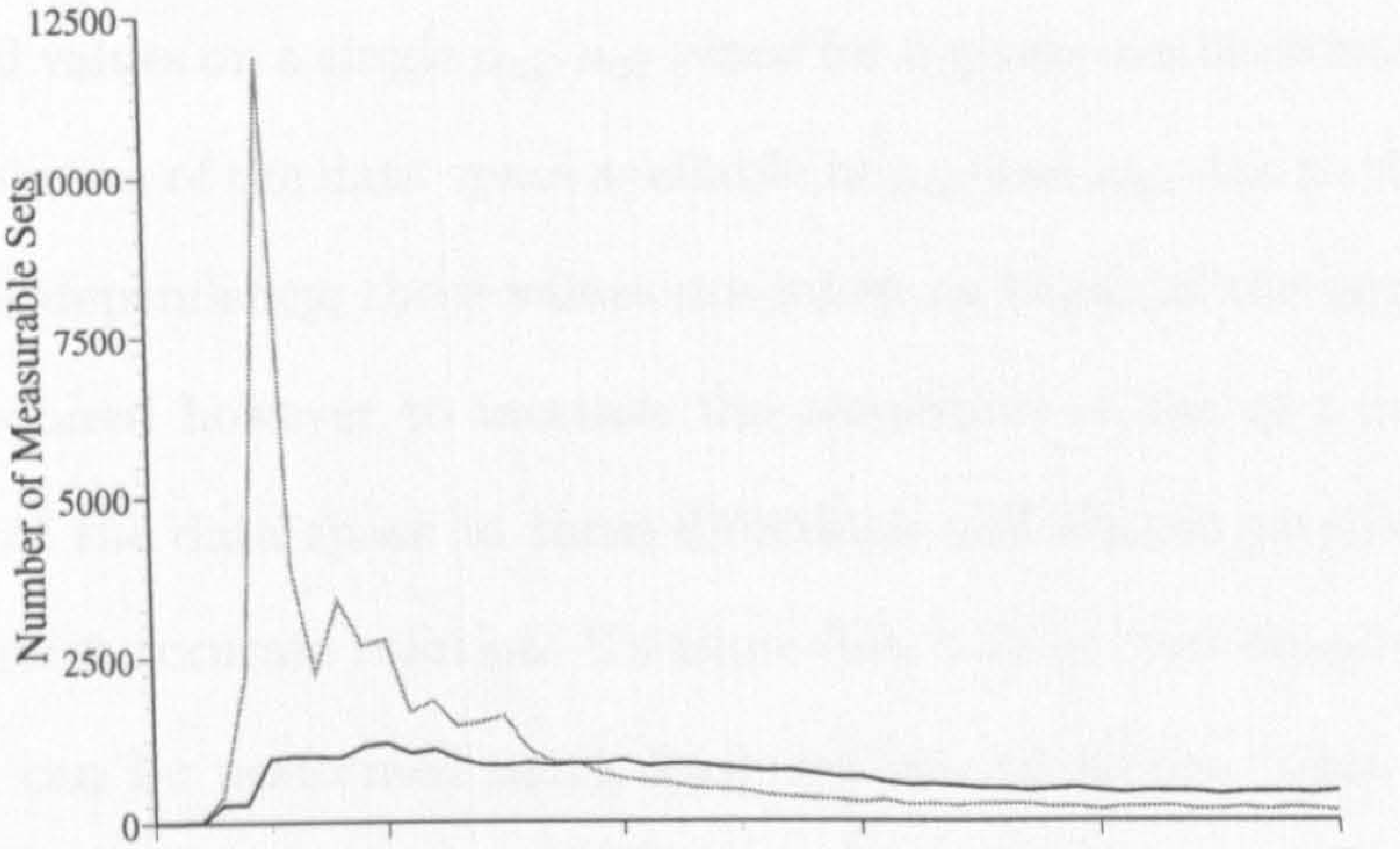

Figure 7.14: *Comparison of the improvement in terms of determined possible solutions with polarization (grey) and no polarization (black).*

table generated through numerical simulations. Discussed here is a consideration of how the solutions flagged by this algorithm can be used to determine individual values for t, μ_{s2}, V_{fmepi}, V_{fhae} and V_{fmder}.

In the ideal case, the result of this combination of measurables will provide a small region of flagged values on a single μ_{a1}-μ_{a2} plane for a given combination of t and μ_{s2}. Due to the high resolution of the data space available in μ_{a1} and μ_{a2} due to the post-simulation inclusion of this dependency, these values are taken as being of the required accuracy. A technique is required however to increase the resolution of the of t and μ_{s2} due to the low resolution of the data space in these directions and also to provide a mechanism to determine the most accurate solution. To allow this, a local, two-dimensional, third order, polynomial fit can be performed using least squares methods. This can be performed by defining a three-by-three matrix formed by the surrounding values in the t and μ_{s2} directions for every flagged value. To provide a more accurate solution the polynomials produced by the fitting algorithm can be solved between measurables. These are solved for corresponding points in the data space for the different measurables. Not only will the solution of these derived polynomials provide an improved result in terms of the resolution available in the t and μ_{s2} directions, but as the problem is over defined (eight measurables defining four variables) two separate systems of equations can be solved for each flagged possible solution point. The difference between the derived result for the two difference sets may then provide an indication of which combination of derived sample parameters is correct. If error free fitting were possible, the correct solution will provide the same solution irrespective of the selected combination of polynomials. Therefore, in the presence of noise, the smallest variation on the derived parameters from the two sets of parameters may provide the most accurate solution.

The fitting of a two dimensional polynomial along the t and μ_{s2} directions is not an error free process. However, errors of this nature will not provide vastly erroneous solutions as the region around which the polynomial is defined is clearly bounded by the three-by-three array. Also, the errors close to the center of the three-by-three matrix, where the result is most likely to occur, are much lower than at the extreme of the two dimensional function.

Initial attempts to provide improved resolution for the determined parameters was performed along all four dimensions of the data. This was in an attempt to improve the resolution along μ_{a1} and μ_{a2} along with t and μ_{s2}. Such fitting however proved impractical due to the large error (up to 20%) resultant from the fitting process. If the resolution along μ_{a1} and μ_{a2} proves a problem, the resolution can be improved by performing more post-simulation analysis on the data with reduced intervals along the two absorption directions.

7.9 Reduction to a Three Variable Problem

Although large regions of the data space are well-conditioned, attempts can be made to reduce the regions of poorly defined measurable sets by reducing the number of variable sample parameters. It has been outlined in the discussion above that the conditioning along the t and μ_{s2} directions proves problematic. Therefore, reduction of the problem to allow variation of only three sample parameters by holding either t and μ_{s2} constant should result in a better conditioned problem. The ability of a clinician to estimate the sample parameters (especially t depending of the site on the body) under certain circumstances may be required. As an alternative to clinician approximation the thickness of the epidermis can be determined using ultrasound techniques[130]. To examine the extent of the improvement provided by the reduction in parameters, the same test of conditioning is performed as for the four dimensional case.

7.9.1 Conditioning with Constant μ_{s2}

Holding the variable μ_{s2} constant at 1.4mm^{-1} will restrict the number of parameter combinations, and therefore input measurable sets, to 9,245. Shown in figure 7.15 are the equivalent plots of figures 7.11 and 7.13 showing the number of flagged solutions for $t = 1.2$mm, 1.4mm^{-1}, for the cases of no dermal melanin and dermal melanin.

It can be seen for the case with no dermal melanin, the number of possible solutions is reduced to proved excellent conditioning for all regions with the exception of high levels of hæmoglobin (V_{fhae}). This is confirmed by assessment of σ_t^2, σ_{a1}^2 and σ_{a2}^2 whilst $\sigma_{s2}^2 = 0$ (due to μ_{s2} being held constant), as shown in figure 7.16.

Conditioning is reduced for high levels of V_{fhae} and begins to mirror the performance for the four dimensional case (figures 7.10 and 7.11). This is due to the increased levels of μ_{a2} suppressing light entering the bottom layer to such an extent that the value of μ_{s2} is insignificant. Therefore, its lack of variation in this three parameter case is inconsequential. This is confirmed when examining the case for dermal melanin. The levels of conditioning and parameter spread for this region has been given in figures 7.15b and 7.17. It is clear from these plots that there is no improvement in conditioning in this region when holding μ_{s2} constant.

7.9.2 Conditioning with Constant t

Reducing the number of variables by holding t constant produces the levels of conditioning, for t = 1.2mm, as shown in figure 7.18. Values of σ_{s2}^2, σ_{a1}^2 and σ_{a2}^2 are plotted for the case of dermal melanin in figure 7.19 and no dermal melanin in figure 7.20. It can be seen from the plots of σ_{a1}^2 and σ_{a2}^2 that the conditioning of these values is extremely good. For low levels of μ_{a2} the performance mirrors that of the previous three parameter problem, however, the performance in an improvement on the previous case for high values of V_{fhae} as the lack of sensitivity to μ_{s2} is tempered by knowledge of the top layer thickness.

It can be seen from figure 7.18b that the conditioning of the problem is much more stable across the region containing dermal melanin than for the four parameter problem. The variation of the parameter values across this region is minimal (figure 7.20). For regions with low levels of dermal melanin the number of data points flagged as possible solutions is reduced by a factor of ten. It was seen in the four parameter problem that

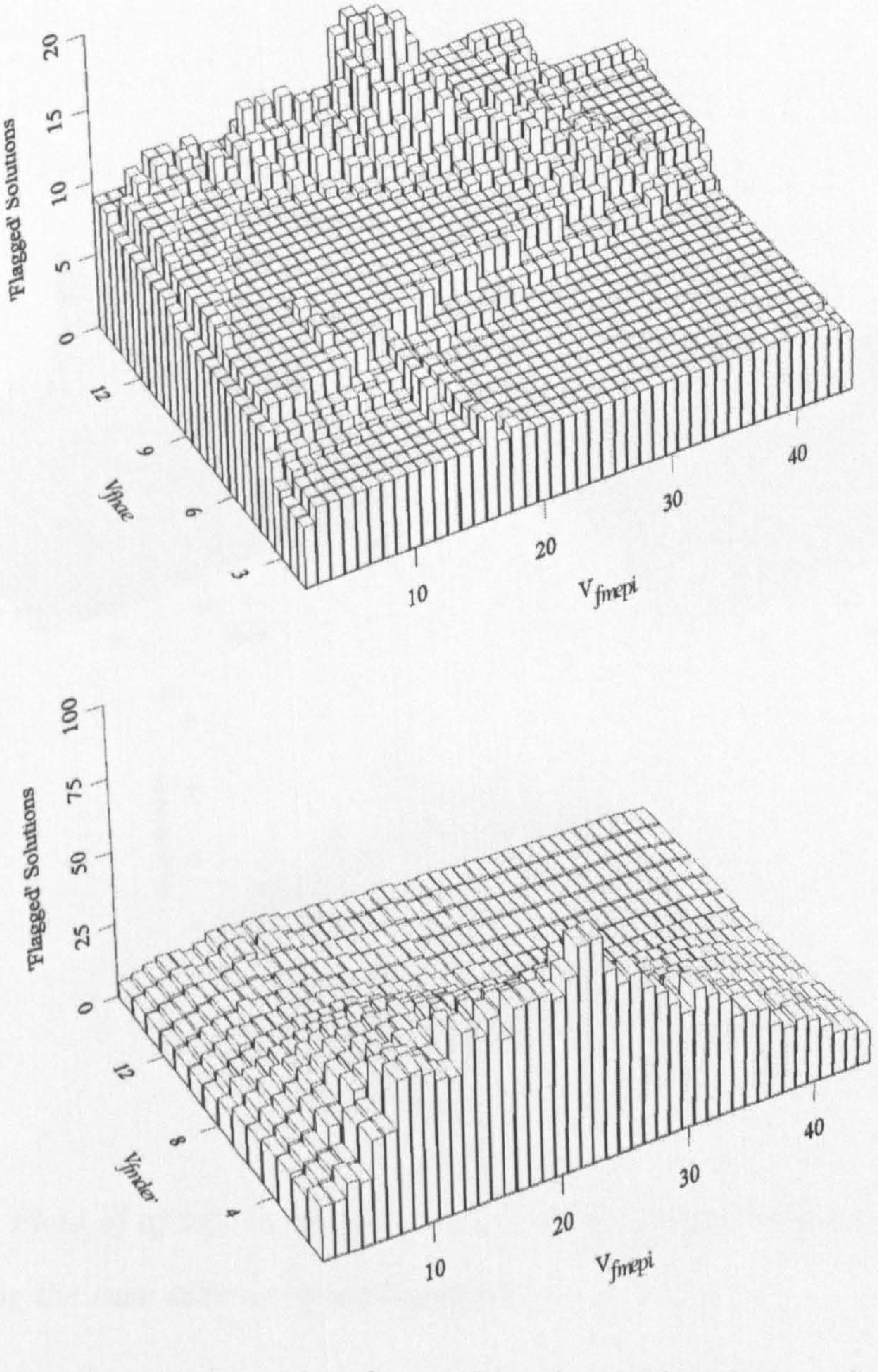

Figure 7.15: *Bar chart representing the number of possible solutions flagged in the regions without dermal melanin (top) and with dermal melanin (bottom) for* $t = 1.2mm$ *and constant* $\mu_{s2} = 1.4mm^{-1}$.

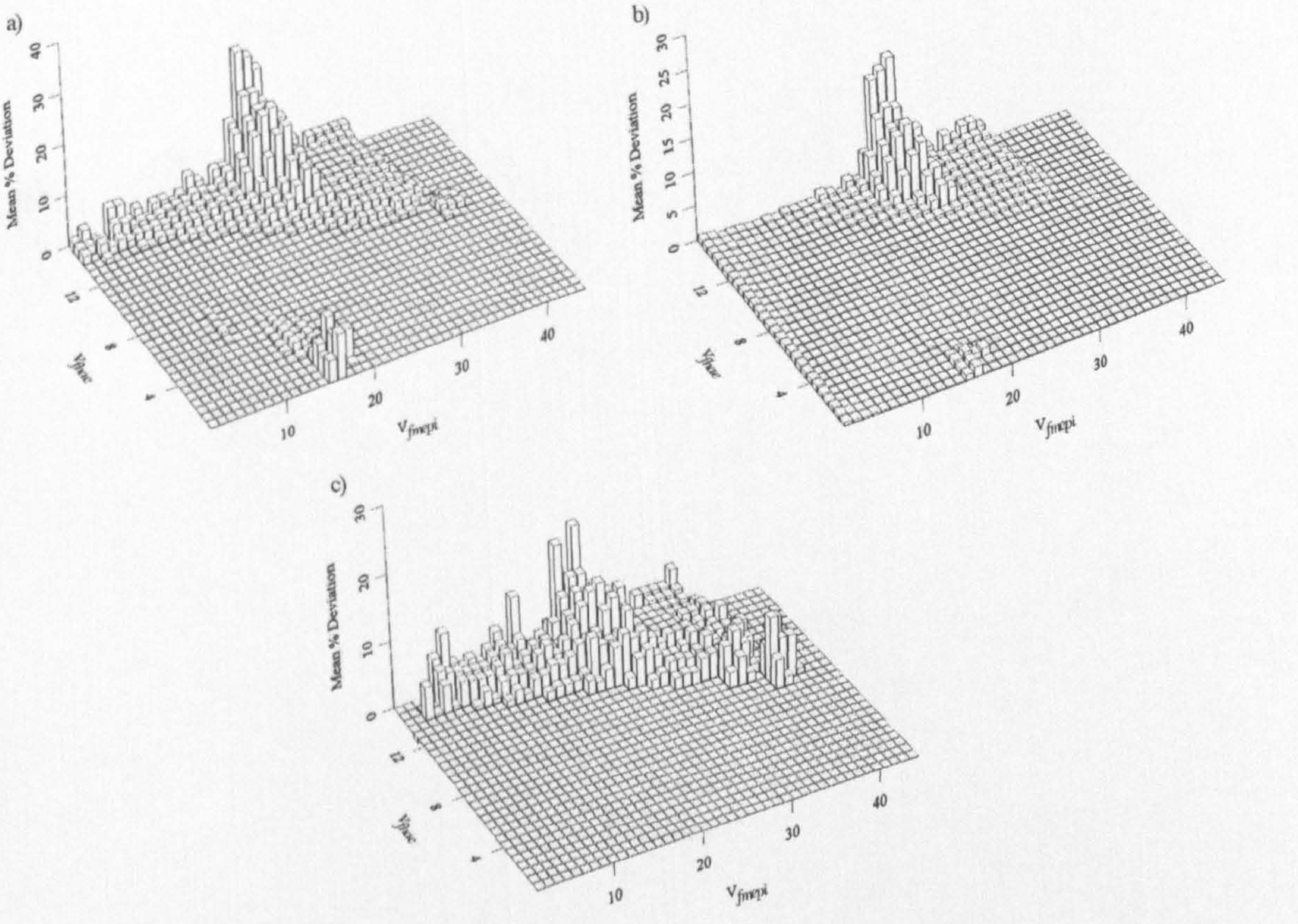

Figure 7.16: *Plots of a)* σ_t^2*, b)* σ_{a1}^2 *and c)* σ_{a2}^2 *for no dermal melanin and d)* σ_t^2*, e)* σ_{a1}^2 *and f)* σ_{a2}^2 *for the case with no dermal melanin.*

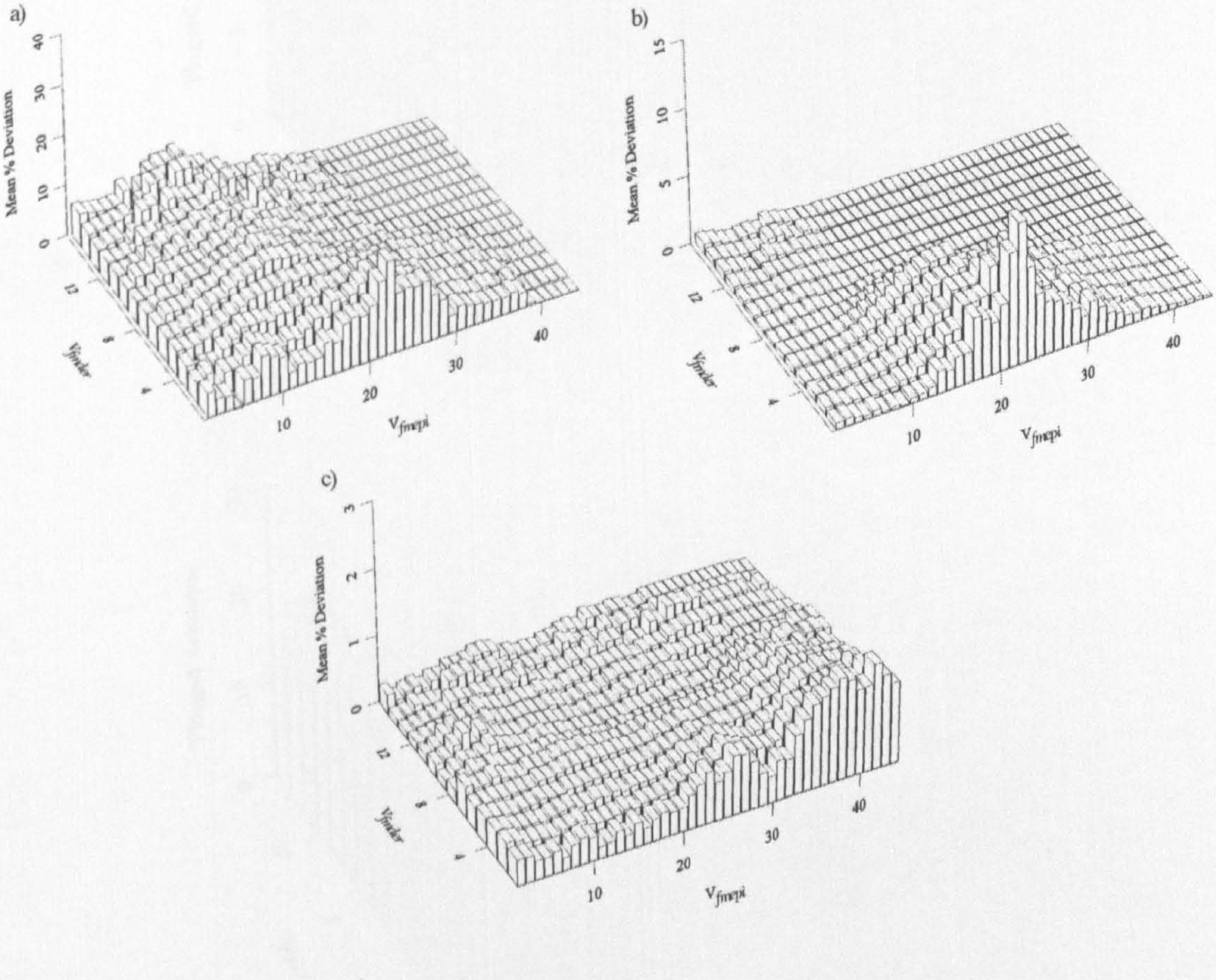

Figure 7.17: *Plots of a)* σ_t^2*, b)* σ_{a1}^2 *and c)* σ_{a2}^2 *for no dermal melanin and d)* σ_t^2*, e)* σ_{a1}^2 *and f)* σ_{a2}^2 *for the case with dermal melanin.*

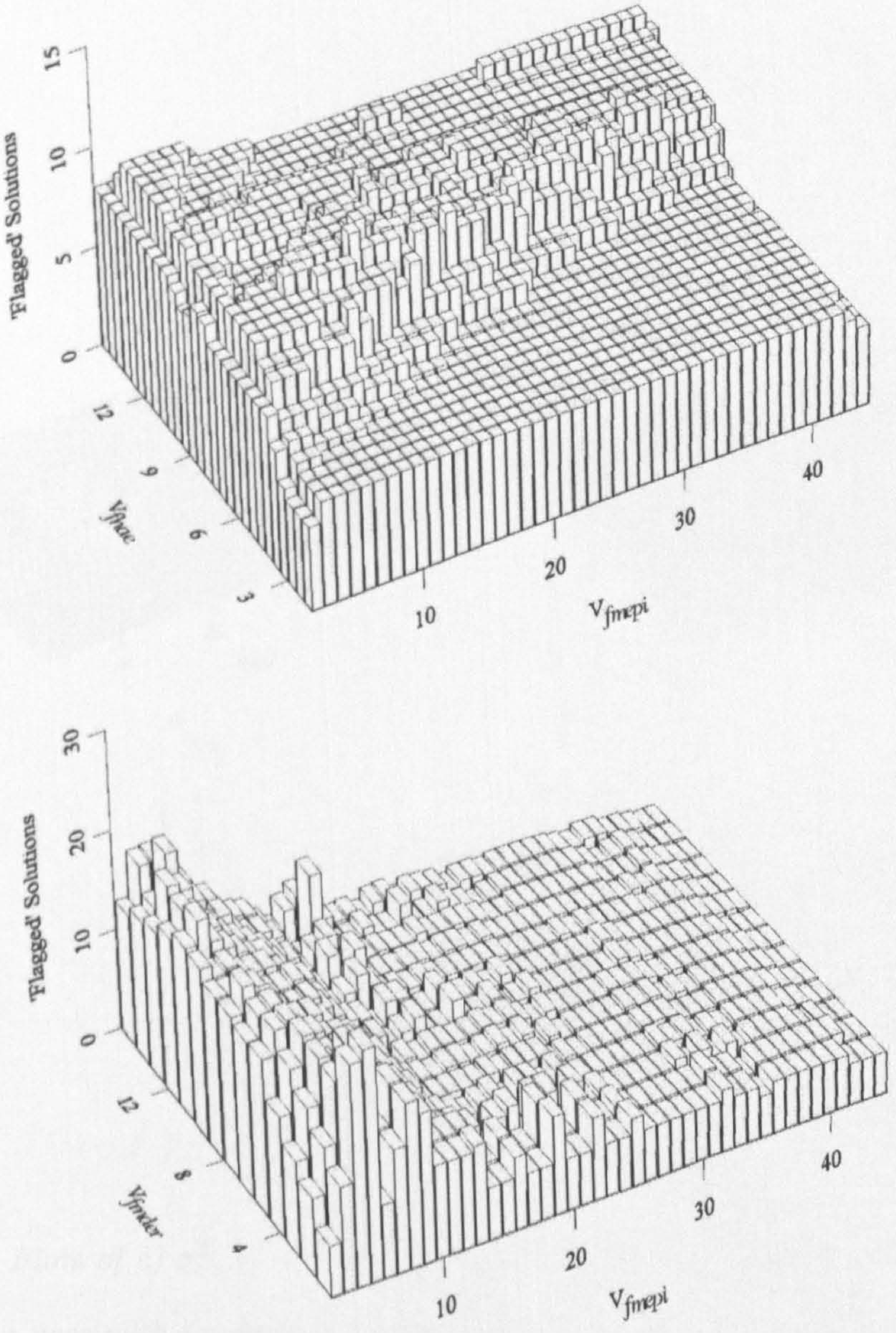

Figure 7.18: *Bar chart representing the number of possible solutions flagged in the regions without dermal melanin (top) and with dermal melanin (bottom) for* $t = 1.2mm$ *and constant* $\mu_{s2} = 1.4mm^{-1}$.

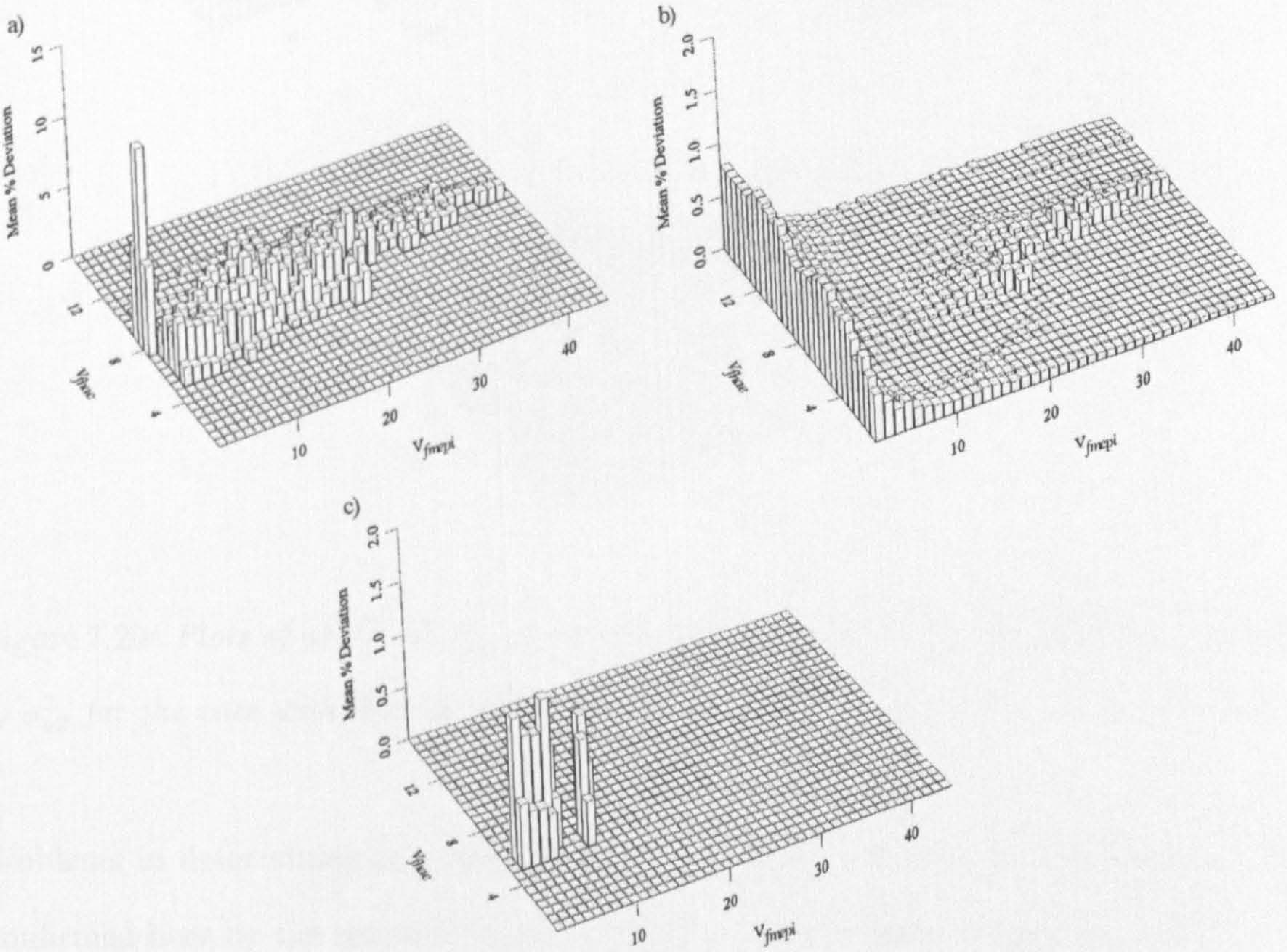

Figure 7.19: *Plots of a) σ_t^2, b) σ_{a1}^2 and c) σ_{a2}^2 for no dermal melanin and d) σ_t^2, e) σ_{a1}^2 and f) σ_{a2}^2 for the case with no dermal melanin with $t = 1.2mm$ and constant $\mu_{s2} = 1.4mm^{-1}$.*

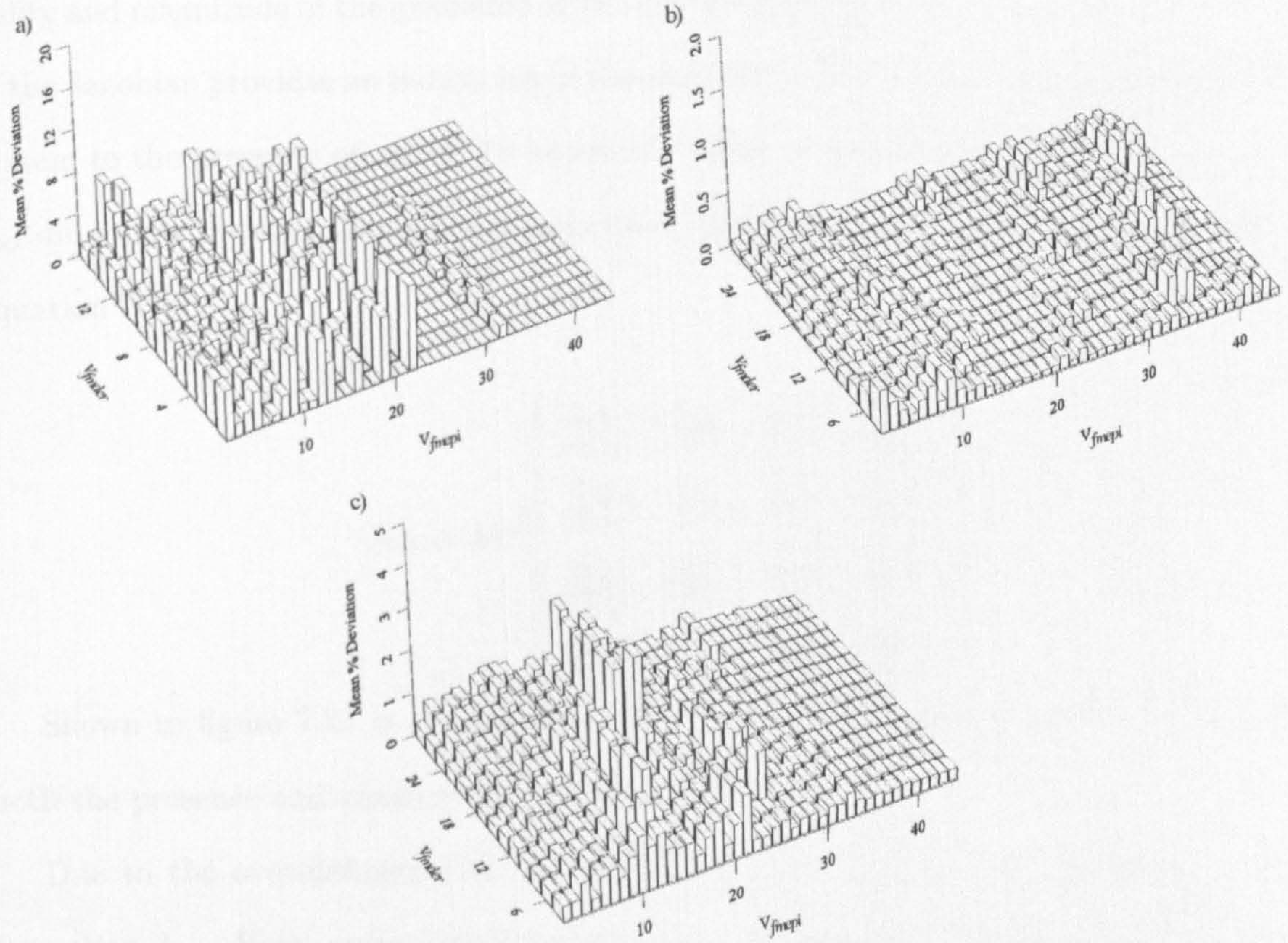

Figure 7.20: *Plots of a) σ_t^2, b) σ_{a1}^2 and c) σ_{a2}^2 for no dermal melanin and d) σ_t^2, e) σ_{a1}^2 and f) σ_{a2}^2 for the case with dermal melanin with $t = 1.2mm$ and constant $\mu_{s2} = 1.4mm^{-1}$.*

problems in determining μ_{s2} lead to the low levels of conditioning encountered. This is confirmed here by the removal of the variable producing much improved result.

7.10 Noise Considerations

Up to this point the determination of possible solutions to the inverse problem has been performed in the absence of noise. The sources of noise in such a system can be introduced experimentally during the detection of the measurables or inherently contained within the simulated model, due to inaccuracies in the modelled absorption spectra or scattering properties of the physical sample.

In section 7.8, the two-dimensional Jacobian has been evaluated to assess the orthogonality and magnitude of the gradients of two measurables with μ_{a1} and μ_{a2}. The evaluation of the Jacobian provides an indication of the sensitivity of the four dimensional measurable system to the presence of noise. To assess the effect of introducing variation in the t and μ_{s2} directions the four dimensional equivalent of equation 7.1, J_{4D}, can be defined, as in equation 7.3.

$$J_{4D} = \det \begin{pmatrix} \frac{\partial M_1}{\partial \mu_{s2}} & \frac{\partial M_1}{\partial t} & \frac{\partial M_1}{\partial \mu_{a1}} & \frac{\partial M_1}{\partial \mu_{a2}} \\ \frac{\partial M_2}{\partial \mu_{s2}} & \frac{\partial M_2}{\partial t} & \frac{\partial M_2}{\partial \mu_{a1}} & \frac{\partial M_2}{\partial \mu_{a2}} \\ \frac{\partial M_3}{\partial \mu_{s2}} & \frac{\partial M_3}{\partial t} & \frac{\partial M_3}{\partial \mu_{a1}} & \frac{\partial M_3}{\partial \mu_{a2}} \\ \frac{\partial M_4}{\partial \mu_{s2}} & \frac{\partial M_4}{\partial t} & \frac{\partial M_4}{\partial \mu_{a1}} & \frac{\partial M_4}{\partial \mu_{a2}} \end{pmatrix} \tag{7.3}$$

Shown in figure 7.21 is the variation of J_{4D} across a plane of constant t and μ_{s2} for both the presence and absence of dermal melanin.

Due to the over-definition of the problem only half of the measurables are used to formulate J_{4D}. Here, polarization maintaining and multiple scatter components are used for illumination at $\lambda = 660$nm and $\lambda = 865$nm wavelengths. The trends observed here are common for each combination of measurables only with varying magnitude. It is intuitive to expect larger orthogonality between extremes of illuminating wavelength (470nm and 865nm) due to the increased contrast in absorption and scattering properties.

It can be seen from the plots that, as initially indicated in section 7.6.1, for low levels of absorption the orthogonality between channels is high. This is due to the different polarization states probing greatly different regions and therefore having varying sensitivity to changes in the properties of the examined sample.

It can be seen that the lowest performance in the presence of noise is found for high values of absorption. This proves to be of increased significance as, not only are the contours in the region more sensitive to noise, but the levels of noise are likely to be more significant due to the low levels of light backscattered under these conditions.

The use of J_{4D} can be exploited further in the minimisation of solutions, which was discussed in section 7.8. Evaluation of J_{4D} can be applied to select the most efficient

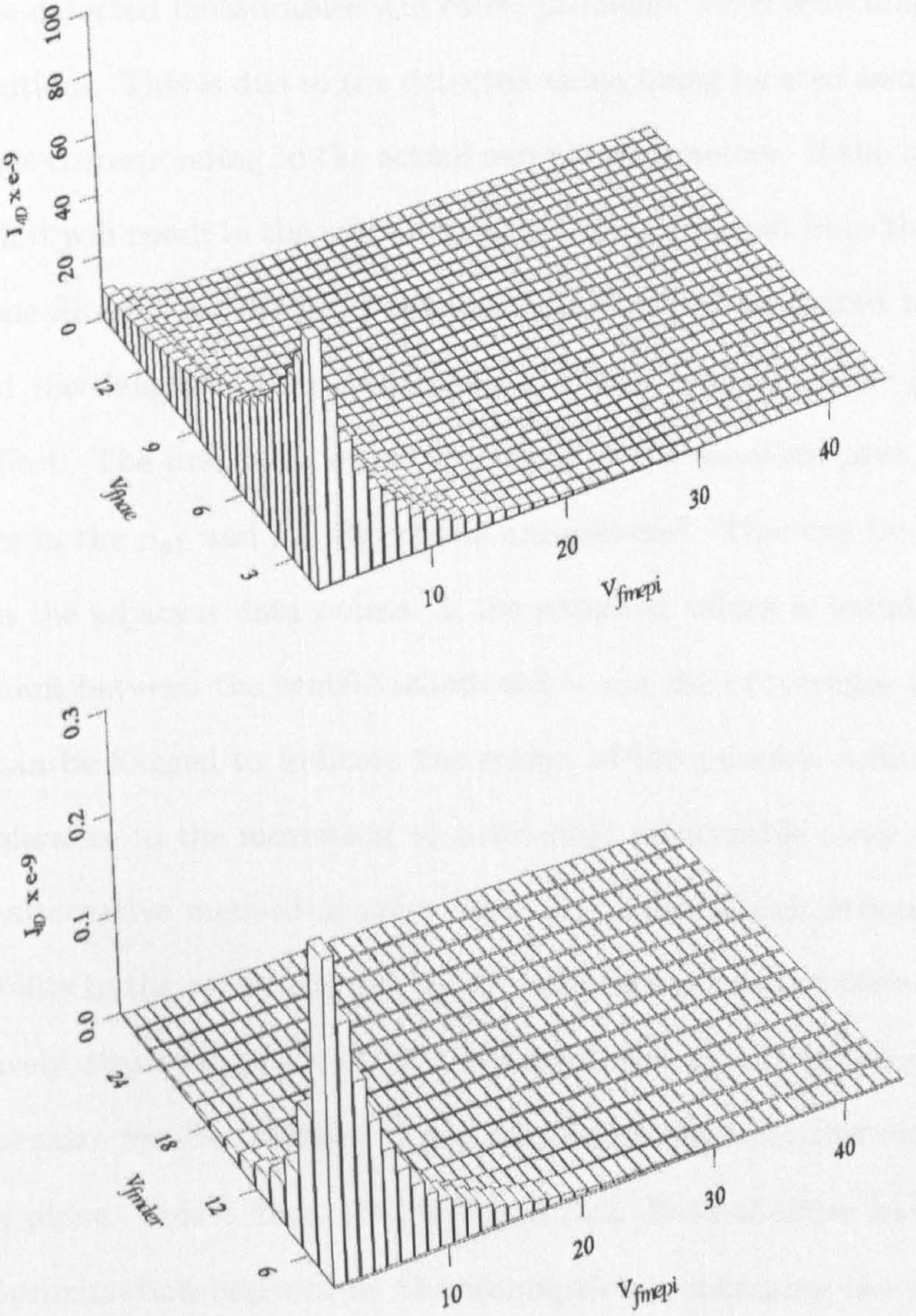

Figure 7.21: *Variation of* J_{4D} *using* $\lambda = 660nm$ *and* $\lambda = 865nm$ *measurables across a* μ_{a1}-μ_{a2} *plane in the regions without dermal melanin (top) and with dermal melanin (bottom) for* $t = 1.2mm$ *and* $\mu_{s2} = 1.4mm^{-1}$.

combination of measurables used to form the two-dimensional polynomials in t and μ_{s2}. The optimum grouping of measurables will produce better performance in the presence of noise when the polynomials are solved between measurables.

Noise on the detected measurables will cause problems when searching the data space for possible solutions. This is due to the detected value being located away from the point in the data space corresponding to the actual sample parameters. If the levels of noise are sufficiently high it will result in the correct solution being rejected from the search process, as it will become filtered out when the possible solutions are compared between polarization states and wavelengths. Two modifications to the techniques are proposed here to combat this effect. The first is to widen the reach of the searched area. Currently, only adjacent values in the μ_{a1} and μ_{a2} directions are assessed. This can be adjusted to span more than just the adjacent data points. If the searched values is found in this extended region, each point between the central search value and the occurrence of the measurable search value can be flagged to indicate the region of the possible solution. This will allow greater tolerance to the movement of a detected measurable away from its expected location. An alternative method of noise tolerance in the search process is presented by allowing flexibility in the overlaying of possible solutions between wavelengths. The arrays can be iteratively displaced by a defined number of data points in the μ_{a1} and μ_{a2} directions to compensate for the presence of a possible solution away from its correct location in the μ_{a1}-μ_{a2} plane. This is illustrated in figure 7.22. Both of these techniques effectively loosen the approximation imposed by the assumptions concerning the absorption spectra of the sample layers.

7.11 Diagnostic Considerations

To evaluate the performance of the data space more usefully it is necessary, not only to examine the mathematical values derived from the processing, but to re-emphasise the relevance of the different regions of the data space in terms of what histological occurrence

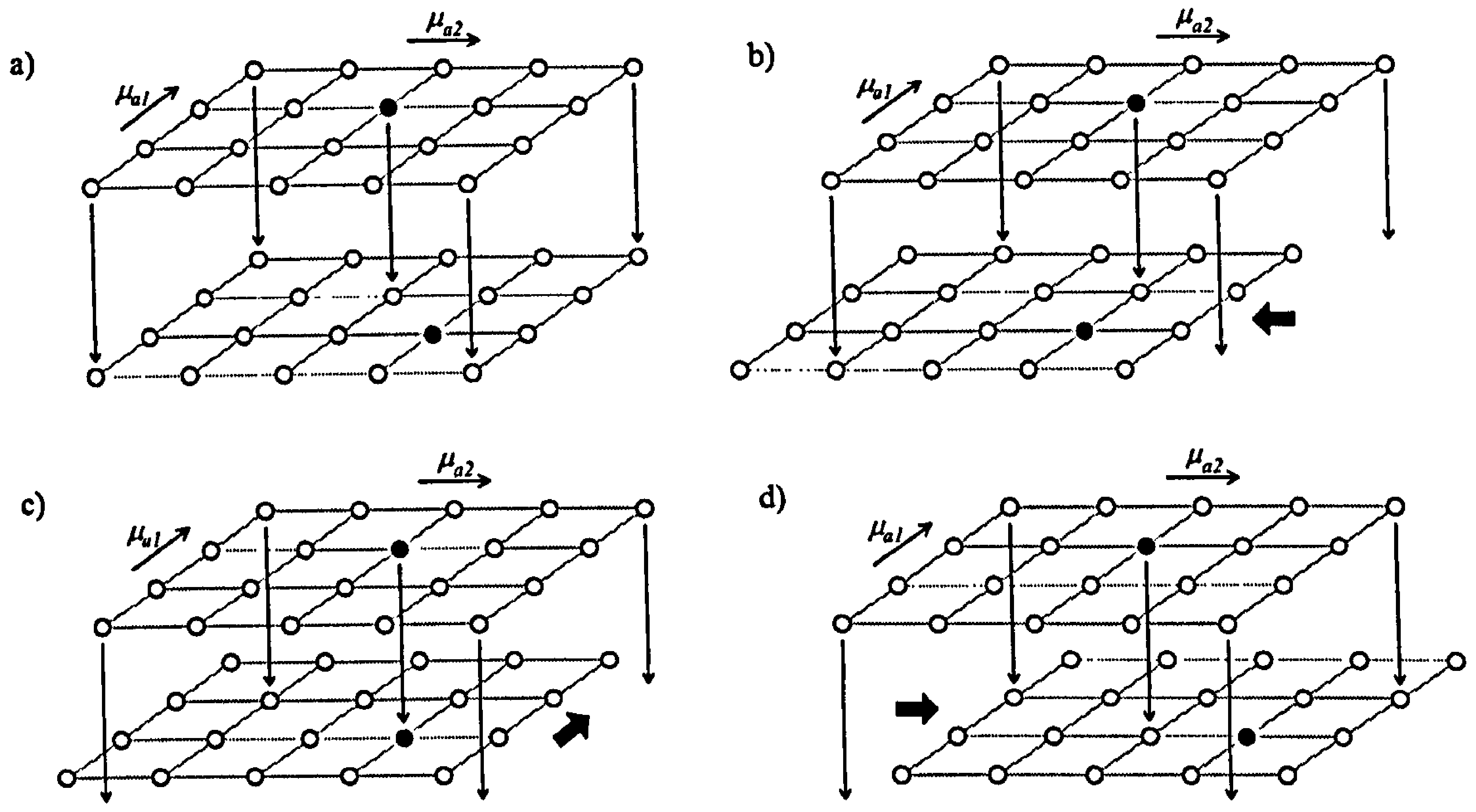

Figure 7.22: *Shown are two measurables with the position of the flagged possible solution at different positions due to the presence of noise. a) shows the case for zero off-set showing the values would be rejected using the standard search. b) shows the array being indexed in the* μ_{a1} *with no match. c) Compensation in the* μ_{a2} *direction in addition finds a match and so the possible solution is maintained. The search continued d) for the defined displacement in all directions on the plane.*

they are intended to represent. This provides an indication of how useful the available data is for diagnosis. It should also be noted that mere quantification of the parameters discussed here does not generally indicate a diagnosis. It is the variation of these parameters over the region of interest which can aid the diagnostic process. For example, in a benign melanocytic lesion, the levels of epidermal melanin can vary greatly between cases. However, it is only when the bulk distribution of the melanin is considered, in terms of its regularity at the margins and variability across the lesion, that the indication of overall histology is provided and commonly used diagnostic mechanisms can be applied.

Considering the results presented in this chapter, it has been shown that, for the levels of pigmentation that would occur for general benign melanocytic lesion and *in-situ* melanoma[16] (high V_{fmepi} and $V_{fmder} = 0$), the data space is well conditioned and may therefore allow determination of the sample properties. For lower levels of epidermal pigmentation, which would occur outside of a lesion, the conditioning has been shown to be detrimented due to the reduced contrast between the illuminating wavelengths. It has been shown however, that reduction to three sample parameters greatly improves the conditioning of the data in this region. Image processing techniques have been widely used to segment pigmented lesions from the surrounding area[102, 103, 104]. Therefore, the determination of properties could be performed using the four parameter data space to analyse the heavily pigmented region and the simplified three parameter model for the surrounding regions. Therefore, if numerical segmentation of the pigmented area is performed, different sample models (with different numbers of variables) can be applied to the different regions.

For the case of dermal melanin, it is apparent from the discussion in section 7.10 that the determination of properties in this region is problematic, not only due to the reduced levels of light producing a higher susceptibility to noise, but also the low orthogonality of the contours of constant measurable value. This is due to reduced contrast between the volumes probed by the different polarization states. Quantification of the levels of dermal melanin may not be as critical as determination of the variation of epidermal melanin across a region. This is due to the tunnelling of melanin in to the dermis indicating more advanced stages of malignancy which, when observed along with other diagnostic indicators to malignant melanoma, may indicate an invasive lesion requiring excision. Therefore, the quantification of V_{fmder} value over an extended region would be desirable, but indication of its presence may prove sufficient for clinical diagnosis.

7.12 Summary

The aim of this chapter has been to investigate the conditioning of a four parameter problem for the determination of the top layer thickness, bottom layer scattering concentration, and top and bottom layer absorption coefficient of a two layer, semi-infinite, scattering medium designed to mimic the properties of healthy and malignant skin tissue. The detection regime used to determine these four parameters uses detection of polarization maintaining and depolarized light at four discrete wavelengths. Examination of the conditioning has been performed through the production of a look-up table using numerical simulations for a range of the four sample parameters which produces eight detectable measurables. It should be remembered that this analysis is performed in the absence of noise to provide a fundamental indication of the potential to perform a successful inversion.

To reduce the complexity of the problem and therefore improve conditioning still further, reduction of the problem to a three variable set of parameters has been investigated. Eliminating the variation of μ_{s2} from the system enhanced the results in the case where no dermal melanin is present, however for the case of dermal melanin, the improvement was minimal. For the three variable problem fixing t the conditioning of the data was greatly enhanced, removing the problems of spectral contrast observed for low values of absorption and reducing the number of possible solutions in the case of dermal melanin.

Results have shown that the four dimensional problem is very well conditioned for large proportions of the data space with a single unique solution being indicated by a small grouping data points indicating the location of a possible solution. Problems occur for low levels of absorption due to lack of contrast between the responses of the different illuminations. However, positioning of the possible solution locations, flagged by the search algorithm, are generally confined to a localised region of the data space, with very few greatly erroneous solutions. This implies that, even though the solution in this region may not be accurate due to the spread of possible solutions, further processing may be able to determine the sample parameters.

Chapter 8

Conclusions

8.1 Summary

This thesis has been concerned with the examination of the interaction of linearly and circularly polarized light with layered scattering media. This has been performed with a view to the development of a clinical instrument used to aid the diagnosis of pigmented skin lesions. The technique takes advantage of the different sources of backscattered light for linear polarization maintaining, circular polarization maintaining and multiply scattered polarization randomised light. Combining these differing properties with the spectral properties of a sample, the aim of the final system would be to extract, from an *in-vivo* human skin tissue sample, values of top layer (epidermal) thickness, top layer absorption (provided by epidermal melanin), bottom layer absorption (due to dermal melanin and hæmoglobin) and bottom layer scattering density (dermal collagen architecture). This extraction is with a view to provide a clinician in a dermatology clinic with histological information to aid the diagnosis of possible malignancies in pigmented lesions. Adaptation of the system could also hold potential for the analysis of burns in a clinical setting evaluating properties such as burn depth which can assist when assessing the need to perform skin grafting.

The first objective of the study was to examine the differing properties of initially linearly and circularly polarized light that are observable when detected after backscatter. This was performed in chapter 3 using Monte Carlo simulations. The polarization maintaining backscatter in these two polarization states were extracted using polarization channel subtraction to remove contributions from the multiple scattered, and hence depolarized, component. The analysis to examine the differences between the two illuminating polarizations initially used the variation of sample thickness to show differences in the depth sensitivity.

Extension to a two layer, semi-infinite medium illustrated that this variation in visitation depth could be exploited to provide differing sensitivity between polarization states to the two different layers within the medium. It was shown that this sensitivity is detectable in the backscatter through assessment of the produced spatial intensity distribution. The model was used to show that the circular polarization maintaining light (for the selected scattering properties) provided increased sensitivity to the bottom layer of the sample, whereas the linear polarization maintaining photons provided sensitivity almost exclusively to the upper region.

Use of the spatial distributions was also applied to illustrate the improvement in lateral confinement provided by the extraction of polarization maintaining light. To confirm the apparent regions of sensitivity of linear polarization maintaining, circular polarization maintaining and depolarized multiple scattered light, the visitation depth into a single layer, semi-infinite medium was evaluated. This illustrated a distribution peak for linearly polarized light at 2MFPs into the sample, a depth of 7MFPs for circular polarization maintaining and 10MFP for the multiple scattered component as shown in figure 3.20.

The concept of both lateral and depth confinement was evaluated in chapter 4. This was provided through numerical modelling and experimental results, imaging a variable depth, sub-surface absorber. The simulated and experimental results were compared and showed good agreement and the simulations illustrated improved resolution of a factor of 31.2 for linear polarization maintaining light and 3.6 for the circular case when the absorber is located within the appropriate depth gate.

The first step towards the evaluation of the investigated techniques on *in-vivo* human skin tissue is provided at the end of chapter 4. These preliminary results indicated a clear difference in the sources of backscatter in the two extracted polarization maintaining channels compared with the multiple scatter which exhibits poor spatial confinement.

The optical system used to obtain these initial skin tissue images was modified to be appropriate for application in a clinical setting and extended to use illumination at multiple wavelengths. The reasoning behind this decision was presented in chapter 5 along with the design of the automated prototype system. The design and construction of this system provided a large step towards achieving the goals of the study as it allows illumination of an *in-vivo* sample with four wavelength of linearly and circularly polarized light and evaluation of a sixteen channel detection scheme using a simple, low cost and rugged system.

The improvement on currently applied techniques, provided by the detection of circular polarization maintaining light as proposed here, is presented in chapter 6. The improvement is summarised graphically in figure 8.1. This shows the result of applying cross-polar detection using linearly polarized illumination to remove the contribution due to surface reflections. This technique produces a low resolution image of the pigmented region. The second image illustrates the effect of applying a flat glass plate and matching fluid to remove surface reflections, coupled with the extraction of linear polarization maintaining backscatter to remove the poorly conditioned multiple scatter. This technique shows good improvement on the previous technique, but large surface texture contributions are still observable, reducing the quality of information available from the sub-surface region.

The final image in figure 8.1 is the result using the techniques proposed here. This image is formed through the extraction of circular polarization maintaining light. Therefore, it is free from surface contributions as the surface components emerge orthogonal to the illumination polarization state. Multiple scatter is removed through polarization subtrac-

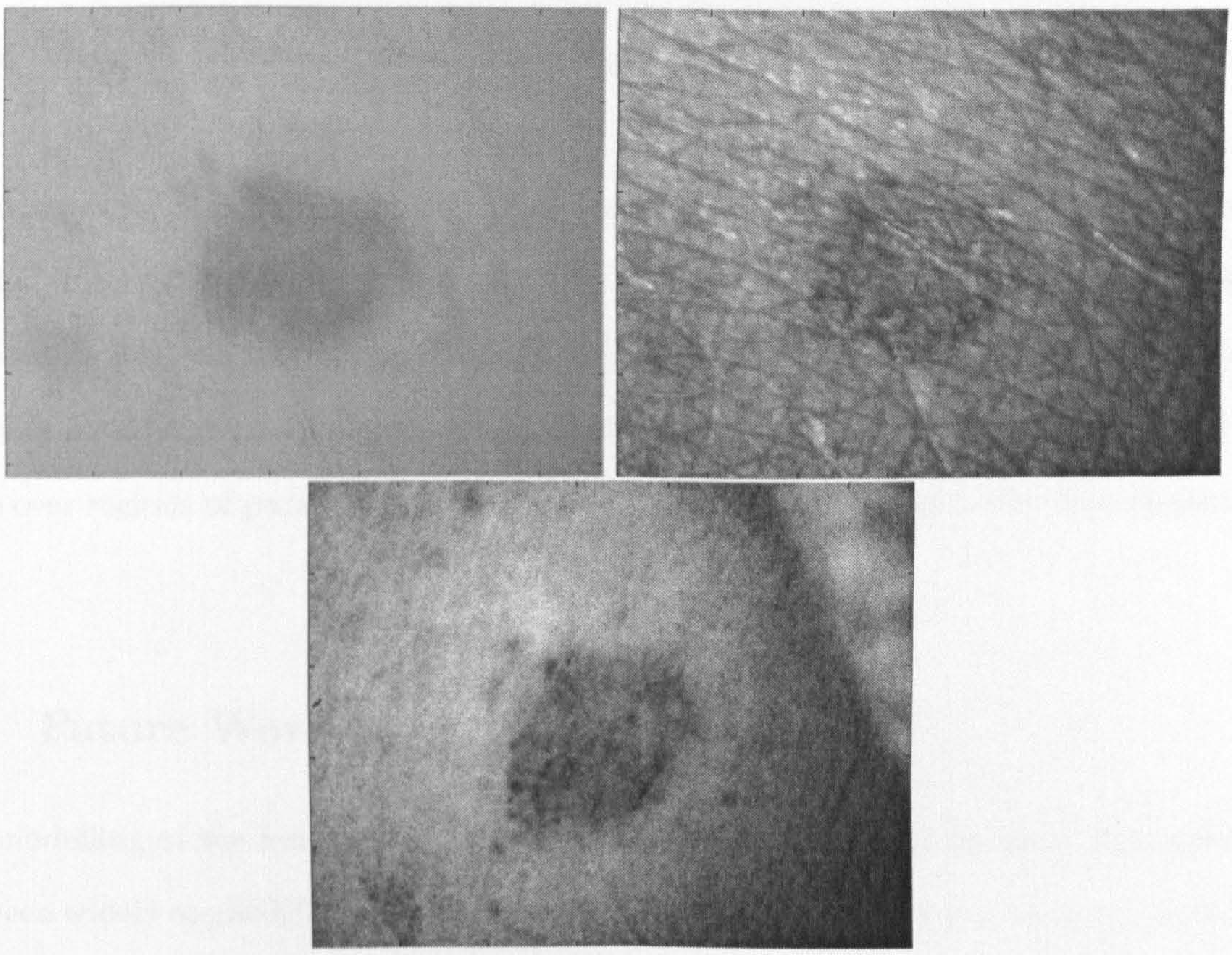

Figure 8.1: *Comparison of existing techniques to provide sub-surface imaging of tissue. The result of detecting linearly polarized light in the plane orthogonal to that of illumination to remove surface reflections (top left) and the result of using a flat glass plate and matching fluid coupled with linear polarization image subtraction to remove surface reflections and multiple scatter (top right). The lower image is the result obtained using the extraction of circularly polarized light to provide a localised sub-surface image free of surface components.*

tion, which means that the circularly polarized light image out performs that observed due to multiple scatter.

Modelling the use of the system developed in chapter 5 to analyse two layer samples representing the skin, is presented in chapter 7. This is toward the assessment of the potential to determine sample parameters using intensities detected in different polarization states at the four illuminating wavelengths. Analysis showed that extraction of top layer thickness, bottom layer scattering along with top and bottom layer absorption may be possible due to the problem being generally well-conditioned in the absence of noise. It has been shown that the reduction of the problem to three parameter variation, by applying prior knowledge concerning the top layer thickness, improves the stability of the data space over regions of parameter variation that proved problematic in the four dimensional case.

8.2 Future Work

The modelling of the human skin using samples composed of independent Mie scatterers has been widely applied[131] as it has been here. However, it has become apparent from the analysis presented in chapter 4 and the results presented in section 4.4 and chapter 6 that there are clear discrepancies between behaviour of polarized light propagating in uniform scattering media compared with skin tissue. This can be observed by the comparison of the differences between the multiple scatter component and the circular polarization maintaining component in the cases of modelling and *in-vivo* tissue, as discussed in section 4.5.

As stated above, the applied model has been used extensively to model the skin, however, in a technique examining such superficial depths of the sample using short path length photons, as is the case here, the validity of the approximation appears questionable. It is observable from skin histology that, rather than being composed of independent scatter centres the structure is made up from tightly packed cells with scattering nuclei.

Effects will therefore be observable due to the microscopic nucleus and the larger encompassing cellular boundary. Efforts to improve the modelling of skin tissue will clearly allow a better understanding of the behaviour of light propagating through the sample.

A very early suggestion towards an improved model of cellular scatterers was presented by Brunsting and Mullaney[132]. This involves scatterers being represented as spheres of constant refractive index 'coated' by a layer of differing refractive index in an attempt to represent the cell's nucleus and surrounding cytoplasm. Other methods have since been reported concerning the modelling of the subtle variations of refractive index within a cell[133] aiming to produce a more realistic model of light interacting with cells.

A major property concerning the propagation of polarized light in skin tissue which has not been considered in this fundamental study is the occurrence of birefringence due to the fibrous nature of collagen. It is clear that the trends illustrated in this study will be altered by this property. However, it is apparent from the tissue images presented in chapters 4 and 6 that the principles of the extraction of circular polarization maintaining light to achieve sub-surface reflection free images still hold. Incorporation of birefringence into the model (as in [76]) however will clearly improve on the approximations applied here.

Further research is also necessary into the possible inversion from the measurables detected by the clinical system to the variable sample parameters. It has been shown in chapter 7 that the four parameter inversion appears well-conditioned in the absence of noise, indicating the potential for successful sample characterisation. The validity of these findings should be confirmed in the presence of noise numerically and experimentally. The continued investigation using the Mie scattering model, rather than an improved model as discussed above, is initially appropriate as the modelled situation can be easily mirrored in an experimental setting using microsphere based phantoms. Therefore, the accuracy due to modelling error is minimised, which is the reason for selection of this sample model, as stated in chapter 7.

The localisation techniques discussed in this thesis may also provide enhancements to current systems. During this research experimental studies have been performed to couple polarization discriminated detection with Doppler flowmetry in an attempt to improve the sensitivity to flowing scatterers used to model blood cells. The localisation abilities of polarization discrimination can also be applied to existing hyperspectral imaging systems as this may allow more accurate determination regions of interest without interference from other layers with differing properties.

Short term further work concerning improvements to the developed system has already been addressed in section 6.4 and therefore shall not be discussed here. However, once multiple wavelength sub-surface images are obtained using the developed system, analysis techniques previously used to determine the malignancy of a lesion (see section 2.4) may be applied to either directly to the extracted polarization images or to maps of the extracted optical coefficients, or physical properties which are derived from them. Therefore, the improved definition of the extracted images that is expected, due to the absence of surface and deeply penetrating light, may prove much better conditioned as an aid to lesion classification.

8.3 Closing Remarks

This study has illustrated the differences in maintenance of initial polarization state of linearly and circularly polarized light for highly forward scattering media composed of spherical scatterers designed to represent the skin. These differences have been shown to provide sensitivity to different depths within a scattering medium using both modelling and experimental investigation.

The differences in the backscattered components from tissue samples due to illumination with the different polarization states has also been shown to allow production of an image representing a sub-surface, localised region, free from surface contributions. This concept has been extended to the design and construction of an automated prototype multiple wavelength imaging system suitable for testing in a clinical setting.

The ability to provide discrimination in depth using different polarization states at different wavelengths has then been extended to show the possibility of extraction of physical and optical properties from a two layer scattering medium representing human skin tissue. This opens up the possibility of extracting histological information from the sample, aiding the diagnostic process.

Appendix A

Effects of Multiple Scatter Subtraction

The extraction of light which has maintained its polarization state after interacting with a scattering medium can be attempted through the subtraction of two orthogonal polarization channels. This is possible as both channels will contain a randomly polarized component that will contribute equally to both channels. Therefore, subtraction of the two channels will remove the contribution to this random component and leave only light which has not undergone enough scattering events to become depolarized.

However, for the case of circularly polarized illumination the polarization channel orthogonal to the illumination (channel 4) contains, in addition to the randomly polarized multiple scatter, a contribution due to singularly scattered photons which will have had the helicity of polarization flipped and emerges in this state. Therefore, subtraction of the co- and cross-polar channels in this case will affect the light interacting with superficial regions in addition to the removal of deeply probing light. Therefore, as an approximation, the multiply scattered light emergent from linearly polarized illumination is subtracted from the co-polar circularly polarized channel (channel 3). This assumes the random component due to multiple scatter in linearly polarized light is the same as that for circular

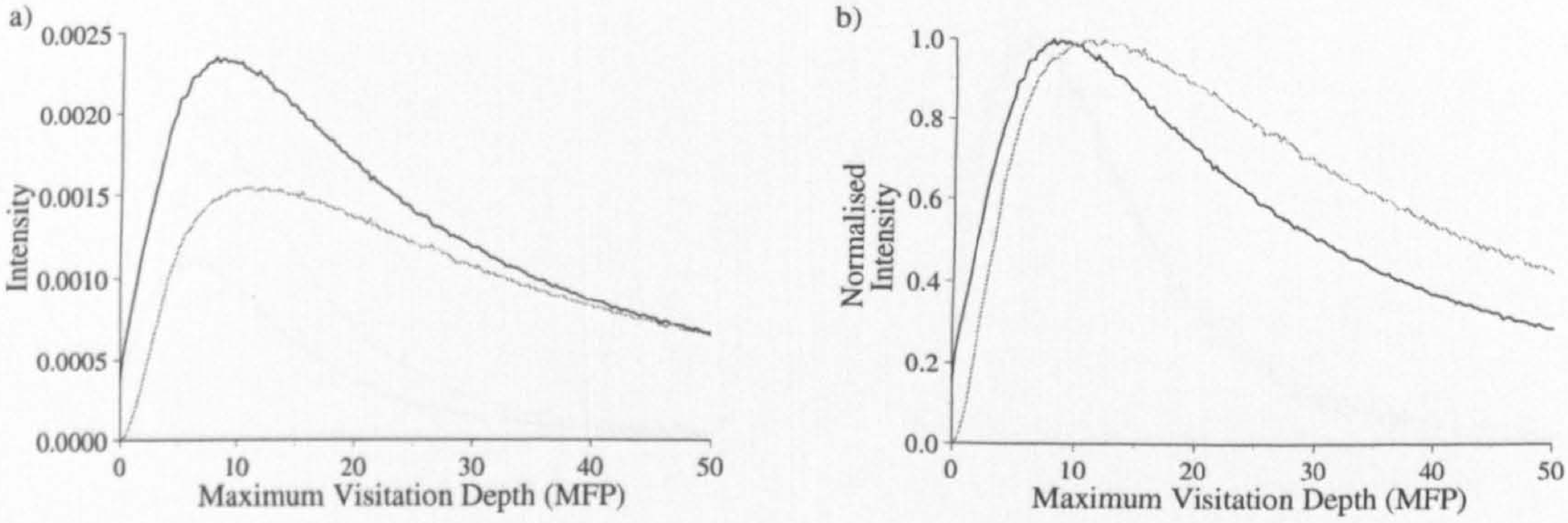

Figure A.1: *a) The backscattered intensity from different visitation depths of linearly polarized multiple scatter (black) and an approximation to circularly polarized multiple scatter (grey) and b) the same distributions normalised to peak intensity.*

polarizations.

Shown in figure A.1 are the visitation depths of multiple scatter due to linearly polarized illumination and an approximation to the multiple scatter component due to circularly polarized illumination. The circularly polarized multiple scatter is formed by detection of the cross-polar channel 4, but rejection of any backscatter that has undergone less than ten scattering events. This provides removal of the directly backscattered photons which have had their helicity reversed and therefore leaves only depolarized light.

It can be seen from these plots that the depths probed by the different polarization states differ. However, to test directly the effect of approximating multiple scatter due to circularly polarized illumination to that of linearly polarized illuminating in extracting circular polarization maintaining light the subtractions for each case can be performed by using the distributions plotted in figure A.1. The results of the two subtractions are shown in figure A.2.

It can be seen from these distributions that there is little different in terms of the depths probed by the different extraction processes. The main observable difference occurs in the intensity of the extracted light. It can be seen that the intensity when subtraction is

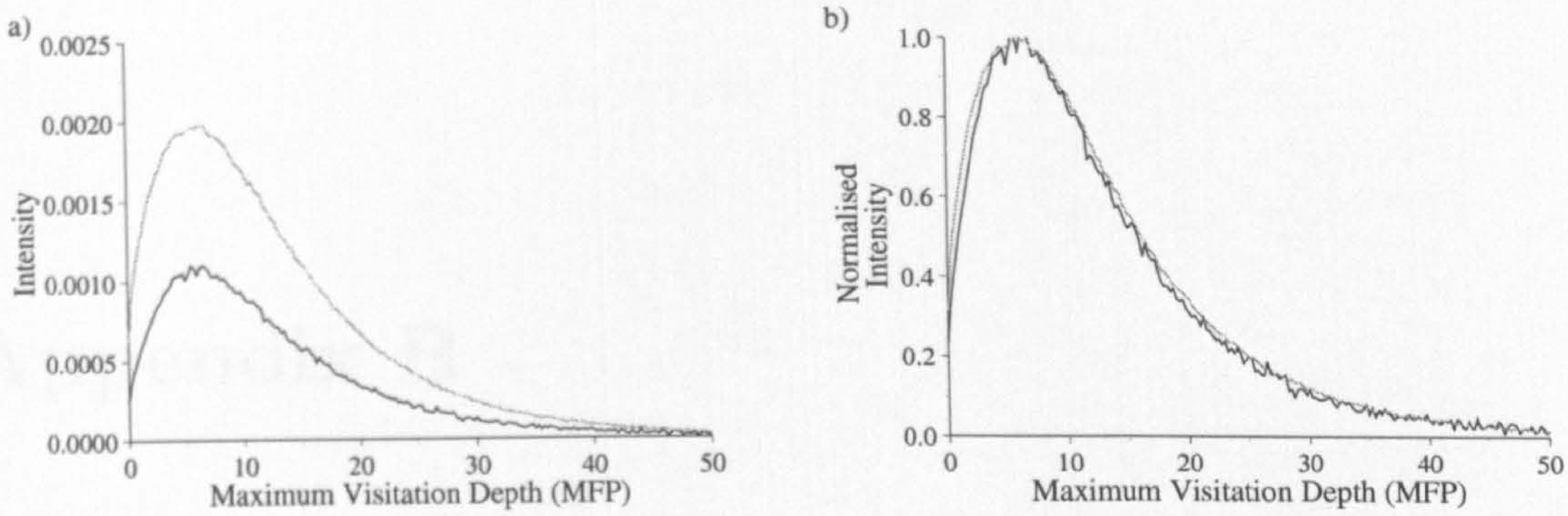

Figure A.2: *Circular polarization maintaining light extracted through subtraction of linearly polarized multiple scatter (black) and circular polarized multiple scatter (grey). This is shown for a) for absolute and b) normalised intensity.*

performed using linearly polarized multiple scatter is approximately half of that for the subtraction of circularly polarized states. This is due to the reduced polarization maintenance of linearly polarized light providing a higher intensity multiple scatter component, for depths less than 50MFPs, compared to the circularly polarized multiple scatter.

From the results presented here it can be seen that the only detriment due to the use of initially linearly polarized multiple scatter over the circularly polarized case is the reduction in intensity, resulting in a reduced SNR.

Appendix B

Retardation Effects on Linear Polarizations

B.1 Introduction

In the initial polarization imaging set-up that is demonstrated in chapter 4 (figure 4.9), quarter wave retardation components are present in both the illumination and detection arms. These are used to produce the circular polarization state in the first instance and to analyse the polarization of the light returned in the second. This situation occurs when the fast axis of these components are aligned at 45 degrees to the initial plane of linear polarization of the incoming light. However, to reduce the effect caused by movement artifacts in the case of *in-vivo* tissue imaging, these components are left in place, but are rotated to align their fast axes parallel to the plane of the linearly polarized light. It has been postulated that the presence of these components will have no effect. However, it is clear that scattered initially linearly polarized light that is returned at 45 degrees to it's initial polarization plane will pass through the quarter wave retardation component at 45 degrees to it's fast axis. This results in a circular polarization state which would not occur if the retardation component were not present in the system. It is clear that this case would result in equal contributions to the co-polar and cross-polar channels. However, for intermediate elliptically polarized states the equivalence to the linear polarization states without the additional retardation is not as clear. Here, it is proven mathematically that, using ideal optical components, there is no effect on the intensity of the emerging light from the polarization analysis components due to the presence of this retardation.

B.2 Analysis with No Additional Retardation

In the perfect system with no quarter wave retardation component present in the detection arm of the system. Imaging would be performed through a single linear polarizer. The light emerging from the sample for detection would not be completely randomised and would have a tendency toward the plane of polarization of the input beam. This subtle non-uniformity is inconsequential to discussion here and therefore, the random polarization can be represented in a single Stokes vector as:

$$S_r = \begin{pmatrix} 1 \\ 0 \\ 0 \\ 0 \end{pmatrix} \tag{B.1}$$

However, here we wish to consider the effect of the polarization analysis system on every angle of linear polarization present within the random polarization (assuming that the backscatter contains solely linear polarizations along all azimuthal planes). Therefore, a single linear plane of polarization present within the randomly polarized beam can be represented as shown in equation B.2.

$$S_{rl}(\theta = \phi) = \frac{1}{N_\theta} \begin{pmatrix} 1 \\ \cos(2\phi) \\ \sin(2\phi) \\ 0 \end{pmatrix} \quad 0 \leq \theta \leq 2\pi \tag{B.2}$$

where θ is the angle away from the horizontal of the plane of polarization and N_θ is the number of azimuthal angular bins.

The polarization state of light emerging from an ideal linear polarizer is intuitive, but can be calculated from the product of the incident Stokes' vector representing the light and the Mueller matrix of a linear polarizer. For our purposes we are interested in a horizontally and vertically orientated polarizer with Mueller matrices M_{ph} and M_{pv} respectively.

$$M_{ph} = \frac{1}{2} \begin{pmatrix} 1 & 1 & 0 & 0 \\ 1 & 1 & 0 & 0 \\ 0 & 0 & 0 & 0 \\ 0 & 0 & 0 & 0 \end{pmatrix} \tag{B.3}$$

$$M_{pv} = \frac{1}{2} \begin{pmatrix} 1 & -1 & 0 & 0 \\ -1 & 1 & 0 & 0 \\ 0 & 0 & 0 & 0 \\ 0 & 0 & 0 & 0 \end{pmatrix} \tag{B.4}$$

Therefore the Stokes' parameters of the output light for the ideal case in the two linearly polarized detection channels can be seen to be, for any arbitrarily orientated linear polarization, as is resultant in equations B.5 and B.6.

$$S_{oh}(\theta=\phi) = \frac{1}{2N_\theta}\begin{pmatrix} 1+\cos(2\phi) \\ 1+\cos(2\phi) \\ 0 \\ 0 \end{pmatrix} \tag{B.5}$$

$$S_{ov}(\theta=\phi) = \frac{1}{2N_\theta}\begin{pmatrix} 1-\cos(2\phi) \\ 1-\cos(2\phi) \\ 0 \\ 0 \end{pmatrix} \tag{B.6}$$

B.3 Analysis with Additional Retardation Component

The analysis with the quarter wave retardation components included with their fast axes aligned with the plane of illuminating polarization begins with the same backscattered components as in the analysis from the previous section represented in equation B.2. This light is then subjected to the retardation component before the linear polarizer. The general form of Mueller matrix to represent a quarter wave retardation component at an angle of θ to the horizontal is given below as defined in [39]:

$$M_q(\psi) = \begin{pmatrix} 1 & 0 & 0 & 0 \\ 0 & \cos^2(2\psi) & \cos(2\psi)\sin(2\psi) & -\sin(2\psi) \\ 0 & \cos(2\psi)\sin(2\psi) & \sin^2(2\psi) & \cos(2\psi) \\ 0 & \sin(2\psi) & -\cos(2\psi) & 0 \end{pmatrix} \tag{B.7}$$

where ψ is the angle made by the fast axis of the quarter waveplate and the plane of illuminating polarizations. As already stated for the linearly polarized channels, the retardation component has it's fast axis aligned to the plane of illuminating polarization, assumed here to be horizontal. Therefore the result of propagation through such a component will result in light with the following Stokes vector.

$$S_{rl}(\theta) \times M_q(\psi=0) = \frac{1}{2N_\theta}\begin{pmatrix} 1 \\ \cos(2\phi) \\ \sin(2\phi) \\ 0 \end{pmatrix}\begin{pmatrix} 1 & 0 & 0 & 0 \\ 0 & 1 & 0 & 0 \\ 0 & 0 & 0 & 1 \\ 0 & 0 & -1 & 0 \end{pmatrix} = \frac{1}{2N_\theta}\begin{pmatrix} 1 \\ \cos(2\phi) \\ 0 \\ -\sin(2\phi) \end{pmatrix}$$

This resulting Stokes vector is then subjected to linear polarizers with the same Mueller matrix properties as in the previous case (equations B.3 and B.4). The resulting Stokes' vectors emerging from the polarization analysis system are shown below:

$$S_{oh}(\theta=\phi) = \frac{1}{2N_\theta}\begin{pmatrix} 1 \\ \cos(2\phi) \\ 0 \\ -\sin(2\phi) \end{pmatrix}\begin{pmatrix} 1 & 1 & 0 & 0 \\ 1 & 1 & 0 & 0 \\ 0 & 0 & 0 & 0 \\ 0 & 0 & 0 & 0 \end{pmatrix} = \frac{1}{2N_\theta}\begin{pmatrix} 1+\cos(2\phi) \\ 1+\cos(2\phi) \\ 0 \\ 0 \end{pmatrix} \tag{B.8}$$

$$S_{ov}(\theta=\phi) = \frac{1}{2N_\theta}\begin{pmatrix} 1 \\ \cos(2\phi) \\ 0 \\ -\sin(2\phi) \end{pmatrix}\begin{pmatrix} 1 & -1 & 0 & 0 \\ -1 & 1 & 0 & 0 \\ 0 & 0 & 0 & 0 \\ 0 & 0 & 0 & 0 \end{pmatrix} = \frac{1}{2N_\theta}\begin{pmatrix} 1-\cos(2\phi) \\ 1-\cos(2\phi) \\ 0 \\ 0 \end{pmatrix} \tag{B.9}$$

It is clear from the comparison of equations B.8 and B.9 with B.5 and B.6 that the system without the quarter wave retardation component is equivalent to that with it present and aligned parallel with the plane of illuminating linear polarization.

Appendix C

Mie Scattering Effects on Spatial Distributions

It has been illustrated by the spatial distribution shown in figure 3.16 that the DOP of linearly polarized light reduces for increasingly large source-detector separations. However, as has been pointed out in section 3.7 the peak in the distribution is slightly away from the point of illumination which is counter-intuitive. This affect can be put down to the specific scattering pattern of the simulated scatterers.

The illumination is provided by an infinitesimally narrow beam entering the medium at a single point and therefore, the first photon-particle collision is always along the $x = 0, y = 0$ line. For this reason, detection of light which is single scattered from the medium will have a tendency to the angular variation of single particle scattering in the backwards direction. The result of such an analysis on the media considered in chapter 3 provides the angular intensity distribution shown in figure C.1. This plot takes into account refraction at the interface due to the refractive index mismatch. The area under the plot is normalised to unity.

From this plot it can be seen that there is a peak at 14 degrees to the normal. Assuming a scattering event 1MFP sub-surface, this would result in an emergence displacement from

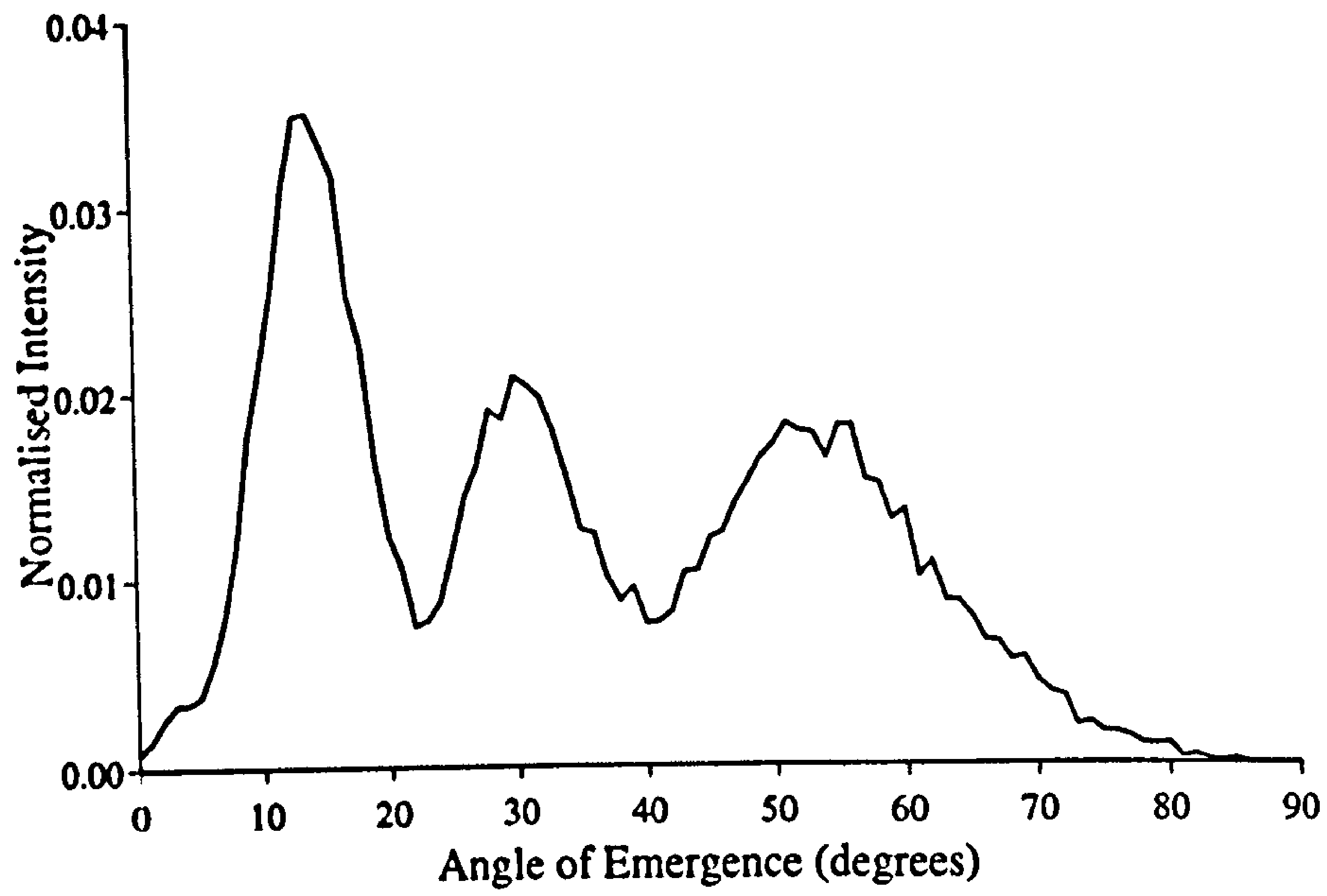

Figure C.1: *Angle of emergence of single scattered photons.*

the source of 0.25MFP, therefore being observed in the second radial bin in figure 3.16.

Appendix D

Tissue Phantom Construction

In scattering media characterisation research there is a great need for the ability to construct permanent scattering phantoms with known properties. Phantoms have been widely constructed from microsphere solutions (as they are in this study) or from media containing particles of irregular size and shape[48, 61].

Permanent solid phantoms are desirable as they allow easy repetition of experiments, provide multiple layer structures without the need for an additional separating interface and can also be machined to allow the addition of internal features or structure. Phantoms containing regular scatterers of known properties are also useful as the behaviour of light propagating in such media can be modelled with reasonable accuracy and can therefore be used to assess experimental system performance reducing modelling errors.

In an attempt to achieve the above, glycol methacrylate resin scattering phantoms containing polystyrene microspheres have been constructed. Glycol methacrylate resin is generally used for the embedding of biological samples for examination by electron microscopy(ref). Before mixing, the resin components are water soluble in a low-viscosity liquid form. This allows easy easy mixing of the solution with scattering microspheres and water based stains for absorption. To ensure the correct dimensions are achieved the resin components can be mixed and poured into a fixed dimension polypropeline mould as

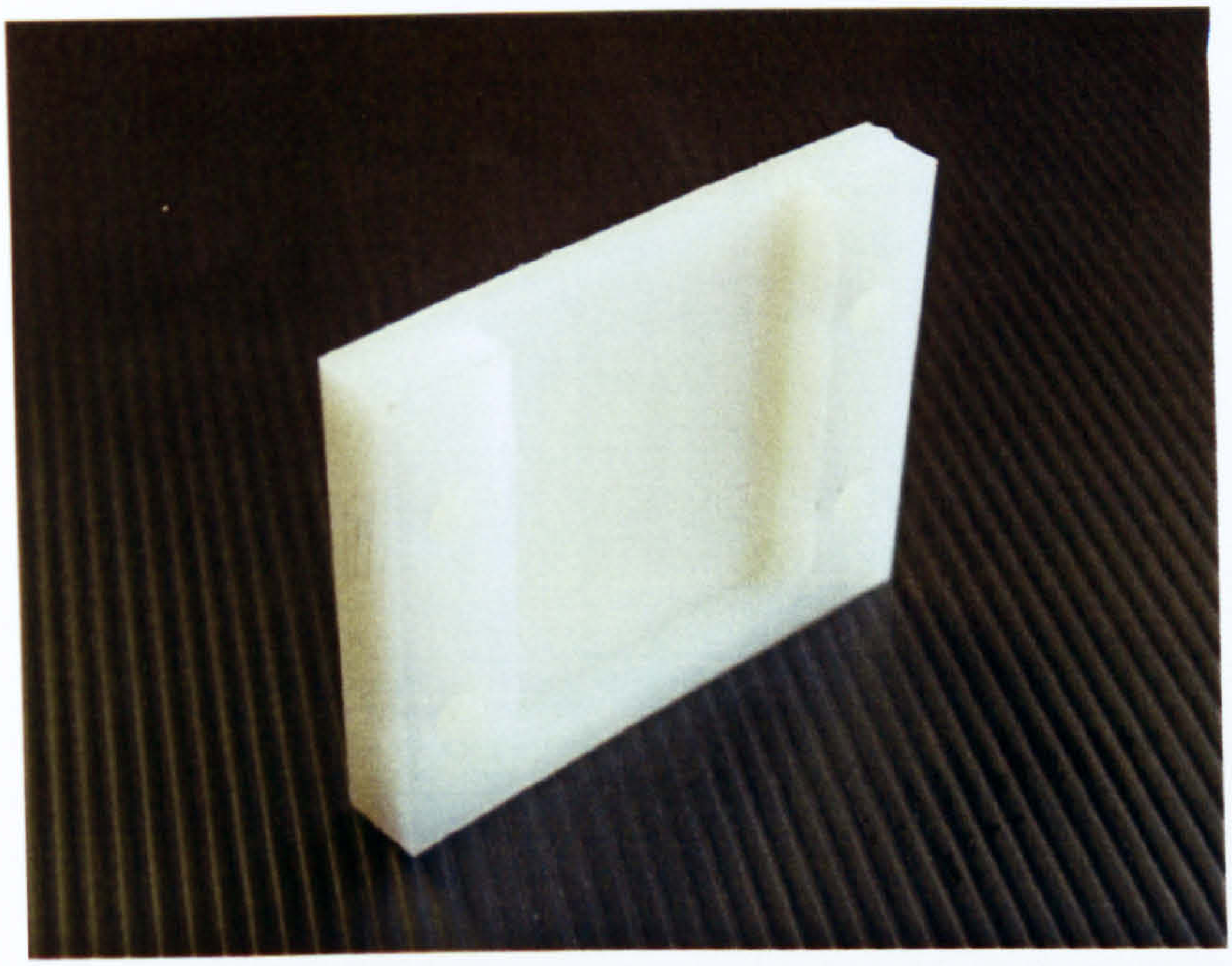

Figure D.1: *A polypropeline mould used to construct a thin scattering phantom.*

pictured in figure D.1. To slow the reaction and hardening the mould and mixed solution is placed in a refrigerator for approximately six hours. Slowing of the reaction reduces the occurrence of bubbles in the resulting phantom and ensures that the heat produced by the reaction is not excessive leading to expansion and distortion of the produced sample.

A range of samples produced using this method are shown in figure D.2. Once a sample is produced it must be stored away from prolonged exposure to ultra-violet radiation as this discolours the sample, hence altering the absorption properties.

The reason for the constructed phantoms not featuring in the experimental results presented here is due to the sample's parameters not being precisely known and therefore the performance of any experimental results may prove more sensitive to inaccuracies in the sample's properties rather than the experimental technique which is being assessed.

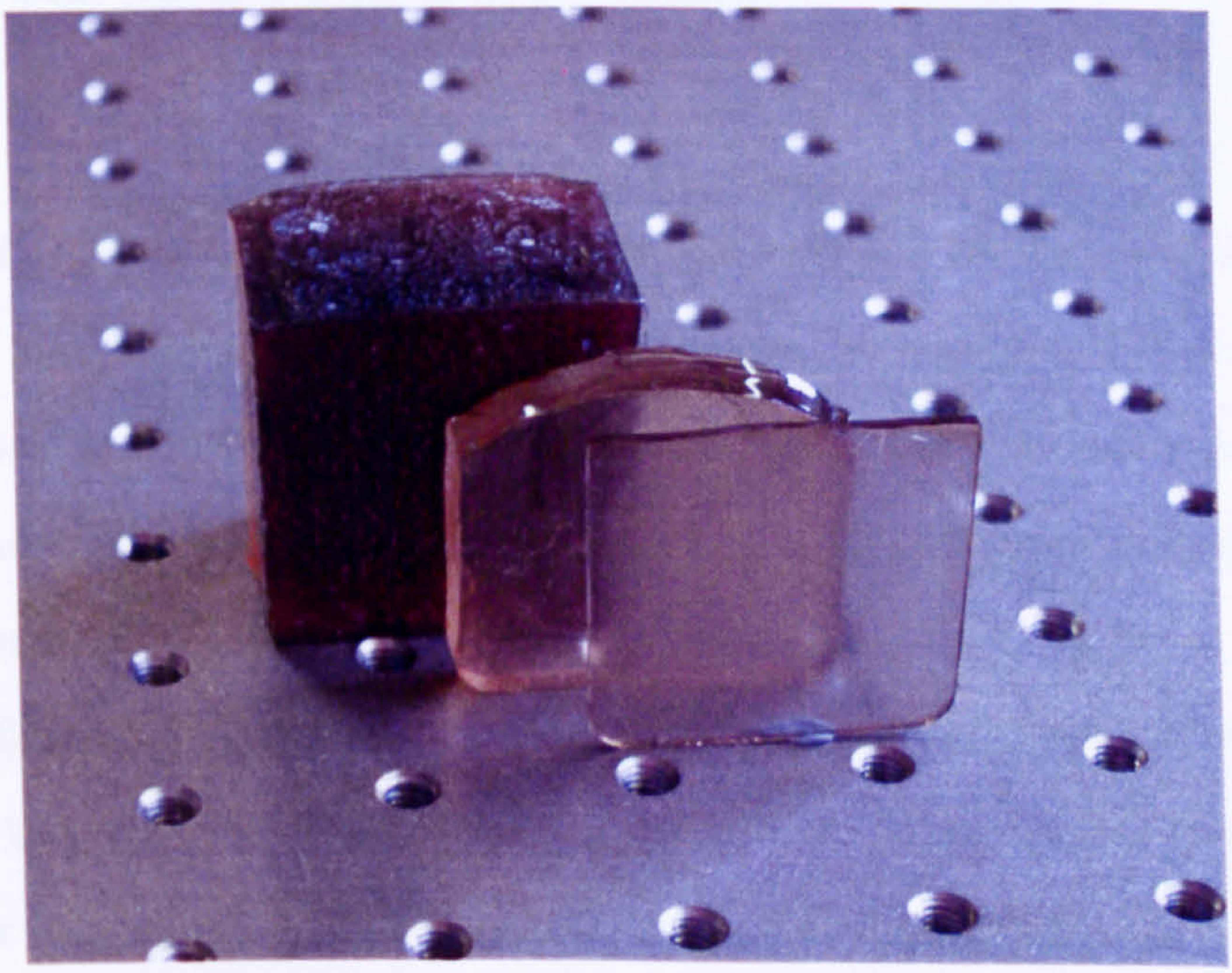

Figure D.2: *A selection of constructed glycol methacrylate resin tissue phantoms.*

Appendix E

Clinical Software Interface

To allow use of the system developed in chapter 5 in a clinical environment a user interface is necessary to allow easy use by a clinician. To achieve this a graphical interface written in Visual C++ has been developed allowing the clinician to enter patient information, view live images and record a sequence of multiple wavelength polarization images for storage with the patient's data.

Shown in figure E.1 is the interface for the clinical imaging software allowing execution of a range of imaging sequences to record a full set of sixteen images (four polarization states at four wavelengths), eight images (only polarization channels 2 and 3 at four wavelengths) or the images at a single wavelength.

These routines are programmed using a scripting language developed to control the movement of the stepper motors controlling the optics, the LED illumination, camera settings and camera image acquisition. An example of such a script is shown in figure E.2, however editing of these scripts is not available to the clinician.

Selection of an imaging sequence prompts the clinician to enter the patients identification number. Once this is entered and confirmed a unique cross-reference number is generated to ensure patient confidentiality. Live images are then streamed to the interface as shown in figure E.3 for alignment of the required area of tissue. Once this is performed

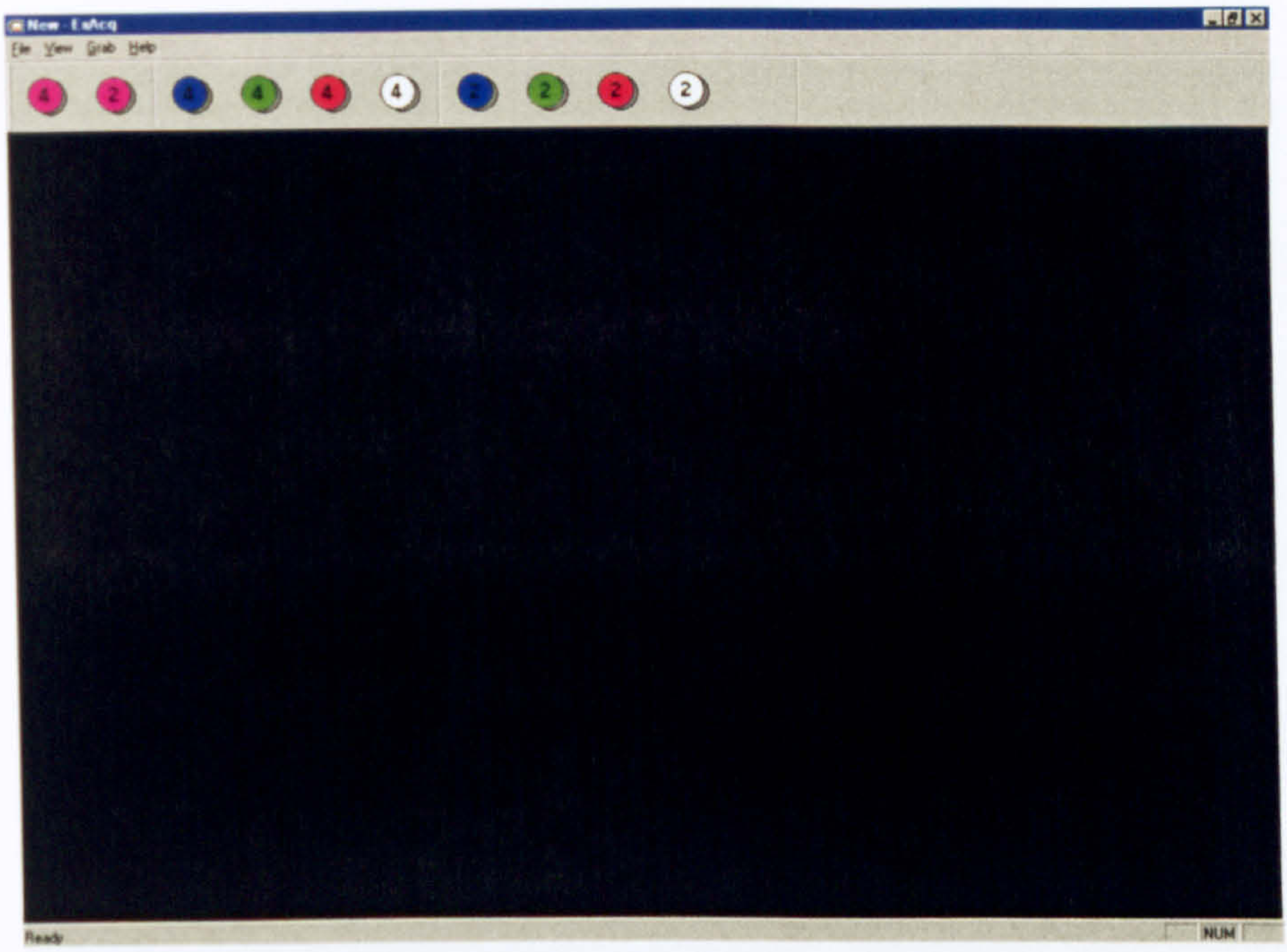

Figure E.1: *The clinical software interface.*

the imaging sequence begins. To record a full set of sixteen images takes approximately forty-five seconds. The recorded images are then stored with the corresponding imaging settings and patient information for later processing.

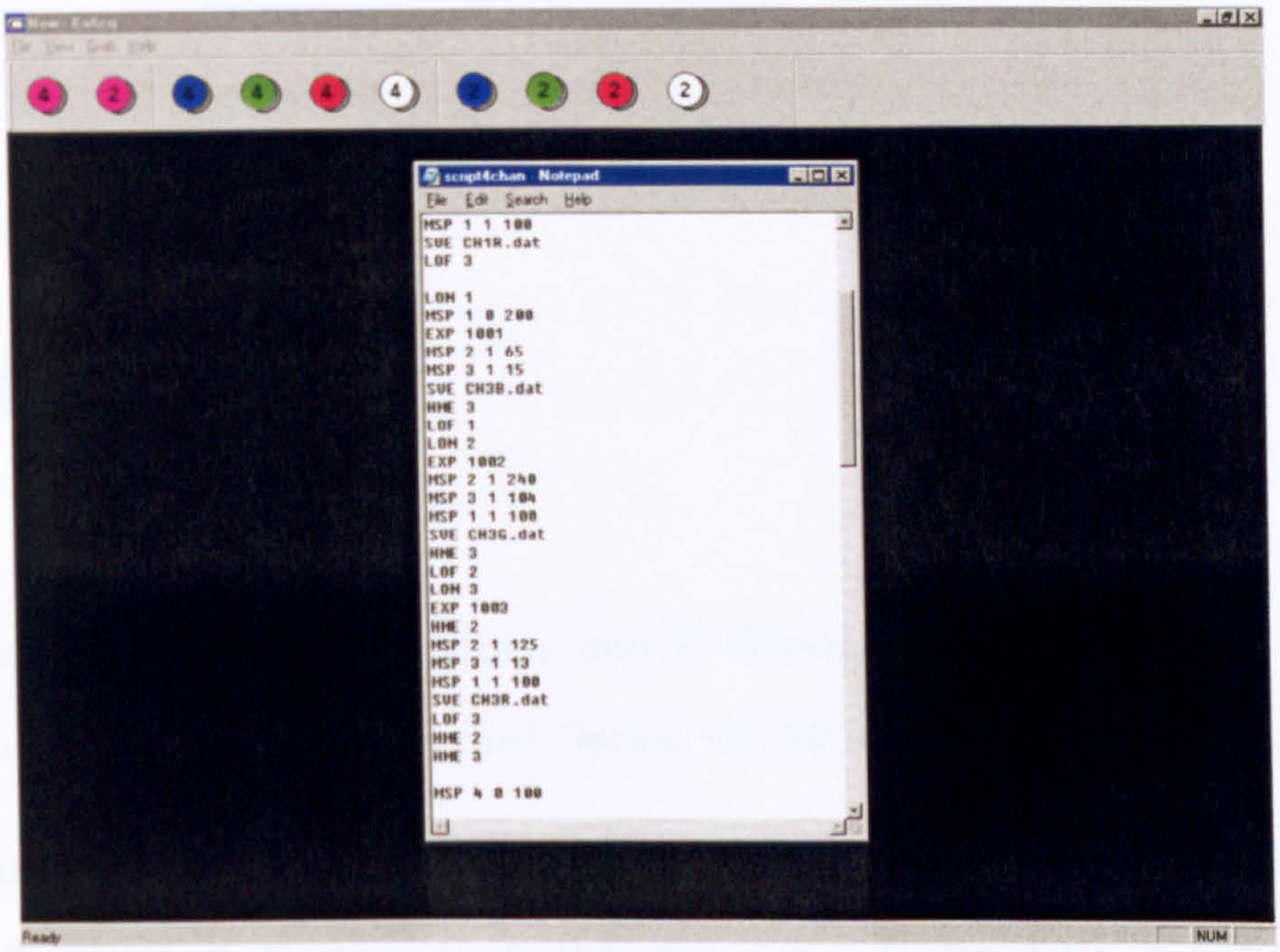

```
MSP 1 1 100
SVE CH1R.dat
LOF 3

LON 1
MSP 1 0 200
EXP 1001
MSP 2 1 65
MSP 3 1 15
SVE CH3B.dat
HME 3
LOF 1
LON 2
EXP 1002
MSP 2 1 240
MSP 3 1 104
MSP 1 1 100
SVE CH3G.dat
HME 3
LOF 2
LON 3
EXP 1003
HME 2
MSP 2 1 125
MSP 3 1 13
MSP 1 1 100
SVE CH3R.dat
LOF 3
HME 2
HME 3

MSP 4 0 100
```

Figure E.2: *The system control scripting language.*

Begin imaging sequence?

Figure E.3: *Live streaming to allow sample positioning.*

Bibliography

[1] J. Cariou, B. L. Jeune, J. Lotrian, and Y. Guern, "Polarization effects of seawater and underwater targets," *Applied Optics*, vol. 29, no. 11, pp. 1689–1695, 1990.

[2] D. Huang, E. A. Swanson, C. P. Lin, J. S. Schman, W. G. Stinson, W. Chang, M. R. Hee, T. Flotte, K. Gregory, C. A. Puliafito, and J. G. Fujimoto, "Optical coherence tomography," *Science*, vol. 254, pp. 1178–1180, 1991.

[3] H. C. van de Hulst, *Light Scattering By Small Particles.* New York, NY, USA: Dover Publications, Inc, 1981.

[4] R. R. Anderson and J. A. Parrish, "The optics of human skin," *The Journal of Investigative Dermatology*, vol. 77, no. 1, pp. 13–19, 1981.

[5] V. V. Tuchin, *Tissue Optics.* Bellingham, WA, USA: SPIE, 2000.

[6] F. C. MacKintosh and S. John, "Diffusing-wave spectroscopy and multiple scattering of light in correlated random media," *Physical Review B*, vol. 40, no. 4, pp. 2383–2406, 1989.

[7] W. F. Lever and G. Schaumburg-Lever, *Histopathology of the Skin.* Philadelphia, PA, USA: J B Lippincott Company, 7th ed., 1990.

[8] R. MacLennan, A. C. Green, G. R. C. McLeod, and N. G. Martin, "Increasing incidence of cutaneous melanoma in Queensland, Australia," *Journal of the National Cancer Institute*, vol. 84, no. 18, pp. 1427–1431, 1992.

[9] P. L. Jelfs, G. Giles, D. Shugg, M. Coates, G. Durling, P. Fitzgerald, and I. Ring, "Cutaneous malignant melanoma in Australia," *The Medical Journal of Australia*, vol. 161, pp. 182–187, 1994.

[10] L. Bischof, H. Talbot, E. Breen, D. Lovell, D. Chan, G. Stone, S. Menzies, A. Gutenev, and R. Caffin, "An automated melanoma diagnosis system," *SPIE Proceedings*, vol. 3747, pp. 130–141, 1999.

[11] J. D. Whited and J. M. Grinchnik, "Does this patient have a mole or a melanoma?," *Journal of the American Medical Association*, vol. 279, no. 9, pp. 696–701, 1998.

[12] R. M. MacKie, "Clinical recognition of early invasive melanoma," *British Medical Journal*, vol. 301, pp. 1005–1006, 1990.

[13] R. J. Friedman, D. S. Rigel, and A. W. Kopf, "Early detection of malignant melanoma: the role of physician examination and self examination of the skin," *A Cancer Journal for Clinicians*, vol. 35, no. 3, pp. 130–151, 1985.

[14] R. J. Motley and J. P. A. Holt, "No case against Mohs' surgery," *Acta Dermato-Venereologica*, vol. 79, no. 6, p. 498, 1999.

[15] G. Colver, ed., *Skin Cancer: A Practical Guide to Management.* London, UK: Martin Dunitz Ltd., 2002.

[16] R. M. MacKie, *Skin Cancer.* London, UK: Martin Dunitz Ltd., 1989.

[17] S. Cotton, *A non-invasive imaging system for assisting in the diagnosis of malignant melanoma.* PhD thesis, The University of Birmingham, 1998.

[18] O. Barajas, A. M. Ballangrud, G. G. Miller, R. B. Moore, and J. Tulip, "Monte Carlo modelling of angular radiance in tissue phantoms and human prostate: PDT light dosimetry," *Physics in Medicine and Biology*, vol. 42, pp. 1675–1687, 1997.

[19] D. T. Delpy, M. Cope, P. van der Zee, S. Arridge, S. Wray, and J. Wyatt, "Estimation of optical pathlength through tissue from direct time of flight measurement," *Physics in Medicine and Biology*, vol. 33, no. 12, pp. 1433–1442, 1988.

[20] A. H. Hielscher, H. Liu, B. Chance, F. K. Tittel, and S. L. Jacques, "Time-resolved photon emission from layered turbid media," *Applied Optics*, vol. 35, no. 4, pp. 719–728, 1996.

[21] T. H. Pham, T. Spott, L. O. Svaasand, and B. J. Tromberg, "Quantifying the properties of two-layer turbid media with frequency-domain diffuse reflectance," *Applied Optics*, vol. 39, no. 25, pp. 4733–4745, 2000.

[22] G. Alexandrakis, D. R. Busch, G. W. Faris, and M. S. Patterson, "Determination of the optical properties of two-layer turbid media by use of a frequency domain hybrid Monte Carlo diffusion model," *Applied Optics*, vol. 40, no. 22, pp. 3810–3821, 2001.

[23] J. M. Schmitt, "Optical coherence tomography (OCT): A review," *Journal of Selected Topics in Quantum Electronics*, vol. 5, no. 4, pp. 1205–1215, 1999.

[24] R. K. Wang, X. Xu, V. V. Tuchin, and J. B. Elder, "Concurrent enhancement of imaging depth and contrast for optical coherence tomography by hyperosmotic agents," *Journal of the Optical Society of America B*, vol. 18, no. 7, pp. 948–953, 2001.

[25] F. C. MacKintosh, J. X. Zhu, D. J. Pine, and D. A. Weitz, "Polarization memory of multiply scattered light," *Physical Review B*, vol. 40, no. 13, pp. 9342–9375, 1989.

[26] S. R. Arridge and J. C. Hebden, "Optical imaging in medicine: II. modelling and reconstruction," *Physics in Medicine and Biology*, vol. 42, pp. 841–853, 1997.

[27] W. F. Cheong, S. A. Prahl, and A. J. Welch, "A review of the optical properties of biological tissues," *IEEE Journal of Quantum Electronics*, vol. 26, no. 12, pp. 2166–2185, 1990.

[28] S. Baker, *Optimal determination of the optical coefficients from scattering media.* PhD thesis, The University of Nottingham, 2002.

[29] S. T. Flock, M. S. Patterson, B. C. Wilson, and D. R. Wyman, "Monte Carlo modeling of light propagation in highly scattering tissues - I: model predictions and comparison with diffusion theory," *IEEE Transactions on Biomedical Engineering*, vol. 36, no. 12, pp. 1162–1168, 1989.

[30] D. Contini, F. Martelli, and G. Zaccanti, "Photon migration through a turbid slab described by a model based on diffusion theory," *Applied Optics*, vol. 36, no. 19, pp. 4587–4599, 1997.

[31] M. S. Patterson, B. Chance, and B. C. Wilson, "Time resolved reflectance and transmittance for the non-invasive measurement of tissue optical properties," *Applied Optics*, vol. 28, no. 12, pp. 2331–2336, 1989.

[32] M. J. C. van Gemert, S. l Jacques, H. J. C. M. Sterenborg, and W. M. Star, "Skin optics," *IEEE Transactions on Biomedical Engineering*, vol. 36, no. 12, pp. 1146–1154, 1989.

[33] F. Martelli, M. Bassani, L. Alianelli, L. Zangheri, and G. Zaccanti, "Accuracy of the diffusion equation to describe photon migration through an infinite medium: numerical and experimental investigation," *Physics in Medicine and Biology*, vol. 45, pp. 1359–1373, 2000.

[34] L. G. Henyey and J. L. Greenstein, "Diffuse radiation in the galaxy," *Astrophysics Journal*, vol. 93, pp. 70–83, 1941.

[35] C. Bohren and D. R. Huffman, *Absorption and Scattering of Light by Small Particles.* New York, USA: John Wiley and Sons, Inc, 1998.

[36] A. Kienle and M. S. Patterson, "Determination of the optical properties of turbid media from a single Monte Carlo simulation," *Physics in Medicine and Biology*, vol. 41, pp. 2221-2227, 1996.

[37] S. Chatigny, M. Morin, D. Asselin, Y. Painchaud, and P. Beaudry, "Hybrid Monte Carlo for photon transport through optically thick scattering media," *Applied Optics*, vol. 38, no. 28, pp. 6075-6086, 1999.

[38] P. C. Y. Chang, J. G. Walker, K. I. Hopcraft, B. Ablitt, and E. Jakeman, "Polarization discrimination for active imaging in scattering media," *Optics Communications*, vol. 159, pp. 1-6, 1999.

[39] W. S. Bickel and W. M. Bailey, "Stokes vectors, Mueller matrices, and polarized scattered light," *American Journal of Physics*, vol. 53, no. 5, pp. 168-640, 1985.

[40] B. R. Masters and P. T. C. So, "Confocal microscopy and multi-photon excitation microscopy of human skin *in-vivo*," *Optics Express*, vol. 8, no. 1, pp. 2-10, 2000.

[41] C. L. Smithpeter, A. K. Dunn, A. J. Welch, and R. Richards-Kortum, "Penetration depth limits of *in-vivo* confocal reflectance imaging," *Applied Optics*, vol. 37, no. 13, pp. 2749-2754, 1998.

[42] M. Mehrubeoglu, N. Kehtarnavaz, G. Marquez, and L. Wang, "Skin lesion classification using reflectance spectroscopic imaging with oblique incidence," *Applied Optics*, vol. 41, no. 1, pp. 182-192, 2002.

[43] V. J. Anselmo and B. E. Zawacki, "A new quantitative tool to assist in the early diagnosis of thermal burn injury," *Annals of Biomedical Engineering*, vol. 5, pp. 179-193, 1977.

[44] M. A. Afromowitz, J. B. Callis, D. M. Heimbach, L. A. DeSoto, and M. K. Norton, "Multispectral imaging of burn wounds: a new clinical instrument for evaluating

burn depth," *IEEE Transactions on Biomedical Engineering*, vol. 35, no. 10, pp. 842–850, 1988.

[45] P. Kubelka, "New contributions to the optics of intensely light-scattering materials. part I," *Journal of the Optical Society of America*, vol. 38, no. 5, pp. 448–457, 1947.

[46] S. J. Matcher and C. E. Cooper, "Absolute quantification of deoxyhæmoglobin concentration in near infrared spectroscopy," *Physics in Medicine and Biology*, vol. 39, pp. 1295–1312, 1994.

[47] L. T. Perelman, V. Backman, M. Wallace, G. Zonois, R. Manoharan, A. Nusrat, S. Shields, M. Seiler, C. Lima, T. Hamano, I. Itzkan, J. van Dam, J. M. Crawford, and M. Feld, "Observation of periodic fine structure in reflectance from biological tissue: A new technique for measuring nuclear size distribution," *Physical Review Letters*, vol. 80, no. 3, pp. 627–630, 1998.

[48] V. Backman, R. Gurjar, K. Badizadegan, I. Itzkan, R. R. Dasari, L. T. Perelman, and M. S. Feld, "Polarized light scattering spectroscopy for quantitative measurement of epithelial cellular structures *in situ*," *IEEE Journal of Selected Topics in Quantum Electronics*, vol. 5, no. 4, pp. 1019–1026, 1999.

[49] M. Bartlett and H. Jiang, "Measurement of particle size distribution in multilayered skin phantoms using polarized light spectroscopy," *Physical Review E*, vol. 65, p. 031906, 2002.

[50] S. G. Demos and R. R. Alfano, "Optical polarization imaging," *Applied Optics*, vol. 36, no. 1, pp. 150–155, 1997.

[51] S. G. Demos, H. B. Radousky, and R. R. Alfano, "Deep subsurface imaging in tissues using spectral and polarization filtering," *Optics Express*, vol. 7, no. 1, pp. 23–28, 2000.

[52] E. A. Swanson, D. Huang, M. R. Hee, J. G. Fujimoto, C. P. Lin, and C. A. Puliafito, "High-speed optical coherence domain reflectometry," *Optics Letters*, vol. 17, pp. 151–153, 1992.

[53] R. K. Wang, "Signal degradation by multiple scattering in optical coherence tomography of dense tissue: a Monte Carlo study towards optical clearing of biotissues," *Physics in Medicine and Biology*, vol. 47, pp. 2281–2299, 2002.

[54] W. Drexler, U. Morgner, F. X. Kärtner, C. Pitris, S. A. Boppart, X. D. Li, E. P. Ippen, and J. G. Fujimoto, "*In vivo* ultra-high resolution optical coherence tomography," *Optics Letters*, vol. 24, no. 17, pp. 1221–1223, 1999.

[55] A. Dubois, G. Moneron, K. Grieve, and A. C. Boccara, "Three-dimensional cellular-level imaging using full-field optical coherence tomography," *Physics in Medicine and Biology*, vol. 49, pp. 1227–1234, 2004.

[56] L. Thrane, M. H. Frosz, T. M. Jorgensen, A. Tycho, H. T. Yura, and P. E. Andersen, "Extraction of optical scattering parameters and attenuation compensation in optical coherence tomography images of multilayered tissue structures," *Optics Letters*, vol. 29, no. 14, pp. 1641–1643, 2004.

[57] L. Thrane, H. T. Yura, and P. E. Andersen, "Analysis of optical coherence tomography systems based on the extended Huygens-Fresnel principle," *Journal of the Optical Society of America A*, vol. 17, no. 3, pp. 484–490, 2000.

[58] U. Morgner, W. Drexler, F. X. Kärtner, X. D. Li, C. Pitris, E. P. Ippen, and J. G. Fujimoto, "Spectroscopic optical coherence tomography," *Optics Letters*, vol. 25, no. 2, pp. 111–113, 2000.

[59] J. C. Hebden, R. A. Kruger, and K. S. Wong, "Time resolved imaging through a highly scattering medium," *Applied Optics*, vol. 30, no. 7, pp. 788–794, 1991.

[60] J. C. Hebden, "Evaluating the spatial resolution of a time resolved optical imaging system," *Medical Physics*, vol. 19, no. 4, pp. 1081–1087, 1992.

[61] J. C. Hebden, D. J. Hall, M. Firbank, and D. T. Delpy, "Time-resolved optical imaging of a solid tissue-equivalent phantom," *Applied Optics*, vol. 34, no. 34, pp. 8038–8046, 1995.

[62] G. Mitic, J. Kőlzer, J. Otto, E. Plies, G. Sőlkner, and W. Zinth, "Time-gated transillumination of biological tissues and tissuelike phantoms," *Applied Optics*, vol. 33, no. 28, pp. 6699–6710, 1994.

[63] S. L. Jacques, "Time-resolved reflectance spectroscopy in turbid tissues," *IEEE Transactions on Biomedical Engineering*, vol. 36, no. 12, pp. 1155–1161, 1989.

[64] S. J. Madsen, B. C. Wilson, M. S. Patterson, Y. D. Park, S. L. Jacques, and Y. Hefetz, "Experimental tests of a simple diffusion model for the estimation of scattering and absorption coefficients of turbid media from time-resolved diffuse reflectance measurements," *Applied Optics*, vol. 31, no. 18, pp. 3509–3517, 1992.

[65] A. Pifferi, P. Taroni, G. Valentini, and S. Andersson-Engels, "Real-time method for fitting time-resolved reflectance and transmittance measurements with a Monte Carlo model," *Applied Optics*, vol. 37, no. 13, pp. 2774–2780, 1998.

[66] A. Pifferi, P. Taroni, A. Torricelli, F. Messina, R. Chubeddu, and G. Danesini, "Four-wavelength time-resolved optical mammography in the 680-980nm range," *Optics Letters*, vol. 28, no. 13, pp. 1138–1140, 2003.

[67] A. Torricelli, A. Pifferi, P. Taroni, E. Giambattistelli, and R. Cubeddu, "*In-vivo* optical characterisation of human tissues from 610 to 1010nm by time-resolved reflectance spectroscopy," *Physics in Medicine and Biology*, vol. 46, pp. 2227–2237, 2001.

[68] V. Ntziachristos, A. G. Yodh, and B. Chance, "Accuracy limits in the determination of absolute optical properties using time-resolved NIR spectroscopy," *Proceedings of the SPIE: Optical Tomography and Spectroscopy of Tissue III*, vol. 3597, pp. 493–502, 1999.

[69] S. J. Madsen, P. Wyss, L. O. Svaasand, R. C. Haskell, Y. Tadir, and B. J. Tromberg, "Determination of the optical properties of the human uterus using frequency-domain photon migration and steady-state techniques," *Physics in Medicine and Biology*, vol. 39, pp. 1191–1202, 1994.

[70] A. Kienle and M. S. Patterson, "Determination of the optical properties of semi-infinite turbid media from frequency-domain reflectance close to the source," *Physics in Medicine and Biology*, vol. 42, pp. 1801–1819, 1997.

[71] L. O. Svaasand, T. Spott, J. B. Fishkin, T. Pham, B. J. Tromberg, and M. W. Berns, "Reflectance measurements of layered media with photon-density waves: A potential tool for evaluating deep burns and subcutaneous lesions," *Physics and Medicine in Biology*, vol. 44, pp. 801–813, 1999.

[72] R. Bays, G. Wagnières, D. Robert, D. Braichotte, J.-F. Savary, P. Monnier, and H. van den Bergh, "Clinical determination of tissue optical properties by endoscopic spatially resolved reflectometry," *Applied Optics*, vol. 35, no. 10, pp. 1756–1766, 1996.

[73] A. Kienle, L. Lilge, M. S. Patterson, R. Hibst, R. Steiner, and B. C. Wilson, "Spatially resolved absolute reflectance measurements for noninvasive determination of the optical scattering and absorption coefficients of biological tissue," *Applied Optics*, vol. 35, no. 13, pp. 2304–2314, 1996.

[74] A. H. Hielscher, H. Liu, B. Chance, F. K. Tittel, and S. L. Jacques, "Influence of particle size and concentration on the diffuse backscattering of polarized light

from tissue phantoms and biological cell suspensions," *Applied Optics*, vol. 36, no. 1, pp. 125–134, 1997.

[75] M. J. Raković, G. W. Kattawar, M. Mehrübeoğlu, B. D. Cameron, L. V. Wang, S. Rastegar, and G. L. Coté, "Light backscattering polarization patterns from turbid media: theory and experiment," *Applied Optics*, vol. 38, no. 15, pp. 3399–3408, 1999.

[76] X. Wang and L. V. Wang, "Propagation of polarized light in birefringent turbid media: time-resolved simulations," *Optics Express*, vol. 9, pp. 254–259, 2001.

[77] D. Bicout and C. Brosseau, "Multiply scattered waves through a spatially random medium: entropy production and depolarization," *Journal De Physique I*, vol. 2, pp. 2047-2063, 1992.

[78] D. Bicout, C. Brosseau, A. S. Martinez, and J. M. Schmitt, "Depolarization of multiply scattered waves by spherical diffusers: influence of the size parameter," *Physical Review E*, vol. 49, no. 2, pp. 1767–1770, 1994.

[79] K. M. Yoo and R. R. Alfano, "Time resolved depolarization of multiple backscattered light from random media," *Physics Letters A*, vol. 142, no. 8, pp. 531-536, 1989.

[80] J. M. Schmitt, A. M. Gandjbakhche, and R. F. Bonner, "Use of polarized light to discriminate short-path photons in a multiply scattering medium," *Applied Optics*, vol. 31, no. 30, pp. 6535–6546, 1992.

[81] O. Emile, F. Bretenaker, and A. L. Floch, "Rotating polarization imaging in turbid media," *Optics Letters*, vol. 21, no. 20, pp. 1706–1708, 1996.

[82] S. P. Morgan and M. E. Ridgway, "Polarization properties of backscattered light from a two layer scattering medium," *Optics Express*, vol. 7, no. 12, pp. 395–402, 2000.

[83] R. R. Anderson, "Polarized light examination and photography of the skin," *Archives of Dermatology*, vol. 127, pp. 1000–1005, 1991.

[84] S. L. Jacques, J. C. Ramella-Roman, and K. Lee, "Imaging skin pathology with polarized light," *Journal of Biomedical Optics*, vol. 7, no. 3, pp. 329–340, 2002.

[85] S. L. Jacques, J. R. Roman, and K. Lee, "Imaging superficial tissues with polarized light," *Lasers in Surgery and Medicine*, vol. 26, pp. 119–129, 2000.

[86] E. Hecht, *Optics*. Reading, MA, USA: Addison Wesley Longman, Inc., 3rd ed., 1998.

[87] J. F. de Boer, T. E. Milner, M. J. C. van Gemert, and J. S. Nelson, "Two-dimensional birefringence imaging in biological tissue by polarization-sensitive optical coherence tomography," *Optics Letters*, vol. 22, no. 12, pp. 934–936, 1997.

[88] Y. Yang, L. Wu, Y. Feng, and R. K. Wang, "Observations of birefringence in tissues for optic-fibre-based optical coherence tomography," *Measurement Science and Technology*, vol. 14, pp. 41–46, 2003.

[89] N. Cascinelli, M. Ferrario, T. Tonelli, and E. Leo, "A possible new tool for clinical diagnosis of melanoma: the computer," *Journal of the American Journal of Dermatology*, vol. 16, no. 2, pp. 361–367, 1987.

[90] E. Claridge, P. N. Hall, M. Keefe, and J. P. Allen, "Shape analysis for classification of malignant melanoma," *Journal of Biomedical Engineering*, vol. 14, pp. 229–234, 1992.

[91] A. Green, N. Martin, J. Pfitzner, M. O'Rourke, and N. Knight, "Computer image analysis in the diagnosis of melanoma," *Journal of the American Academy of Dermatology*, vol. 31, no. 6, pp. 958–963, 1994.

[92] N. Cascinelli, M. Ferrario, R. Bufalino, S. Zurrida, V. Galimberti, L. Mascheroni, C. Bartoli, and C. Clemente, "Results obtained by using a computerized image

analysis system designed as an aid to diagnosis of cutaneous melanoma," *Melanoma Research*, vol. 2, no. 3, pp. 163–170, 1992.

[93] T. Schindewolf, R. Schiffner, W. Stolz, R. Albert, W. Abmayr, and H. Harms, "Evaluation of different image acquisition techniques for a computer vision system in the diagnosis of malignant melanoma," *Journal of the American Journal of Dermatology*, vol. 31, no. 1, pp. 33–41, 1994.

[94] H. P. Soyer, J. Smolle, H. Kerl, and H. Steiner, "Early diagnosis of malignant melanoma by surface microscopy," *The Lancet*, vol. 2, p. 803, 1987.

[95] D. S. Riegel, "Epilluminescence microscopy in clinical diagnosis of pigmented skin lesions," *The Lancet*, vol. 349, pp. 1566–1567, 1997.

[96] M. Coppleson, B. L. Reid, V. N. Skladnev, and J. C. Dalrymple, "An electronic approach to the detection of pre-cancer and cancer of the uterine cervix: a preliminary evaluation of polarprobe," *International Journal of Gynecological Cancer*, vol. 4, pp. 79–83, 1994.

[97] L. Breiman, J. Friedman, R. Olshen, and C. Stone, *Classification and Regression Trees*. Belmont, CA, USA: Wadsworth, 1984.

[98] S. W. Menzies, C. Ingvar, K. A. Crotty, and W. H. McCarthy, "Frequency and morphologic characteristics of invasive melanomas lacking specific surface microscopic features," *Archives of Dermatology*, vol. 132, pp. 1178–1182, 1996.

[99] A. Gutenev, V. N. Skladnev, and D. Varvel, "Acquisition-time image quality control in digital dermatoscopy of skin lesions," *Computerized Medical Imaging and Graphics*, vol. 25, pp. 495–499, 2001.

[100] S. W. Menzies, A. Gutenev, M. Avramidis, A. Batrac, and W. H. McCarthy, "Short-term digital surface microscopy monitoring of atypical or changing melanocytic lesions," *Archives of Dermatology*, vol. 137, pp. 1583–1589, 2001.

[101] K. Hoffmann, T. Gambichler, A. Rick, M. Kreutz, M. Anschuetz, T. Grünendick, A. Orlikov, S. Gehlen, R. Perotti, L. Andreassi, J. Newton-Bishop, J. P. Césarini, T. Fischer, P. J. Frosch, R. Lindskov, R. MacKie, D. Nashan, A. Sommer, M. Neumann, J. P. Ortonne, P. Bahadoran, P. F. Penas, U. Zoras, and P. Altmeyer, "Diagnostic and neural analysis of skin cancer (DANAOS). a multicentre study for collection and computer-aided analysis of data from pigmented skin lesions using digital dermatoscopy," *British Journal of Dermatology*, vol. 149, pp. 801–809, 2003.

[102] F. Ercal, M. Moganti, W. V. Stoecker, and R. H. Moss, "Detection of skin tumor boundaries in color images," *IEEE Transactions on Medical Imaging*, vol. 12, no. 3, pp. 624-627, 1993.

[103] L. Xu, M. Jackowski, A. A. Goshtasby, D. Roseman, S. Bines, C. T. Yu, A. Dhawan, and A. Huntley, "Segmentation of skin cancer images," *Image Vision Computing*, vol. 17, no. 1, pp. 65–74, 1999.

[104] P. Schmid, "Segmentation of digitized dermatoscopic images by two-dimensional color clustering," *IEEE transactions on Medical Imaging*, vol. 18, no. 2, pp. 164–171, 1999.

[105] W. V. Stoecker, C. S. Chiang, and R. H. Moss, "Texture in skin images: comparison of three methods to determine smoothness," *Computerized Medical Imaging and Graphics*, vol. 16, pp. 179–190, 1992.

[106] F. Ercal, A. Chawla, W. V. Stoecker, H. C. Lee, and R. H. Moss, "Neural network diagnosis of malignant melanoma from color images," *IEEE Transactions on Biomedical Engineering*, vol. 41, no. 9, pp. 837–845, 1994.

[107] T. O. Nelson, "ROC curves and measures of discrimination accuracy: A reply to Swets," *Psychological Bulletin*, vol. 100, no. 1, pp. 128–132, 1986.

[108] P. Rubegni, M. Burroni, G. Cevenini, R. Perotti, G. Dell'Eva, P. Barbini, M. Fimiani, and L. Andreassi, "Digital dermoscopy analysis and artificial neural network for the differentiation of clinically atypical pigmented skin lesions: A retrospective study," *The Journal of Investigative Dermatology*, vol. 119, no. 2, pp. 471–474, 2002.

[109] P. Bauer, P. Cristofolini, S. Boi, M. Burroni, G. Dell'Eva, R. Micciolo, and M. Christofolini, "Digital epilluminescence microscopy: usefulness in the differential diagnosis of cutaneous pigmentary lesions. a statistical comparison between visual and computer inspection," *Melanoma Research*, vol. 10, pp. 345–349, 2000.

[110] P. Rubegni, G. Cevenini, M. Burroni, R. Perotti, G. Dell'Eva, P. Sbano, C. Miracco, P. Luzi, P. Tosi, P. Barbini, and L. Andreassi, "Automated diagnosis of pigmented skin lesions," *International Journal of Cancer*, vol. 101, pp. 576–580, 2002.

[111] M. Moncrieff, S. Cotton, E. Claridge, and P. Hall, "Spectrophotometric intracutaneous analysis: A new technique for imaging pigmented skin lesions," *British Journal of Dermatology*, vol. 146, pp. 448–457, 2002.

[112] F. A. Bahmer, P. Fritsch, J. Kreusch, H. Pehamberger, C. Rohrer, I. Schindera, J. Smolle, P. Soyer, and W. Stolz, "Terminology in surface microscopy," *Journal of the American Journal of Dermatology*, vol. 23, no. 6, pp. 1159–1162, 1990.

[113] A. A. Marghoob, L. D. Swindle, C. Z. M. Moricz, F. A. S. Negron, B. Slue, A. C. Halpern, and A. W. Kopf, "Instruments and new technologies for the *in vivo* diagnosis of melanoma," *Journal of the American Academy of Dermatology*, vol. 49, no. 5, pp. 777–797, 2003.

[114] I. M. Stockford, S. P. Morgan, P. C. Y. Chang, and J. G. Walker, "Analysis of the spatial distribution of polarized light backscattered from layered scattering media," *Journal of Biomedical Optics*, vol. 7, no. 3, pp. 313–320, 2002.

[115] M. Born and E. Wolf, *Principles of Optics*. Cambridge, UK: Cambridge University Press, 7th (expanded) ed., 1999.

[116] W. A. G. Bruls and J. C. van der Leun, "Forward scattering properties of human epidermal layers," *Photochemistry and Photobiology*, vol. 40, no. 2, pp. 231–242, 1984.

[117] R. Graaff, J. G. Aarnoudse, J. R. Zijp, P. M. A. Sloot, F. F. M. de Mul, J. Greve, and M. H. Koelink, "Reduced light-scattering properties for mixtures of spherical particles: A simple approximation derived from Mie calculations," *Applied Optics*, vol. 31, no. 10, pp. 1370–1376, 1992.

[118] R. Graaff, A. C. M. Dassel, M. H. Koelink, , F. F. M. de Mul, J. G. Aarnoudse, and W. G. Zijlstra, "Optical properties of human dermis *in-vitro* and *in-vivo*," *Applied Optics*, vol. 31, no. 10, pp. 1370–1376, 1992.

[119] W. A. G. Bruls and J. C. van der Leun, "Forward scattering properties of human epidermal layers," *Photochemistry and Photobiology*, vol. 40, no. 2, pp. 231–242, 1984.

[120] S. G. Demos and R. R. Alfano, "Temporal gating in highly scattering media by the degree of optical polarization," *Optics Letters*, vol. 21, no. 2, pp. 161–163, 1996.

[121] J. G. Walker, P. C. Y. Chang, and K. I. Hopcraft, "Visibility depth improvement in active polarization imaging in scattering media," *Applied Optics*, vol. 39, no. 27, pp. 4933–4941, 2000.

[122] S. P. Morgan, M. P. Khong, and M. G. Somekh, "Effects of polarization state and scatterer concentration on optical imaging through scattering media," *Applied Optics*, vol. 36, no. 7, pp. 1560–1565, 1997.

[123] S. F. Baker, J. G. Walker, and K. I. Hopcraft, "Optimal extraction of optical coefficients from scattering media," *Optics Communications*, vol. 187, pp. 17–27, 2001.

[124] S. P. Morgan and I. M. Stockford, "Surface-reflection elimination in polarization imaging of superficial tissue," *Optics Letters*, vol. 28, no. 2, pp. 114–116, 2003.

[125] W. Stolz, O. Braun-Falco, P. Bilek, M. Landthaler, and A. B. Cognetta, *Color Atlas of Dermatoscopy.* Oxford, UK: Blackwell Science, 1993.

[126] W. Groner, J. W. Winkelman, A. G. Harris, C. Ince, G. J. Bouma, K. Messmer, and R. G. Nadeau, "Orthogonal polarization spectral imaging: A new method for study of the microcirculation," *Nature Medicine*, vol. 5, no. 10, pp. 1209–1212, 1999.

[127] A. R. Young, "Chromophores in human skin," *Physics in Medicine and Biology*, vol. 42, pp. 789–802, 1997.

[128] M. C. Pitter, R. A. Light, M. G. Somekh, M. Clark, and B. R. Hayes-Gill, "Dual-phase synchronous light detection with 64 × 64 CMOS modulated light camera," *Electronics Letters (Currently Under Review)*, 2004.

[129] A. Yodh and B. Chance, "Spectroscopy and imaging with diffusing light," *Physics Today*, vol. 48, no. 3, pp. 34–40, 1995.

[130] S. Nouveau-Richard, M. Monot, P. Bastien, and O. de Lacharriere, "In vivo epidermal thickness measurement: ultrasound vs. confocal imaging," *Skin Research and Technology*, vol. 10, no. 2, pp. 136–140, 2004.

[131] J. Schmitt and G. Kumar, "Optical scattering properties of soft tissue: a discrete particle model," *Applied Optics*, vol. 37, pp. 2788–2797, 1998.

[132] A. Brunsting and P. F. Mullaney, "Light scattering from coated spheres," *Applied Optics*, vol. 11, no. 3, pp. 675–680, 1972.

[133] R. Drezek, A. Dunn, and R. Richards-Kortum, "Light scattering from cells: finite-difference time-domain simulations and goniometric measurements," *Applied Optics*, vol. 38, no. 16, pp. 3651–3661, 1999.